The Volatility of Far-Ultraviolet Radiation from Low-Mass Stars and Planetary Implications

by

R. O. Parke Loyd

B.S., Virginia Tech, 2009

M.S., University of Colorado, 2013

A thesis submitted to the

Faculty of the Graduate School of the

University of Colorado in partial fulfillment

of the requirements for the degree of

Doctor of Philosophy

Department of Astrophysical and Planetary Sciences

2017

This thesis entitled:
The Volatility of Far-Ultraviolet Radiation from Low-Mass Stars and Planetary Implications
written by R. O. Parke Loyd
has been approved for the Department of Astrophysical and Planetary Sciences

Prof. Kevin France

Prof. David Brain

Prof. James Green

Prof. Nils Halverson

Dr. Eric Wolf

Date

The final copy of this thesis has been examined by the signatories, and we find that both the content and the form meet acceptable presentation standards of scholarly work in the above mentioned discipline.

Loyd, R. O. Parke (Ph.D., Astrophysics)

The Volatility of Far-Ultraviolet Radiation from Low-Mass Stars and Planetary Implications

Thesis directed by Prof. Kevin France

A low-mass star emits only 0.001 – 0.01% of its electromagnetic energy in the ultraviolet (100 – 1700 Å), yet the implications for planets are profound. Radiation at the short-wavelength end of this range, the extreme ultraviolet (100 – 912 Å), powers planetary atmospheric escape that can be observed through transit spectroscopy in the far ultraviolet (FUV; 912 – 1700 Å). In addition, FUV light that penetrates further into a planet's atmosphere photolyzes molecules, driving nonthermal chemistry capable of producing O_2 and O_3 abiotically. I present results from extensive Hubble Space Telescope (HST) observations of the FUV emission from low-mass stars, focusing on its variability in time. Using all available archival data, I determined an astrophysical noise floor on detectable absorption in the C II, Si III, and Si IV FUV lines due to a transiting evaporating planet. I analyzed such a transit of the evaporating hot-Neptune GJ 436b, finding no detectable absorption in C II or Si III despite a large (>50%) transit in Lyα, but placing upper limits that agree with a photochemical-hydrodynamical model of the planetary outflow. These observations of GJ 436 were part of the MUSCLES Treasury Survey, a much larger dataset covering 7 M and 4 K dwarf stars. A time series analysis of all of these data constrained FUV flares on the surveyed M dwarfs, which I augmented with archival data on well-studied flare stars. The analysis confirmed that M dwarf flares are ubiquitous. In relative units, the FUV flares of the "inactive" MUSCLES M dwarfs are equally as energetic and frequent as those of the M dwarf flare stars. Both flare ~3 orders of magnitude more frequently than the sun. Indeed, flares possibly (if not probably) dominate the energy budget of FUV emission from M dwarf stars. Highly energetic flares occurring roughly yearly could annihilate most of the ozone from an Earth-like atmosphere. However, the effect is short-lived, unless additional reactions not accounted for or particle events play a dominant role.

Dedication

I dedicate this thesis to Karen Gill. Her clever instruction was the spark that caught.

Acknowledgements

I owe a massive debt of gratitude to the professors, peers, and friends who assisted me academically. Most notable is my wonderful advisor Kevin France. It is hard for me to imagine a more perfect mentor to guide me as I progressed from a student to a contributor in the fields of ultraviolet astronomy, low-mass stars, and exoplanets. In addition, Wendeline Everett, as a housemate, peer, and adventure partner, was a cornerstone of the environment that enabled me to succeed in my graduate career. I could devote many pages to reminiscing about all of the positive experiences we shared. Allison Youngblood was an excellent cubicle-mate with which to spend so many hours of the second half of my graduate school career. I will carry fond memories of the random questions, rants, brainstorms, and stories we shared with me for the rest of my life. Similarly, Chris Moore was an excellent office mate during my second year of research and a great friend through my entire time at CU that I will miss. Thomas Ayres and David Schenck suffered through my tedious first paper to provide an insightful critique, for which I am very grateful. Jeffrey Linsky warmed my heart through his genuine, albeit brusque, zeal for the improvement of the field and the students making their way into it. Christian Schneider was a fantastic overseas collaborator, sending emails that made me both smile and think. Tommi Koskinen was a fantastic collaborator and might have precipitated a transition for me from working with data to working with atmospheric models – time will tell. Jay Kroll and Rebecca Rapf guided enjoyable Astrobiology Journal Club sessions and were always ready to field my questions about chemistry. Michael Chaffin provided perhaps the best perspective on scientific concepts and the communication of science that I have ever encountered. I cannot express enough my gratitude for his assistance in the final months

and days before I defended. Bang Nahn and Julia Stawarz were delightful study partners as we all prepared for our comprehensive written exam.

I also owe a debt of thanks to the friends and family that have kept my extracurricular life happy and healthy: Donna Hutton, Herb Loyd, The Mollypups, Tara Loyd, Brooke Loyd, Haley Frazier, Emily Seider, Carrie Cimo, Smitha Hosmani, James Ruger, Sara Ruger, Robert Hutton, Jacqueline Hutton, Nick Verocchi, Suzanne Segalowitz, Chad Volk, Chelsie Benca, Phillip Lauffenberger, Katie Baldwin, Alex Biale, Matteo Crismani, Briana Ingermann, Adalyn Fyhrie, Brian Crosby, Mirna Estrada, Joseph Lasky, Carina Uraiqat, and Elizabeth Milliken.

Contents

Tables

Table

Figures

Figure

Structure of this Thesis

Herein the reader will find a description of the work I have completed on the time-domain analysis of stellar far-ultraviolet radiation observed with photon-counting detectors, with forays into assessing the effects of this radiation on the exoplanets orbiting these stars. This thesis will begin in Chapter 1 with a phenomenological overview of stars and exoplanets, how they are formed, how they evolve, and how they interact. I include a description of how exoplanets are detected, since this is a non-trivial and relatively recent development. The thesis will then delve in Chapter 2 into the observational techniques that form the basis of the work I have completed, detailing the physical underpinnings that enable the study of stars and planets through ultraviolet radiation as well as the mechanics of the instrumentation involved. These initial sections are written in a pedagogical style, providing in-line citations only when information specific to a single source has been given and instead providing an end-of-chapter bibliography. They progress in scope from broad to narrow, with a corresponding increase in detail.

With this foundation to work from, the reader will then be presented with three published works: observations of stellar UV variability (Chapter 3), a spectral atlas for low-mass planet hosting stars (Chapter 4), and observations of the transit of the hot-Neptune GJ 436b (Chapter 5). These are followed by an as-yet-unpublished analysis of flares detected in the same treasury-scale dataset that yielded the stellar spectral atlas and an examination of the potential implications of these flares plus the unobserved, more energetic flares they imply, on orbiting planets (Chapter 6). This completed work will then be summarized, followed by a discussion of three follow-on projects already underway.

Chapter 1

Introduction

1.1 Origins: The Formation and Evolution of Stars and Planets

1.1.1 Formation of Stars

One of the most striking aspects of stellar formation is that it continues to occur, despite the great age of the universe. This is due, in part at least, to the violent death of stars, which ejects stellar material back into the interstellar medium (ISM), the matter between stars. Because stars fuse lighter elements into heavier ones, the ISM has been enriched as it has cycled its way through stars.

In the present day universe, star formation is observed to occur within molecular clouds, regions where gas is cool enough that collisions are not sufficiently energetic to break apart molecular bonds. Despite their namesake constituent, clouds are multi-phase. In particular, they also contain dust grains.

For stars to form out of a molecular clouds, the essentially homogeneous medium of the cloud must somehow begin to become significantly inhomogeneous. This is the great challenge of star formation, as the characteristic structural lengths must progress from the many-parsec scales of the cloud to that of a stellar radius, some $7 - 10$ orders of magnitude. Classically, this problem has been formulated as one of a battle between the collapsing force of gravity and the opposing force of thermal pressure. However, observations and simulations have made it clear that supersonic turbulence and magnetic fields play key roles in mediating this collapse. In particular, molecular

clouds are riddled with supersonic turbulence. This turbulence yields the overdensities that give rise to gravitationally bound cores. However, it is also capable of disrupting these cores, and only the tail-end of the statistical distribution of these overdensities are actually dense enough to resist such disruption. This is a determining factor in the fraction of a molecular cloud's mass that will ultimately become stars.

The actual collapse of gas into stars, once overdensities sufficient to become gravitationally bound have developed, is thought to progress through several stages. In order for the gravitationally bound cloud of gas to collapse, it must rid itself of the thermal energy that is the inevitable outcome of its contraction, lest the gas pressure resulting from the particle thermal motions grow sufficient to balance the gravitational compression.

In the initial stages of collapse, the cloud is optically thin to infrared radiation, so gas thermal energy is easily disposed of through radiation out of the cloud. This conversion of thermal energy into radiation is rapid, much faster than the free-fall timescale of the cloud, the time it would take for the cloud to collapse with no force to oppose that of gravity. Therefore, initially the cloud is in a state of free-fall collapse. Eventually, the cloud becomes dense enough to be opaque to infrared emission lines from molecules, but it is still transparent to thermal submm emission from the dust grains, so the radiation simply gets reprocessed (absorbed and re-emitted) by the dust and escapes, still in a timescale short relative to the cloud's rate of collapse. When the cloud collapses to a density sufficient to be opaque even to dust emission, its collapse is checked for the first time. The core of the cloud heats until thermal pressure abruptly halts collapse, a shock forms from this abrupt halt, and further collapse progresses through this shock onto the core.

As the core grows, it heats further until thermal collisions are sufficiently energetic to dissociate hydrogen molecules, 1000 – 2000 K. Since this dissociation consumes energy from the collision, the dissociation serves as an internal, readily available energy sink and the core begins another phase of free-fall collapse until all of the molecules have been dissociated and a second shock front forms. Similarly, a third phase of collapse might occur once temperatures become sufficient to ionize atoms. The core begins to transport energy to its surface through gas convection, where it is

radiated away. When the core becomes sufficiently hot and dense to initiate fusion, the (proto)star has begun its life. This process occupies just the period between the first two frames of the diagram in Figure 1.1.

Any core with a mass greater than 0.08 $M_\odot$ can initiate hydrogen fusion. Of course, objects with masses both lower and greater than this limit can form as well. Below the limit, objects are not considered stars. They are brown dwarfs or, if below $\sim$13 M_J, free-floating planets (planets without a parent star). Above this limit, stars can reach masses several hundred times that of the sun before encountering the Eddington limit, at which radiation pressure overcomes the binding force of the star's self-gravity. The distribution of the number of objects that form as a function of mass is termed the initial mass function (IMF). Observations of present-day mass functions serve to constrain the IMF: examples from a variety of nearby groupings of stars are shown in Figure 1.2, with fits to "tapered" power laws. Above about 0.5 $M_\odot$ IMFs follow a power law with a slope of -2.35, the Salpeter distribution. The IMF clearly shows that low-mass stars dominate stellar populations, an important point to the relevancy of the work in this thesis, which focuses, for the most part, on this most numerous stellar constituent of the universe. However, an important note is that massive stars impose a disproportionate influence on the galactic environment, ionizing and compressing their surroundings with strong radiation and stellar winds and eventually disrupting and chemically enriching them when they die as supernovae.

In the next subsection, I will outline the first few stages of a star's life, stages that include the formation of orbiting planets.

1.1.2 Early Evolution of Stellar Systems

Thus far, I have neglected to introduce a critical factor in the birth of stars: angular momentum. The natal angular momentum of the cloud that becomes the star must be effectively transported outward of the core for its continued collapse. Otherwise, the core would eventually attain a spin rapid enough to prevent further collapse, well before becoming dense enough for hydrogen fusion. This transport is likely accomplished through the stresses imposed by magnetic

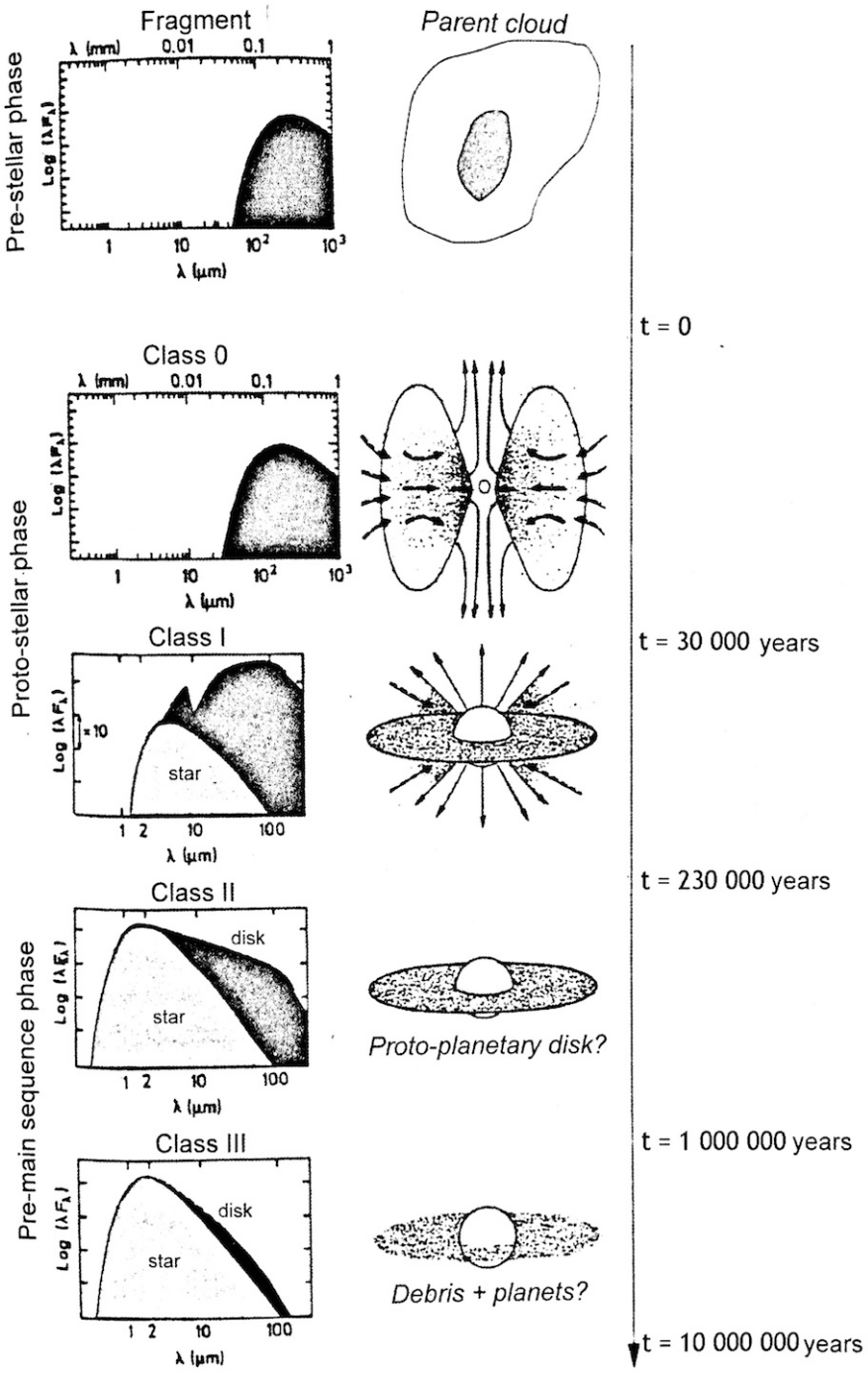

Figure 1.1 Schematic of the steps in the star formation process and the associated spectrum of emitted radiation, reproduced from Lequeux (2013) and originally attributed to Philipe André and collaborators.

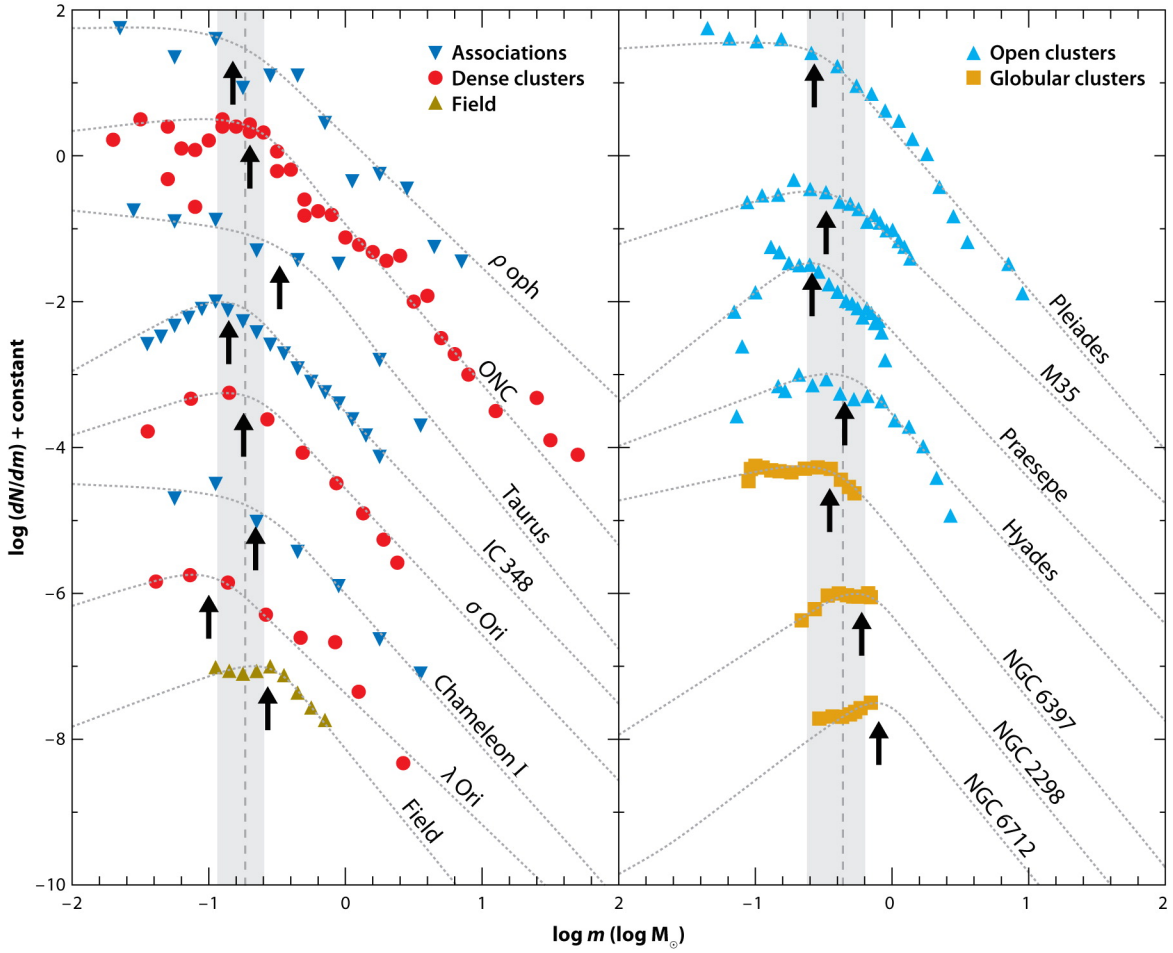

Figure 1.2 The present-day mass functions of nearby associations and clusters, reproduced from Bastian et al. (2010). Dotted lines are fits of a "tapered" power-law and the arrows show the location of the parameter specifying the transitional point of this power law, termed the characteristic mass. The vertical dashed lines are the mean of the characteristic mass parameters and the shaded area is their standard deviation.

fields and tidal forces, though these require a sufficiently ionized or dense medium, respectively. Regardless, enough angular momentum is offloaded into the surrounding medium to permit the formation of a star (they do, after all, exist). The remaining angular momentum results in the formation of a disk around the protostar.

The coalescence of this disk from the material surrounding the core is gradual enough that observations have captured stars at a variety of stages along this progression. These are the lower four panels in 1.1. Before disk coalescence, the still rapidly-accreting protostar is almost entirely obscured by the ample material surrounding it, and the spectral energy distribution (SED; left panel of 1.1) is that of the cooler surrounding material, a class 0 object. Once the majority of this envelope has been accreted by the star, coalesced into a disk, or otherwise dissipated, the stellar spectrum emerges, but the SED still rises toward far IR wavelengths, a Class I object. When the surrounding material has sufficiently cleared that the SED falls off toward the far IR, but the disk still supplements the system's SED with substantial IR emission, the protostar has become a Class II object. The first prototype of such a star was discovered in the Taurus region, resulting in the labeling of these objects as T Tauri stars.

In addition to an excess of continuum IR radiation, these stars also boast molecular line emission from the disk and strong ultraviolet emission with regular flares as a result of accretion of the disk onto the star. This accretion process is mediated by the star's magnetic field, which truncates the disk at the point where the Keplerian orbit of the disk produces a rotation rate equal to that of the star and its dipolar magnetic field. The ionized disk gas at this boundary cannot accrete in the plane of the disk because the entrained stellar magnetic field prevents the gas from slowing, as would be necessary for the gas to move inward on a Keplerian orbit. Despite this barrier, observations confirm that gas is still accreting. Therefore, it is believed that disk gas is funneled along the magnetic field, accreting where this field intersects the stellar surface away from the stellar equator. The protostellar disk produces a strong outflow due to ionization heating from the star. This material is also funneled inward, but much of it gets collimated to form a jet, a phenomenon that was first observed rather than predicted. Indeed, jets are a characteristic of

protostars even when they are still buried in their accreting envelopes.

A final stage is defined wherein the star has blown away most of the gas from its disk, leaving only a slight IR excess in the SED from the remaining gas, dust, and debris. These are Class III objects and are termed Weak-line T Tauri Stars, WTTS, because of their mild H_α line emission in comparison to "classical" T Tauri Stars, CTTS. Throughout this process, low-mass stars are thought to follow the Hyashi track down the H-R diagram, maintaining a roughly constant surface temperature but contracting as thermal energy is radiated away.

It is in the T Tauri phase of the early stellar evolution that planets form, the subject of the next subsection.

1.1.3 The Formation of Planets

Two theories have been proposed for the formation of planets[1] out of a circumstellar disk capable of reaching gas giant proportions. The first, direct gravitational collapse, is analogous to stellar formation. For collapse to occur, the self gravitation of a parcel of disk material must be strong enough to overcome gas pressure as well as viscous disruption. The latter is simply a result of the dependence of orbital period on distance: material further from the star orbits more slowly, setting up shear between material at different radii. This stability is quantified by the Toomre Q parameter. Modeling of the concentration of material to the disk midplane, a necessary criterion for portions of the disk to become unstable to collapse, appears to have yielded a consensus that direct collapse is only possible beyond about 50 AU. Therefore, while it might explain some directly imaged planets that are ∼100 AU distant from their host star, it does not explain the Solar System planets or the vast majority of exoplanets.

The alternative theory, core accretion, is currently accepted to explain the formation of gas giants within 50 AU. This theory is an extension of that which explains the formation of terrestrial planets. Like star formation theories, it is tasked with explaining how many orders of magnitude

[1] Throughout this thesis, and particularly in the first two chapters, I will use the term planet for objects orbiting both the Sun and other stars.

in the size of a structure are traversed in a relatively short period of time, within about 10 Myr. However, this process operates in the reverse, beginning with dust grains at the μm level that somehow grow to the Mm scales of a planet. The composition and total mass of solid material in the disk is a function of the disk radius, with a considerable increase in solids beyond the "frost line", where the temperature of the disk drops below the freezing point of water (Figure 1.3). The disk is heated both by stellar radius and viscous dissipation as material moves inward and accretes onto the star. Since the accretion rate changes with time, so does the location of the frost line, but in the solar system the frost line appears to have hovered around 3 AU. Beyond the frost line, $2 - 3\times$ as much solid material is available for the planet formation process.

The first phase of planet formation is the coagulation of this dust into bodies that become gravitationally bound. Pairwise collisions between dust grains can explain this growth up to about mm or cm sizes, possibly larger beyond the snow line. This process is essentially one of statistics. Grains will collide with some distribution of relative velocities, and experiments in free-fall vacuum chambers have shown that those that collide slowly enough, below $1 - 10$ m s^{-1}, can stick. As the grains grow, however, they encounter a problem: drag from the gas of the disk. The gas disk orbits just slightly slower than the Keplerian speed because the pressure of the gas acts against gravity. The adjustment to the gas speed is small, $< 1\%$, but this small difference is critical.

The sub-Keplerian speed of the gas means that objects orbiting the star experience a decelerating drag that causes their orbit to decay inward. The acceleration due to drag of a body moving through a gas follows a cube-square law. That is, the drag goes as the square of the body's linear size, whereas its mass goes as the cube of its linear size. For very small bodies, such as dust grains, drag easily overcomes the body's inertia, quickly accelerating it to the same velocity of the gas. For very large bodies, such as planets, drag is weak relative to the body's inertia and acceleration is slow. Therefore, for dust grains drag is so dominant that any inward motion is effectively halted, and for planets drag is so weak that they are not effectively decelerated and their orbits are not affected. In the middle ground drag is strong enough to cause orbital decay but too weak to effectively slow the object's inward migration. This balance is shown in Figure 1.4. The problem

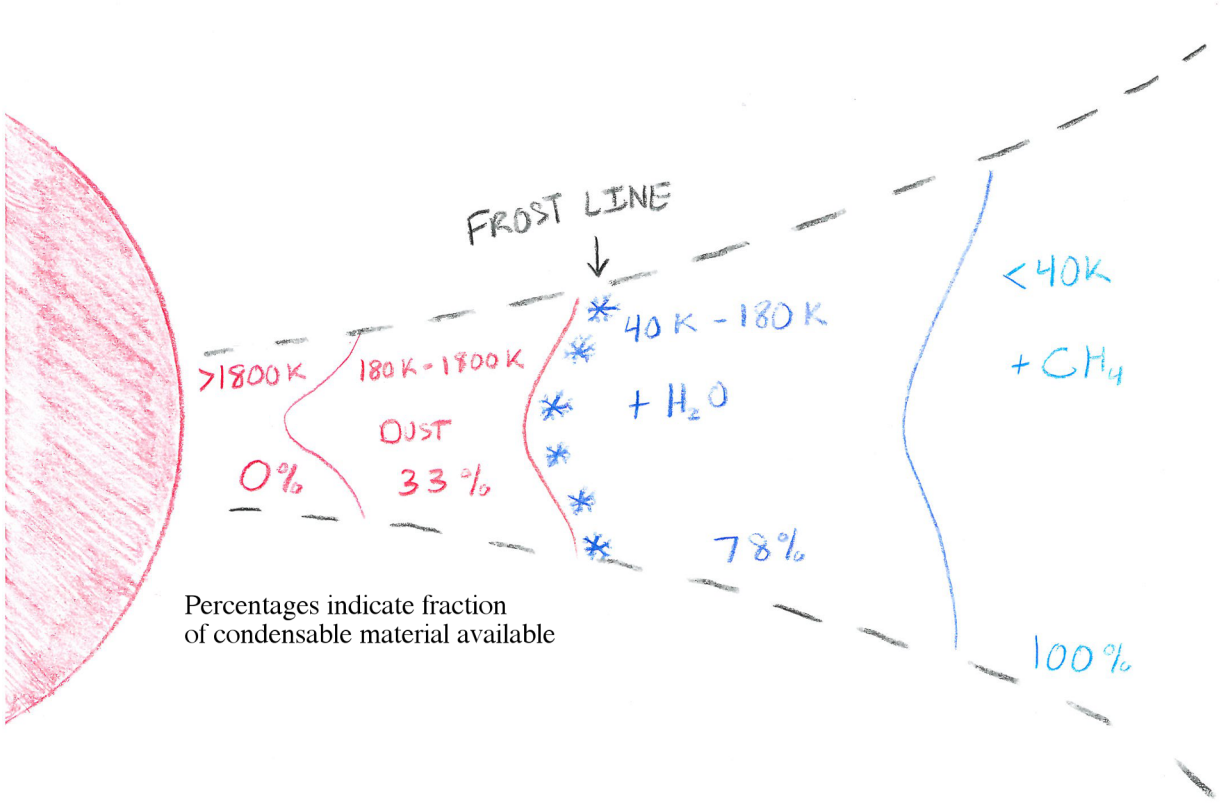

Figure 1.3 Sketch of the distribution of solids in a protoplanetary disk as a function of the disk's radially declining temperature. (Not to scale.)

peaks for objects of about 1 m in size, which could spiral into the star from 1 AU in roughly 100 y, hardly any time to make a planet. This problem is termed the "meter size barrier."

A promising avenue for overcoming the meter size barrier is the concentration of solids through hydrodynamic means rather than stochastic collisions. In particular, a hydrodynamic instability termed the Streaming Instability has been identified in numerical simulations that acts to concentrate solids (Figure 1.5). These concentrations might become compact enough that they become gravitationally bound and reach planetesimal size rapidly enough to circumvent the meter size barrier.

Once planetesimals have formed, they undergo a period of collisional growth. Similar to the coagulation of dust grains, this process is essentially stochastic, with collisions resulting in growth or disruption depending on their essentially random level of energy. Significant growth might also occur through "pebble accretion" if enough small particles are left in the disk. In this process, these particles, still coupled to the gas disk, are swept onto the planetesimals traveling through this gas. As the mass of any object increases, its growth is aided by the attractive force of its gravity, called gravitational focusing. At this phase, it is possible that a few large, strongly gravitating bodies grow greedily, accreting material that would otherwise have eventually made it onto smaller planetesimals.

Growth slows as the largest bodies become massive enough to begin efficiently gravitationally scattering planetesimals. As relative planetesimal speeds increase, only the largest planets continue to accrete while the smallest get disrupted through energetic collisions, a phase termed "oligarchic growth." Growth is further slowed as all the remaining solids accessible to the planetesimals' gravitational influence are accreted. Eventually, only relatively isolated bodies remain, but the probability of collisions between the large planetary embryos remains elevated for around 100 Myr. Earth's moon could be a product of such a collision.

The formation of gas giants also occurs in this timeframe. As planetary embryos grow, they will eventually have sufficient gravity to hold on to gas out to radius that depends on the gas pressure (and thus the thermal structure of the atmosphere), tidal effects, and the planet's

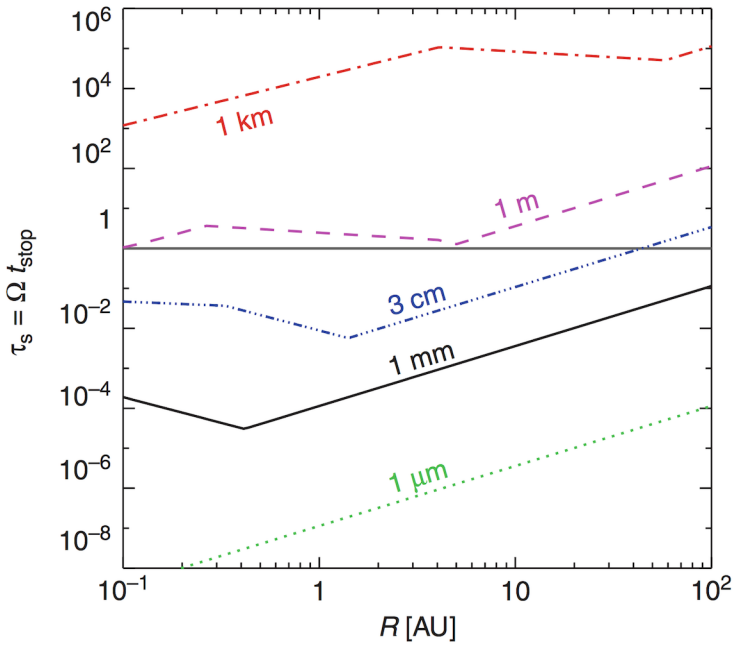

Figure 1.4 Aerodynamic stopping time for objects of various sizes as a function of disk location, normalized by the orbital angular rate. For the meter-sized objects, the influence is near the timescale of an orbit, meaning the object would be slowed enough to disrupt its orbit (unlike the km-sized objects) but not enough to prevent the inward motion from this disruption from carrying it into the star (unlike the μm-sized objects). Kinks are due to the use of differing drag laws in different fluid regimes. Reproduced from Youdin & Kenyon (2013).

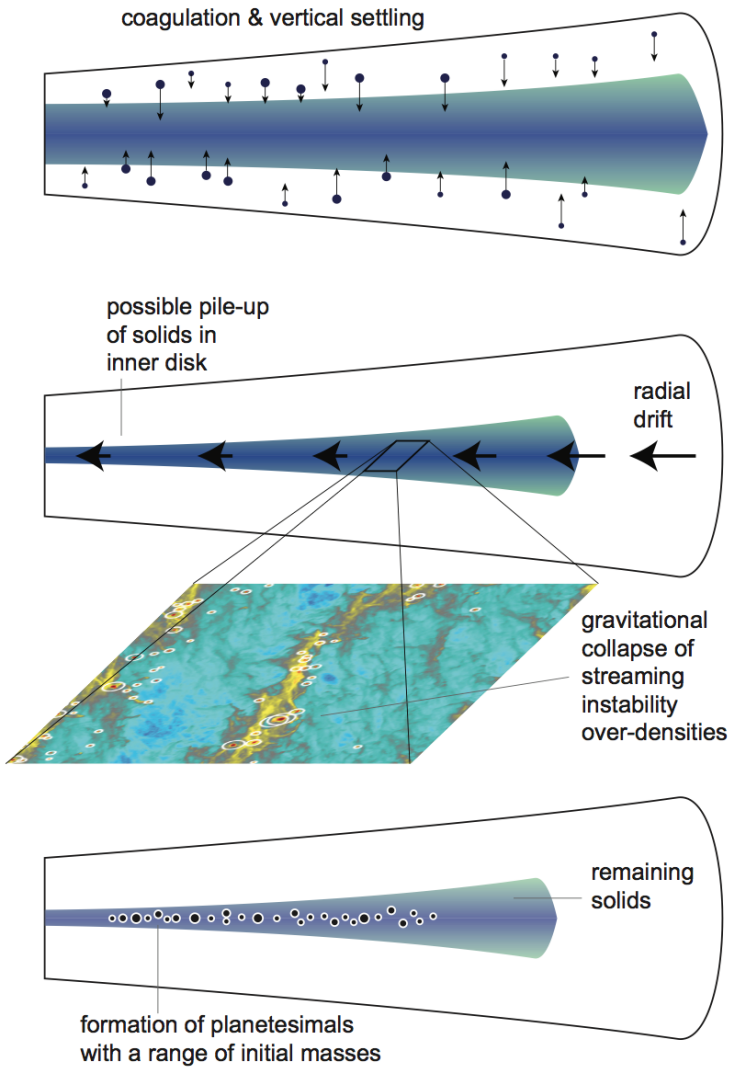

Figure 1.5 Sketch of one possible avenue for planetesimal coagulation to self-gravitating sizes through the streaming instability. Reproduced from Armitage (2007).

gravity. In general, the addition of more gas in this envelope increases the the atmospheric pressure sufficiently to support the atmosphere against the added mass of the new gas. However, there is a critical mass of the embryo's core beyond which the increase in self-gravity from the additional mass exceeds the increase in atmospheric pressure. At this point, the atmosphere contracts at whatever rate its gravitational potential energy can be radiated away and the planet experiences rapid atmospheric growth. This growth terminates only when the planet has cleared its orbit of all gas within its gravitational influence or the disk gas is dispersed by the star.

Throughout the growth of planets, another phenomenon has been underway: evolution of the planetary orbits. Several different mechanisms for orbital evolution are possible. Migration involves gravitational interactions between planets and the disk at orbital resonances, radii where the orbital period of the planet is some integer ratio of the orbital period at those radii. At these positions, the disk material exerts periodic gravitational tugs in the same direction that accumulate over many such periods, significantly altering the location of the planet. The details of this process are still nebulous, but modeling of the effect requires numerical simulations of the planet-disk interactions. If the planet is massive enough, the resonant torques can open a gap in the disk and the planet's migration becomes locked to that of the disk, termed Type II migration. If this does not happen, migration is Type I.

Orbital evolution can also occur through interactions with remnant planetesimals in the disk. The orbital perturbations from repeated scattering of planetesimals can build up to yield a significant change in the orbit of a much larger planet. This mechanism, applied to the Solar system, has come to be known as the Nice model (for its origins in Nice, France), and could explain some features of the solar system like the structure of the Kuiper belt. Orbital evolution via migration and scatterings is currently considered by most to be a process that all planetary systems likely undergo. In particular, planetary migration is invoked to explain the existence of hot Jupiter exoplanets that could not have formed in place due to a lack of available solids for core accretion at distances so near the host star. Indeed, much of the current picture of planet formation has arisen from the recent explosion of planetary systems with which to test various theories, the

exoplanet revolution.

1.2 The Detection of Exoplanets

Because much of the work in this thesis has been motivated by exoplanets and because an entire chapter is devoted to one such system, a brief overview of their detection is germane. The methods for detecting exoplanets are diverse, and, with the exception of direct imaging, they are indirect. Figure 1.6 shows the tally of confirmed exoplanets as of 2017 July 20, distributed in mass and orbital period and colored according to the detection method. I will focus only on those techniques that have detected the bulk of known exoplanets, the radial velocity and transit techniques.

Most of the earliest detections were made with the radial velocity technique. This includes the first detection of a planet around a main-sequence star, the hot-Jupiter 51 Peg b detected by Mayor & Queloz (1995). The method relies on the measurement of periodic variations in the Doppler shift of stellar emission that results from its reflex motions as a planet orbits. The motions that must be detected are small; Jupiter's affect on the sun is of order 10 m s^{-1} and Earth's is of order 0.1 m s^{-1}. Such velocities require the detection of wavelength changes at sub-ppb levels. Consequently, the stability of the spectrograph's wavelength solution and the star's own surface oscillations become limiting factors for this technique. Because the stellar reflex motion is directly related to the orbiting planet's distance and mass, this method favors the detection of nearby, massive planets. This has led to a preponderance of hot Jupiters detected with the radial velocity technique.

The radial velocity technique provides a means of estimating the planet's mass. However, because the inclination of the planet's orbit relative to the line of sight is (in general) unknown, the measurement that is actually made is of $m \sin i$, where m is the planet's mass and i is the inclination, where zero inclination implies that the orbit normal is aligned with the line of sight. The true planet mass is very likely near this value because the probability of a near-face on orbit is low. For isotropically distributed orbits, the probability of a given inclination angle goes as $\sin i$

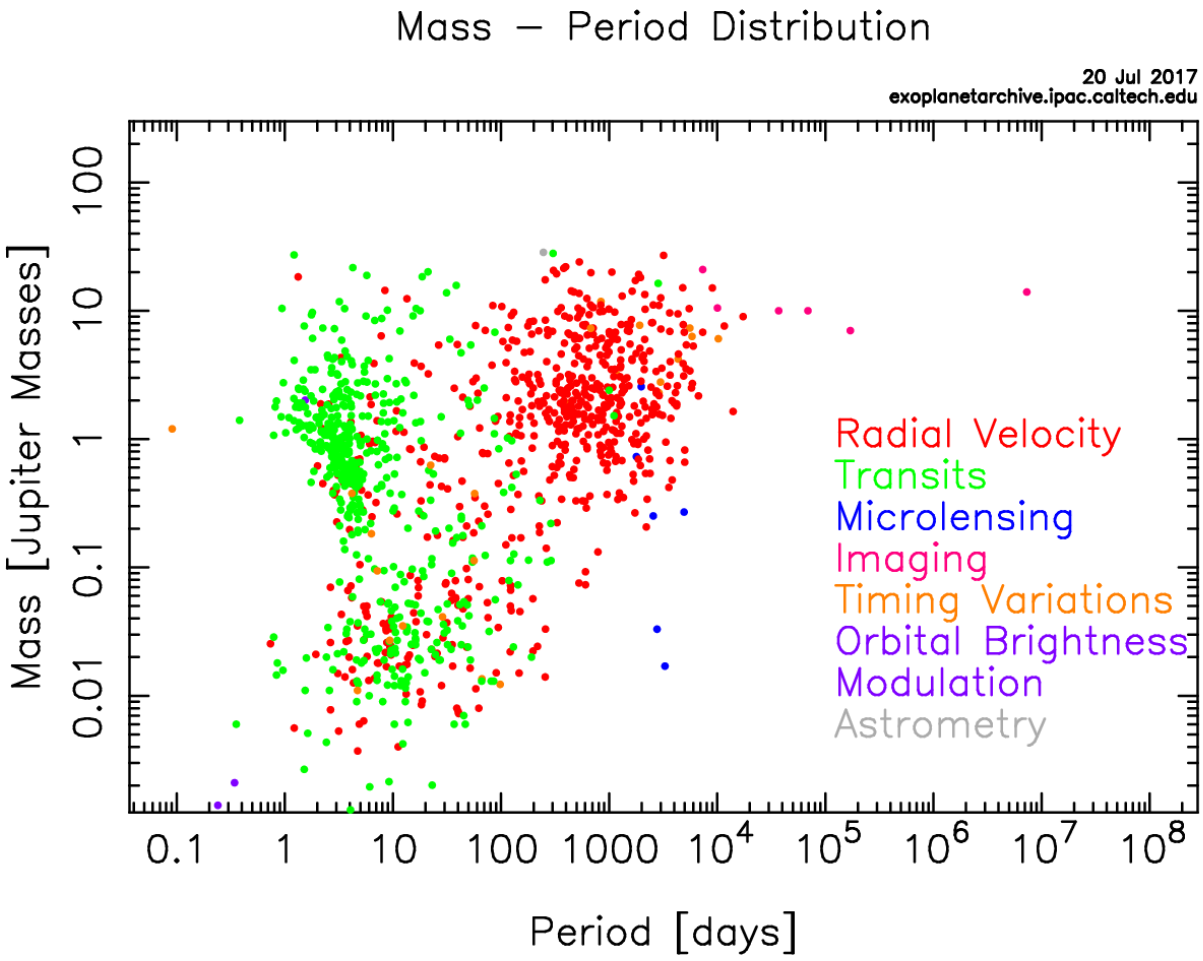

Figure 1.6 The mass-period distribution and detection technique of confirmed exoplanets, retrieved from the NASA Exoplanet Archive.

and the probability that the planet mass is within a factor of 2 of the measured $m \sin i$ is 87%.

By far the most successful detection technique employs planetary transits. This involves staring observations of a star (or field of stars) in search of periodic drops in stellar flux that correspond to an orbiting planet obscuring a portion of the stellar disk. Figure 1.7 provides a sketch of the transit geometry and resulting evolution of the observed stellar flux, the transit "lightcurve." Transit searches suffer from a number of false positives, in particular the transits of background eclipsing binaries that, when diluted by the foreground star's flux, have a depth that would suggest a planet-sized object. However, careful vetting by spectroscopy, high resolution images, and careful analysis of the transit shape, among other techniques, can filter out such false positives. A great advantage of the transit method is that it is well-suited to extensive surveys by monitoring a field of stars for an extended period of time, the strategy adopted by the *Kepler* mission.

Transit lightcurves hold a great deal of information about the planet and the star producing them. The primary piece of information is the planetary radius relative to the star, as this determines the transit's depth. The occultation of the planet as it passes behind the star allows its albedo and infrared emission to be measured. Gradual changes with the planet's phase can determine how this reflection and emission changes with planetary longitude for planets expected to be tidally locked (where the rotation rate is known to equal the orbital period). The timing of the occultation and the shape of the transit constrain the orbital parameters. Variations in the timing of transits produced by gravitational tugs can reveal the presence of additional planets in the system that either don't transit or are too small for the transit to be readily detectable. Further, these variations constrain the masses of the interacting planets. The mass of a planet can be more confidently determined, however, with complimentary radial velocity measurements.

Like the radial velocity method, the transit method is also biased toward large, closely-orbiting planets, as these produce deeper and more frequent transits. Indeed, the necessity of observing multiple transits to ensure that the signal is that of an orbiting planet typically restricts this method to shorter period objects than the radial velocity method, as Figure 1.6 illustrates.

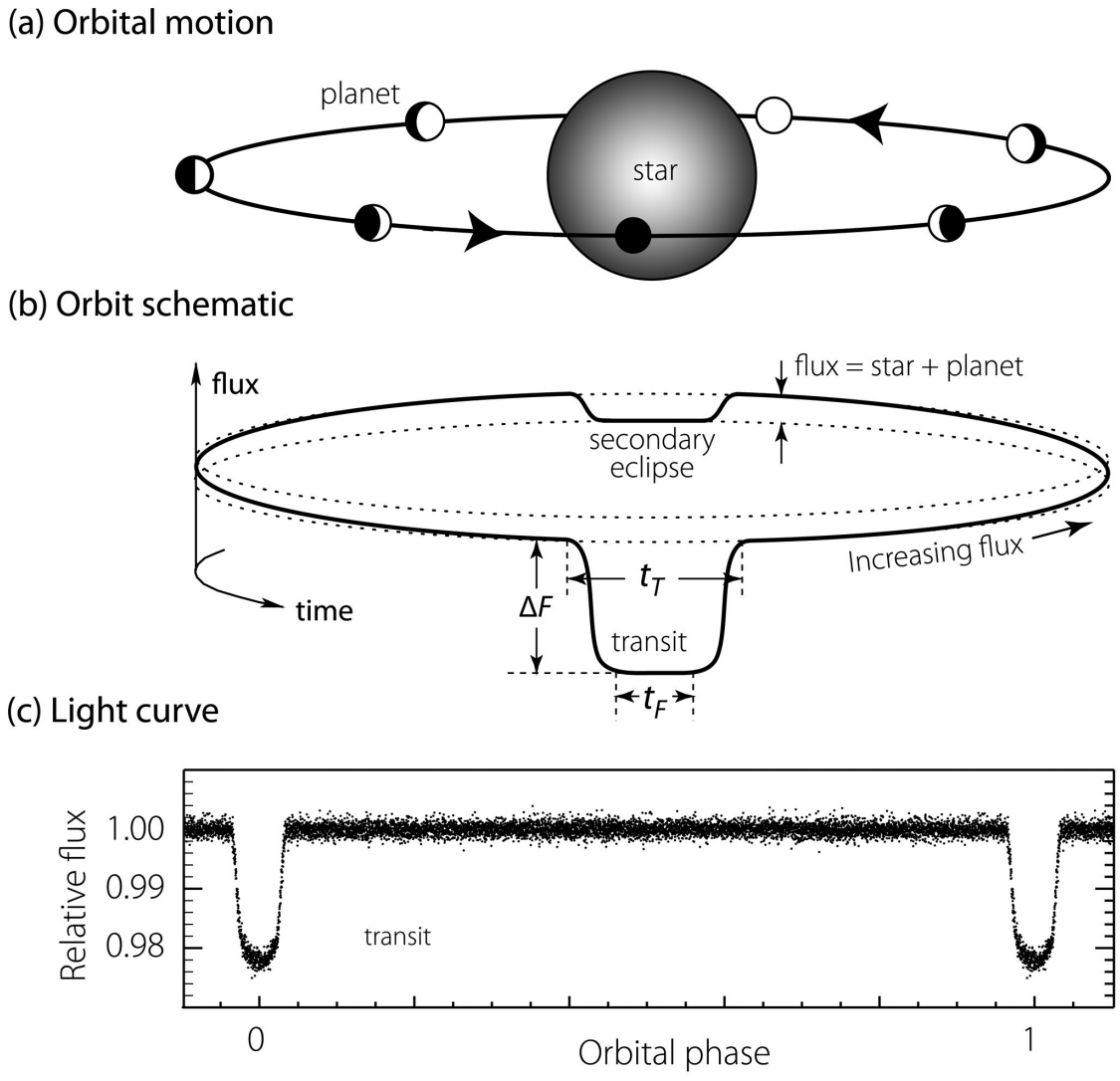

Figure 1.7 Sketch of transit geometry and associated lightcurve. Reproduced from Perryman (2014).

While observational limitations make it challenging to detect Earth-like planets (though hardly impossible), the bias towards planets orbiting very near their star has sparked growth in the study of how these objects interact.

1.3 Stars and Planets, Interacting

Stars have an obvious influence on their orbiting planets. One could perhaps identify the first such critical influence as the clearing of the protoplanetary disk by stellar radiation and winds. If this occurs quickly, it could quench planet growth before they have reached their full potential in mass.

After planets have formed, the clearest influence of the star is heating from the bolometric flux of its electromagnetic radiation (flux integrated over all wavelengths). A simple energy balance using the Stefan-Boltzmann Law and assuming isotropic stellar and planetary flux yields a planetary "effective" temperature for a spherical body of any size of

$$T_{\text{eff}}^4 = (1 - a)\,\frac{L_\star}{16\pi\sigma d^2}, \tag{1.1}$$

where a is the Bond albedo of the planet (the amount of incident stellar radiation reflected by the body), $L_\star$ is the bolometric luminosity of the star, d is the distance between planet and star, and σ is the Stefan-Boltzmann constant. The term effective temperature is used because it does not necessarily reflect the physical temperature of the planet. In particular, the surface temperature of a planet is raised by the insulating "greenhouse effect" of its atmosphere. Most realistic atmospheres are not entirely transparent to to the infrared blackbody radiation emitted from the planets surface, in particular due to the IR absorption bands of H_2O and CO_2. Thus, some fraction of the surface-emitted radiation does not escape to space, but is absorbed and re-radiated back toward the planetary surface. The result is that, for a thermal energy balance to be achieved, the planet's surface must achieve a higher temperature.

The surface temperature of a planet gives rise to the concept of the liquid-water habitable zone. This is the range of orbital distances from a star in which it is plausible that a terrestrial

planet could support liquid water on its surface, thus increasing the chances that it could have generated an Earth-like biosphere. There are no exact limits of the habitable zone, as they differ for different planetary properties, in particular atmospheric properties. Some limits are shown in Figure 1.8.

Not only is a planet's surface temperature different than its effective temperature, this surface temperature varies as a function of position on the planet's surface (as one is viscerally aware on earth). These variations are particularly pronounced for a specific class of planets: those that are tidally locked. Tidal locking refers to the synchronization of the planet's rotational period with its orbital period. When this happens, the same hemisphere of the planet faces the star at all times, meaning there is a permanent day side and permanent night side with corresponding temperature extremes. As a familiar example, Earth's moon is tidally locked with Earth.

This locking is not coincidental, but rather is a product of the variation in the gravitation field that the star exerts on the planet. This causes a slight elongation of the planet along the radial coordinate from the star, a "tidal bulge." If the planet is rotating faster than it orbits (as would be expected after formation), the planet's shape cannot adjust rapidly enough to keep up with this rotation and the elongated axis of the planet is offset. The gravitational pull on the planet is then asymmetric, with the bulge nearest the star experiencing a greater force than the further bulge, and this exerts a torque that slows the planet's rotation. The strength of this effect is dependent on the star-planet distance and the material properties of the planet, its elasticity, as often characterized by a set of dimensionless parameters known as Love numbers after their inventor. Figure 1.8 shows a rough estimate from Kasting et al. (1993) of the orbital distances within which terrestrial planets will become tidally locked to their host star.

Tidal interactions do not only effect planetary rotation rates, their orbits are effected as well. This arises not from the tidal bulge raised on the planet by the star, but the reverse, the bulge raised on the star by the planet. As with the planet, the star's rotation will cause its tidal bulge to deviate ahead or behind of the orbiting planet causing it, and the asymmetric gravitational forces on these bulges will apply an orbital torque. If the star's rotation is slower than the planet's orbit,

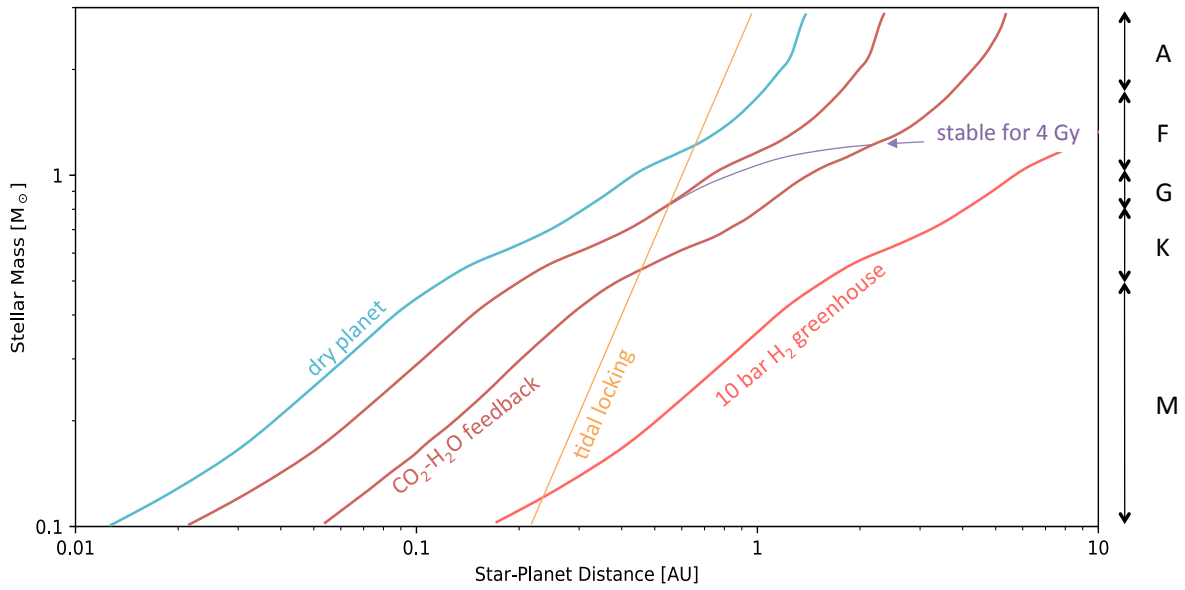

Figure 1.8 Habitable zone limits based on a number of different studies. Letters to the right give the range of stellar spectral types. The maroon lines give the inner and outer limits when including an H_2O + CO_2 greenhouse, according to the model of Kasting et al. (1993). The blue line gives the inner habitable zone edge for planets with a limited water inventory that yields a low water vapor content in the atmosphere, from Abe et al. (2011). The red line gives the outer habitable zone edge for planets with a thick hydrogen atmosphere, where pressure-induced hydrogen absorption creates a powerful greenhouse, from Pierrehumbert & Gaidos (2011). Also shown are an estimate of the distance at which tidal locking can be expected and an upper limit on the region where the habitable zone is stable for at least 4 Gy against the evolving luminosity of the host star.

as is generally the case for close-in planets like hot-Jupiters, the orbit-lagging stellar bulge tends to slow the planet, causing an orbital decay that can eventually lead to the planet's consumption by the star. This effect also tends to dampen any eccentricity to the planet's orbit, as it is more pronounced when the planet passes through periastron.

Tides provide a mechanism by which planets can also influence the star. The ability of planets to measurably affect their stars is a topic of some debate at the moment. The various processes involved are generally referred to as star-planet interactions, SPIs, though this terminology is somewhat misleading since it is generally used only to refer to interactions by which the planet influences the star and not the reverse. Because the SPI field is nascent and there are no general texts addressing it, I will provide more specific references in the following paragraphs.

Tides are one avenue for an SPI. The same torque that slows a planet's orbit also speeds the rotation of the star. Some recent compelling evidence for this has been found through discrepancies in the gyrochronology (ages estimated from rotation rates based on a model of stellar spin-down with age) in binary systems where one of the pair hosts a close-in planet. Under the reasonable assumption that the pair formed together, their age estimates should agree within uncertainties, but instead the planet-hosting star was found to be rotating at pace suggesting a younger age (Poppenhaeger & Wolk, 2014).

A star's rotation rate is linked to its level of magnetic activity, believed to be responsible for the elevated temperatures and associated short-wavelength radiation from its upper atmosphere (to be discussed further in Chapter 2). Therefore, the retardation of stellar spin down due to a closely-orbiting, massive planet is also likely to result in enhanced activity.

It is also possible that planets directly influence the magnetic activity of a star through interactions between the stellar and planetary magnetic fields, a second form of SPI. As a planet's orbital velocity carries it through the (more slowly rotating) stellar field, it initiates magnetic Alfvén waves in the stellar field (Preusse et al., 2006; Kopp et al., 2011) and reconnection between the stellar and planetary fields (Lanza, 2008, 2009; Cohen et al., 2009). If the planet orbits within the star's Alfvén radius, the radius at which the speed of the accelerating stellar wind matches the

speed of magnetic Alfvén waves, then the disturbance from reconnection can propagate back to the stellar surface. Magnetic SPIs are of particular importance because they have the potential, with further observational development, of helping to constrain planetary magnetic fields. A magnetic SPI dissipates energy at a rate that is proportional to the relative velocity of the planet, the stellar magnetic field strength, and the planetary magnetic field strength (e.g. Lanza 2009). All but the planetary field strength can be determined with current observational tools, meaning that a measurement of SPI power would provide an estimate of a planet's magnetic field strength.

A final form of SPI is material interactions between the star an planet. These include (1) beams of electrons or ions directed through magnetic flux tubes (Gu & Suzuki, 2009) and (2) the accretion of gas escaping a planet's atmosphere (Matsakos et al., 2015). Electron beams (1) have an observational basis in Jupiter, where several moons produce footprints of UV emission on the planet that are observable with *HST* (Clarke et al., 2002). The accretion hypothesis (2) is bolstered by the several exoplanets with atmospheres known to be escaping at hydrodynamic rates. Simulations show that some of the gas escaping such planets could be funneled onto the star (Matsakos et al., 2015; Pillitteri et al., 2015). Both beams and accretion are magnetically controlled, and therefore could also eventually yield observational tools to constrain planetary magnetic fields.

I have omitted two means by which stars influence their planets in the above discussion because they play a central role in this thesis work. Therefore, they merit individual treatments, which I provide in the next two sections.

1.3.1 Stellar Ultraviolet Radiation and Planetary Atmospheric Escape and Chemistry

The effect of a star's radiation on a planet cannot be simplified to a single number, the bolometric flux. The spectral content of this radiation is too important to be so disregarded. In particular, the ultraviolet radiation from a star influences planetary atmospheres in two critical ways.

At far-ultraviolet wavelengths, photons have sufficient energy to dissociate most single and

double molecular bonds, such as O_2, H_2O, CO_2, and CH_4. As a representative example, the double bond of O_2 requires 5.15 eV to cleave, corresponding to a <2400 Å photon. The photolysis cross-section of O_2, however, varies by many orders of magnitude in the FUV, with a broad local maximum in the 1400 – 1600 Å range, well below the limiting wavelength for dissociation. Many simple atmospheric molecules have photolysis cross sections that peak in the FUV, so FUV photons are primarily responsible for non-thermal chemistry (photochemistry) in exoplanet atmospheres. Evaluating the ultimate outcome of this chemistry requires modeling of chemical networks in exoplanetary atmospheres.

Photochemistry is responsible for the ozone layer (the Chapman layer) on Earth, which peaks at roughly the millibar level. The dissociation of oxygen by FUV photons creates free oxygen atoms that then react with molecular oxygen to create ozone. This process is highly relevant to Earth's organisms because ozone strongly absorbs NUV light that can interact with and destroy DNA molecules in organisms. On Earth, ozone is ultimately attributable to life because the O_2 from which it originates is produced by photosynthesizing organisms. However, photochemical simulations of H_2O and CO_2 dominated atmospheres under the influence of the spectra of M dwarf stars have predicted a buildup of O_2 and O_3 in the absence of life, a result that is attributed to the roughly 1000× higher FUV/NUV ratio of these stars (Figure 1.9; Tian et al. 2014).

At extreme ultraviolet (EUV) wavelengths, photons have sufficient energy to eject electrons from atoms. Whereas NUV photons penetrate to roughly the mbar level and FUV photons to the μbar level in Earth's atmosphere, EUV photons encounter enough neutral atoms to ionize that they penetrate only roughly to the nbar level. The excess kinetic energy of ejected electrons is sufficient to heat Earth's upper atmosphere to roughly 1000 K. On close-in exoplanets, in particular hot Jupiters, temperatures of 10000 K are typical. At these temperatures, the thermal energy of the atoms and ions nears the binding energy of the planet's gravity. In consequence, a significant fraction of the atoms and ions acquire sufficient energy to escape. Because the binding energy of gravity depends on the mass of the particle but the gas thermal energy does not, lighter species escape preferentially, causing a depletion of these species. Atomic hydrogen, of course, is the most

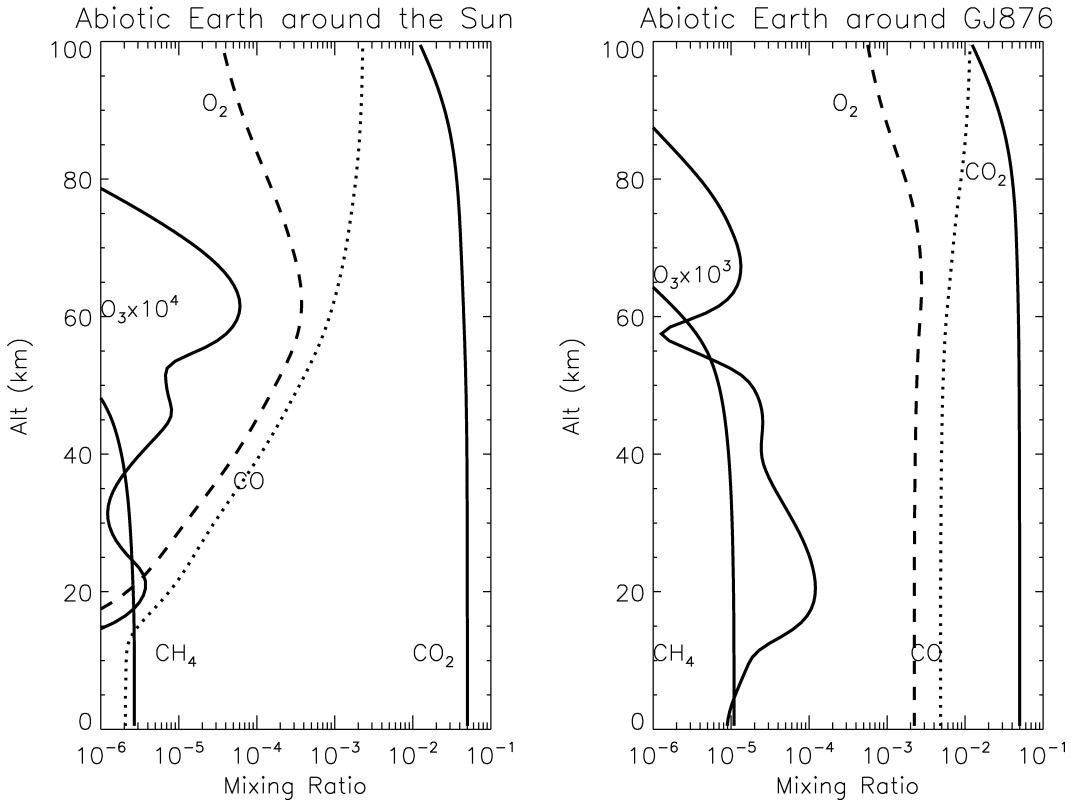

Figure 1.9 Example of abiotic oxygen and ozone buildup predicted by the model of Tian et al. (2014) (from which this figure is reproduced) for a 95% N_2, 5% CO_2 atmosphere assuming a solar spectrum or the spectrum of the M dwarf GJ 876 is incident.

likely to escape, a fact which can have dire consequences for a planet's water inventory.

A division is often made between thermal escape (or Jeans escape, named after the pioneering researcher) and hydrodynamic escape. In thermal escape, particle thermal energies are small relative to the gravitational binding energy. As a result, only a small fraction of the particle velocity distribution exceeds the planetary escape velocity. Above the exobase, the altitude at which the atmospheric density has dropped to the point that the mean free path of a particle is equal to the atmospheric scale height, particles with escape velocity have a reasonable chance of escaping the atmosphere. Since the escaping fraction of particles is small, their distribution remains near enough to the Maxwell-Boltzmann distribution that simply integrating the tail of this distribution to determine the escape rate yields an answer that more sophisticated treatments have shown to be correct to within a factor of a few. Essentially, the atmosphere remains in hydrostatic equilibrium, with light particles "evaporating" from its upper reaches.

The accuracy of this picture breaks down when the ratio of gravitational binding to thermal energy of atmospheric particles,

$$\lambda = \frac{GMm}{kTr} \tag{1.2}$$

(G = gravitational constant, M = planetary mass, m = particle mass, k = Boltzmann constant, T = temperature, r = radial distance from the planet's center), known as the Jean's ratio, drops below $\sim$2. Beyond this point, the thermal energy of the gas is sufficient to power a bulk upward motion at a rate that is renders the atmosphere no longer in (quasi)hydrostatic equilibrium. Hence, the atmosphere experiences "hydrodynamic" escape, also termed "blowoff." For a typical hot Jupiter in which the (hydrogen-dominated) upper atmosphere reaches temperatures of 10000 K, blowoff is likely the norm. If the escape is rapid enough, heavier species in the atmosphere can be dragged along with the lighter species out of the planet's gravitational well, despite having thermal velocities that are small relative to the planet's escape velocity. Escape of hydrogen as well as some heavier species (C, O, and Si) has been detected from hot-Jupiters HD 209458b (Vidal-Madjar et al., 2003), HD 189733b (Lecavelier Des Etangs et al., 2010), WASP-12b (Fossati et al., 2010) and the

hot-Neptune GJ 436b (Kulow et al., 2014).

Hot Jupiter escape rates are often estimated using a simple energy balance between the input EUV energy and the work done against the gravitational potential well. This yields a mass loss rate of

$$\dot{M} = \epsilon \frac{\pi R^3 F_{\mathrm{EUV}}}{GM}. \tag{1.3}$$

Here F_{EUV} is the EUV flux of the star at the planet and R is the radial distance from the planet's center to which the EUV radiation penetrates. The most important component of this equation is ϵ, the efficiency factor. It represents the fraction of EUV energy that actually goes into liberating mass, rather than, for example, being radiated away or conducted to lower regions of the atmosphere. It also conveniently hides the ambiguity associated with what is truly the appropriate radius to choose when determining the amount of work that must be done against the gravitational well. Hydrodynamic simulations and observations of exoplanet escape have constrained ϵ to typical values of order 0.1 (e.g. Murray-Clay et al. 2009; Koskinen et al. 2013b; Ehrenreich et al. 2015; Loyd et al. 2016).

Ultimately, the energy-limited escape formulation is an oversimplification. Hydrodynamic simulations by Murray-Clay et al. (2009); Owen & Alvarez (2016) have shown that, while hot-Jupiter escape might operate in a state where mass loss is balanced against absorbed energy, many others likely inhabit regimes where the recombination rate of ionized atoms or the photon flux are actually what physically limit the rate of mass loss.

Perhaps more importantly, considering only thermal energy as a factor in atmospheric escape neglects many other avenues by which atmospheric mass can be lost to space. On Earth, these non-thermal escape mechanisms account for the majority of hydrogen escape. For some of these, the energy for the escape could still originate with an EUV photon. For example, a photoelectron can recombine with an ionized molecule and the energy of that recombination go into dissociating the molecule and ejecting the neutral products at above escape speed. Other mechanisms rely entirely upon the solar wind or electric fields as an energy source, such the pinching off of "blobs"

of magnetically contained plasma. However, as this thesis relies on observations of FUV radiation, it is appropriate to end the discussion of escape and move on (after a brief but necessary aside) to stellar flares.

1.3.2 Aside: The Structure of Solar and Stellar Atmospheres

Beginning in the following section and continuing throughout this thesis, regular reference will be made to various strata of stellar atmospheres. These are based on a canonical one-dimensional description of the solar atmosphere. Though this neglects the considerable three-dimensional structure of stellar atmospheres, it might be thought of as an approximate average of this structure across shells of the stellar atmosphere at different radii, and it provides a useful reference in which to couch discussions of stellar emission and the structure of flares.

This 1D profile is shown in Figure 1.10. Temperature falls with radius in the photosphere to a temperature minimum, then rises though the chromosphere with characteristic temperatures of order 10^4 K before undergoing a sharp rise through the transition region to the MK temperatures of the corona. Semi-empirical modeling of the M dwarf GJ 832 by Fontenla et al. (2016) has shown that qualitatively the atmospheric strata are similar (Figure 1.11). Most of this thesis is founded on observations of transition-region emission.

1.3.3 Stellar Flares

Stellar flares subject orbiting planets to brief periods of enhanced photochemistry and escape-driving FUV and EUV flux. They likely also shower the planets with energetic particles and impact them with coronal mass ejections. However, these latter effects are conjectural, based purely on analogy to the Sun. Thus far, no observational techniques have yielded confident measurements of accelerated particles or coronal mass ejections.

Flares are caused by the abrupt reconnection of stellar magnetic fields. The microphysical details of how this reconnection takes place and converts the stored magnetic energy into the observed energy sinks are still not well understood. For solar flares, a standard model for the

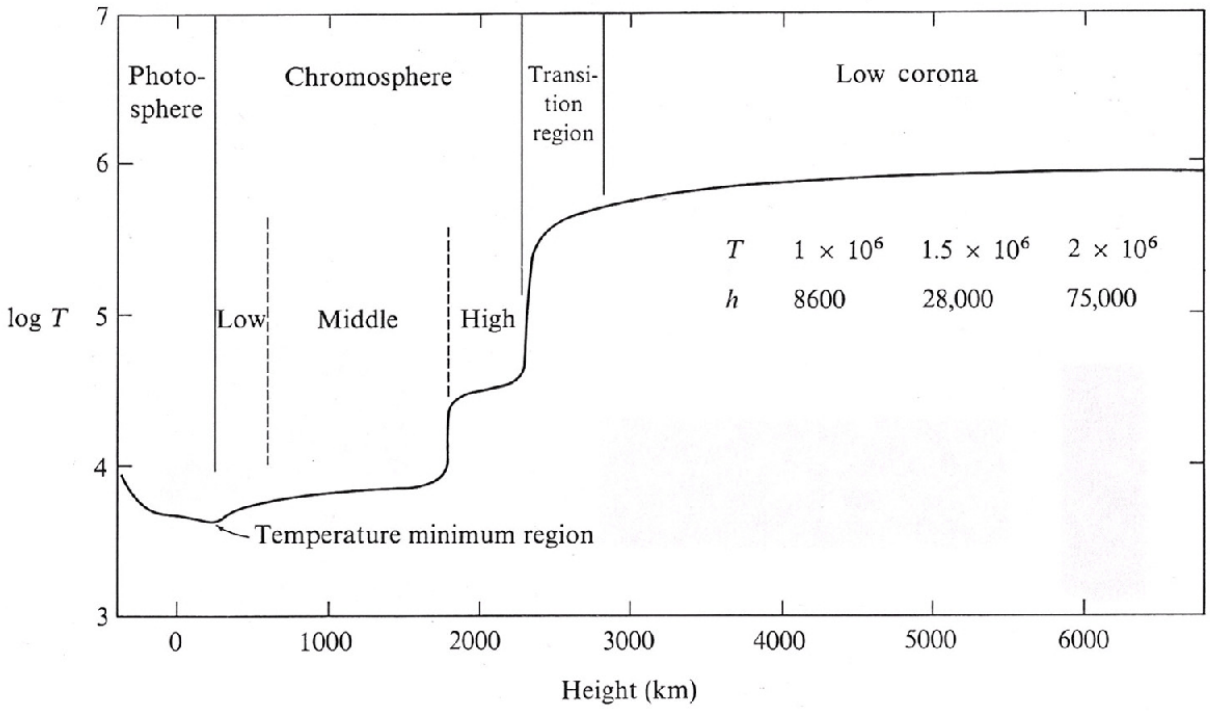

Figure 1.10 Sketch of the strata of the solar atmosphere. Temperatures are in K. From Athay (1976).

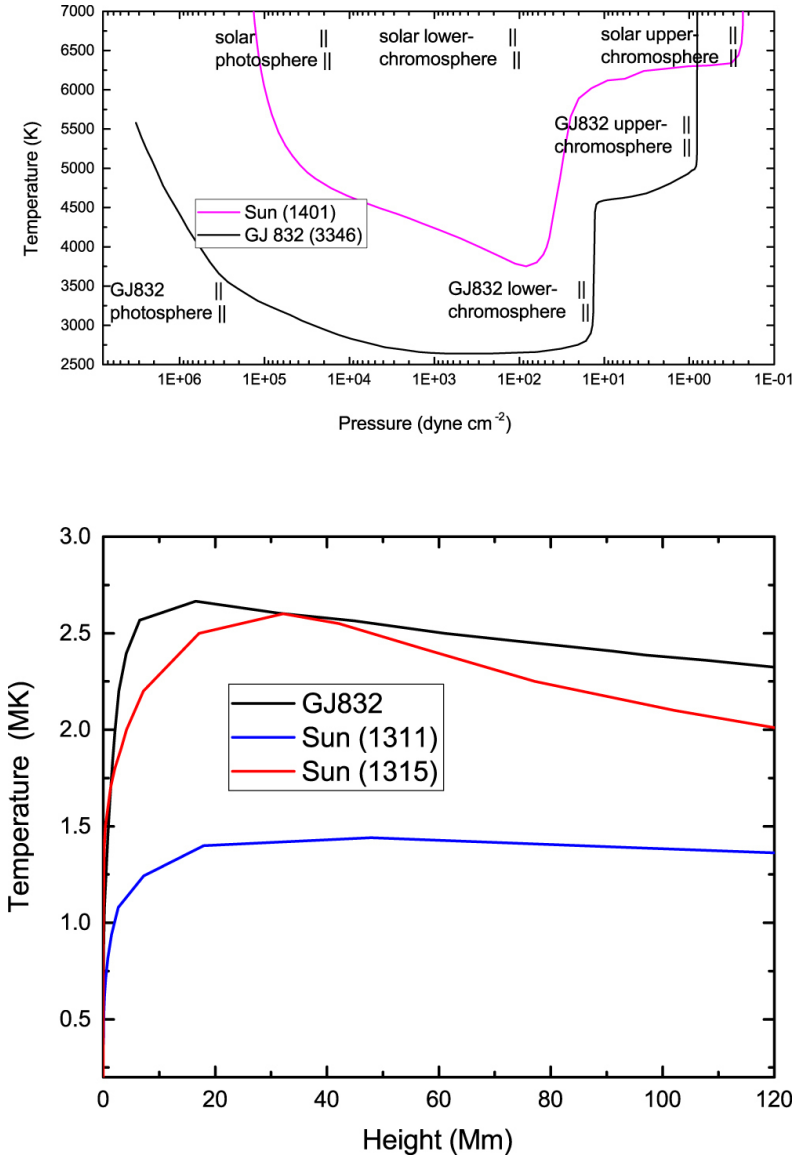

Figure 1.11 Figure from Fontenla et al. (2016) showing the results of semi-empirical modeling of the M dwarf GJ 832. Qualitatively, this M dwarf atmosphere has the same structure as the solar atmosphere.

macroscopic mechanics of these events has emerged, a schematic of which is shown in Figure 1.12. In this model, a flux rope, confined by nearly circumferential magnetic field lines, emerges from the solar surface to become a solar prominence. The sketch in Figure 1.12 is drawn in plane transverse to the rope, which lies off the top edge of the sketch.

As the prominence rises, the confining field lines reconnect beneath the loop, releasing beams of nonthermal electrons that compress and heat chromospheric plasma. Evidence of these nonthermal particle beams is seen as X-ray bremsstrahlung and microwave gyrosynchrotron radiation. The beams evaporate chromospheric material at the footpoints of the reconnecting field, filling the field structure with order 10^7 K plasma radiating in the X-ray. As the plasma cools, its radiation progresses to longer and longer wavelengths, passing through the EUV, UV, and optical. Meanwhile, the compressed chromospheric material at the footpoints of the reconnecting field appears in observations as ribbons of H_α emission aligned with the solar prominence.

If the prominence continues to rise it can leave the sun as a coronal mass ejection (CME). All of the Sun's most energetic flares produce CMEs. At lower flare energies, this association becomes less secure (Figure 1.13). The broader morphology of a CME is sketched with a corresponding representative observation in Figure 1.14. Above the emerging prominence, a region of bright, compressed plasma forms, led by a shock wave. This shock releases energetic particles flowing outward along open field lines. These can go on to impact planets, even if they are not in view of the flare due to the curvature of the field lines directing the particles. In space weather, these are known as solar energetic particle (SEP) events. Planets can also later be impacted by the CME itself. Another important point for planetary implications is that CMEs can occur without an associated flare.

Solar flares are conventionally classified by their peak flux in the 1 – 8 Å band of the GOES satellites. This system assigns letters based on the logarithm of the peak flux, following the progression B (peak flux 10^{-7} W m^{-2}), C (10^{-6} W m^{-2}), M (10^{-5} W m^{-2}), X (10^{-4} W m^{-2}), then X10 (10^{-3} W m^{-2}) and so forth. X10 class flares, which are essentially always associated with a CME, occur only once every few years, though their rate varies with the 11 year solar activity

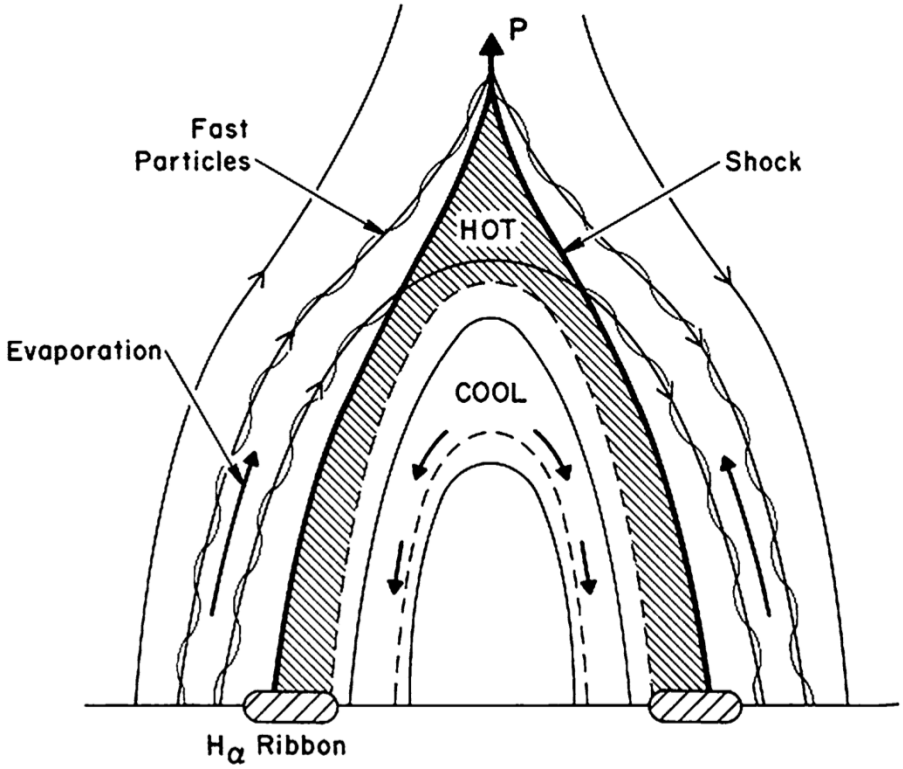

Figure 1.12 Sketch of the standard model of a solar flare. Reproduced from Hudson (2011).

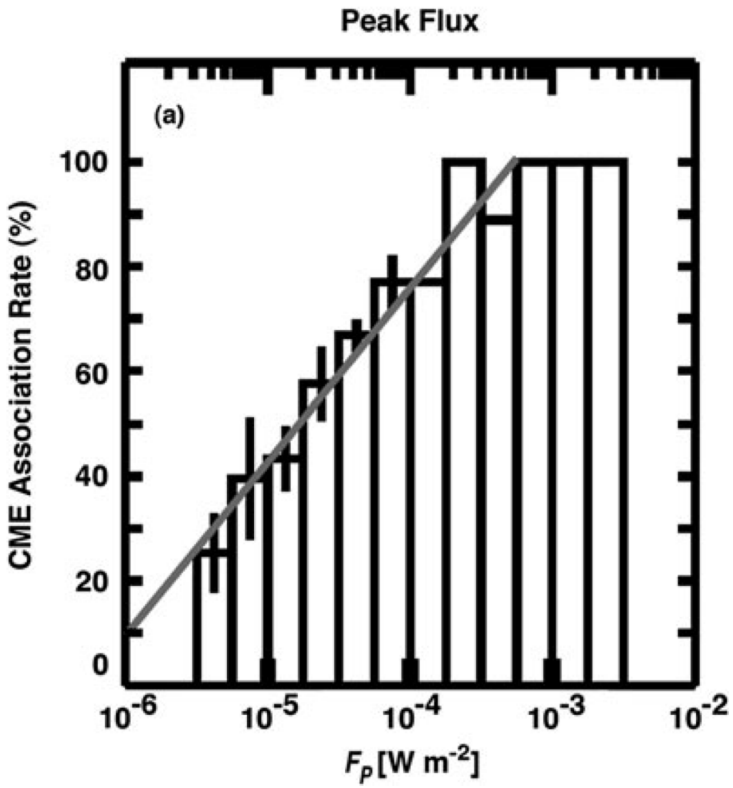

Figure 1.13 Relationship between solar flares and associated CMEs. Reproduced from Yashiro et al. (2006).

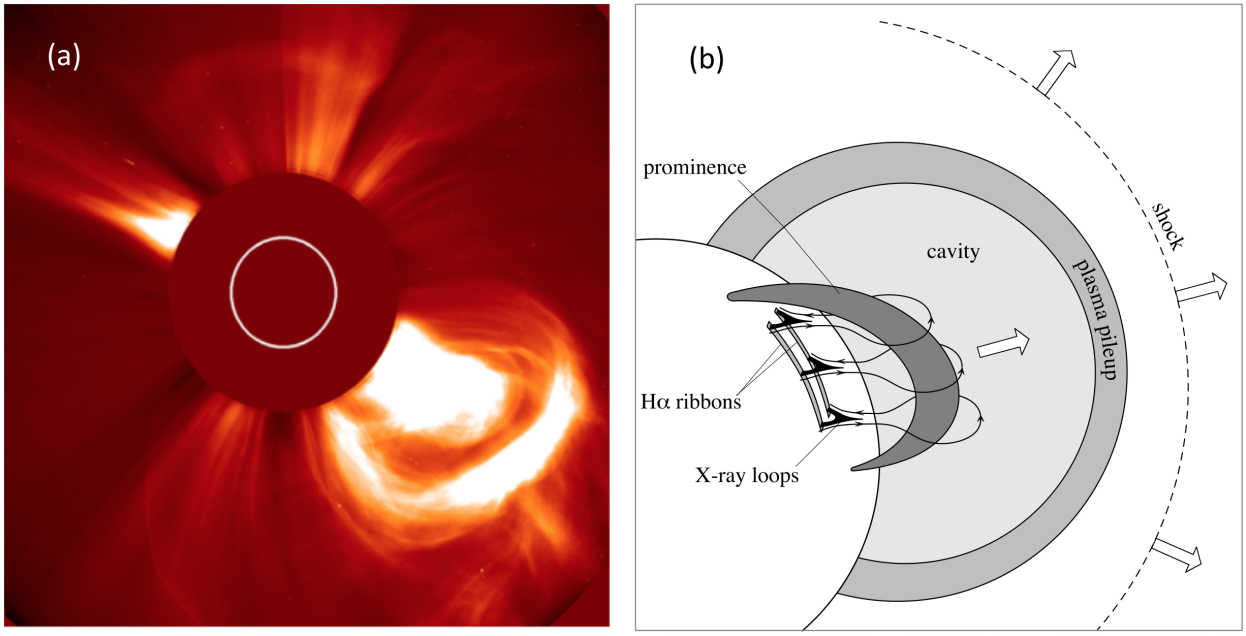

Figure 1.14 SOHO observations of a CME, and an accompanying sketch of the typical CME geometry. Reproduced from Schmieder et al. (2015).

cycle. The actual occurrence of flares is stochastic. In general, the wait-times between flares can be well described by an exponential distribution,

$$p(\Delta t) = e^{-\Delta t/\mu}/\mu \tag{1.4}$$

(p = probability density, μ = flare rate, Δt = wait time), implying that Poisson statistics can be applied. However, flares can trigger sympathetic events, meaning events are not always independent and Poisson statistics are not a perfectly accurate description of this stochastic process.

The study of solar flares has a great advantage over stellar flares in that the disk of the sun is easily resolved. Empirical knowledge of stellar flares is limited to disk-integrated observations. Another challenge of stellar flare observations is the practical difficulty of coordinating observations at multiple wavelengths. A great resource in this regime is the multiwavelength observations of (Hawley et al., 2003) that captured flares from AD Leo, enabling correlations between energy radiated in different wavelength regimes. However, because of absorption in the interstellar medium, observations of stellar flares at the EUV wavelengths $\gtrsim$ 300 Å that are frequently used for solar flares are not possible.

1.4 Bibliography

The below have been employed as general references in the construction of the above sections.

- Armitage, P. J. 2007, ArXiv Astrophysics e-prints, astro-ph/0701485
- Armitage —. 2013, Astrophysics of Planet Formation
- Hudson —. 2011, Space Sci. Rev., 158, 5
- Hunten, D. M. 1982, Planet. Space Sci., 30, 773
- Lequeux, J. 2013, Birth, Evolution and Death of Stars (World Scientific Publishing Co), doi:10.1142/8820
- McKee, C. F., & Ostriker, E. C. 2007, ARA&A, 45, 565

- Perryman, M. 2014, American Journal of Physics, 82, 552
- Smith, M. D. 2004, The Origin of Stars (World Scientific Publishing Co), doi:10.1142/p353
- Youdin, A. N., & Kenyon, S. J. 2013, From Disks to Planets, ed. T. D. Oswalt, L. M. French, & P. Kalas, 1

Chapter 2

Physics and Techniques

2.1 The Basics of Emission and Absorption

Emission lines from atoms and ions are a product of the transition of a bound electron from one orbital state to another. These orbital states of a single electron are described by the quantum numbers

- n, the principal quantum number. Can be any integer value > 0. Corresponds to the number of relative maxima (nodes) in the radial distribution of the electron's wavefunction if it has zero orbital angular momentum. Loosely speaking, electrons of higher n orbit further from the nucleus.

- l, the angular momentum in units of $\hbar$. Can be 0,1...$n-1$. These are commonly denoted by characters rather than numbers, in the sequence s, p, d, and f for $l = 0$, 1, 2, and 3.

- m, component of the angular momentum along an arbitrary z axis, in units of $\hbar$. Can be any integer $-l, -l+1, ..., l-1, l$.

- m_s, electron spin momentum, in units of $\hbar$. Can only assume values of -$\frac{1}{2}$ and +$\frac{1}{2}$.

The configuration of multiple electrons orbiting an atom is frequently specified by giving the number of electrons in each nl "subshell." This notation is best described by example: an atom with the electron configuration specified as $1s^2 2s^2 2p^3$ has two electrons in the 1s ($n = 1, l = 0$) subshell, two in the 2s ($n = 2, l = 0$) subshell, and three in the 2p ($n = 2, l = 1$) subshell. The

Pauli exclusion principle requires that no two electrons occupy the same state, i.e. have the same n, l, m, m_s. Consequently, only $2(2l+1)$ electrons can occupy each subshell. When $2(2l+1)$ electrons occupy a subshell, that subshell is said to be "filled."

For a single-electron atom[1] , the energy of an electron can be approximated from n alone as

$$E_n = -13.6 \text{ eV } \frac{Z^2}{n^2} \tag{2.1}$$

where Z is the net charge of the atom (the nuclear charge less the charge of the electrons in orbitals "interior" to the electron in question). However, the state of the electron's angular momentum (l) and spin (s) influence this energy. In a multi-electron atom, the energy of a given state is determined by the total angular momentum (orbit-orbit coupling), total spin momentum (spin-spin coupling), and the vector sum of these momenta (spin-orbit coupling). For the electrons in filled shells, these couplings are always the same (momenta sum to zero) and can be effectively ignored. The state of an atom is specified using "term notation" from the quantum numbers S for the total spin momentum, L for the total orbital angular momentum, and J for the total (spin + orbital) momentum as ${}^{2S+1}L_J$, where L is given as S, P, D, F, ... rather than a numeric value. The perturbations on the energy of a given electron configuration, in order of decreasing magnitude, follow Hund's rules:

(1) Energy increases with decreasing S.

(2) Energy increases with decreasing L.

(3) Energy increases with increasing J for less than half-filled shells and decreasing J for more than half-filled shells.

Figure 2.1 sketches the differences in the energy levels dues to the perturbations from each coupling for a 4p4d electron configuration.

[1] For brevity, I will refrain from repeatedly including "or ion," but the reader should understand that this is typically implied.

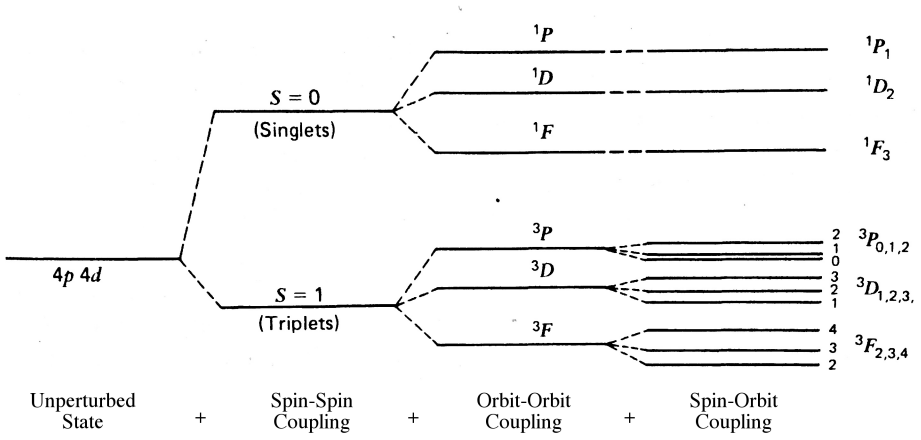

Figure 2.1 Term diagram sketching the energy level splittings due to the interaction of two electrons, one each in the 4p and 4d subshells of an atom. Adapted from Rybicki & Lightman (2004).

The perturbation from spin-orbit coupling is what gives rise to the "fine-structure" splitting of atomic emission lines. For a single-electron atom, this energy splitting is

$$\Delta E = \frac{1}{2}\left(\frac{e^2}{\hbar c}\right)^2 E_n. \tag{2.2}$$

This is typically on the order of 10^{-2} eV, corresponding to an order 0.1% wavelength shift (1 Å at 1000 Å). The total angular momentum number, J, that determines the fine-structure splitting can take on only integer values in the range $|L-S| \leq J \leq L+S$. Therefore, $2S+1$ different values of J are possible for states where $L \geq S$, making the $2S+1$ in term notation convenient for specifying the number of fine-structure levels that a state will split into.

Emission lines result from the transition of an atom from a higher-energy to a lower-energy state where the energy of the transition is carried away by a photon. Such a transition can be spontaneous or stimulated by a photon field. Roughly speaking, the probability of a spontaneous radiative transition, and thus its rate, can be classified according to "selection rules" that must hold in order for the transition to be possible under a specific quantum-mechanical approximation. The most likely transitions obey the rules necessary for the transition probability to be nonzero under the dipole approximation, i.e. "dipole-allowed." For these transitions, one electron must jump n values, have a unit change in l, have a zero or unit change in m, and have no change in m_s. For the multi-electron state, it must be that S does not change, L has zero or unit change, and J has zero or unit change (but J cannot start zero and remain zero). If a dipole-allowed transition brings the atom into its ground state, then the emission line resulting from the transition is sometimes called a resonance line.

Two less-likely ("forbidden") transitions are those that are allowed under the magnetic dipole approximation and the electric quadrupole approximation. Both violate the parity-change rule of the dipole-allowed transition. Transitions allowed by the magnetic dipole approximation also require that the configuration of the electrons does not change.

The rates of transitions involving photons are termed Einstein coefficients, and typically the symbology of A_{ul} for spontaneous emission, B_{ul} for stimulated emission, and B_{lu} for absorption

is used. Both stimulated emission and absorption depend on the density of the photon field. Generally, the B coefficients are defined such that their product with the mean intensity J yields a transition rate with units of $[\text{time}]^{-1}$. For these rates to be compatible with the Planck function when thermodynamic equilibrium is enforced, it must be that

$$g_l B_{lu} = g_u B_{ul}, \tag{2.3}$$

where g is the degeneracy of the state (namely, $2J+1$ unless an external magnetic or electric field causes additional energy level splitting due to the interaction of the field with the total momentum) and

$$A_{ul} = \frac{2h\nu^3}{c^2} B_{lu}. \tag{2.4}$$

where $\nu = (E_u - E_l)/h$ is the frequency of a photon with energy equal to the difference of the upper and lower state energies.

Transitions between states are also possible through collisions, and it is this process which is often crucial for determining the rate at which a high-energy state is populated such that it can radiatively decay or for determining the population of atoms in a low-energy state available to absorb a photon. In thermodynamic equilibrium, the ratio of populations in two differing states is

$$\frac{n_u}{n_l} = \frac{g_u}{g_l} e^{-(E_u - E_l)/kT}. \tag{2.5}$$

The above considers only transitions between states where all electrons remain bound to the atom, "bound-bound" transitions. However, it is of course possible that a bound electron transitions to an unbound state or vice versa, "bound-free" (or "free-bound") transitions. When this transition is mediated by the release or absorption of a photons, then the outcome is an ionization (absorption) or recombination (emission) edge in a spectrum. The edge shape is an outcome of the impossibility of a photon with energy less than the ionization energy of the atom ejecting an electron or being produced by a captured electron, producing an abrupt step in absorption or emission at frequencies near the ionization energy. For recombination, the absorption cross section falls off rapidly as photon frequency increases, specifically as ν^{-3}. Determining the precise shape of an emission

edge requires knowledge of the electron temperature (if in thermodynamic equilibrium) or velocity distribution (non-equilibrium).

When a bound-free transition is mediated by a collision, the same Boltzmann statistics that yield Equation 2.5 can be applied to determine the ratio of populations for an atom in different ionization states. The result is the Saha equation,

$$\frac{N_{j+1}N_e}{N_j} = \frac{2U_{j+1}(T)}{U_j(T)}\left(\frac{2\pi m_e kT}{h^2}\right)^{3/2} e^{-\chi_{j,j+1}/kT}, \tag{2.6}$$

where the Ns are number densities, Us are partition functions, j specifies the ionization state, and χ is the ionization energy. The Saha equation and Equation 2.5 address a simple, albeit important point in the use of emission and absorption features to study astrophysical phenomena. In order for an emission or absorption line to be observed, the appropriate lower or upper state must be populated. This, for example, is why one would not expect to observe absorption from N V lines in an exoplanet atmosphere, as no such atmosphere is likely to be hot enough to collisionally ionize N all the way to N^{4+} nor is the radiation field from stars sufficient to produce this level of ionization.

Returning to the topic of radiative bound-bound transitions, it is important to note that the emission or absorption associated with these transitions does not always occur at precisely the same wavelength. At the most fundamental level, the energy of a state is not exact, but instead varies according to the Heisenberg uncertainty principle. The shorter-lived the state, the less precise its energy. This produces a "natural" broadening of emission and absorption lines, producing a Lorentzian line profile of the form

$$\phi(\nu) = \frac{\gamma/4\pi^2}{(\nu-\nu_0)^2 + (\gamma/4\pi)^2}, \tag{2.7}$$

where ν_0 is frequency at line center and γ is, loosely speaking, the rate of transitions out of the upper and lower states. At a minimum, γ is the sum of the spontaneous emission rates A and for a dipole-allowed transition is usually dominated by the rate of the transition that is producing the observed line. However, stimulated emission and collisions can also depopulate the involved states. If collisions are fast enough to depopulate either state at a rate exceeding that of spontaneous

emission, then these will dominate γ and the line is said to be "pressure broadened," though the root cause of the broadening is still the same as a naturally-broadened line.

Additional broadening arises from non-zero velocities of the emitting and absorbing atoms. Any velocity will result in a Doppler shift and the frequency of the absorbed or emitted photon will be shifted accordingly. The most ubiquitous such motions are thermal motions. If the gas is in thermodynamic equilibrium, the resulting thermally broadened line profile is

$$\phi(\nu) = \frac{1}{\Delta\nu_D\sqrt{\pi}} e^{-(\nu-\nu_0)^2/(\Delta\nu_D)^2}, \tag{2.8}$$

where

$$\Delta\nu_D = \frac{\nu_0}{c}\sqrt{\frac{2kT}{m_a}} \tag{2.9}$$

and m_a is the mass of the transitioning atoms. Another source of stochastic motion is turbulence, often included by adding the root mean-square turbulent velocity, $v_{\rm turb}$, in quadrature with the thermal velocity to yield

$$\Delta\nu_D = \frac{\nu_0}{c}\sqrt{\frac{2kT}{m_a} + v_{\rm turb}^2}. \tag{2.10}$$

Strictly speaking, the line would only maintain the profile specified in Equation 2.8 if the turbulent velocities follow a Gaussian distribution, but fitting any "superthermally broadened" line with a profile of the form just specified is common nonetheless.

Doppler broadening need not arise only from randomly distributed motions; organized motions can also produce broadening. A common example is broadening by the Keplerian motion of gas in a disk. Radial outflow from an evaporating planet or stellar wind can also produce broadening. If the velocity field is known, then the associated Doppler shifts can be integrated over the emitting volume to determine the line profile. At a minimum, all lines will exhibit both natural and thermal broadening. The resulting line profile is the convolution of these two profiles and is given by

$$\phi(\nu) = \frac{H(a,u)}{\Delta\nu_D\sqrt{\pi}}, \tag{2.11}$$

where

$$H(a,u) \equiv \frac{a}{\pi}\int_{-\infty}^{\infty}\frac{e^{-y^2}dy}{a^2+(u-y)^2}, \tag{2.12}$$

$$a \equiv \frac{\gamma}{4\pi\Delta\nu_D}, \tag{2.13}$$

and

$$u \equiv \frac{v-v_0}{\Delta\nu_D}. \tag{2.14}$$

At line center, the profile can be dominated by the Doppler or Lorentz profile according to the value of a, but at some point beyond the center the "wings" of the Lorentzian will begin to dominate.

All the line profiles that have been introduced are normalized such that $\int_0^\infty \phi(\nu)d\nu = 1$. Generally, one desires to use these profiles in radiative transfer calculations. The radiative transfer equation (neglecting scattering) is

$$dI = -I\kappa ds + jds \tag{2.15}$$

where s is the pathlength, I is the radiation specific intensity (power per unit area, solid angle, and frequency interval), κ is the absorptivity (units of [length]$^{-1}$), and j is the emissivity (power per unit volume, solid angle, and frequency interval). The absorptivity is more easily conceptualized by noting that

$$\kappa = n\sigma, \tag{2.16}$$

where σ is the cross section for absorption and n the particle density.

For an absorption line, the absorption cross-section can be computed from the oscillator strength, f_{lu}, as

$$\sigma_{lu} = \frac{\pi e^2}{m_e c} f_{lu}\phi(\nu). \tag{2.17}$$

The more fundamental A_{ul} is related to the more directly measured f_{lu} via

$$A_{ul} = \frac{8\pi^2 e^2 \nu_{ul}^2}{m_e c^3}\frac{g_l}{g_u} f_{lu}. \tag{2.18}$$

Stimulated emission can be thought of as "negative absorption," with $g_u f_{ul} = -g_l f_{lu}$. The emissivity due to spontaneous emission, which is isotropic, is

$$j = \frac{1}{4\pi} n_u A_{ul} E_{ul}\phi(\nu). \tag{2.19}$$

It is generally convenient to recast the radiative transfer equation with optical depth, $\tau = \kappa ds$, as the independent coordinate. Then

$$dI = -Id\tau + Sd\tau, \tag{2.20}$$

where $S \equiv j/\kappa$. These tools and concepts form the basics of the radiative processes that apply to the work in this thesis. From here the discussion will move on to the specific emission and absorption features observed and modeled in this thesis.

2.2 FUV Emission from Stars

The work in this thesis primarily relies on observations of far-ultraviolet (FUV; 912 – 1700 Å) emission lines from M dwarf stars, specifically that which is observed in the roughly 1150 – 1450 Å bandpass of the *Hubble Space Telescope's* (*HST's*) Cosmic Origins Spectrograph (COS) G130M spectrograph. A selection of prominent or noteworthy emission lines included in this bandpass are tabulated in Table 2.1.

The areas of the stellar atmosphere from which these lines emanate is primarily a function of the density and temperature of the atmosphere, which determines the rate and energy of collisions that can ionize atoms to the required level and populate the excited state such that it can radiatively decay. As discussed in Section 1.3.2, the temperature of stellar upper atmospheres increases with height (see Figures 1.10 and 1.11), so there are confined regions in which the line emission (or, for that matter, continuum emission) is formed. A treatment assuming local thermodynamic equilibrium (LTE) could use Equations 2.6 and 2.5 to determine these regions, but modern models including non-LTE effects do better.

Such non-LTE models reveal that the lines presented in Table 2.1 are formed mostly in the transition region that spans roughly $10^{4.5}$ – $10^{5.5}$ K. Lyα, C II, and O I, are formed at least partially (wholly for O I) in the upper chromosphere and the iron lines are formed in the corona.

Detailed profiles of the contribution function to various emission lines and continuum are provided by the non-LTE, 1D, semi-empirical models of Avrett & Loeser (2008) for the quiescent

Table 2.1. Selected stellar emission lines in the *HST* COS G130M bandpass (FUV).

Ion	$\lambda_{\rm rest}$ Å	$\log_{10}(T_{\rm peak}/{\rm K})$ [a]	Transition	A_{ul} 10^8 s^{-1}	f_{ul}
C III	1174.93	4.8	$2p^2\ ^3{\rm P}_2 \rightarrow 2s2p\ ^3{\rm P}_1$	3.293	0.1136
	1175.26	4.8	$2p^2\ ^3{\rm P}_1 \rightarrow 2s2p\ ^3{\rm P}_0$	4.385	0.2724
	1175.59	4.8	$2p^2\ ^3{\rm P}_1 \rightarrow 2s2p\ ^3{\rm P}_1$	3.287	0.06810
	1175.71	4.8	$2p^2\ ^3{\rm P}_2 \rightarrow 2s2p\ ^3{\rm P}_2$	9.856	0.2042
	1175.99	4.8	$2p^2\ ^3{\rm P}_0 \rightarrow 2s2p\ ^3{\rm P}_1$	13.13	0.09074
	1176.37	4.8	$2p^2\ ^3{\rm P}_1 \rightarrow 2s2p\ ^3{\rm P}_2$	5.468	0.06807
Si III	1206.51	4.7	$3s3p\ ^1{\rm P}_1 \rightarrow 3s^2\ ^1{\rm S}_0$	25.5	1.67
H I[b,c]	1215.67	4.5	$2p\ ^2{\rm P}_{3/2} \rightarrow 1s\ ^2{\rm S}_{1/2}$	6.2649	0.41641
	1215.67	4.5	$2p\ ^2{\rm P}_{1/2} \rightarrow 1s\ ^2{\rm S}_{1/2}$		
N V	1238.82	5.2	$2p\ ^2{\rm S}_{1/2} \rightarrow 1s\ ^2{\rm P}_{3/2}$	3.40	1.56
	1242.80	5.2	$2p\ ^2{\rm S}_{1/2} \rightarrow 1s\ ^2{\rm P}_{1/2}$	3.37	0.780
Fe XII	1242.00	6.2	$3p^3\ ^4{\rm S}_{3/2} \rightarrow 3p^3\ ^2{\rm P}_{3/2}$	3.17×10^{-6}	7.33×10^{-8}
O I[b]	1302.17	3.8	$2p^3 3s\ ^3{\rm S}_1 \rightarrow 2p^4\ ^3{\rm P}_2$	3.41	0.0520
	1304.86	3.8	$2p^3 3s\ ^3{\rm S}_1 \rightarrow 2p^4\ ^3{\rm P}_1$	2.03	0.0518
	1306.03	3.8	$2p^3 3s\ ^3{\rm S}_1 \rightarrow 2p^4\ ^3{\rm P}_0$	0.676	0.0519
C II	1334.53	4.5	$2s2p^2\ ^2{\rm D}_{3/2} \rightarrow 2s^2 2p\ ^2{\rm P}_{1/2}$	2.41	0.129
	1335.71	4.5	$2s2p^2\ ^2{\rm D}_{5/2} \rightarrow 2s^2 2p\ ^2{\rm P}_{3/2}$	2.88	0.115
Fe XII	1349.40	6.2	$3s^2 3p^3\ ^2{\rm P}_{1/2} \rightarrow 3s^2 3p^3\ ^4{\rm S}_{3/2}$	1.73×10^{-6}	2.36×10^{-8}
Fe XXI[d]	1354.08	7.1	$2s^2 2p^2\ ^3{\rm P}_1 \rightarrow 2s^2 2p^2\ ^3{\rm P}_0$	6.49×10^{-5}	5.35×10^{-6}
Si IV	1393.76	4.9	$3p\ ^2{\rm P}_{3/2} \rightarrow 3s\ ^2{\rm S}_{1/2}$	8.80	0.513
	1402.77	4.9	$3p\ ^2{\rm P}_{1/2} \rightarrow 3s\ ^2{\rm S}_{1/2}$	8.63	0.255

[a]Peak formation temperatures of the C, O, and H lines are from Avrett & Loeser (2008), using the values at line center. Other lines are from a CHIANTI spectral synthesis using a differential emission measure estimated from data during an M2 class solar flare (retrieved from `http://www.chiantidatabase.org/chianti_linelist.html` on 2017 July 31; Dere et al. 2009).

[b]Also emitted by Earth's upper atmosphere ("geocorona"), contaminating stellar observations.

[c]Lyα. Doublet is not generally resolved, so the provided A and f values yield the appropriate natural width and line intensity for the combined profile.

[d]Blended with a C I line.

Note. — All transitions are electric dipole-allowed (permitted) except those of the Fe ions, which are magnetic dipole-allowed (forbidden).

solar atmosphere and Fontenla et al. (2016) for the atmosphere of the M dwarf GJ 832. Figure 2.2 plots the contribution function (change in intensity with height) from the Fontenla et al. (2016) model of several lines from Table 2.1, showing that C II is partially formed in the chromosphere, and Si IV and N V squarely in the transition region. The Fe XII 1242 Å line is formed in the corona, as are the other Fe lines in Table 2.1. Similar plots from the Avrett & Loeser (2008) model show that O I is formed almost entirely in the upper chromosphere. The diversity of the regions in which FUV emission lines are formed make the FUV band valuable for the study of stellar upper atmospheres.

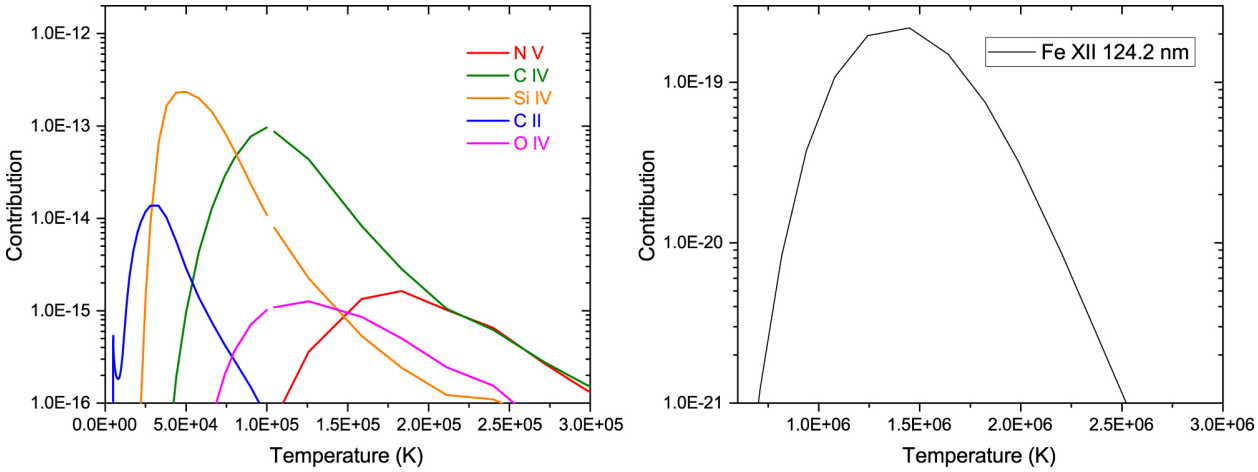

Figure 2.2 Contribution function of several of the FUV lines listed in Table 2.1 from a semi-empirical, non-LTE model of the upper atmosphere of the M dwarf GJ 832 (Fontenla et al. 2016; reproduced from that work).

The dominant source of emission in the FUV is Lyα. The high optical thickness of this line influences its profile. Multiple inelastic scatterings of photons can push their wavelengths into the wings of the line where optical depths are lower until the photons escape. Consequently, photons in the core of the Lyα line are produced higher in the atmosphere than photons in the wings. This is demonstrated by the results of Avrett & Loeser (2008), shown in Figure 2.3, where the contribution functions of emission at various points in the Lyα profile are shown. Such a formation height dependence on wavelength is also present in other lines, though not to the same extent.

The energy source for these FUV emission lines – the process that heats the stellar upper

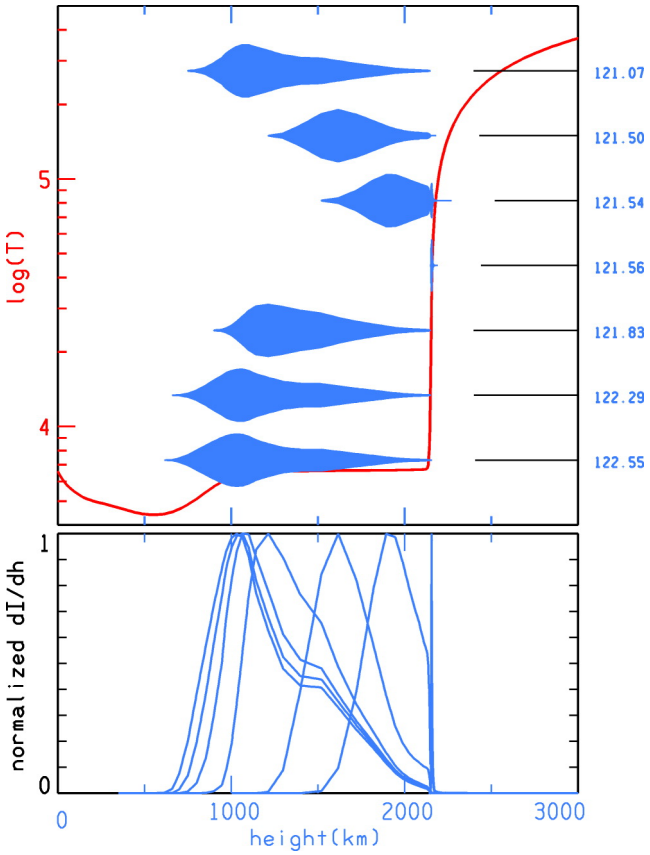

Figure 2.3 Contribution functions for different portions of the Lyα line from a non-LTE model of the solar chromosphere (Avrett & Loeser 2008; reproduced from that work). In the top plot, the normalized contribution function is depicted as the thickness of the blue regions shown over the temperature distribution adopted by the model (red line). The bottom panel plots the normalized contribution functions directly.

atmosphere to such high temperatures – is still a matter of debate. It is generally accepted that the heating is likely to be mediated by magnetic fields, and two leading mechanisms for the dissipation of magnetic energy are magnetohydrodynamic (MHD) waves and small-scale reconnection of magnetic fields. Though often seen as competing theories, these might not be distinct (Jess et al., 2015). Because heating is expected to be magnetic, emission from lines formed in the upper atmosphere are frequently taken to be a direct proxy for magnetic activity. The correlation between the age, rotation rate, and chromospheric flux of stars (e.g., Noyes et al. 1984; Vilhu 1984) is consistent with the theory that magnetic fields heat the upper atmosphere.

The observation of some FUV lines can be complicated by interstellar absorption. These are the lines of species where the lower state is in the ground level, as the ISM cannot generally support excited states through collisions. This includes Lyα for which absorption by the ISM completely annihilates the line core, as well as the O I 1302 and C II 1334 Å lines. Consequently, the intrinsic flux of these lines can only be estimated, commonly through model fits to the transmitted portions, a process that is particularly important for estimates of the Lyα flux to which exoplanet atmospheres are exposed.

2.3 FUV Spectrographs and Data Analysis

An understanding of the instrumentation used for observations of FUV spectra is necessary for the correct interpretation of those data. The data used in this thesis mostly originate from the Cosmic Origins Spectrograph (COS; Green et al. 2012) and Space Telescope Imaging Spectrograph (STIS; Woodgate et al. 1998) spectrographs aboard *HST*. Both instruments employ microchannel plate detectors (MCPs). A generic setup of such a detector is diagrammed in Figure 2.4.

MCPs are constructed of a honeycomb of electron-emissive glass channels. On the side of the MCP upon which photons are incident, a photocathode is placed, sometimes deposited directly onto the MCP itself. Incoming photons strike the photocathode and release an electron that is then accelerated into the glass channels by a cathode that establishes an electric field for the purpose. Upon impacting the wall of the (slanted) channel, more electrons are released that also impact

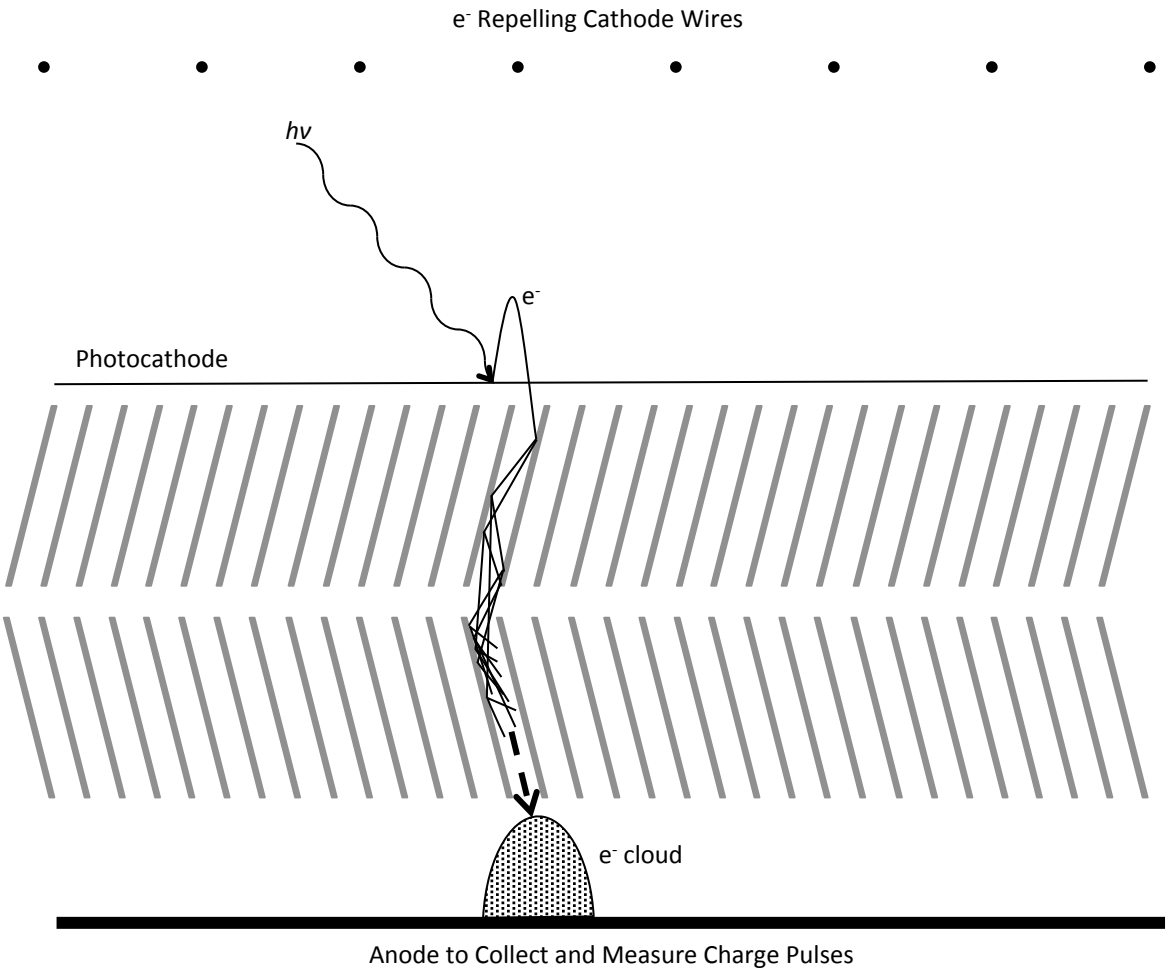

Figure 2.4 Sketch of the working principle of a microchannel plate detector (not to scale).

the glass, beginning a cascade that amplifies the single initial electron into a cloud of 10^3 – 10^8 electrons. These exit the opposing side of the detector, where they are collected by an anode designed to measure the location and time (and generally also the magnitude) of the resulting charge pulse. Such anodes can take the form of, e.g., CCDs that collect the charge to be read out on command, phosphor screens that create visible light pulses, and grids of wires that channel the charge into read out electronics.

This process allows each photon that strikes the detector and successfully creates a charge cloud to be counted, a key difference from CCDs and other integrating detectors that record only the total number of photons absorbed in a fixed pixel. The raw data from an MCP is simply a list of the location, time, and charge of each recorded electron pulse. This event list can then be binned in position and time in whatever manner is desired, within the limits of the instrument's spatial and temporal resolution, after the data have been collected. Hence, MCPs provide a desirable degree of flexibility.

Another advantage of MCPs is that there are essentially no sources of random error except the shot noise associated with the source events and spurious background events. These background events are generally low, around 10^{-4} s^{-1} per pixel for the STIS FUV detector and 10^{-6} s^{-1} per pixel for the COS FUV detector. However, there are several systematic effects of which to be wary with MCPs. Like any detector, imperfections in the manufacturing will produce differing sensitivity over the area of the detector, including hot spots and dead zones. The gain (magnitude of the charge cloud produced by a single photon) of the detector degrades with use, such that portions of the detector repeatedly exposed to bright sources lose sensitivity out of proportion with the rest of the detector, known as "gain sag."

Perhaps the most notable systematic of MCPs is "dead time." Upon registering a pulse, there is generally a brief period during which additional pulses will not be registered. The fraction of events that occur during this dead time increases until it plateaus at the point where the count rate is so high that the detector is essentially dead at all times and the registered count rate is equal to $1/t_d$, where t_d is the dead time following an event. The result is a nonlinearity in the detector

sensitivity. Under the assumption of a constant dead time, a functional form for this nonlinearity is easily derived:

$$f = \frac{1}{1/f' - t_d}, \tag{2.21}$$

where f is the true event rate and $f' \in [0, 1/t_d)$ is the measured event rate. Dead time can have several sources, the most fundamental being the replenishment of electrons in the walls of a channel after it "fires." This results in a nonlinearity that is localized to the single-pore level. However, the read-out electronics of an MCP can also impose a global dead time, preventing the registration of an event occurring anywhere on the detector while a previous event is being processed.

Of course, each specific instrument design will have its own special characteristics and sources of systematic errors. Therefore, a discussion of some specific features of the *HST* COS and STIS spectrographs relevant to this work is merited. STIS, installed on *HST* in 1997 and repaired after a five-year loss of service in 2009, is a general-purpose slit spectrograph prioritizing spatial and spectral resolution for spectral imaging. COS, installed in 2009, is a wide-aperture spectrograph specifically prioritizing sensitivity to faint point sources in the FUV.

Effective area curves of the two instruments are shown in Figure 2.5, demonstrating the substantially greater sensitivity of COS in the FUV. In addition, COS has roughly $10 - 100\times$ lower background levels in the FUV. This makes COS useful for faint sources, while STIS is useful for brighter sources that would violate the count rate safety limits of COS. STIS observations are also required for measuring the flux of lines that are contaminated by Earth airglow. With STIS, the slit aperture allows the airglow to be spectrally resolved, allowing a correction to be applied by simply subtracting a measurement of the airglow made at a detector location offset from the target source. With cos, the large 2.5" primary science aperture does not resolve airglow, making corrections difficult (but not, at least for O I impossible: Ben-Jaffel & Ballester 2013). Both STIS and COS have time resolutions that do not pose a practical limitation for the observations in this work, 125 μs for STIS and 32 ms for COS. STIS is capable of higher wavelength resolution, reaching up to a resolving power of 200,000 for the E140H grating. The COS G130M configuration has a resolving

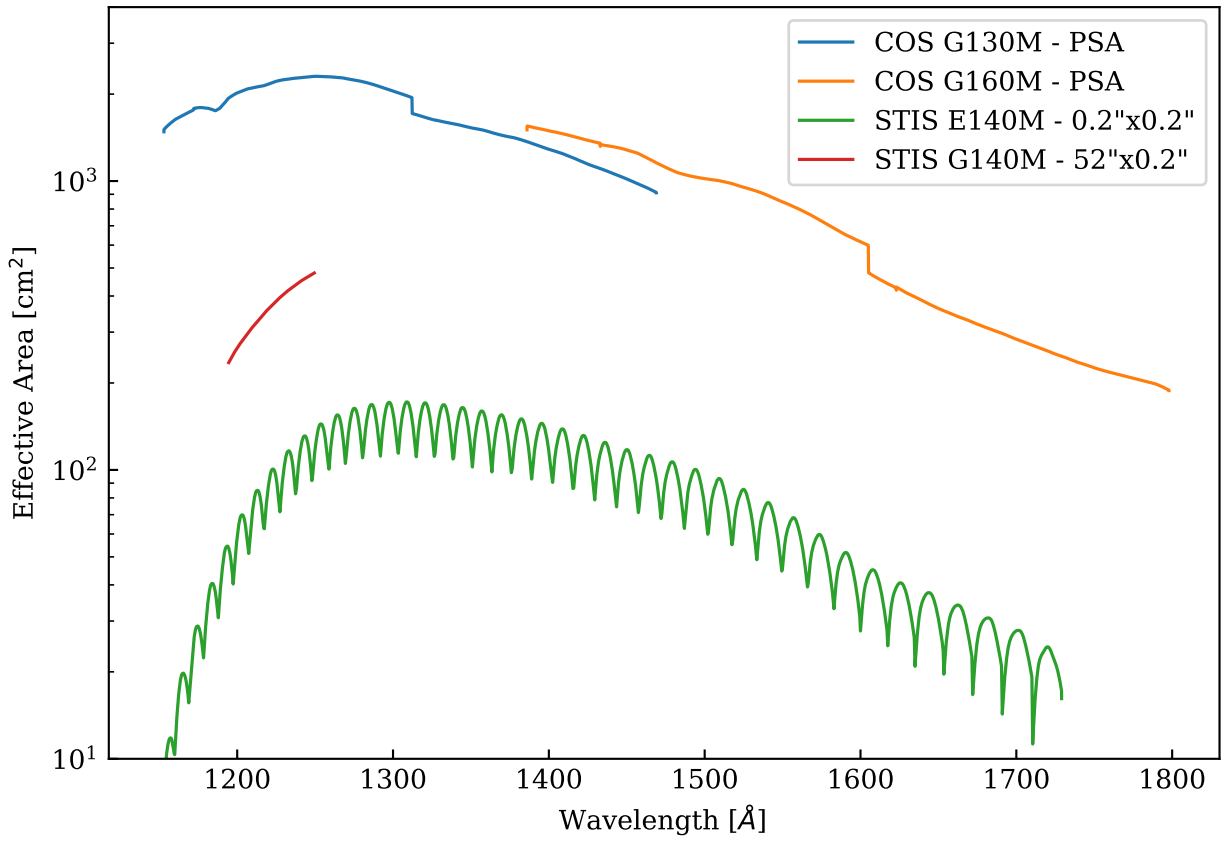

Figure 2.5 Effective areas of several COS and STIS configurations and apertures. PSA stands for the primary science aperture. The STIS G140M line plots only the 1222 central wavelength setting. Oscillations in the STIS E140M effective area curve correspond to Echelle orders.

power of 15,000 – 20,000, STIS E140M 46,000, and STIS G140M 10,000.

A notable systematic with STIS results from poor centering of the source in the slit aperture. In the MUSCLES observations discussed in Chapter 4, I concluded that this was the likely cause of substantial (tens of percent) differences in absolute fluxes measured in spectral ranges overlapped by COS and STIS observations. A related effect causing flux variations over the course of an orbit due to thermal movements that change the source alignment in the slit has been formally documented (Bohlin & Hartig, 1998).

For many of the time-series data presented in this thesis, variations induced by the dithering of fixed pattern noise is an issue. This dithering is done with the intent of mitigating the effect of fixed-pattern noise on the profiles of emission and absorption features. However, when relative photometric accuracy is the desired outcome, this dithering introduces and additional source of noise. Inaccuracies due fixed pattern noise can be as high as 5 – 10% at the pixel level, though integrated over an emission line this reduces to the 1% level. A prominent source of fixed-pattern noise for COS is the 10 – 20% shadows cast by the grid of electron repeller wires in the optical path. STIS has a single repeller wire that is generally positioned to avoid the spectral trace on the detector.

The absolute wavelength accuracy of STIS is superior to COS, at a few km s^{-1} for STIS and 15 km s^{-1} for COS in the medium-resolution FUV configurations. Another noteworthy systematic for COS is wavelength shifts introduced between exposures, particularly when the FPPOS setting is changed (i.e. the spectrum is dithered). This can introduce spurious changes in time series of narrow integrations of line flux if spectra from different exposures are not carefully aligned.

Bibliography

The below have been employed as general references in the construction of the above sections.

- Darling, Jeremy 2012, Atomic and Molecular Processes Lecture Notes
- Draine, B. T. 2011, Physics of the Interstellar and Intergalactic Medium

- Fox, A. J., et al. 2017, Cosmic Origins Spectrograph Instrument Handbook, Version 9.0
- Riley, A., et al. 2017, STIS Instrument Handbook, Version 16.0
- Rybicki, G. B., & Lightman, A. P. 2004, Radiative Processes in Astrophysics, 400
- Ladislas Wiza, J. 1979, Nuclear Instruments and Methods, 162, 587
- Linsky, J. L. 2017, ARA&A, 55, 159

Chapter 3

Fluctuations and Flares in FUV Stellar Emission

Preface

This chapter is a reproduction of the paper "Fluctuations and Flares in the Ultraviolet Line Emission of Cool Stars: Implications for Exoplanet Transit Observations," published in 2014 January in the *The Astrophysical Journal Supplements* (Loyd & France, 2014).

Abstract

Variations in stellar flux can potentially overwhelm the photometric signal of a transiting planet. Such variability has not previously been well-characterized in the ultraviolet lines used to probe the inflated atmospheres surrounding hot Jupiters. Therefore, I surveyed 38 F-M stars for intensity variations in four narrow spectroscopic bands: two enclosing strong lines from species known to inhabit hot Jupiter atmospheres, C II $\lambda\lambda$1334,1335 and Si III λ1206; one enclosing Si IV $\lambda\lambda$1393,1402; and 36.5 Å of interspersed continuum. For each star/band combination, I generated 60 s cadence lightcurves from archival *HST* COS and STIS time-tagged photon data. Within these lightcurves, I characterized flares and stochastic fluctuations as separate forms of variability. **Flares:** I used a cross-correlation approach to detect 116 flares. These events occur in the time-series an average of once per 2.5 h, over 50% last 4 min or less, and most produce the strongest response in Si IV. If the flare occurred during a transit measurement integrated for 60 min, 90/116 would destroy the signal of an Earth, 27/116 Neptune, and 7/116 Jupiter, with the upward bias in flux ranging from 1-109% of quiescent levels. **Fluctuations:** Photon noise and underlying stellar

fluctuations produce scatter in the quiescent data. I model the stellar fluctuations as Gaussian white noise with standard deviation σ_x. Maximum likelihood values of σ_x range from 1-41% for 60 s measurements. These values suggest that many cool stars will only permit a transit detection to high confidence in ultraviolet resonance lines if the radius of the occulting disk is $\gtrsim 1$ R_J. However, for some M dwarfs this limit can be as low as several $R_\oplus$.

3.1 Introduction

Transit observations in the far-ultraviolet (FUV, $1200 \leq \lambda \leq 1400$ Å) have revealed the existence of inflated atmospheres surrounding the hot Jupiters HD209458b (Vidal-Madjar et al., 2003, 2004; Linsky et al., 2010) and HD189733b (Lecavelier Des Etangs et al., 2010; Bourrier et al., 2013; Ben-Jaffel & Ballester, 2013). During the transit of these planets, the UV resonance transitions of several species in their atmospheres – H I, C II, O I, and Si III – produce detectable absorption against the background stellar emission. The depth of the absorption indicates that these species occupy a volume overfilling the planets' Roche lobes, suggesting atmospheric escape. Furthermore, such UV transit spectrophotometry can constrain the atmospheric mass loss rate (e.g. Vidal-Madjar et al. 2004; Lecavelier Des Etangs et al. 2010) and characterize the atmospheric response to changes in the stellar radiation and particle flux (Lecavelier des Etangs et al., 2012; Bourrier et al., 2013).

However, variability in the background flux source itself – the host star – presents additional, instrument-independent challenges for all transit observations. In a lightcurve, the transit signal can be spuriously weakened, sometimes completely obliterated, by flares buried within it, or amplified by flares flanking it. Outside of flares, the transit signal can be obscured by stochastic fluctuations in stellar luminosity that act as additional noise, compounding that of photon statistics and instrumental sources. These forms of stellar variability fundamentally limit transit observations. Therefore, evaluating the possibilities for future transit work necessitates measurements of this variability for potential host stars.

The list of potential targets is diverse, encompassing stars beyond those just on the main

sequence, such as HD209458b and HD189733b. Such candidate targets could include stars with transitional or debris disks (encompassing weak-line T-Tauri stars, WTTS) where planets might be in the process of coalescing from disk material. For example, van Eyken et al. (2012) report on the transit signature of a super-Jupiter orbiting a WTTS star in the Orion-OB 1a/25-Ori region. High contrast imaging of stars with disks has also revealed (proto)planetary objects or evidence for these objects through disk gaps, such as LkCa15 (Kraus & Ireland, 2012), PDS 70 (Hashimoto et al., 2012), RX J1633.9-2442 (Cieza et al., 2012), and TW Hya (Debes et al., 2013). Candidate targets also include post main-sequence stars. The evolved F5-F7 stars WASP-76, WASP-82, and WASP-90 host transiting hot Jupiters (West et al., 2013), as does the G8III giant HIP 63242 (Jones et al., 2013). In addition, observations of remnant debris orbiting white dwarfs (e.g. Farihi et al. 2013) hint at the possibility of detecting extant or decomposing planets around stars nearing the end of their lives.

To begin characterizing the range of background fluctuations faced by FUV transit observations, I have conducted a survey of stellar flares and stochastic fluctuations for the largest possible sample of stars with archival FUV photon event data from *HST* covering C II $\lambda\lambda$1334,1335 and Si III λ1206, two key lines for probing outer atmospheres of close-in exoplanets. I also include Si IV $\lambda\lambda$1394,1403 and a composite of interspersed continuum bands. I did not attempt to include H I λ1216 (Lyα) or O I λ1302 due to the correction for geocoronal emission that is required. This survey relies on UV data acquired by the two powerful UV spectrographs on board the *Hubble Space Telescope (HST)*: the Cosmic Origins Spectrograph (COS), with its G130M and G140L gratings, and the Space Telescope Imaging Spectrograph (STIS) with its E140M grating. To enable an analysis of temporal variability, I traded spectral resolution for temporal resolution. Thus, I employed short, 60 s time bins and summed photon counts over roughly the full width ($\sim$ 1-2 Å) of each line and 36.5 Å of interspersed continuum to create lightcurves. In comparison, transit observations have achieved resolutions of $\sim$ 0.1 Å (roughly 20-30 km s^{-1}) when coadding an entire transit dataset. However, these same observations commonly integrate over the full line-widths for increased signal to noise (e.g. Vidal-Madjar et al. 2003; Lecavelier Des Etangs et al. 2010).

I present the results of an analysis of 153 lightcurves of 60 s cadence, including (1) 116 flares I identified by cross-correlating with a flare-like kernel and (2) estimates or upper limits for the standard deviation of stochastic fluctuations in the quiescent portions of the lightcurve. In the remainder of this introduction, I expand upon the implications and physical sources of stellar variability and provide pointers to previous variability surveys. In Section 3.2, I describe the stellar sample and process of generating lightcurves from the FUV time-tagged photon data. In Section 3.3 I outline the variability analysis, treating flares and stochastic fluctuations separately. In Section 3.4, I present the results, followed in Section 3.5 by a discussion, including the implications for observing transits. I summarize the work in Section 3.6.

Throughout this paper, I will treat 3.5 h as the typical transit timescale. This is near the average transit duration of 3.6 h (sample standard deviation 1.9 h) for exoplanets listed in the Exoplanet Data Explorer (Wright et al., 2011a) as of 2013 October.

3.1.1 A Brief Discussion of Stellar Variability

Stellar variability can be divided into three categories based on the differing implications for transit observations:

(1) Periodicities: Oscillations of the stellar flux by phenomena that can be sufficiently characterized to predict the level of modulation over the course of a transit.

(2) Flares: Bursts of brightness isolated in time with respect to the cadence of the data, and well above the quiescent scatter in the lightcurve.

(3) Stochastic Fluctuations: Variations in the stellar flux that are too chaotic to be accurately predicted on transit timescales.

Predictable periodic signals are surmountable obstacles. Any periodic signal strong enough to be even modestly detected would allow an accurate model fit, bootstrapped over many cycles, such that removing or accounting for the signal would not obscure an otherwise detectable transit.

Strong flares complicate the lightcurve analysis. While it is possible to describe the distribution of solar flares in both strength and frequency (Cassak et al., 2008), a statistical model cannot predict the onset, magnitude, and evolution of flares for any specific timeline, such as during a transit. Strong flares thus pose the risk of overwhelming, and weak flares of attenuating, a transit signal. Flares occurring near a transit could augment estimates of the out-of-transit flux, spuriously deepening the transit signal. Beyond interfering with transit observations, flares might also impact the atmospheres of exoplanets, such as the stripping of atomic hydrogen from HD189733b conjectured by Bourrier et al. (2013) to be caused by an observed host-star flare.

Stochastic fluctuations, however, represent the greatest barrier to transit photometry. Because these fluctuations cannot be predicted deterministically over the course of a transit, they must be treated as noise. As with photon noise, they pose the risk of obscuring a true signal or causing a false one. This "noise" can be overcome by averaging measurements until the uncertainty is within tolerable limits, but with a caveat: Unlike photon noise, stochastic fluctuations are probably not white noise. For example, in 60 s cadence, broadband optical photometry from *Kepler*, stochastic fluctuations of stellar flux (attributed to granulation and magnetic activity) have a power spectrum that, unlike white noise, is not flat (Gilliland et al., 2010). Although *Kepler* measures broadband optical flux, not the chromosphere and transition region FUV emission line flux I analyzed, the fluctuations of the chromospheric near UV flux from YZ CMi also show a frequency-dependent power spectrum (Robinson et al., 1999). Therefore, it seems probable that stochastic fluctuations in stellar flux will not behave as white noise in any band. What appears as true noise at one cadence would resolve into smooth variations at some faster cadence. Below this threshold cadence, lightcurve points will be highly correlated. Binning adjacent flux measurements in this regime will not average out the scatter.

The emission line flux I analyzed samples regions with temperatures of $10^4 - 10^5$ K in the outer atmospheres of stars. Specifically, the peak formation temperatures of the lines in solar conditions are estimated by Dere et al. (2009) to be 3.2×10^4 K for C II $\lambda\lambda$1334,1335, 5×10^4 K for Si III λ1206, and 8×10^4 K for Si IV $\lambda\lambda$1393,1402. Reference models of the solar atmosphere place

emission from these lines in the thin transition region between the chromosphere and the corona. In contrast to the lines, the solar FUV continuum (shortward of 1500 Å) forms at slightly lower altitudes, primarily in a region of initial chromospheric temperature rise above the photospheric temperature minimum (Linsky et al., 2012a).

Variability in these regions of stellar atmospheres can result from several phenomena. Although drawing conclusions about these underlying physical phenomena is not the objective, the generally accepted origins of periodicities, flares, and stochastic fluctuations bear mentioning.

Periodic variability can be the result of a pulsational instability in the star (Gautschy & Saio, 1995, 1996) and/or rotation of long-lived, localized brightness variations (starspots, faculae, etc.) through the observer's field of view (Vaughan et al., 1981). A periodic signal can result from extrinsic phenomena as well. Gradual oscillations in flux are produced by phase changes of an orbiting planet (e.g. Borucki et al. 2009). Isolated, but nonetheless periodic, dips in flux occur when an orbiting object, such as an exoplanet or stellar companion, transits the host star (e.g. Wilson & Devinney 1971).

Flares are generally thought to be the result of magnetic reconnection events in the corona that abruptly convert magnetic energy into plasma kinetic energy. Some of this energy is deposited in the chromosphere and photosphere and radiated away (Haisch et al., 1991; Gershberg, 2005). Flares commonly produce a sharp rise in flux followed by an exponential decay lasting from hours to minutes, possibly even seconds (Pettersen, 1989; Gershberg, 2005). Within a single flare, multiple peaks and changes in the decay rate are possible. Some researchers have identified as flares events in which the stellar flux rises and fades more gradually (Houdebine, 2003; Tovmassian et al., 2003).

The strength and frequency of flares typically exhibit an inverse power-law relationship (e.g. Shakhovskaia 1989; Audard et al. 2000 for stellar flares, Lin et al. 1984; Nita et al. 2002 for solar flares). This implies that weaker flares are more prevalent than conspicuous events, such that many flares will occur in observations that cannot be clearly resolved as such. In fact, if the power law is steep enough, the lowest energy flares, often termed microflares, might inject enough heat into the corona of a star to explain the high temperatures present there (Hudson, 1991; Audard et al.,

2000).

Low energy "microflares" or even "regular" flares, if the data is not of sufficient quality to resolve them, will contribute to the observed stochastic fluctuations of a target. For instance, Robinson et al. (1999) suggest microflaring as an explanation for the quiescent stochastic fluctuations in near UV flux that they observed from YZ CMi . They simulate the production of such stochastic fluctuations with a microflare model and find that it closely resembles the YZ CMi quiescent data. Ultimately, the extent of the contribution of flares to the observed stochastic fluctuations of any target is determined by the level of stellar magnetic activity, the photometric quality of the data, and the threshold set for identifying a lightcurve anomaly as a flare rather than fluctuation.

The remaining proportion of stochastic fluctuations in transition region line emission could be explained by several phenomena. Transition region explosions, smaller events possibly associated with magnetic restructuring at the edges of newly emerging flux loops (Gershberg, 2005), could introduce variability while also serving as a dominant heating source for the transition region. Wood et al. (1997) suggested such events might explain broad components of Si IV and C IV emission in the FUV spectra of 11 late-type stars. However, Peter (2006) suggests magnetic flux braiding and consequent Joule dissipation might be the dominant heat source for the transition region. Both braiding of surface field and the emergence of field loops produce pockets of rapid heating in the three-dimensional MHD models of Hansteen et al. (2010) that could explain much of the temporal variability of line emission originating in the transition region. In the Hansteen et al. (2010) model, the injected energy results from work done on the magnetic field by photospheric motions, tying transition region variability to the convective cells and p-mode oscillations within the star. These convective cells and p-mode oscillations also affect the transition region environment by initiating high altitude shock waves (Wedemeyer-Böhm et al., 2009).

Variability of a planet-hosting star could be influenced by the planet itself. Planets orbiting close enough to a star will interact tidally and, possibly, magnetically with the host (Cuntz et al., 2000). Magnetic interactions could lead to flares from the reconnection of planetary and stellar fields (Rubenstein & Schaefer, 2000; Lanza, 2008), increased stochastic fluctuations from overall

magnetic activity enhancements (Cuntz et al., 2000), or periodicities from enhanced plages and faculae surrounding the sub-planetary point on the star (Lanza, 2008; Cohen et al., 2009; Kopp & Lean, 2011). Tidal interactions could produce flows and turbulence associated with the tidal bulge (Cuntz et al., 2000). They could also spin up the star (Aigrain et al., 2008), indirectly increasing overall stellar magnetic activity. These interactions are supported by some evidence (beginning with Shkolnik et al. 2003), but more definitive conclusions require future, dedicated observations (Lanza, 2011).

3.1.2 A Selection of Relevant Flare and Variability Studies

There is a long history of research into the frequency and intensity of flares on the Sun and other stars. Especially relevant is recent work by Hilton et al. (2010) and Davenport et al. (2012), and references therein, examining large (several 10^4) samples of M dwarf stars using multi-epoch data in the optical from the Sloan Digital Sky Survey (SDSS) and in the infrared from the Two Micron All Sky Survey (2MASS). Tofflemire et al. (2012) specifically assessed the impact of M dwarf flares on exoplanet observations in the infrared using three such stars. Recently, Kowalski et al. (2013) conducted a detailed spectrophotometric study in the near UV and optical of 20 M dwarf flares in order to probe the various mechanisms responsible for flare emission. Previous studies in the far and extreme UV are scarcer. Welsh et al. (2007) leveraged data from the *Galaxy Evolution Explorer* in the broadband near and far-ultraviolet to find 49 variable sources exhibiting 52 flares. The *Galaxy Evolution Explorer* FUV band data contain the Si IV line I analyzed for variability. In addition, Mullan et al. (2006) examined 44 F-M stars in broadband extreme UV time-series data from the *Extreme Ultraviolet Explorer*. The band they utilized is dominated by emission lines of Fe XVIII – Fe XXII formed at coronal temperatures upwards of 10^7 K, expected in magnetically active regions.

Several previous studies have quantified the stochastic variability of large samples of stars in the optical, most notably employing *Kepler* results to place the Sun's well-characterized variability in the context of other stars (see Basri et al. 2010 and McQuillan et al. 2012 for examples using

Kepler data and Eyer & Grenon 1997 for one using *Hipparcos* data). In addition, it is standard practice to quantify the variability of the exoplanet host star complimentary to radial-velocity or transit measurements, so many individual measurements of stellar variability exist (e.g. Dragomir et al. 2012; Kane et al. 2011; Berta et al. 2011). However, to the knowledge of the authors this paper presents the first analysis, focusing specifically on the implications for transit observations, of stellar variability in UV line emission flux.

3.2 Stellar Sample and Data Reduction

3.2.1 Sample Selection

Because the motivation for this work is the characterization of stellar variability in all potential targets for FUV transit work (Section 3.1), I constructed a stellar sample of **all** F-M stellar targets with archival *HST* time-tagged photon data covering the wavelengths of the C II, Si IV, and occasionally (27/42 datasets) Si III lines. These wavelengths are observed with the STIS E140M, COS G130M, and COS G140L gratings. Thus, I retrieved all public time-tagged photon data for the sample acquired with these gratings from the Mikulski Archive for Space Telescopes (MAST). I also obtained some data still proprietary under program 12464 (France et al., 2013).

I culled datasets from target stars known to have circumstellar gas disks or outflows because: (1) the hot gas lines have a (sometimes large) contribution from accretion of circumstellar gas onto the star and (2) emission from photoexcited H_2 and CO can overwhelm the chromospheric signal (France et al., 2011; Herczeg et al., 2002; Ardila et al., 2013). However, I retained many Weak-line T Tauri stars (WTTS) for which there did not seem to be significant contamination of the spectrum by disk or accretion-related emission because there is promise of finding transiting (proto)planets around such stars (Section 3.1). I also culled datasets where line emission was very weak compared to the background plus continuum (where the ratio of fluxes was roughly less than half). Lastly, I discarded individual exposures (but not entire datasets) where the exposure contained some portion of a known planet's transit.

After culling, 42 datasets remained covering 38 stars. (Four stars have data from two different instrument/grating configurations that I keep separate.) For these stars, I retrieved fundamental properties from a wide range of catalogs and individual studies. These properties include spectral type; age; temperature, $T_\star$; mass, $M_\star$; surface gravity, $\log_{10} g$; luminosity, $L_\star$; radius, $R_\star$; rotation period P_{rot}; and projected equatorial velocity, $v \sin i$. Table 3.1 lists the 38 stars, together with an abridged summary of properties.[1] (The online table lists all properties.[2]) The sample contains 5 F stars, 12 G stars, 8 K stars, and 13 M stars. According to the SIMBAD database (Wenger et al., 2000), 3 stars are characterized as Cepheids, 5 as flare stars, and 12 as variable stars. Another 8 are designated WTTS by either Herbig & Bell (1988), Alcala et al. (1995), Sterzik et al. (1999), or Neuhäuser et al. (2000). The remaining 10 members have no unusual classifications. The sample is diverse, ranging in age from roughly 2 Myr to 10,500 Myr; mass from 0.08 $M_\odot$ to 7.7 $M_\odot$; $\log_{10} g$ from 1.6 to 5.3 (cgs units); luminosity from 0.0003 $L_\odot$ to 5300 $L_\odot$; radius from 0.1 $R_\odot$ to 71 $R_\odot$; effective temperature from 2564 K to 6959 K; $v \sin i$ from < 1 km s^{-1} to 163 km s^{-1}; and rotation period from 0.4 d to 286 d. The dataset(s) analyzed for each star are summarized in Table 3.2 (the online table has information on each exposure).

[1] References for Table 3.1 (1) Rodríguez et al. (2000); (2) Che et al. (2011); (3) Holmberg et al. (2009a); (4) Acharova et al. (2012); (5) this work; (6) Caputo et al. (2005); (7) Tetzlaff et al. (2011); (8) Hatzes & Cochran (1995); (9) Lyubimkov et al. (2010); (10) Takeda et al. (2007); (11) Casagrande et al. (2011); (12) Linsky et al. (2012b); (13) Allende Prieto & Lambert (1999); (14) Montes et al. (2001b); (15) Silva-Valio (2008); (16) Torres et al. (2008); (17) Gray et al. (2006); (18) Telleschi et al. (2005); (19) Strassmeier (2009); (20) Metchev & Hillenbrand (2009); (21) Hartman et al. (2010); (22) Strassmeier & Rice (1998); (23) König et al. (2005); (24) Montes et al. (2001a); (25) Gaidos et al. (2000); (26) Cenarro et al. (2007); (27) Sousa et al. (2011); (28) Shenavrin et al. (2011); (29) Valenti & Fischer (2005); (30) Petit et al. (2008); (31) Jetsu et al. (1993); (32) Eggen & Iben (1989); (33) Isaacson & Fischer (2010); (34) Mamajek & Hillenbrand (2008); (35) Baliunas et al. (1996); (36) Herbig & Bell (1988); (37) Kraus & Hillenbrand (2009); (38) Watson (2006); (39) van Belle & von Braun (2009); (40) Henry & Winn (2008); (41) Bouchy et al. (2005); (42) Santos et al. (2005); (43) Pojmanski et al. (2005); (44) Torres et al. (2006); (45) Alcala et al. (1995); (46) Weise et al. (2010); (47) Messina et al. (2011); (48) Messina et al. (2010); (49) Palla & Stahler (2002); (50) Kraus et al. (2011); (51) White et al. (2007); (52) Robrade et al. (2012); (53) Donahue et al. (1996); (54) Riviere-Marichalar et al. (2012); (55) Bertout et al. (2007); (56) Xiao et al. (2012); (57) Koen et al. (2010); (58) Bailey et al. (2009); (59) Sterzik et al. (1999); (60) Plavchan et al. (2009); (61) Manara et al. (2013); (62) Kalas et al. (2004); (63) Neuhäuser et al. (2000); (64) Jenkins et al. (2009a); (65) Demory et al. (2007); (66) von Braun et al. (2012); (67) Torres (2007); (68) Önehag et al. (2012); (69) Shkolnik et al. (2009); (70) Hempelmann et al. (1995); (71) Correia et al. (2010); (72) Rivera et al. (2005); (73) Selsis et al. (2007); (74) Vogt et al. (2010); (75) Yıldız (2007); (76) Kiraga & Stepien (2007); (77) Demory et al. (2009); (78) Reiners & Basri (2009); (79) Martin et al. (1994)

[2] Online tables and figure sets available at http://iopscience.iop.org/0067-0049/211/1/9/

Table 3.1. Abridged properties of the stars in the sample[a]

Star	Spectral Type[b]	Ref	Other Class.[b]	Ref	N_p	Age (Myr)	Ref	P_{rot} (d)	Ref	M ($M_\odot$)	Ref
β Cas	F2IV		δ Sct Var	1		1124±45[c]	2,3	0.89±0.03	2	1.91±0.02	2
δ Cep	F5Iab		Cepheid Var			66	4	<114[d]	5	4.82±0.26[c]	6
α Per	F5Iab		Var			45.9±4.2	7	87.7	8	7.3±0.3	9
β Dor	F6Ia		Cepheid Var			42.5±2.7	7	<286±98[d]	5	7.7±0.2	7
Polaris	F7Ib-IIv		Cepheid Var			50±11	7	<79[d]	5	6.9±0.5	7
HD25825	G0					3700±1200[c]	10,11	∼6.5	12	1.055±0.024[c]	10,13
HD209458	G0V	14			1	2900±870[c]	10,3,11	11.4	15	1.128±0.018[c]	10,13,16
χ^1 Ori	G0V	17	RS CVn Var			2160±870[c]	10,11	5.1	18	0.90±0.01[c]	10,13
HII314	G1-2V	19	BY Dra Var			126	20	1.47851	21	1.1	20
EK Dra	G1.5V	14	BY Dra Var			27.6±4.2	7	2.686[c]	22,23	$1.044^{+0.014}_{-0.02}$	10
π^1 UMa	G1.5Vb	14	BY Dra Var			300	24	4.89	25	1	20
HD90508	G1V	26				10500±2000[c]	3,11	<21[d]	5	1.02±0.13	13
HD199288	G2V	17				7700±2400[c]	3,11	<12[d]	5	0.896±0.017[c]	13,27
18 Sco	G2Va	28	Var			5500±1400[c]	29,10,11	22.7±0.5	30	1.008±0.024[c]	29,10,13
FK Com	G4III	19	Rot Var			···		2.40025	31	1.5	32
HD65583	G8V					5300±2600[c]	10,11	40	33	$0.816^{+0.02}_{-0.042}$	10
HD103095	G8Vp					8300^{+3900}_{-3800}	34	31	35	$0.661^{+0.028}_{-0.006}$	10
HD282630	K0V		WTTS	36		6.9^{+6}_{-4}	37	2.2321	38	$1.35^{+0.19}_{-0.16}$	37
HD189733	K1V	39			1	6800^{+5200}_{-4400}	16	11.95±0.01	40	0.816±0.025[c]	16,41
HD145417	K3V	17				7100±4700	11	<6.9[d]	5	0.62	42
V410-τ	K4IV	19	WTTS	36		2.0±0.4	7	1.872	43	1.2±0.2	7

Table 3.1 (cont'd)

Star	Spectral Type[b]	Ref	Other Class.[b]	Ref	N_p	Age (Myr)	Ref	P_{rot} (d)	Ref	M ($M_\odot$)	Ref
EG Cha	K4Ve	44	WTTS	45		5±2	46	4.5±0.04	47	1	48
HBC427[e]	K5		WTTS	36		3.3	49	9.3898	38	1.4	50
61 Cyg A	K5V	51	BY Dra Var			6000±1000	52	35.37	53	$0.66^{+0.01}_{-0.002}$	10
LkCa 4	K7V	54	WTTS	36		2.7±1.5	55	3.371	56	0.77±0.09	55
GJ832	M1.5	57			1	···		···		0.45±0.05	58
TWA13B	M1Ve	44	WTTS	59		8±2	60	5.35±0.03	48	0.68	61
TWA13A	M1Ve	44	WTTS	59		8±2	60	5.56±0.03	48	0.7	61
AU Mic	M1Ve	44	BY Dra Var			12±2	60	4.85±0.02	47	0.47±0.12[c]	60,48,62
CE Ant	M2Ve	44	WTTS	63		5.3±1.9[c]	46,63	5±0.03	48	0.55±0.15	63
GJ436	M3.5V	64			1	6000^{+4000}_{-5000}	16	48	65	0.445±0.008[c]	66,67,68
EV Lac	M4.5V	64	Flare			25	69	4.38	70	0.315±0.002	64
AD Leo	M4.5Ve	14	Flare			25	69	2.6	70	0.390±0.032	64
IL Aqr	M5.0V	64	BY Dra Var		4	2600±2500	71	96.7±1	72	0.33±0.01	68
HO Lib	M5.0V	64	BY Dra Var		4	9000±2000	73	94.2±1	74	0.3087±0.0057[c]	64,68
Prox Cen	M6Ve	44	Flare			5750±150	75	82.53	76	0.123±0.006	77
GJ3877	M7.0V	64	Flare			3100	78	<1.2±0.5[d]	5	0.10±0.02[f]	
GJ3517	M9.0V	64	Flare			3100	78	<0.4[d]	5	0.08±0.02	79

[a]Some stellar properties, uncertainty digits, planet references, and footnotes omitted for brevity. The full table is available at http://iopscience.iop.org/0067-0049/211/1/9/.

[b]Reproduced from the SIMBAD database (Wenger et al., 2000) with associated references when available. References for the WTTS classifications are not taken from SIMBAD.

[c]Mean of multiple values found in the reference(s), using $1/\sigma^2$ weighting factors when possible. When uncertainties on a particular value were asymmetric, I used the average of the two uncertainties as σ. When the literature provided four or more values **without uncertainties**, I estimated the uncertainty as the sample standard deviation of the values.

[d]Represents the upper limit, $P/\sin i$, computed from the $v \sin i$ and R values. Where possible, I used simple propagation of errors to estimate the uncertainty.

[e]Unresolved binary system (see Section 3.2).

[f]Value assumed from stars of similar spectral type.

References. — See text for list of references.

Table 3.2. Abridged catalog of observations

Dataset[a] No.	Star	Inst.	Grating	Start (UT)	N_{exp}	T_{obs} (h)	$\sum T_{exp}$ (h)	Percent Observed	$T_{\max}$ (h) [b]
1	β Cas	COS	G130M	2010 Jun 07 18:00:37 UT	2	0.39	0.36	91.63%	0.38
2	δ Cep	COS	G130M	2010 Oct 19 00:12:10 UT	18	5705.01	2.38	0.04%	0.37
3	α Per	COS	G130M	2010 Jul 13 07:32:49 UT	2	0.42	0.39	92.18%	0.41
4	β Dor	COS	G130M	2010 Nov 14 01:53:04 UT	14	6301.48	1.91	0.03%	0.36
5	Polaris	COS	G130M	2009 Dec 25 08:56:39 UT	4	48.62	1.31	2.70%	0.70
6	HD25825	COS	G130M	2010 Feb 20 23:15:33 UT	2	0.36	0.32	90.06%	0.35
7	HD209458	COS	G130M	2009 Sep 19 10:10:15 UT	14	698.99	5.75	0.82%	0.65
8	HD209458	STIS	E140M	2001 Aug 11 13:41:50 UT	4	1925.79	2.11	0.11%	0.57
9	χ^1 Ori	COS	G130M	2010 Mar 19 06:47:26 UT	2	0.39	0.36	91.63%	0.38
10	HII314	COS	G130M	2009 Dec 16 09:28:55 UT	3	2.15	0.89	41.53%	0.38
11	EK Dra	COS	G130M	2010 Apr 22 09:18:42 UT	18	16970.70	2.30	0.01%	0.74
12	π^1 UMa	COS	G130M	2010 Feb 28 22:31:16 UT	2	0.39	0.36	91.63%	0.38
13	HD90508	COS	G140L	2010 Jun 19 03:55:21 UT	4	2.14	1.40	65.35%	0.85
14	HD199288/G140L	COS	G140L	2009 Nov 23 03:31:07 UT	5	3.58	1.32	36.77%	0.71
15	HD199288/G130M	COS	G130M	2009 Nov 23 07:58:43 UT	4	2.46	1.61	65.62%	0.40
16	18 Sco/G140L	COS	G140L	2011 Feb 04 20:19:10 UT	2	1.24	0.46	37.60%	0.23
17	18 Sco/G130M	COS	G130M	2011 Feb 04 21:46:43 UT	3	1.68	0.75	44.72%	0.54
18	FK Com	COS	G130M	2011 Mar 07 01:31:09 UT	47	2079.45	9.19	0.44%	0.81
19	HD65583	COS	G140L	2010 Mar 27 09:38:51 UT	4	2.18	1.34	61.81%	0.81
20	HD103095/G140L	COS	G140L	2010 May 27 06:00:33 UT	3	0.59	0.53	88.83%	0.58
21	HD103095/G130M	COS	G130M	2010 May 27 09:34:00 UT	2	0.84	0.79	94.11%	0.38

Table 3.2 (cont'd)

Dataset[a] No.	Star	Inst.	Grating	Start (UT)	N_{exp}	T_{obs} (h)	$\sum T_{exp}$ (h)	Percent Observed	$T_{\max}$ (h) [b]
22	HD282630	COS	G130M	2011 Mar 30 23:21:36 UT	4	1.94	0.54	27.90%	0.34
23	HD189733	COS	G130M	2009 Sep 16 18:31:52 UT	6	6.65	1.29	19.45%	0.82
24	HD145417	COS	G140L	2010 Mar 11 21:57:16 UT	4	2.22	1.49	66.82%	0.88
25	V410-τ	STIS	E140M	2001 Jan 30 10:35:33 UT	4	5.25	2.66	50.70%	0.80
26	EG Cha	COS	G130M	2010 Jan 22 07:53:57 UT	4	0.94	0.82	87.38%	0.44
27	HBC427	COS	G130M	2011 Mar 29 23:42:24 UT	4	1.83	0.59	32.27%	0.34
28	61 Cyg A	COS	G130M	2010 Mar 28 23:08:26 UT	2	0.39	0.36	91.62%	0.38
29	LkCa 4	COS	G130M	2011 Mar 30 06:05:02 UT	4	1.39	0.64	45.95%	0.34
30	GJ832	COS	G130M	2012 Jul 28 22:12:56 UT	2	1.26	0.60	47.68%	0.33
31	TWA13B	COS	G130M	2011 Apr 02 04:26:51 UT	4	0.82	0.71	85.65%	0.38
32	TWA13A	COS	G130M	2011 Apr 02 01:26:37 UT	4	0.68	0.55	81.49%	0.31
33	AU Mic	STIS	E140M	1998 Sep 06 12:17:14 UT	4	5.35	2.81	52.45%	0.73
34	CE Ant	COS	G130M	2011 May 05 06:33:24 UT	4	1.63	0.52	32.06%	0.28
35	GJ436	COS	G130M	2012 Jun 23 07:22:56 UT	3	1.74	0.94	53.82%	0.62
36	EV Lac	STIS	E140M	2001 Sep 20 16:45:48 UT	4	5.30	3.03	57.21%	4.04
37	AD Leo	STIS	E140M	2000 Mar 10 03:28:05 UT	26	19540.16	18.62	0.10%	4.01
38	IL Aqr	COS	G130M	2012 Jan 05 01:36:44 UT	2	1.58	0.56	35.47%	0.33
39	HO Lib	COS	G130M	2011 Jul 20 13:47:36 UT	3	1.36	0.41	30.20%	0.17
40	Prox Cen	STIS	E140M	2000 May 08 00:58:04 UT	7	29.10	9.92	34.08%	6.01
41	GJ3877	COS	G140L	2011 Jan 30 18:11:23 UT	6	2.38	1.40	58.88%	0.82
42	GJ3517	COS	G140L	2011 Feb 15 12:30:49 UT	12	7.02	2.81	39.96%	0.81

3.2.2 Lightcurve Extraction

The data retrieved from MAST ("tag" files for STIS and "corrtag" files for COS) consist of event lists of the time and detector coordinates for each recorded count. To process these data, I developed a customized IDL pipeline that constructs lightcurves by identifying a region corresponding to a chosen wavelength band (or regions if multiple orders in STIS/E140M exposures contain appropriate wavelengths) to extract signal counts, then bins these counts by the chosen cadence. It also identifies an adjacent background region, and subtracts the cadence-binned counts (adjusted according to difference in areas) from the signal. Each lightcurve point is assigned a photometric uncertainty equal to the sum, in quadrature, of the Poisson errors of the signal and background counts.

A portion of the event-list data from a STIS exposure is displayed in Figure 3.1, overplotted with the dispersion axis of each spectral order produced by the Echelle grating. From these data, assigning a wavelength to each count according to the nearest order and recording its cross-dispersion (vertical) distance from that order's dispersion axis produces Figure 3.2a. Finally, accumulating all of the counts within the signal ribbon in Figure 3.2a and subtracting the area-scaled background ribbon counts, results in the accumulated spectrum of Figure 3.2b. Figure 3.3 is analogous to Figure 3.2 for example COS data. A plot similar to Figure 3.1 is unnecessary for COS exposures because they contain only a single spectral order.

I used the custom pipeline to create lightcurves with a uniform cadence of $\Delta t = 60$ s for the C II, Si IV, FUV continuum, and where possible, Si III bands outlined in Table 3.3. The OIV] λ1401 line falls between the two Si IV bands, but a visual inspection of the spectra for each star revealed no contamination. A $\Delta t = 60$ s cadence provided a balance between higher signal-to-noise, a greater number of lightcurve data points, and the ability to resolve flares. In addition, it nearly matches the $\Delta t = 58.85$ s short cadence *Kepler* data (Koch et al., 2010), facilitating comparisons between the datasets. (Appendix A.2 provides an analysis of the effect of cadence on precision in estimating white-noise levels that also supports the use of a short cadence.) In Figures 3.1 and 3.3a,

Table 3.2 (cont'd)

Dataset[a] No.	Star	Inst.	Grating	Start (UT)	N_{exp}	T_{obs} (h)	$\sum T_{exp}$ (h)	Percent Observed	$T_{\max}$ (h) [b]

[a]Corresponds to the numbering of Figure Sets 4 and 9.

[b] Longest single block of **quiescent** data with $\geq 50\%$ time exposed and constant central wavelength setting of the detector (i.e. the longest timescale of sampled variability).

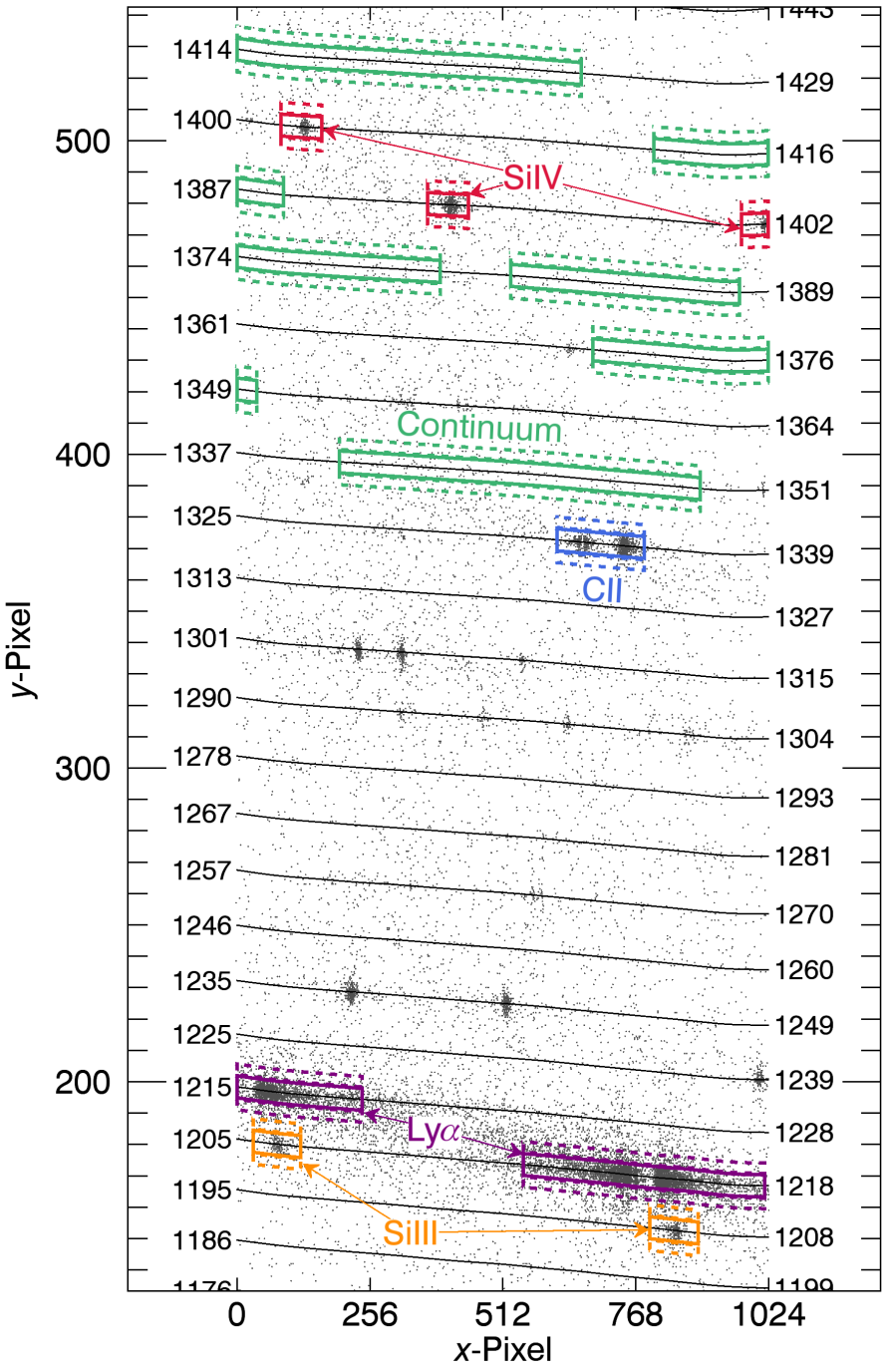

Figure 3.1 Portion of exposure o61s01010 (MAST ID) from STIS of AD Leo. The figure has been cropped and stretched for display. Dots represent ∼30% of the detected counts (many overlap). Spectral orders appear as black lines with labels showing the endpoint wavelengths in Å of each order's dispersion axis. Signal and background count extraction areas are shown as solid and dashed lines respectively.

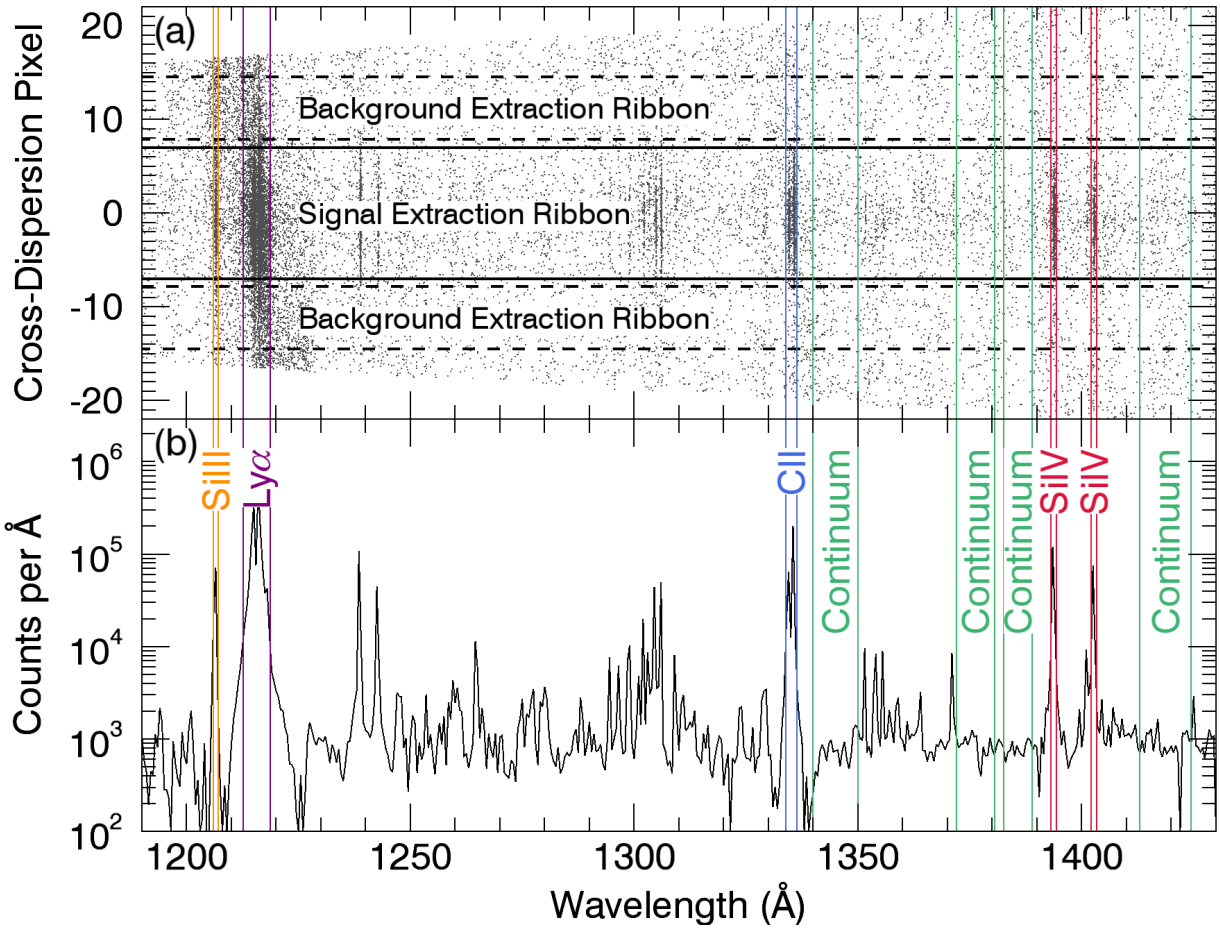

Figure 3.2 (a) Example STIS counts from AD Leo after wavelength assignment (Figure 3.1). Dots represent ∼1% of the detected counts (many overlap). The upper and lower limits of the count cross-dispersion pixels increase with wavelength because the spectral orders are spaced farther apart (see Figure 3.1). (b) Spectrum from the full set of background-subtracted signal counts histogrammed into 0.5 Å bins. Vertical lines highlight the bands used to extract lightcurves. The dips to either side of strong lines are an artifact of light from bright lines scattered diagonally into the background ribbons and subtracted off (visible in Figure 3.1).

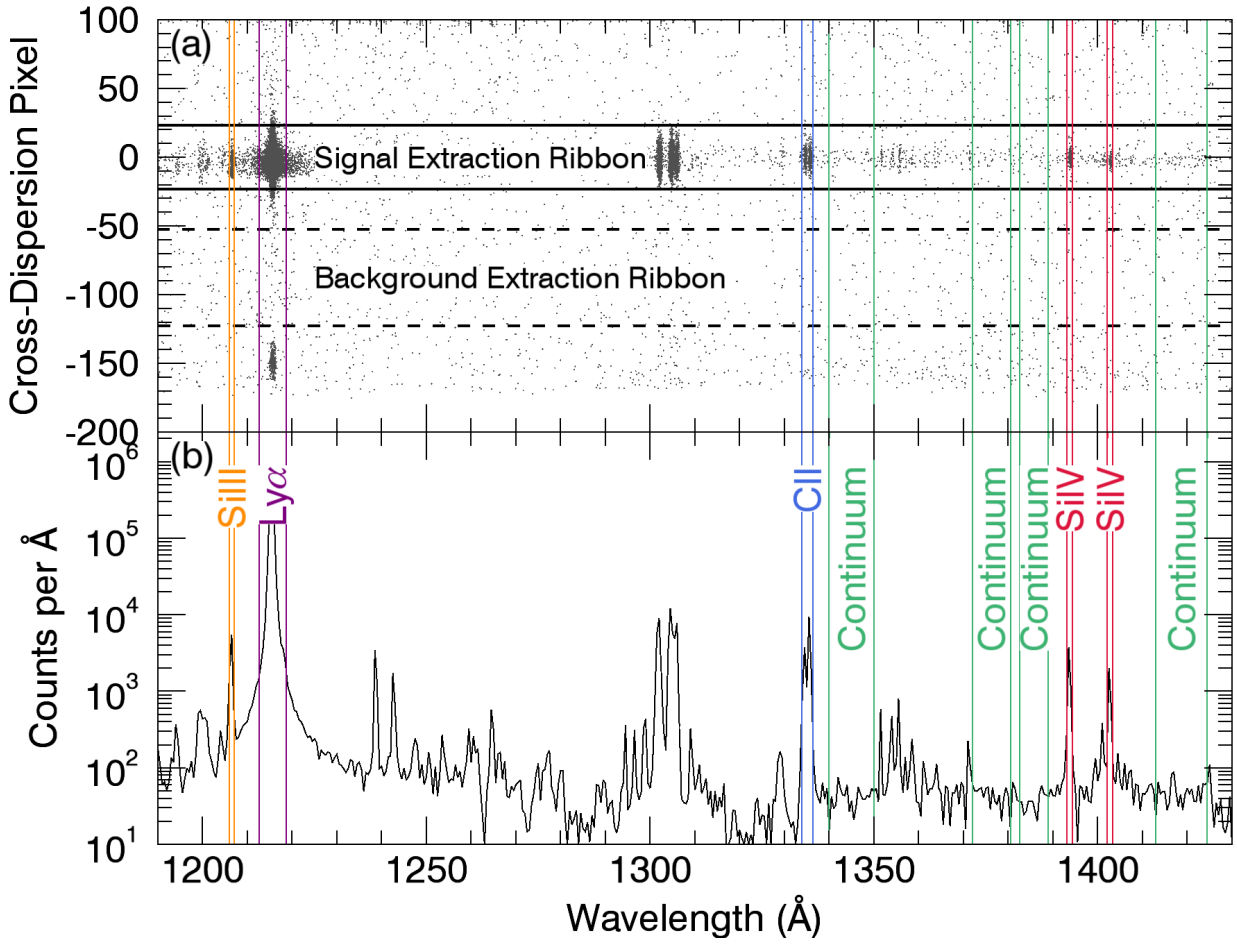

Figure 3.3 Example COS G130M counts from CE Ant (Table 3.2), following the same format as Figure 3.2 and plotting ∼4% of the counts.

Table 3.3. Observed line bands

Ion/Line[a]	λ_{rest}[b] (Å)	Band (Å)
Si III	1206.51	1205.92 – 1207.12
Si IV	1393.76	1393.16 – 1394.36
	1402.77	1402.17 – 1403.37
C II	1334.53	1333.90 – 1336.30
	1335.71	
FUV Continuum		1340.00 – 1350.00
		1372.00 – 1380.50
		1382.50 – 1389.00
		1413.00 – 1424.50
Lyα[c]	1215.67	1212.67 – 1218.67
	1215.67	

[a]Throughout the paper I refer to these emission lines and bands simply by this identifier.

[b]These values were retrieved from the National Institute of Standards and Technology Atomic Spectra Database at http://www.nist.gov/pml/data/asd.cfm (Kramida et al., 2012).

[c]While not analyzed for variability, I included the Lyα line to compare to the lightcurves of other lines in search of contamination by geocoronal emission.

solid lines outline signal extraction regions corresponding to the bands in Table 3.3 and dotted lines outline background extraction regions. For each star, I concatenated all exposures from the same grating into a single temporal dataset.

Figures 3.4 and 3.5 provide example lightcurves drawn from the full set of 153, viewable online as Figure Set 4. Both figures also exhibit high-pass filtered (Section 3.3.1) versions of these data and highlight flare points (Section 3.3.2) in red. The full set of lightcurves exhibit a wide range of signal-to-noise; quoted as range (median) these are C II: 0.8-150 (8.6), Si III: 0.8-22 (5.2), Si IV: 0.5-115 (6.5), and FUV continuum: 0.8-222 (3.9). The lightcurves also vary substantially in the number and spacing of points, containing from $\sim$20 to $\sim10^3$ (median $\sim$50) points. Consequently, some small datasets sample the stellar flux over less than 0.5 h, and some large datasets sample (exceedingly sparsely) the stellar flux over the course of several years.

3.2.3 Continuum Subtraction

In addition to the total flux within each line at 60 s time steps, I also computed the continuum subtracted flux in the lines. To this end, I totaled the photon counts in two bands near the line of interest. These were 1324.5-1328.3 Å and 1338-1350.5 Å for C II, 1203-1205 Å and 1208-1210 Å for Si III, and 1382.5-1389 Å and 1413-1424.5 Å for Si IV. The blueward C II band fell on the detector gap for some COS datasets. In these instances, I halved the redward band and extrapolated from those two points. I assumed the counts in each pair of bands represented the integration of a linear continuum. With this assumption, I estimated the number of counts integrated over the emission line band attributable to the continuum. Subtracting this estimate from the line counts and augmenting the line flux error with the error in the continuum estimate completed the continuum subtraction.

The continuum contributes significantly to the line flux of the F stars in the sample, with a median contribution of 27% in C II, 11% in Si III, and 40% in Si IV. In the G, K, and M stars the median contribution is 2% in C II, 8% in Si III, and 4% in Si IV. The contribution to Si III is similar in all the stars because the "continuum" is actually the blueward wing of the stellar Lyα that

forms the base flux beneath that line in the spectra of all 38 stars. I use the continuum-subtracted data when identifying and characterizing flares but not when quantifying stochastic fluctuations, for reasons discussed in Section 3.3.3.

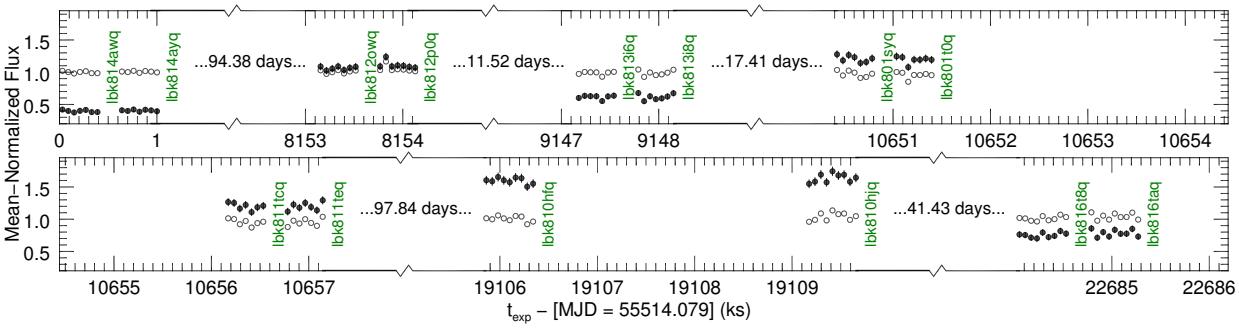

Figure 3.4 Example lightcurve of a quiescent star created from 14 COS/G130M exposures of the Cepheid variable β Dor in the C II band. Solid points are the unfiltered values, while open points are high-pass filtered with cutoff frequency $(7\ \mathrm{h})^{-1}$. The lightcurve is normalized by the mean quiescent flux of $3.88 \pm 0.23 \times 10^{-14}$ erg s^{-1} cm^{-2}. A label of the MAST identifier (in green) marks the end of each exposure. Figure Set 4, available at http://iopscience.iop.org/0067-0049/211/1/9/, presents lightcurves like this for each star + band.

3.3 Variability Analysis

3.3.1 High-Pass Filtering

Filtering the lightcurves was necessary because low-frequency periodicities or overall drifts can sometimes dominate the signal. For example, the roughly two-day rotation of FK Com produces a periodic signal of much greater amplitude than rapid fluctuations visible in the lightcurve. Left unaddressed, such signals result in the misidentification of flares (Section 3.3.2) and excess noise estimates (Section 3.3.3) that overestimate the host-induced uncertainty in a transit depth measurement. However, precisely characterizing these signals is beyond the scope of this work because they do not seriously threaten transit observations – they can generally be fitted and removed. Thus, rather than attempt to characterize low-frequency periodicities and drifts (difficult with highly clustered data), I mitigate their effects with a high-pass filter. The algorithm I employed is an exponential filter developed by Rybicki & Press (1995) for irregularly spaced data.

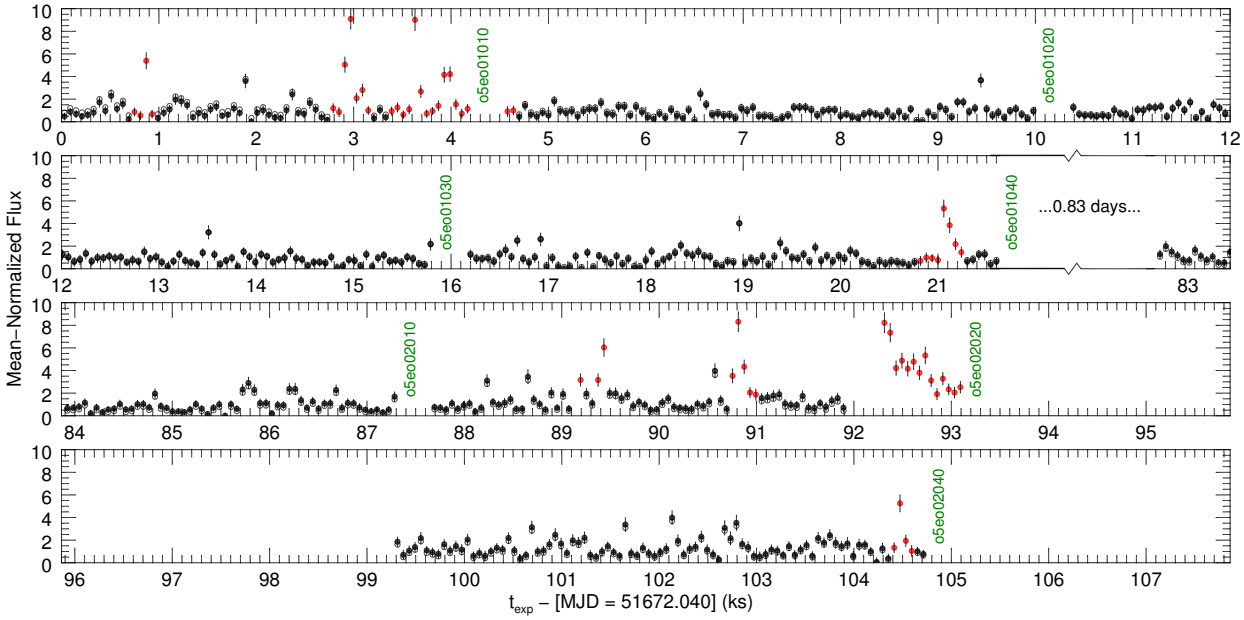

Figure 3.5 Example lightcurve of a flaring star created from 7 STIS/E140M exposures of Prox Cen in the Si IV band following the same formatting as Figure 3.4, but with the y-axis clipped at 10. Points identified as flaring are red. The mean quiescent flux is $5.24 \pm 0.42 \times 10^{-15}$ erg s^{-1} cm^{-2}. Some flare points exceed the y-axis maximum.

As formulated by Rybicki & Press (1995), the filter accepts as input a 3 dB cutoff frequency (in power). For this I chose 7 h, twice the typical transit duration. Figure 3.6 displays the full filter amplitude response.

Filtering the data has several side effects concerning the identification of flares and quantification of stochastic fluctuations. Most importantly, filtering shifts isolated clusters of points containing a large flare down due to their greater mean. This can significantly increase the scatter in the quiescent data. Consequently, after I filtered all of the data to identify flares, I then filtered only the quiescent data before quantifying stochastic fluctuations in the lightcurves. This and other effects of filtering are further addressed in the Sections 3.3.2 and 3.3.3.

3.3.2 Sweeping for Flares

I sought to identify flares both to characterize the risk they pose to transit observations and to prevent them from driving estimates of stochastic fluctuations. When selecting a means of sweeping for flares, I made two important choices. First, I wished to treat the large volume of data consistently throughout. Thus, I avoided a by-eye approach. Second, I recognized that UV transit data will not always encompass the same set of chromospheric lines available in these data. Thus, I did not utilize a flare in one band to confirm a questionable, simultaneous event in another.

Initially, I hoped to identify flares by mimicking the methodology of one or more previous studies, thus facilitating comparison of the results of this analysis to the literature. However, I found no objective flare detection strategy well suited to this dataset. Therefore, I created a custom algorithm that identifies flares by cross correlating the lightcurve with a flare-shaped kernel.

In outline, the algorithm operates by first high-pass filtering the continuum-subtracted data, subtracting the mean, and normalizing by the sample standard deviation, σ, computed excluding outliers beyond 2.5σ. Once in σ units, the algorithm correlates the lightcurve with the flare kernel (defined in σ units as well, see below) and flags points where the correlation exceeds the value of the flare kernel correlated with itself. For each group of newly flagged points, the algorithm records the index of the peak point. The algorithm then repeats the filtering, mean-subtracting, and σ-

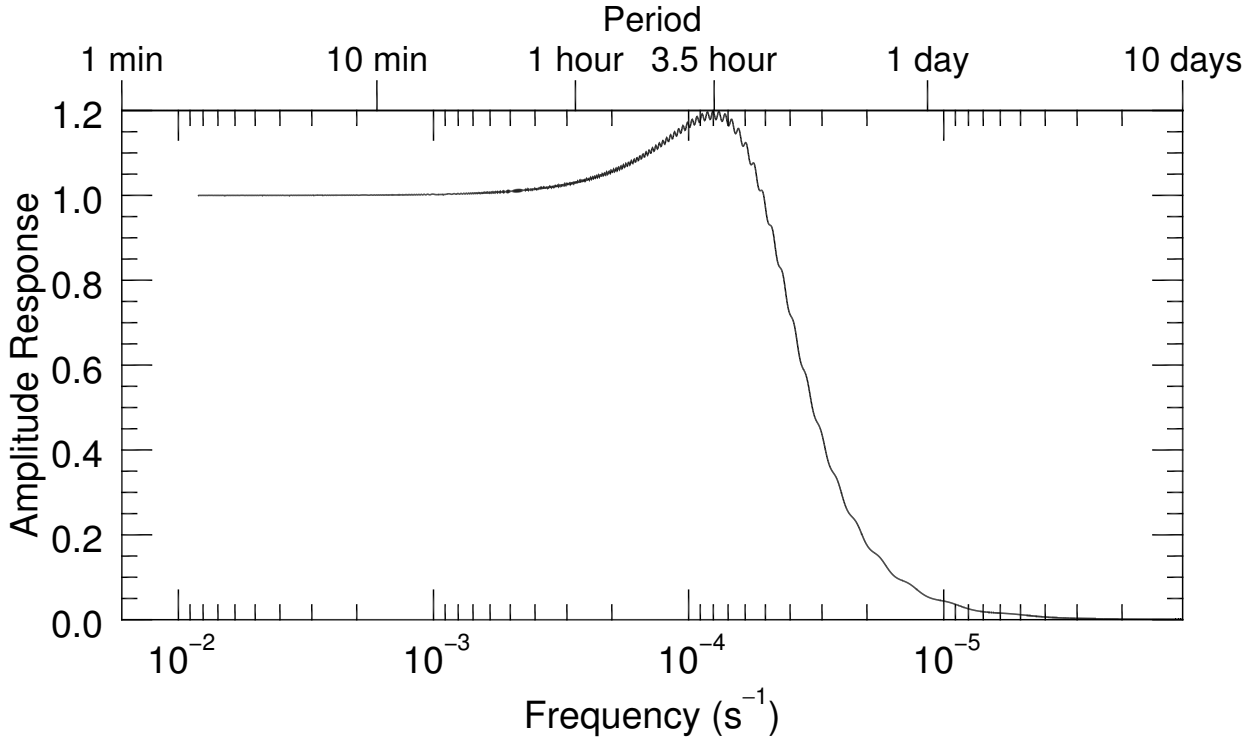

Figure 3.6 Frequency response of the numerical technique I employed to high-pass filter the data with cutoff frequency $(7\ \mathrm{h})^{-1}$.

normalizing steps with the original data but excluding the recorded points and again searches for flares. As this process is repeated, the algorithm adds and removes points from the list of recorded flare points one by one out to the first point at or below the quiescent mean. This slow growth of the identified regions avoids large changes between iterations that can prevent convergence. When points are no longer being added or removed, or when the same points are being added and removed in repetition, the process is stopped.

Since the flare kernel used for correlating is in σ units, the actual energy of a flare precisely matching the flare kernel is different for each lightcurve: The algorithm will identify flares only down to a minimum energy level appropriate to the noise in the given lightcurve. I chose a flare kernel that is an exponentially decaying curve with time constant of $2\Delta t$ (120 s) and lasting for six points, thus representing the canonical (see, e.g., Moffett 1972) impulse-decay flare shape. This is near the lower bound of the decay times of flares observed by Mullan et al. (2006) in their extreme-UV data for 44 F-M stars. While shorter flares are possible, most observations have insufficient signal-to-noise to resolve them.

After choosing the shape of the flare kernel, its amplitude remained an open parameter. This amplitude determines how conservative the algorithm will be when identifying flares. To set it, I ran the algorithm on simulated datasets of Gaussian white noise with flare kernels of varying amplitude until the algorithm made, on average, about one spurious detection. The simulated datasets had the same point spacing as the true datasets with 19,095 lightcurve points in total between all star and band combinations. Through these simulations, I found that a flare kernel with an amplitude of 3.5σ, i.e. the function $3.5e^{-t/(120\text{ s})}$ evaluated at the points $t = 0, 60, 120, 180, 240, 300$ s, produced about one false detection. More precisely, in 10^4 simulations of the entire dataset (i.e., all stars, all bands), the algorithm with these definitions made on average 1.5 spurious flare detections, flagging 0.08% of the simulated data. I used this same kernel for each lightcurve.

The results are moderately sensitive to the amplitude of the flare kernel. Decreasing the amplitude to 2.5σ identified over twice as many events as flares (compared to a 3.5σ-amplitude kernel) but also produced 43 false detections on average in simulated data. Consequently about a

third of the additional detections in the actual data resulting from using a 2.5σ-amplitude kernel were likely spurious. Alternatively, increasing the kernel amplitude to 4.5σ identified about 2/3 as many flares, but reduced spurious detections in simulated white-noise data to 0.03 events on average. The results are also sensitive to the shape of the flare kernel, particularly for events that are near the threshold of detection. For example, employing a boxcar kernel with the same area as the 3.5σ impulse-decay kernel (six points at 1.4σ) identified about 50% more events as flares and produced 23 spurious detections in simulated white-noise data.

Although the kernel shape affects identifications near the threshold, an event of any shape can trigger a detection if it causes enough of a flux boost. For example, a single point at 5.5σ followed by five at the mean or six consecutive points at 2.3σ above the mean would both result in a "flare" detection. Figure 3.5 is an example of a star, Prox Cen, with multiple flares identified by the routine in the Si IV band, whereas the C II band of β Dor in Figure 3.4 is an example where the algorithm identified no flares.

High-pass filtering the lightcurves (Section 3.3.1) when searching for flares strongly mitigated the false identification of more gradual but long-lived changes in stellar flux (e.g. pulsations of Cepheid variables). Although the filter will affect the flare signals, Figure 3.7 shows that the effect of filtering on the shape of flares lasting minutes is negligible and the effect on flares lasting tens of minutes (the longest detected, see Section 3.4.1) is marginal. However, this is only true when the flares are surrounded by quiescent data: Without quiescent reference points flanking a flare, the filter would slide it down to the lightcurve mean, possibly preventing identification. Filtering also introduces slight changes in the amplitude of quiescent lightcurve scatter (Section 3.3.3), but these are well below the level of any detectable flare signal.

3.3.3 Quantification of Stochastic Fluctuations (Excess Noise)

Stochastic fluctuations of stellar flux will produce scatter in lightcurves beyond that attributable to Poisson noise. It is simplest to treat these stochastic fluctuations as white noise. This is especially true given that these data have short temporal baselines and are highly clustered (see

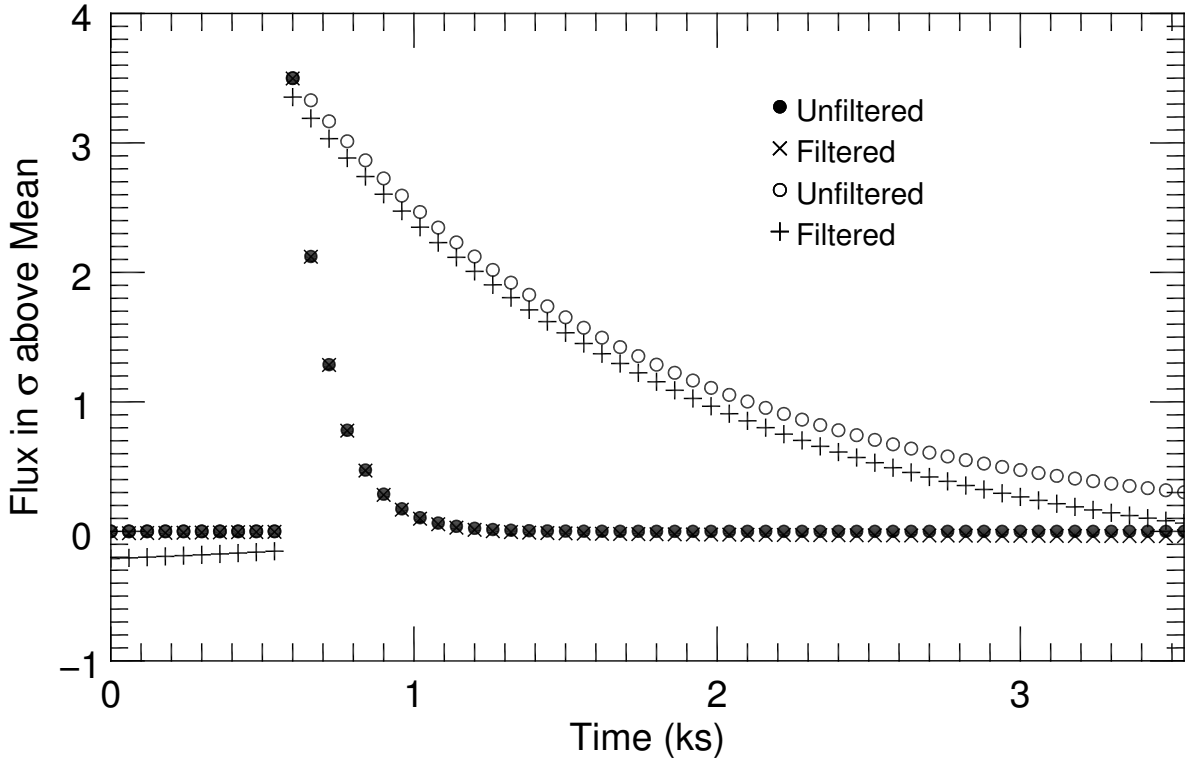

Figure 3.7 The effect of high-pass filtering on canonical impulse-decay flare signals with 2 min and 20 min decay times. The short signal is identical to the flare kernel used to identify flares by cross-correlation, extended beyond the six points of the kernel.

Table 3.2), unlike the lengthy sets of evenly spaced *Kepler* data that enable power spectrum analyses of stellar lightcurves for asteroseismology (e.g. Gilliland et al. 2010). In the white-noise model, the excess noise, with standard deviation σ_x, compounds the photometric noise, σ_p, in the data. The photometric noise is a combination of counting errors in the signal and background counts. Figure 3.8 illustrates the σ_x parameter using the Prox Cen Si IV data as an example, comparing Gaussians with $\sigma^2 = \langle\sigma_p^2\rangle$ and $\sigma^2 = \langle\sigma_p^2\rangle + \sigma_x^2$ to a histogram of the lightcurve points. I take care to use the average, $\langle\sigma_p^2\rangle$, because the photometric noise varies from point to point.

Several previous studies have estimated σ_x (or the equivalent) by computing the sample standard deviation of the lightcurve, σ, and subtracting an estimate of σ_p in quadrature (e.g. Gilliland et al. 2011; Ben-Jaffel & Ballester 2013). However, in the Gilliland et al. (2011) data the photometric errors are relatively constant, whereas in these data large variations in flux between points (sometimes factors of a few or more, as in Figure 3.5) produce substantial variations in the photometric errors.

Therefore, rather than subtracting some representative value of σ_p from σ to estimate σ_x, I instead conducted a maximum likelihood analysis. For the analysis, I modeled each point in the high-pass filtered lightcurves as a random draw from its own Gaussian distribution. I let the distribution for point i have variance $\sigma_i^2 = \sigma_x^2 + \sigma_{p,i}^2$ and mean equal to the quiescent lightcurve mean. Then I sampled the likelihood of the data for values of σ_x ranging from zero to where the likelihood reached 10^{-5} times the maximum to generate a likelihood distribution for σ_x.

Intentionally, I do not utilize the continuum-subtracted data for this analysis. Both continuum and emission line photons will be indiscriminately absorbed by species in the atmosphere of a transiting exoplanet. As such, separating the relative contribution of each is irrelevant to this work; it is the variability of the two combined that will limit transit observations. With a few exceptions (most notably the F stars and HD103095) the continuum emission contributed $< 10\%$ to the stellar flux in the emission line bands.

Prior to the maximum likelihood analysis, I removed data points flagged as flaring (Section 3.3.2) to avoid contaminating the estimate of stochastic fluctuations. After removing the flares

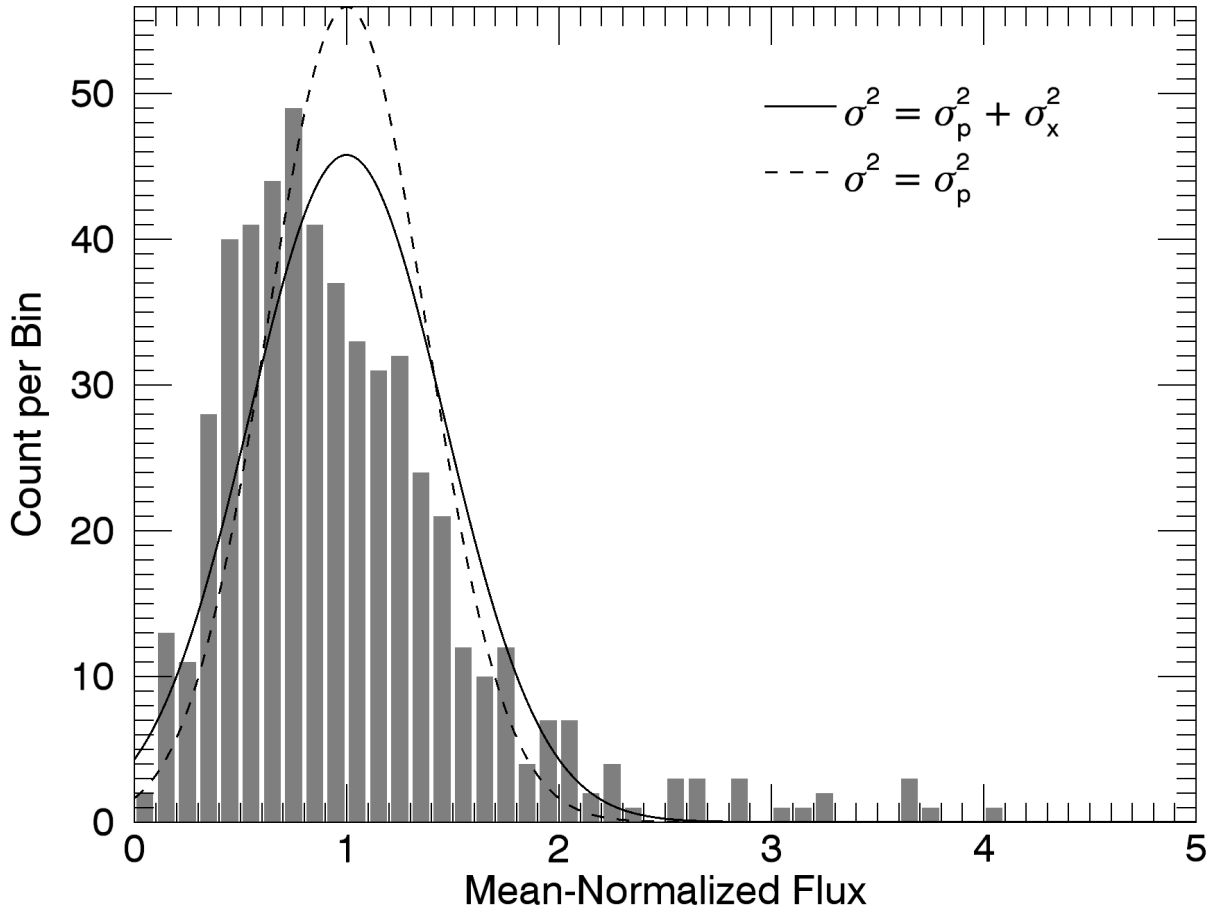

Figure 3.8 A histogram of the high-pass filtered, quiescent lightcurve points from the Prox Cen Si IV data (see Figure 3.5). The lines represent normalized Gaussians with and without excess noise.

(for the reasons discussed in Section 3.3.1), I high-pass filtered the remaining data. Filtering does not perfectly preserve the white noise in the data. Thus, the σ_x values estimated before and after filtering would differ even in data exhibiting purely white noise and no periodic signals. Filtering thus introduces extra uncertainty in σ_x because the effect of the filtering on white noise is not known (in some realizations of white noise filtering might increase scatter, while in others it might decrease it). I accounted for this uncertainty, to a reasonable approximation, through simulated white-noise data. This accounting process and the overall computation of maximum likelihoods are detailed in Appendix A.3.

Once I specified a likelihood distribution for σ_x, I located the maximum and, as error bars, the equal-probability endpoints enclosing 68.3% of the area under the curve. If the distribution was one sided, I instead set a 95% upper limit on σ_x. Plots of the likelihood distribution of σ_x for each lightcurve are available online as Figure Set 9. Figure 3.9 is an example likelihood curve showing a clear detection of σ_x, and Figure 3.10 is an example likelihood curve that permits only an upper limit on σ_x.

3.3.3.1 Contamination in Excess Noise

The lightcurve scatter I quantified as excess noise could result from the star, another source in the aperture, or the instrument. To address additional sources, I searched the SIMBAD database for known objects within the view of the aperture. One star, HBC427 = V397 Aur, is a spectroscopic binary with angular separation 32.3±0.1 mas (as of 2008 December) and *Kp* band magnitude difference 0.87±0.01 (Kraus et al., 2011). For this system, the secondary likely contributes a significant portion of the flux in the observed spectral bands, as noted in Table 3.1. Other targets with secondary, but insignificant, FUV sources within the instrument aperture are listed in Appendix A.1.

Another non-stellar source is certain to be present in the aperture during each observation: geocoronal emission from H I and O I. This sky background is discussed in Section 7.4 of the *COS Instrument Handbook* (Fox et al., 2017). To check for contamination from this source, I constructed

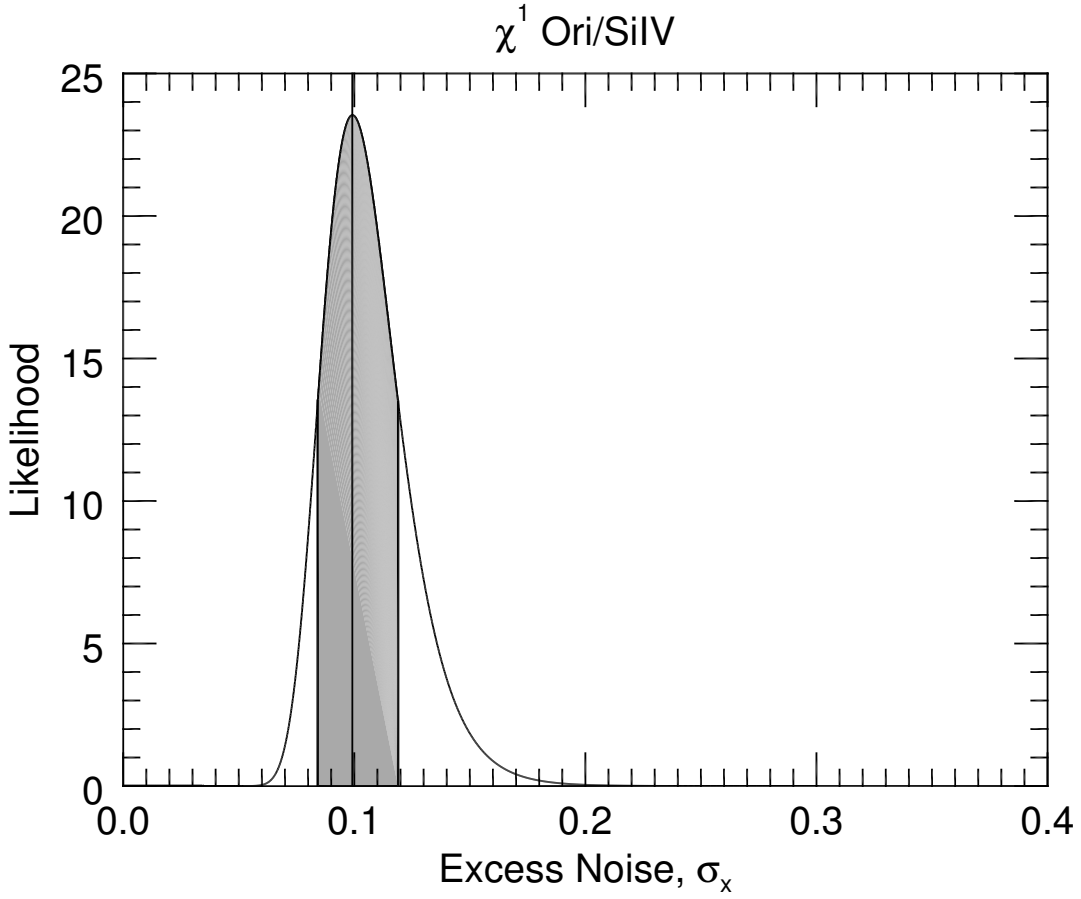

Figure 3.9 Example likelihood distribution showing a clear detection of excess noise for χ^1 Ori in the Si IV band. The 68.3% confidence interval is shaded and the maximum marked by a vertical line.

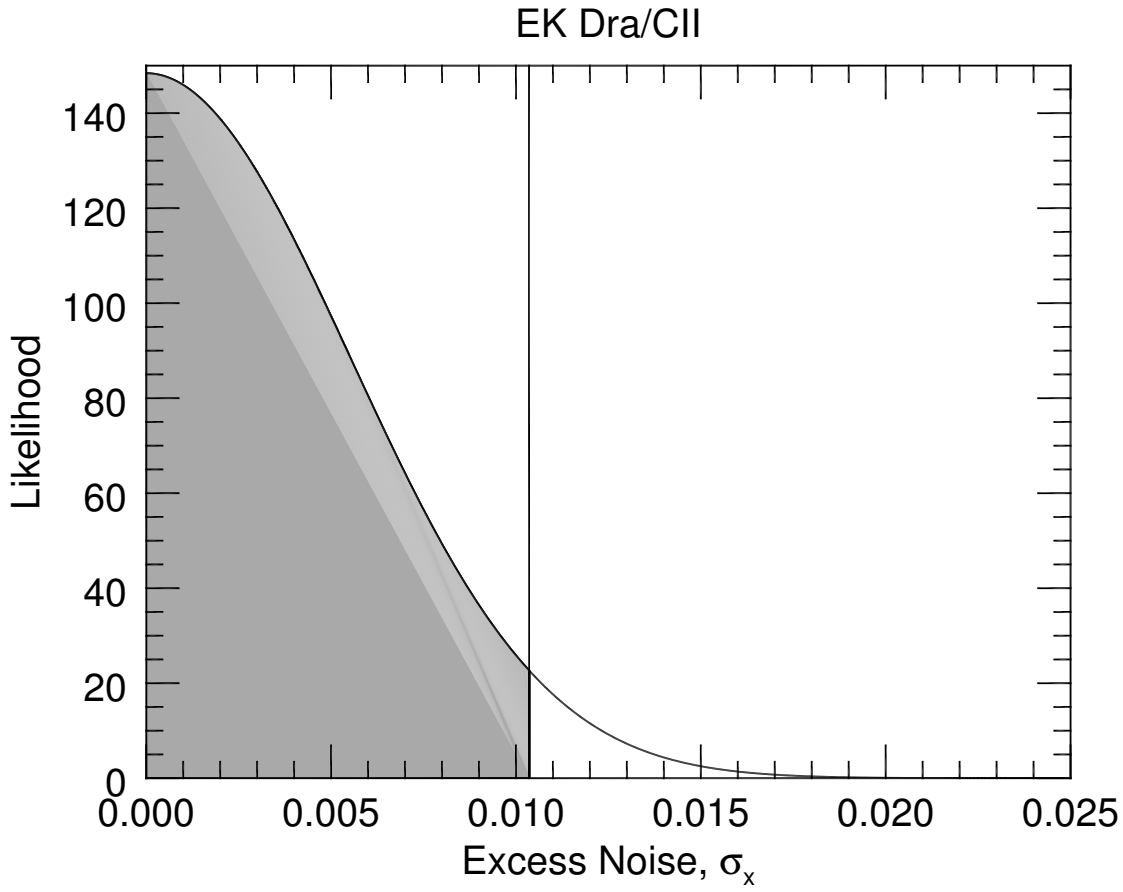

Figure 3.10 Another example likelihood distribution from Figure Set 9, this time showing a non-detection of excess noise for EK Dra in the C II band. The 95% upper limit interval is shaded and the 95% edge marked by a vertical line.

lightcurves in a Lyα band (Table 3.3) for each star and visually compared the trends in these lightcurves to those of the other bands. I found no obvious contamination. Other non-instrumental sources of variability external to the star (e.g. planet phase changes, see Section 3.1.1) cannot be excluded.

Variability attributable to the instrument is a serious concern. Slow drifts in the instrument response are suppressed by high pass filtering. However, changes in the instrument configuration between exposures can alter its response on timescales too rapid for the effects to be filtered out. Most notably, grid wires cast shadows of about 20% depth over the COS detector at configuration-dependent locations (see Figure 5.10 of the COS Instrument Handbook, Fox et al. 2017). Thus I separately normalize any exposures with different settings of the detector position before estimating σ_x. While this will exclude true changes in the stellar luminosity between such exposures from σ_x, it should strongly suppress variability resulting from different instrument configurations.

3.4 Results

3.4.1 Flares

Both the number of flares identified in each star and the flare duty cycle (the fraction of lightcurve points flagged as flaring) are included in Tables 3.4–3.7. The lightcurve of each specific flare may be found within the applicable stellar lightcurves in Figure Set 4, available online. However, to avoid clutter, these lightcurves do not include the continuum-subtracted, filtered data used to compute flare properties. Figure 3.11 depicts the distribution of all detected flares in energy and duration (defined in the next paragraph). When flares were detected in multiple bands, the plot contains a separate point for the flare energy and duration as measured in each band. The plot also contains curves showing typical sensitivity limits for data with different ratios of mean signal to quiescent scatter. In the figure, some notable flares are labeled with the dataset number (from Table 3.2) of the star on which they occurred. These are discussed in Section 3.5.1. The figure omits two events flagged in all bands on FK Com, as these are likely a vestige of the strong stellar

rotational signal that the high-pass filtering does not suppress below the level of quiescent scatter in that lightcurve (see Section 3.3.2). As such, they will be excluded from all further discussion.

I define duration as the time from the peak value to the first point below one sample standard deviation above the quiescent flux. As a metric of the total energy of a flare relative to the quiescent stellar emission, I use the photometric equivalent width (also termed equivalent duration), EW_p (Gershberg, 1972). The photometric equivalent width is the integral of the mean-normalized, mean-subtracted flux over the flare duration and amounts to

$$EW_p = \int_{flare} \frac{F_f - \langle F_q \rangle}{\langle F_q \rangle} dt, \tag{3.1}$$

for a star with continuously sampled flux F_q during quiescent periods and flux F_f during the flare. The result has units of time (I use s). By this definition, multiplying EW_p by the quiescent stellar luminosity in the applicable band gives the absolute energy radiated by the flare. I computed these values from the continuum-subtracted, high-pass filtered data. Because filtering suppresses lower frequencies more (see Figure 3.7), the energies of longer duration flares are systematically reduced.

The flare sweeping algorithm flagged 116 flares (24 C II, 28 Si III, 49 Si IV, and 15 continuum), with median duration 6 min, median peak normalized flux 3.2, and median EW_p 352 s. Of these flares, 62 were found in the AD Leo data, while 25 more were found in the Prox Cen data. Many of the 116 flares overlap with events flagged in other bands. Counting events that overlap as the same flare results in a tally of 58 separate events. The algorithm flagged data in only one band in 25 events, two bands in 17 events, three bands in 7 events, and all four bands in 9 events. The single band detections were dominated by events flagged in Si IV data with 17, while C II tallied 4, Si III tallied 2, and the continuum tallied 2. In the seven cases where a flare was detected in all bands but one, that missing detection was always the continuum.

The 9 flares detected in all four bands invite comparisons of the flare response of each band's flux. In 7 of these 9 the Si IV band showed the greatest EW_p. Also in 7 of the 9, EW_p was the lowest in the C II data. Flare durations were mixed – no band's response was typically longer or shorter than another. As for normalized peak flux, the Si IV values were the highest in 6 of the

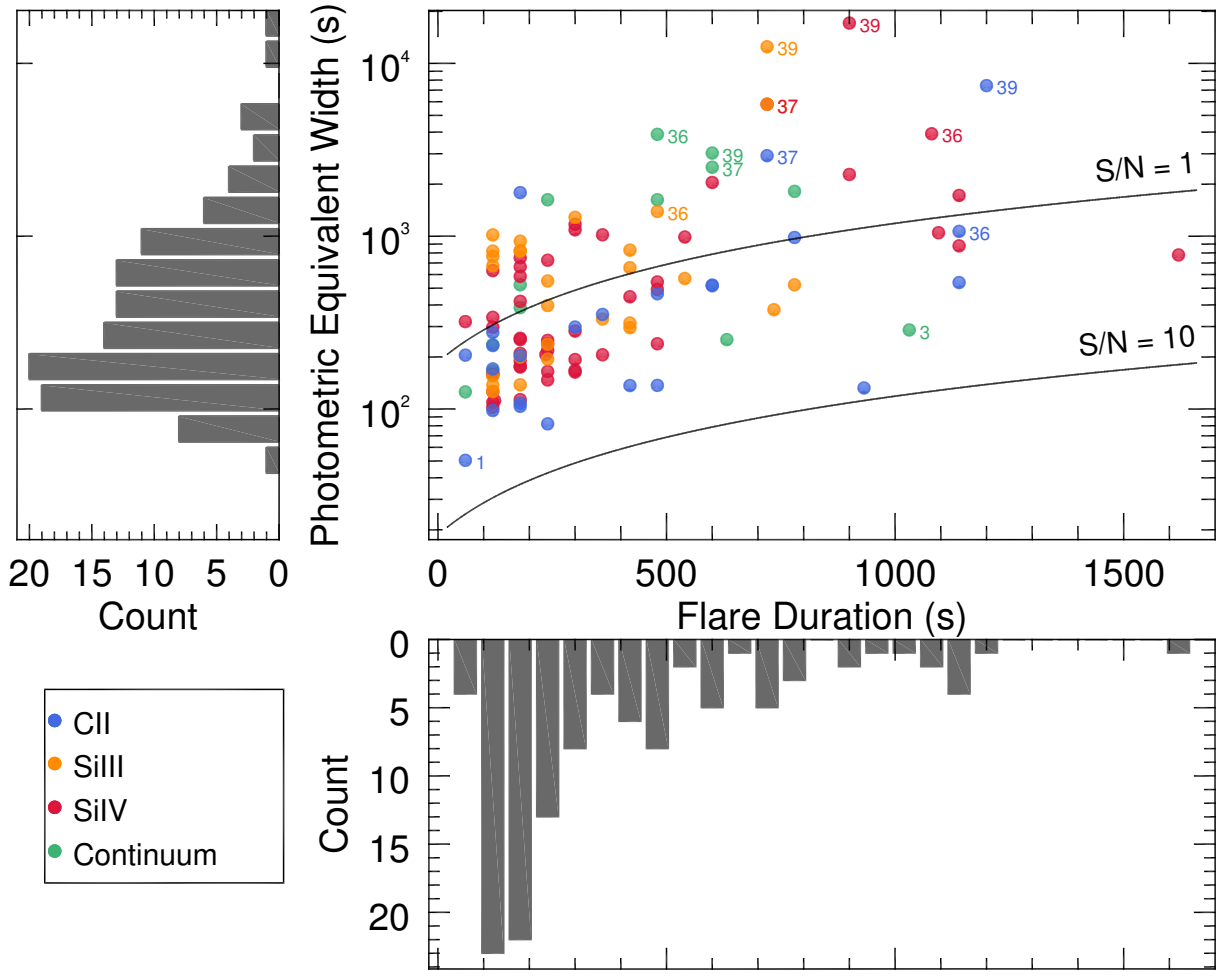

Figure 3.11 The distribution of flares in duration and photometric equivalent width. See the text for definitions of these metrics and a discussion of expected biases. Solid black lines represent minimum detectable energies given a signal-to-noise of 1 or 10 in the quiescent 60 s lightcurve data. In this case alone, I use signal-to-noise to refer to all noise – including stellar stochastic fluctuations – rather than just photometric noise.

9 flares, while the continuum peaked the highest in the other three cases. The C II data peaked lowest in 8 of the 9.

As expected, the histograms in Figure 3.11 show that the number of detected flares increases with decreasing energy and duration until the detection limits are approached. Figure 3.11 also shows a clear trend between the duration and radiated energy of a flare, confirmed to $> 99.99\%$ confidence by a Spearman Rank-Order test (Press et al., 2002). However, the trend could be explained by the sensitivity limits that increase with duration (example sensitivity curves are shown in the figure). For each lightcurve, the minimum EW_p of a detectable flare depends on the scatter in the lightcurve. This minimum results when a single point occurs at 5.5 times the sample standard deviation of the quiescent lightcurve points with a subsequent point below the sample standard deviation. The minimum possible EW_p value for each lightcurve is included in Tables 3.4 - 3.7.

This work is the first to investigate flares as detected in the C II, Si III, and Si IV emission lines in more than a few stars. Even so, the sample of detected flares is too small to permit a detailed analysis of the distribution of events in energy and duration, or an analysis of the relationship between their frequency and stellar properties. Furthermore, weaker flares are not detectable in data where quiescent scatter is large. As the level of quiescent scatter relative to the mean varies by an order of magnitude or more between lightcurves, flares detectable in some lightcurves are not detectable in others, biasing the population of low-energy flares. An additional bias results from gaps in the lightcurves. These restrict clusters of data points to shorter than an hour for most stars (see Table 3.2); even if a flare longer than a cluster were detected, the data provide no information on its true length.

3.4.2 Stochastic Fluctuations

The excess noise parameter used to quantify stochastic fluctuations represents the most probable standard deviation one would compute from 60 s cadence, mean-normalized flux data of the target in the absence of photometric noise. Tables 3.4 – 3.7 give the maximum-likelihood value or 95% upper bound of σ_x for all lightcurves. I detect excess noise in 19 C II, 7 Si III, 17 Si IV, and

6 FUV continuum lightcurves. In Si III fewer detections primarily result from lack of data for 15 stars. However, in the FUV continuum fewer detections could be a result of the lower integrated flux compared to C II and Si IV in about 2/3 of the datasets or lower excess noise. Quoted as range (median), the mean-normalized σ_x estimates are 1-41% (10%) in C II, 8-18% (15%) in Si III, 0.9-26% (10%) in Si IV, and 1-22% (5%) in the FUV continuum. The remaining 101 lightcurves exhibited σ_x below the sensitivity permitted by the quantity and photometric noise of the data (see Appendix A.2). In these cases, I computed upper limits on σ_x, and many of these are below the typical values of the σ_x detections. Some are under $\sim$1%, making them valuable constraints on the stochastic fluctuations of the target stars.

Assuming that the stochastic fluctuations can be approximated as white noise , σ_x will diminish with cadence length as $\Delta t^{-1/2}$. Without sufficient data for a detailed spectral analysis, this assumption is necessary. However, it is incorrect (see Section 3.1.1), and projecting as $\Delta t^{-1/2}$ will underestimate σ_x at longer timescales. The severity of the underestimation will be dependent on the power spectrum of the star's stochastic fluctuations and will be different for different stars. Figures 3.12 and 3.12 illustrate the spread of mean-normalized excess noise estimates and upper limits projected by $\Delta t^{-1/2}$ to a timescale more meaningful to transit spectroscopy, the 3.5 h typical transit duration. These diagrams, in effect, illustrate the approximate error that would be associated with a 3.5 h integrated flux measurement due simply to stochastic fluctuations of the host star's emission lines. In actual data, these noise values would be compounded by additional photometric noise from photon statistics and instrumental sources.

For many lightcurves, the estimates of σ_x at $\Delta t = 3.5$ h are subject to one or more shortcomings not inherently evident from the information in Tables 3.4 – 3.7. To begin with, as just mentioned above, σ_x is unlikely to diminish by $\Delta t^{-1/2}$ for many, possibly all, stars in the sample. Additionally, most lightcurves do not contain any long enough blocks of closely spaced points to sample fluctuations over at least one full transit timescale (Table 3.2). Finally, lightcurves exhibiting low mean flux (generally $\lesssim 5 \times 10^{-16}$ erg s^{-1} cm^{-2}) contain many time bins with zero counts after background subtraction. I model bins with even a single count as random draws from a Gaussian

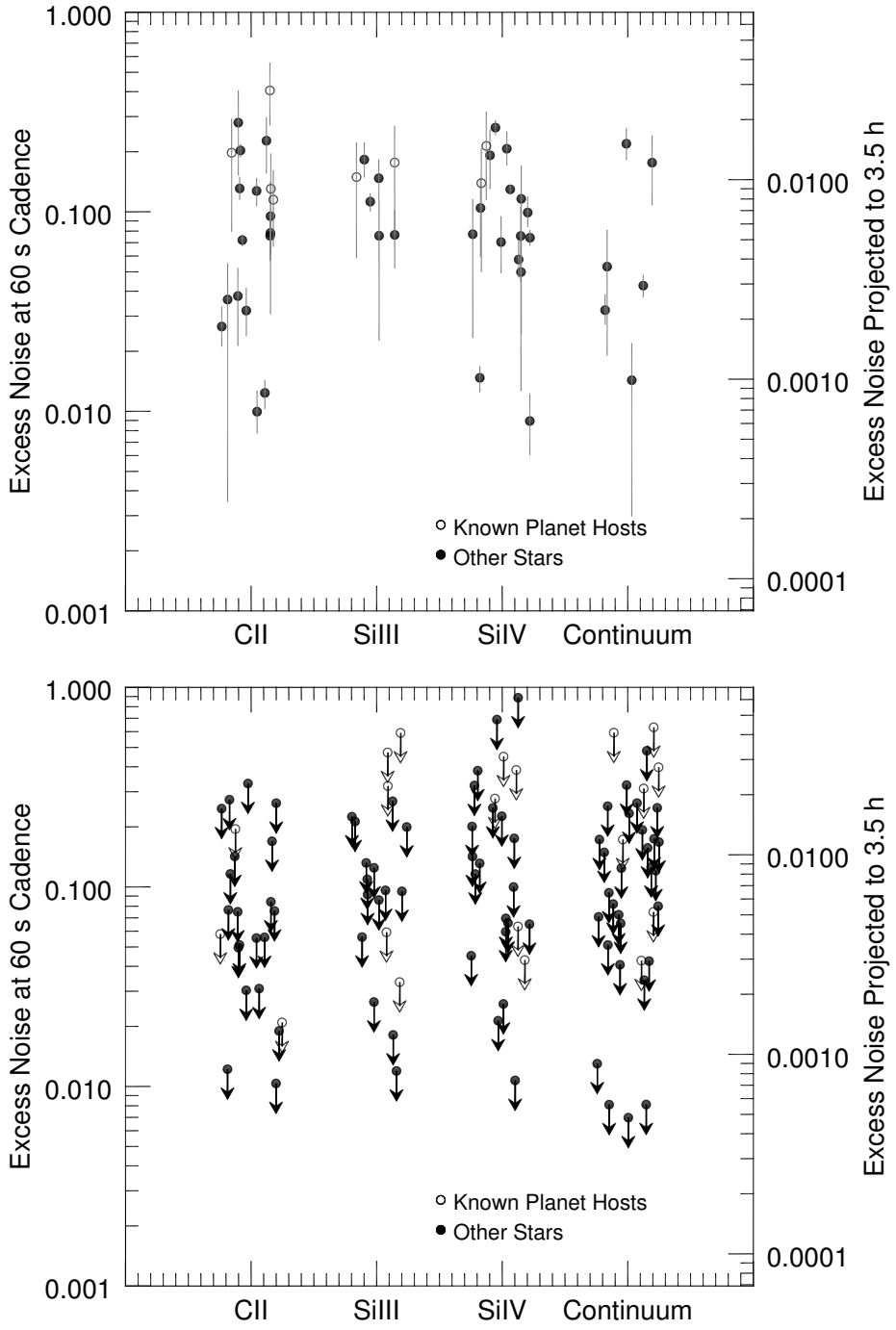

Figure 3.12 Top: Reliable measurements of the excess noise, σ_x, at 60 s (this work) and projected to 3.5 h (typical transit duration). Gray bars give the 68.3% confidence interval. Known planet hosts are GJ832, IL Aqr, and HO Lib in C II; GJ832, IL Aqr, and GJ436 in Si III; and GJ832, IL Aqr, and HD209458 (E140M data) in Si IV. Bottom: Upper limits on the excess noise for lightcurves where excess noise was not clearly detected for comparison to the detections (axes are identical). Known planet hosts are HD209458 (G130M and E140M data), HD189733, and GJ436 in C II; HD209458 (G130M and E140M data), HD189733, and HO Lib in Si III; HD209458 (G130M data), HD189733, GJ436, and HO Lib in Si IV; and all in the continuum. In both plots, random x-axis scatter was added for display.

(not Poisson) distribution, though the subtraction of Poisson distributed background counts from Poisson distributed signal + background makes the distribution of the result very nearly Gaussian. To allow readers to form their own judgments of the quality of the excess noise measure for any given star, I have made all lightcurves and the associated σ_x likelihood distributions available as Figure Sets 4 and 9.

A case of particular constancy in the sample is β Cas, with estimated σ_x values of under 1% in the C II and Si IV bands, and about 3% in the continuum band. Yet β Cas is classified as a δ Scuti variable. Its pulsations have a period of $\sim$0.1 d (Riboni et al., 1994), so are not strongly suppressed by the high-pass filtering. However, the dataset for β Cas spans 1419 s, only about 16% of the total pulsation period. Were these sub-transit timescale pulsations observed in full, the value of σ_x for β Cas would likely be substantially higher.

Table 3.4. Variability Statistics in C II

Star	$\langle \mathbf{F} \rangle$ 10^{-17} erg s^{-1} cm^{-2}	σ_x[a]	R_{σ_x}[b] R_J		N_f[c]	Duty[d] Cycle	EW_p[e] s
β Cas[f]	249700 ± 4000	$0.0100^{+0.0027}_{-0.0022}$	0.88 $^{+0.12}_{-0.10}$	g	0	0.000	3.03
δ Cep	280 ± 53	$0.038^{+0.014}_{-0.016}$	22.4 $^{+5.9}_{-6.4}$		1	0.054	48.7
α Per	1680 ± 300	$0.036^{+0.019}_{-0.033}$	27 $^{+8}_{-13}$		0	0.000	22.7
β Dor	3880 ± 230	< 0.0122	< 20.1		0	0.000	14.0
Polaris	2520 ± 190	< 0.0190	< 7.04		0	0.000	18.0
HD25825	1950 ± 350	< 0.0757	< 0.767		0	0.000	18.6
HD209458/G130M	234 ± 27	< 0.0580	< 0.711		0	0.000	59.2
HD209458/E140M	40 ± 52	< 0.195	< 1.30		0	0.000	255
χ^1 Ori	45800 ± 1700	$0.0266^{+0.0067}_{-0.0054}$	0.437 $^{+0.056}_{-0.045}$		0	0.000	7.82
HII314	830 ± 130	< 0.0559	< 0.381		0	0.000	30.5
EK Dra	11630 ± 420	< 0.0104	< 0.252		1	0.100	11.6
π^1 UMa	17300 ± 1000	$0.0320^{+0.0095}_{-0.0080}$	0.432 $^{+0.065}_{-0.055}$		0	0.000	10.3
HD90508	304 ± 28	< 0.116	< 0.592		0	0.000	68.0
HD199288/G140L	210 ± 23	< 0.0842	< 0.719		0	0.000	65.2
HD199288/G130M	350 ± 62	< 0.0554	< 0.583		0	0.000	45.9
18 Sco/G140L	1600 ± 120	< 0.0751	< 0.728		0	0.000	25.4
18 Sco/G130M	2010 ± 230	< 0.0496	< 0.592		0	0.000	20.4
FK Com[f]	18820 ± 240	$0.0124^{+0.0019}_{-0.0020}$	2.42 $^{+0.18}_{-0.20}$	g	2	0.110	9.26
HD65583	33.7 ± 8.4	$0.227^{+0.069}_{-0.071}$	0.94 $^{+0.14}_{-0.15}$		0	0.000	123
HD103095/G140L	33 ± 14	$0.28^{+0.12}_{-0.13}$	0.89 $^{+0.20}_{-0.20}$		0	0.000	138
HD103095/G130M	48 ± 32	< 0.247	< 0.838		0	0.000	107
HD282630	1140 ± 200	< 0.0767	...		0	0.000	29.9
HD189733	2620 ± 200	< 0.0209	< 0.280		0	0.000	15.9
HD145417	7.2 ± 3.9	< 0.263	< 0.801		0	0.000	226
V410-τ	420 ± 180	< 0.169	< 2.84		0	0.000	141
EG Cha	2680 ± 250	$0.131^{+0.018}_{-0.015}$	1.66 $^{+0.12}_{-0.10}$	g	0	0.000	45.0
HBC427	370 ± 110	< 0.142	< 1.77		0	0.000	54.1
61 Cyg A	10350 ± 790	< 0.0309	< 0.122		0	0.000	8.22
LkCa 4	300 ± 100	$0.095^{+0.045}_{-0.064}$	1.47 $^{+0.35}_{-0.50}$	g	0	0.000	55.2
GJ832	420 ± 120	$0.115^{+0.046}_{-0.048}$	0.433 $^{+0.087}_{-0.091}$		0	0.000	56.9
TWA13B	1580 ± 220	$0.078^{+0.021}_{-0.019}$	0.715 $^{+0.095}_{-0.089}$	g	0	0.000	30.3

Table 3.4 (cont'd)

Star	$\langle \mathbf{F} \rangle$ 10^{-17} erg s^{-1} cm^{-2}	σ_x [a]	R_{σ_x} [b] R_J	N_f [c]	Duty [d] Cycle	EW_p [e] s
TWA13A	1660 ± 250	< 0.0512	< 0.636	0	0.000	23.6
AU Mic	26000 ± 1200	< 0.0303	< 0.373	0	0.000	28.5
CE Ant	3020 ± 380	$0.076^{+0.021}_{-0.019}$	$0.703^{+0.095}_{-0.087}$ [g]	0	0.000	27.9
GJ436	11 ± 13	$0.20^{+0.09}_{-0.12}$	$0.50^{+0.12}_{-0.15}$	1	0.073	132
EV Lac	6220 ± 570	$0.127^{+0.020}_{-0.020}$	$0.337^{+0.026}_{-0.026}$ [g]	0	0.000	75.0
AD Leo	25530 ± 490	$0.0721^{+0.0044}_{-0.0045}$	$0.3111^{+0.0094}_{-0.0097}$ [g]	11	0.150	35.1
IL Aqr	270 ± 140	$0.130^{+0.064}_{-0.068}$	$0.345^{+0.085}_{-0.090}$ [g]	1	0.375	53.3
HO Lib	7 ± 14	$0.41^{+0.15}_{-0.13}$	$0.487^{+0.091}_{-0.082}$	0	0.000	159
Prox Cen	2910 ± 180	$0.203^{+0.015}_{-0.014}$	$0.1623^{+0.0099}_{-0.0099}$	8	0.176	101
GJ3877	6.9 ± 4.0	< 0.274	< 0.160	0	0.000	234
GJ3517	2.7 ± 2.2	< 0.330	< 0.148	1	0.030	478

[a] Mean-normalized excess noise at 60 s cadence.

[b] Radius of an occulting disk that would produce a transit depth equivalent to σ_x projected to 3.5 h.

[c] Number of flares identified.

[d] Fraction of lightcurve points encompassed by flares.

[e] Min photometric equivalent width of a detectable flare given the lightcurve scatter.

[f] Data contain a periodic signal not fully suppressed by the high-pass filtering.

[g] The literature did not provide an uncertainty on the stellar radius. The uncertainty on R_{σ_x} accounts only for uncertainty in σ_x.

Table 3.5. Variability Statistics in Si III

Star	$\langle \mathbf{F} \rangle$ 10^{-17} erg s^{-1} cm^{-2}	σ_x[a]	R_{σ_x}[b] R_J	N_f[c]	Duty[d] Cycle	EW_p[e] s
β Cas[f]	...	...	...	...	...	...
δ Cep	312 ± 57	< 0.0265	< 18.7	0	0.000	41.5
α Per	...	...	...	...	...	...
β Dor	4940 ± 260	< 0.0120	< 19.9	0	0.000	11.9
Polaris	2720 ± 200	< 0.0181	< 6.88	0	0.000	16.3
HD25825	...	...	...	...	...	...
HD209458/G130M	189 ± 24	< 0.0593	< 0.718	0	0.000	64.2
HD209458/E140M	13 ± 57	< 0.320	< 1.67	0	0.000	425
χ^1 Ori	...	...	...	...	...	...
HII314	510 ± 110	< 0.0961	< 0.499	0	0.000	48.1
EK Dra	...	...	...	...	...	...
π^1 UMa	...	...	...	...	...	...
HD90508	...	...	...	...	...	...
HD199288/G140L	...	...	...	...	...	...
HD199288/G130M	197 ± 47	< 0.0950	< 0.763	1	0.052	59.7
18 Sco/G140L	825 ± 86	$0.076^{+0.038}_{-0.053}$	$0.73^{+0.19}_{-0.26}$	0	0.000	42.1
18 Sco/G130M	1250 ± 180	< 0.0561	< 0.629	0	0.000	23.9
FK Com[f]	...	...	...	...	...	...
HD65583	...	...	...	...	...	...
HD103095/G140L	...	...	...	...	...	...
HD103095/G130M	113 ± 51	< 0.200	< 0.754	0	0.000	75.9
HD282630	540 ± 140	< 0.125	...	0	0.000	45.3
HD189733	1130 ± 140	< 0.0333	< 0.353	0	0.000	25.8
HD145417	...	...	...	...	...	...
V410-τ	3 ± 31	< 0.269	< 3.58	0	0.000	397
EG Cha	1230 ± 180	$0.077^{+0.025}_{-0.024}$	$1.27^{+0.21}_{-0.20}$ [g]	1	0.250	30.9
HBC427	132 ± 67	< 0.213	< 2.16	0	0.000	72.5
61 Cyg A	...	...	...	...	...	...
LkCa 4	110 ± 59	< 0.225	< 2.26	0	0.000	79.5
GJ832	126 ± 60	$0.149^{+0.072}_{-0.090}$	$0.49^{+0.12}_{-0.15}$	0	0.000	93.8
TWA13B	600 ± 130	$0.147^{+0.035}_{-0.032}$	$0.98^{+0.12}_{-0.11}$ [g]	0	0.000	55.1

Table 3.5 (cont'd)

Star	$\langle \mathbf{F} \rangle$ 10^{-17} erg s^{-1} cm^{-2}	σ_x [a]	R_{σ_x} [b] R_J	N_f [c]	Duty [d] Cycle	EW_p [e] s
TWA13A	700 ± 160	< 0.0860	< 0.824	0	0.000	32.5
AU Mic	4400 ± 1100	< 0.0915	< 0.648	1	0.144	83.5
CE Ant	1420 ± 260	$0.183^{+0.039}_{-0.033}$	$1.09^{+0.12}_{-0.10}$ [g]	0	0.000	58.1
GJ436	1.1 ± 4.5	< 0.472	< 0.778	1	0.164	323
EV Lac	820 ± 400	< 0.109	< 0.312	2	0.166	128
AD Leo	11260 ± 530	$0.112^{+0.011}_{-0.011}$	$0.388^{+0.019}_{-0.019}$ [g]	14	0.110	70.4
IL Aqr	167 ± 99	$0.177^{+0.091}_{-0.097}$	$0.40^{+0.10}_{-0.11}$ [g]	1	0.375	83.6
HO Lib	1.8 ± 8.1	< 0.592	< 0.588	0	0.000	252
Prox Cen	188 ± 87	< 0.132	< 0.131	7	0.082	250
GJ3877	...	...	...	...	...	...
GJ3517	...	...	...	...	...	...

[a] Mean-normalized excess noise at 60 s cadence.

[b] Radius of an occulting disk that would produce a transit depth equivalent to σ_x projected to 3.5 h.

[c] Number of flares identified.

[d] Fraction of lightcurve points encompassed by flares.

[e] Min photometric equivalent width of a detectable flare given the lightcurve scatter.

[f] Data contain a periodic signal not fully suppressed by the high-pass filtering.

[g] The literature did not provide an uncertainty on the stellar radius. The uncertainty on R_{σ_x} accounts only for uncertainty in σ_x.

Table 3.6. Variability Statistics in Si IV

Star	$\langle \mathbf{F} \rangle$ 10^{-17} erg s^{-1} cm^{-2}	σ_x [a]	R_{σ_x} [b] R_J	N_f [c]	Duty [d] Cycle	EW_p [e] s
β Cas[f]	81500 ± 1700	$0.0089^{+0.0032}_{-0.0029}$	$0.84^{+0.15}_{-0.13}$ [g]	0	0.000	3.16
δ Cep	231 ± 36	< 0.0259	< 18.5	0	0.000	29.6
α Per	1890 ± 240	< 0.0452	< 30.6	0	0.000	14.1
β Dor	2840 ± 140	< 0.0107	< 18.9	0	0.000	11.9
Polaris	1800 ± 120	< 0.0214	< 7.47	0	0.000	20.8
HD25825	690 ± 160	$0.050^{+0.027}_{-0.037}$	$0.62^{+0.17}_{-0.23}$	0	0.000	24.5
HD209458/G130M	73 ± 11	< 0.0634	< 0.743	1	0.044	77.9
HD209458/E140M	16 ± 28	< 0.277	< 1.55	0	0.000	344
χ^1 Ori	20160 ± 920	$0.099^{+0.020}_{-0.015}$	$0.844^{+0.086}_{-0.066}$	0	0.000	25.5
HII314	255 ± 55	< 0.0660	< 0.414	0	0.000	40.5
EK Dra	4280 ± 190	$0.0741^{+0.0066}_{-0.0061}$	$0.675^{+0.035}_{-0.033}$	0	0.000	35.2
π^1 UMa	7030 ± 480	$0.058^{+0.014}_{-0.011}$	$0.580^{+0.070}_{-0.055}$	0	0.000	16.3
HD90508	37.1 ± 6.9	$0.116^{+0.054}_{-0.092}$	$0.59^{+0.14}_{-0.23}$ [g]	0	0.000	111
HD199288/G140L	32.6 ± 6.8	< 0.142	< 0.934	0	0.000	104
HD199288/G130M	93 ± 24	< 0.0696	< 0.653	0	0.000	63.2
18 Sco/G140L	370 ± 44	< 0.131	< 0.963	0	0.000	40.5
18 Sco/G130M	506 ± 84	< 0.0650	< 0.678	0	0.000	27.7
FK Com[f]	8110 ± 120	$0.0147^{+0.0020}_{-0.0022}$	$2.64^{+0.18}_{-0.19}$ [g]	2	0.110	10.6
HD65583	8.6 ± 3.8	< 0.249	< 0.985	0	0.000	226
HD103095/G140L	20.2 ± 8.8	< 0.383	< 1.04	0	0.000	153
HD103095/G130M	37 ± 21	< 0.201	< 0.756	0	0.000	101
HD282630	333 ± 83	< 0.0999	...	0	0.000	34.2
HD189733	470 ± 63	< 0.0430	< 0.401	0	0.000	33.5
HD145417	4.8 ± 2.9	< 0.322	< 0.887	0	0.000	324
V410-τ	33 ± 47	< 0.175	< 2.89	0	0.000	257
EG Cha	587 ± 95	$0.076^{+0.030}_{-0.031}$	$1.27^{+0.25}_{-0.26}$ [g]	1	0.354	34.0
HBC427	64 ± 33	$0.192^{+0.065}_{-0.061}$	$2.05^{+0.35}_{-0.33}$ [g]	0	0.000	80.6
61 Cyg A	1510 ± 220	$0.070^{+0.024}_{-0.021}$	$0.184^{+0.031}_{-0.028}$	0	0.000	24.7
LkCa 4	59 ± 34	< 0.226	< 2.27	0	0.000	86.2
GJ832	88 ± 40	$0.139^{+0.067}_{-0.089}$	$0.48^{+0.12}_{-0.15}$	0	0.000	80.1
TWA13B	267 ± 67	$0.104^{+0.042}_{-0.045}$	$0.83^{+0.16}_{-0.18}$ [g]	1	0.100	49.6

Table 3.6 (cont'd)

Star	$\langle \mathbf{F} \rangle$ 10^{-17} erg s^{-1} cm^{-2}	σ_x [a]	R_{σ_x} [b] R_J	N_f [c]	Duty [d] Cycle	EW_p [e] s
TWA13A	264 ± 74	$0.077^{+0.038}_{-0.054}$	$0.78^{+0.19}_{-0.27}$ [g]	0	0.000	44.9
AU Mic	3320 ± 340	< 0.0596	< 0.523	4	0.174	50.0
CE Ant	560 ± 120	$0.207^{+0.044}_{-0.035}$	$1.16^{+0.12}_{-0.10}$ [g]	1	0.143	78.9
GJ436	1.8 ± 4.3	< 0.386	< 0.703	1	0.091	215
EV Lac	1160 ± 210	< 0.116	< 0.322	2	0.265	94.3
AD Leo	5870 ± 170	$0.1296^{+0.0063}_{-0.0063}$	$0.417^{+0.010}_{-0.010}$ [g]	28	0.303	54.3
IL Aqr	88 ± 53	$0.21^{+0.10}_{-0.10}$	$0.44^{+0.11}_{-0.10}$ [g]	1	0.375	97.4
HO Lib	1.8 ± 6.7	< 0.450	< 0.512	0	0.000	208
Prox Cen	524 ± 42	$0.264^{+0.022}_{-0.021}$	$0.185^{+0.012}_{-0.012}$	9	0.114	157
GJ3877	1.6 ± 2.3	< 0.887	< 0.289	0	0.000	691
GJ3517	1.3 ± 1.5	< 0.690	< 0.214	0	0.000	938

[a]Mean-normalized excess noise at 60 s cadence.

[b]Radius of an occulting disk that would produce a transit depth equivalent to σ_x projected to 3.5 h.

[c]Number of flares identified.

[d]Fraction of lightcurve points encompassed by flares.

[e]Min photometric equivalent width of a detectable flare given the lightcurve scatter.

[f]Data contain a periodic signal not fully suppressed by the high-pass filtering.

[g]The literature did not provide an uncertainty on the stellar radius. The uncertainty on R_{σ_x} accounts only for uncertainty in σ_x.

Table 3.7. Variability Statistics in Continuum

Star	$\langle \mathbf{F} \rangle$ 10^{-17} erg s^{-1} cm^{-2}	σ_x[a]	R_{σ_x}[b] R_J	N_f[c]	Duty[d] Cycle	EW_p[e] s
β Cas[f]	194000 ± 2900	$0.0321^{+0.0063}_{-0.0048}$	$1.59^{+0.16}_{-0.12}$ [g]	0	0.000	8.21
δ Cep	668 ± 61	$0.0427^{+0.0055}_{-0.0051}$	$23.8^{+4.6}_{-4.6}$	0	0.000	23.8
α Per	13840 ± 640	< 0.0130	< 16.4	0	0.000	4.27
β Dor	2640 ± 160	< 0.00810	< 16.4	1	0.132	11.0
Polaris	6310 ± 220	< 0.00698	< 4.27	0	0.000	6.22
HD25825	186 ± 81	< 0.193	< 1.22	0	0.000	48.7
HD209458/G130M	91 ± 13	< 0.0427	< 0.610	0	0.000	63.9
HD209458/E140M	33 ± 36	< 0.173	< 1.23	0	0.000	225
χ^1 Ori	5110 ± 390	$0.014^{+0.007}_{-0.011}$	$0.32^{+0.08}_{-0.13}$	0	0.000	7.72
HII314	49 ± 24	< 0.124	< 0.567	0	0.000	76.6
EK Dra	850 ± 130	< 0.0407	< 0.500	1	0.100	37.3
π^1 UMa	1670 ± 220	< 0.0341	< 0.446	0	0.000	11.9
HD90508	211 ± 17	< 0.0656	< 0.445	0	0.000	44.6
HD199288/G140L	228 ± 18	< 0.0725	< 0.667	0	0.000	54.6
HD199288/G130M	233 ± 38	< 0.0425	< 0.510	0	0.000	37.0
18 Sco/G140L	401 ± 44	< 0.0935	< 0.813	0	0.000	32.2
18 Sco/G130M	374 ± 72	< 0.0708	< 0.707	0	0.000	29.2
FK Com[f]	2332 ± 97	< 0.00812	< 1.96	2	0.101	12.2
HD65583	49.9 ± 7.9	< 0.126	< 0.700	0	0.000	89.2
HD103095/G140L	87 ± 18	< 0.173	< 0.701	0	0.000	71.4
HD103095/G130M	80 ± 33	$0.176^{+0.063}_{-0.068}$	$0.71^{+0.13}_{-0.14}$	0	0.000	80.4
HD282630	32 ± 27	< 0.234	...	0	0.000	112
HD189733	99 ± 29	< 0.0749	< 0.529	0	0.000	58.6
HD145417	29.3 ± 5.6	< 0.157	< 0.618	0	0.000	109
V410-τ	31 ± 43	< 0.149	< 2.66	0	0.000	240
EG Cha	147 ± 42	$0.219^{+0.041}_{-0.037}$	$2.15^{+0.20}_{-0.18}$ [g]	0	0.000	87.3
HBC427	12 ± 17	< 0.324	< 2.67	0	0.000	158
61 Cyg A	620 ± 140	$0.053^{+0.028}_{-0.034}$	$0.160^{+0.042}_{-0.051}$	0	0.000	25.2
LkCa 4	2.1 ± 8.0	< 0.481	< 3.31	0	0.000	239
GJ832	16 ± 16	< 0.311	< 0.712	0	0.000	134
TWA13B	45 ± 27	< 0.174	< 1.07	0	0.000	92.8

3.5 Discussion

3.5.1 The Range of Flare Behavior

3.5.1.1 Strong Flares

Several flares appear in the data that peak at tens of times the quiescent flux. The strongest of these is a flare on Prox Cen, displayed in Figure 3.13a (see also Christian et al. 2004). This flare raises the continuum-subtracted flux in each band, normalized by the quiescent mean, to values at the peak data point of 27.5 ± 0.2 in C II, 66.7 ± 1.2 in Si III, 91.6 ± 0.3 in Si IV, and 13.5 ± 0.6 in the continuum. The EW_p and duration of this flare in each band can be compared with the rest of the flare sample in Figure 3.11, where these data points are labeled with 39, Prox Cen's dataset number from Table 3.2. Very strong flares also appear in the AD Leo (dataset no. 36; see also Hawley et al. 2003) and IL Aqr (dataset no. 37; see also France et al. 2012a) data and are also labeled in Figure 3.11. The AD Leo flare peaks at 8.2 ± 0.1 in C II, 14.0 ± 0.2 in Si III, 33.7 ± 0.1 in Si IV, and 45.9 ± 0.3 in the continuum (Figure 3.13b). The IL Aqr flare peaks at 15.4 ± 0.3 in C II, 36.9 ± 0.3 in Si III, 46.5 ± 0.3 in Si IV, and 20.1 ± 1.4 in the continuum (not included in Figure 3.13).

3.5.1.2 Symmetric Flares

Some of the flares in the sample show roughly equal rise and decay times, in contrast to the impulse-decay shape of many flares. The clearest example of such a flare is that which appears in the EG Cha data, plotted in Figure 3.13c. Note that this event was not flagged in the continuum or C II data because the short span of the data, 0.82 hours, resulted in a poor determination of the quiescent scatter. The continuum and C II did not sufficiently exceed the estimated scatter to result in an identification. Other flares that show a relatively clear symmetric photometric profile (though not nearly as clear as that of EG Cha) appear in the Si IV data of EV Lac at mean Julian Date 52172.709 and the AD Leo data at mean Julian Date 51616.119. Many flares in the data appear as though they might be symmetric, but their rise and fall are not adequately resolved.

Table 3.7 (cont'd)

Star	$\langle \mathbf{F} \rangle$ 10^{-17} erg s^{-1} cm^{-2}	σ_x[a]	R_{σ_x}[b] R_J	N_f[c]	Duty[d] Cycle	EW_p[e] s
TWA13A	56 ± 37	< 0.254	< 1.42	0	0.000	104
AU Mic	269 ± 84	< 0.0821	< 0.613	1	0.048	91.2
CE Ant	149 ± 61	< 0.168	< 1.05	1	0.071	54.5
GJ436	1.6 ± 7.8	< 0.398	< 0.714	0	0.000	296
EV Lac	156 ± 70	< 0.121	< 0.328	0	0.000	164
AD Leo	355 ± 33	< 0.0512	< 0.262	9	0.056	99.9
IL Aqr	2 ± 13	< 0.593	< 0.736	1	0.344	307
HO Lib	2 ± 11	< 0.631	< 0.607	0	0.000	291
Prox Cen	77 ± 24	< 0.0801	< 0.102	1	0.022	208
GJ3877	7.0 ± 3.3	< 0.263	< 0.157	0	0.000	248
GJ3517	1.5 ± 1.3	< 0.249	< 0.129	0	0.000	356

[a]Mean-normalized excess noise at 60 s cadence.

[b]Radius of an occulting disk that would produce a transit depth equivalent to σ_x projected to 3.5 h.

[c]Number of flares identified.

[d]Fraction of lightcurve points encompassed by flares.

[e]Min photometric equivalent width of a detectable flare given the lightcurve scatter.

[f]Data contain a periodic signal not fully suppressed by the high-pass filtering.

[g]The literature did not provide an uncertainty on the stellar radius. The uncertainty on R_{σ_x} accounts only for uncertainty in σ_x.

3.5.1.3 F Star Anomalies

The flare identification algorithm flagged two events on F stars, one in C II on δ Cep and another in the continuum on β Dor. The latter is displayed in Figure 3.13d. Both events are gradual elevations of the flux in a single band relative to the other three. The β Dor flare is particularly curious, as the other three bands clearly do not show the same consistent decline in flux that the elevated continuum flux does. These events seem likely to be true anomalies rather than spurious detections.

3.5.1.4 Multi-peak Flares

Many of the flares in the data exhibit complicated shapes, and might be a superposition of nearby small flares. Figure 3.13e depicts a flare on AD Leo that exhibits two peaks, separated by 240 s. This was the clearest specimen of a multi-peak flare. In most such flares, the data are not as clearly resolved above the surrounding scatter and/or different bands show different behavior.

3.5.1.5 Response in Different Lines

I found that flare signals generally vary significantly between bands. In addition, these variations are not consistent from flare to flare. The difference in the response between bands is clear in Figure 3.13. For example, the Prox Cen, EG Cha, and AD Leo flares of subplots a, c, and e peak highest in Si IV, with a roughly similar shape in each band. Alternatively, the AD Leo flare depicted in subplot b is the strongest in the continuum, and that of Prox Cen depicted in subplot f is the strongest in Si III. For the latter, the continuum shows essentially no response, though better signal to noise might reveal otherwise. (Note in Figure 3.13f that some Si III points are negative because the subtracted signal from the Lyα wing sometimes exceeds the low Si III signal.) Differences between lines in emitted flux during a flare have also been observed on the Sun (e.g. Brekke et al. 1996) and other low mass stars (e.g. GJ876, Ayres & France 2010; France et al. 2012a).

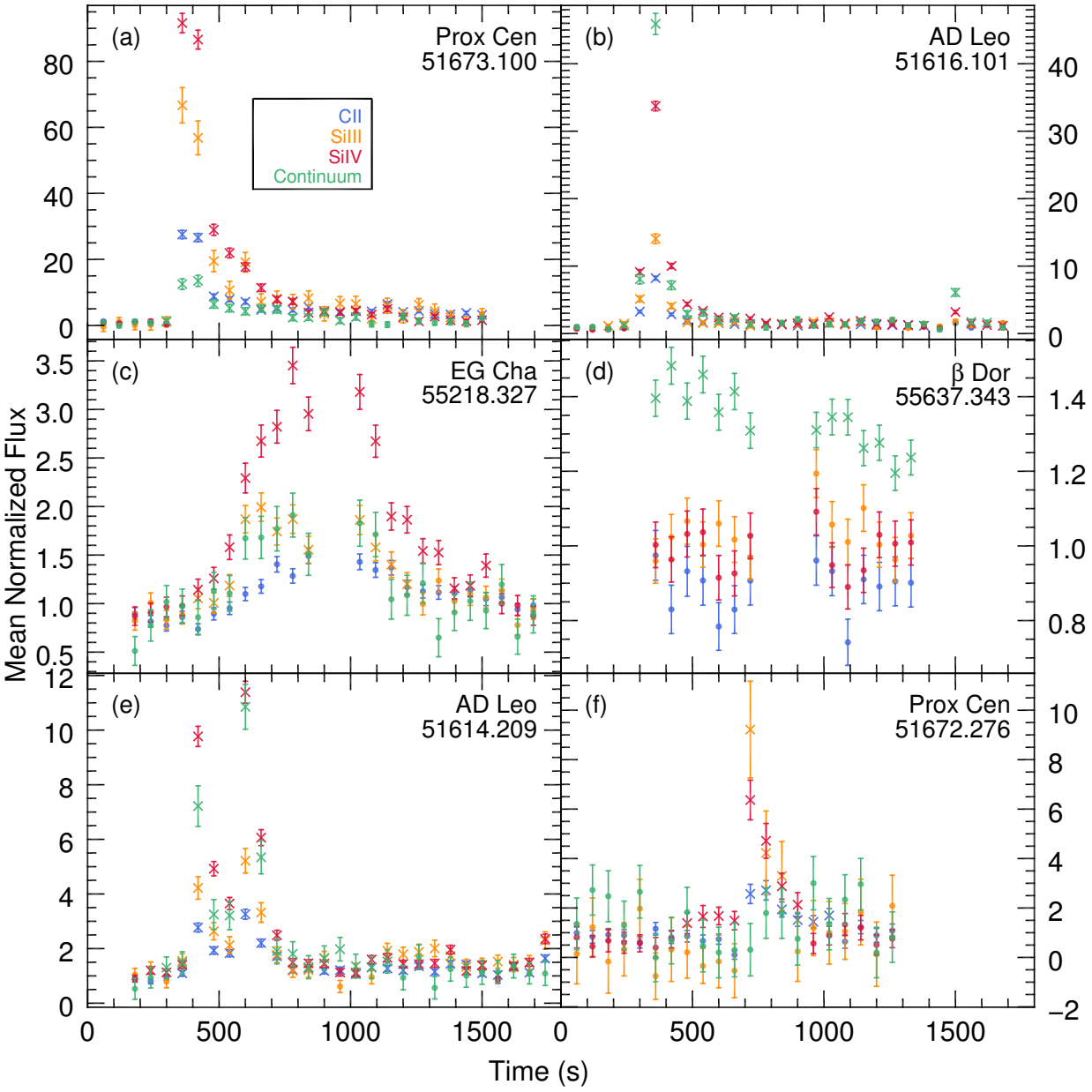

Figure 3.13 A palette of flare behaviors, discussed in Section 3.5.1. Each subplot is labeled with the star and the mean Julian Date of $t = 0$. The fluxes are continuum-subtracted, high-pass filtered, and normalized to the mean of the quiescent points. The x symbols denote points flagged for removal before computing excess noise values (**not** equivalent to the flare duration, see Section 3.4.1. Note that the y-axis scales differ.

3.5.2 Risks Flares Pose to Transit Measurements

All of the detected flares are short lived, with one lasting 27 min, the others lasting less than 20 min, and over half lasting 4 min or less. These could easily be hidden by longer cadence data. Typical cadences in UV exoplanet transit observations are $\Delta t \approx$ 30-60 min, based on recent literature. While hour or longer cadences might often be unavoidable due to instrument or signal-to-noise limitations, a flare hidden in such data could bias a measurement of transit depth (see Section 3.1.1).

Of the 116 flares I identified (again, excluding FK Com), 57 (roughly one event per 5 h of data) would boost a 60 min integrated flux measurement by $\gtrsim$ 10%, and all flares (roughly one event per 2.5 h of data) would boost a 60 min flux measurement by $\gtrsim$ 1%. Flares produced the largest EW_p values in the Si IV band in roughly 2/3 of the 60 separate events and 7/9 of the events that registered a detection in all four bands. Thus, it appears that transit observations in Si IV are somewhat likely to be more strongly affected by flaring.

The flare stars (namely AD Leo and Prox Cen) account for most of the flares I detected, 92 of 116. However, 24 flares were identified on objects not classified as "flare stars." Such flares are of particular interest because these stars are more likely to be targeted in exoplanet search programs. These occurred on 5/8 M, 1/8 K, 3/11 G, and 2/5 F stars, and occurred roughly once per 5 h in the time all 32 stars were observed. Of these 24 flares, 9 (roughly one event per 13 h) would boost a 60 min integrated flux measurement by $\gtrsim$ 10%. Most such flares occurred on M stars (7/9), while the remaining 2/9 are the same event observed in two different bands on the K star EG Cha.

A 10% boost in flux exceeds the transit depth in C II or Si III of HD209458b (Vidal-Madjar et al., 2004; Linsky et al., 2010). However, not all stars in the sample are similar in size to HD209458, and it is the relative size of the star and planet that determines the transit depth and thus the impact of a flare. In other words, a strong flare will have less of an impact on a measurement of a Jupiter transiting and M star than a Jupiter transiting an F star. I used the stellar radii from the literature to determine the size of an object that would produce a transit signal of the same

amplitude as the boost in flux from a flare in a 60 min integration. These range from 0.02 R_J to 12.5 R_J for the 116 flares identified. Of these, 90 (one flare per 3 h of data) would boost a 60 min flux integration by an amount larger than the signal of an Earth transiting the flaring star, 23 (one flare per 13 h) would boost flux by an amount exceeding a Neptune transit, and 7 (one flare per 42 h) would boost flux by an amount exceeding a Jupiter transit. Limiting the sample to the 24 events on non-flare stars only, 5 flares (one per 31 h) boost flux beyond an Earth signal, 2 (one per 76 h) beyond a Neptune signal, and 1 (one per 153 h) beyond a Jupiter signal.

I did not explore trends in flare rates with respect to stellar properties because the rates were only well constrained on Prox Cen and AD Leo. In addition, the small size, high diversity, and, most importantly, range of flare detection limits in the sample pose problems to such an analysis. The general conclusion is that all low-mass stars likely pose a risk of flaring near or within a transit observation. Because flares might be so easily hidden in long-cadence data, I recommend that, when possible, transit observers employ minute-scale cadences to inspect their data prior to employing longer cadences for noise suppression. This would enable a sweep of the lightcurve for obvious flare events below the transit timescale. Flares could then be excised and the data, if desired, binned to a longer cadence, correcting for the "dead time." Cadences of arbitrary length are possible with data from the photon-counting detectors common in UV work, provided the data are recorded as a time-tagged event list, rather than time-integrated counts.

3.5.3 Flare Statistics on AD Leo

I detected enough flares on AD Leo to examine their distribution in EW_p. As such, Figure 3.14 plots the frequency of flares, ν, with $> EW_p$ versus EW_p. I fit a power law to these distributions of the form

$$\nu = \alpha EW_p^{\beta} \tag{3.2}$$

using the maximum likelihood method of Crawford et al. (1970). The resulting values of β are -0.90 ± 0.29 for C II, -0.92 ± 0.27 for Si III, and -0.82 ± 0.17 for Si IV. In comparison, previous values include

- -0.82 ± 0.27 from 21 h of visible and near-ultraviolet observations (Lacy et al., 1976)
- -0.62 ± 0.09 from 111.5 h (spread over > 5 years) of U band observations (Pettersen et al., 1984)
- -1.01 ± 0.28 from < 72 h of extreme-ultraviolet observations (Audard et al., 2000)
- -0.68 ± 0.16 from 139.7 h of visible observations (Hunt-Walker et al., 2012).

The above values all agree with those I computed for each band. This agreement is consistent with the response of each band tracing common energy deposition events, even for emission resulting from different regions of the stellar atmosphere. To explore further how impulsive energy deposition affects differing regions of a stellar atmosphere, simultaneous, panchromatic flare observations would be desirable.

3.5.4 Size of Detectable Transiting Objects

This work aims to explore the boundaries placed on transit observations by stellar variability in the ultraviolet. Stochastic fluctuations in the host star determine the minimum transit depth that will stand out from these fluctuations, consequently limiting the minimum detectable size of transiting objects. As a metric for this limitation set by each star + band's stochastic fluctuations, I computed the radius of an occulting disk that would produce a transit signal equivalent to σ_x projected to 3.5 h, R_{σ_x} – in essence, the object size needed for a 1-σ detection of a single transit in the absence of photometric noise. Explicitly, I compute R_{σ_x} from

$$R_{\sigma_x}^2 = \sigma_x R_\star^2, \tag{3.3}$$

where $R_\star$ is the radius of the host star. This R_{σ_x} does not represent an actual detection limit. The true minimum detectable object size depends on the instrument and observing time available. Instead of a true limit, R_{σ_x} is an instrument independent means of comparing the suitability of stars for transit measurements. This metric is thus free from any assumptions about the number of photons an instrument will collect from the star or what other noise the instrument will add.

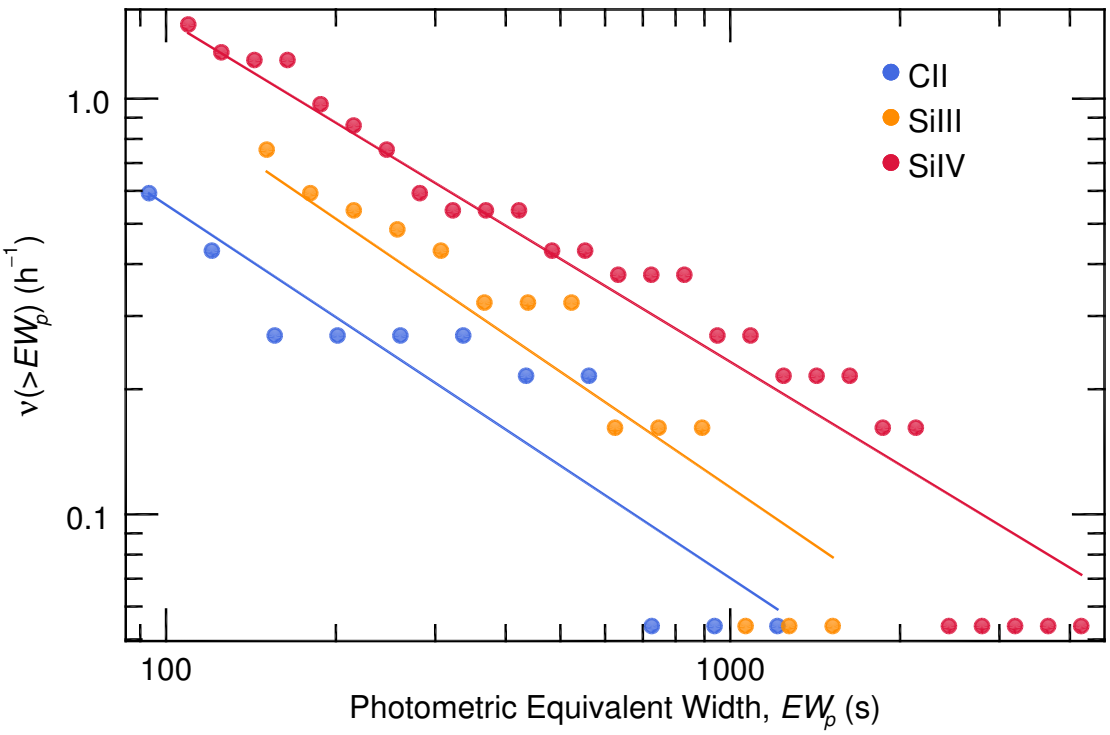

Figure 3.14 A cumulative flare-frequency distribution for the flares identified in data for AD Leo. Power-law fits are overplotted. While the data are binned for display, following the methodology of Crawford et al. (1970) they were not binned when fitting the power laws.

Figure 3.15 shows the results, grouped by spectral type. These suggest that, in the absence of photometric uncertainties, roughly Jovian-size disks would produce the smallest detectable transit signal (for a reasonable quantity of data) in a typical system. Indeed, HD209458b, HD189733b, and WASP-12b (see Section 3.1) are all of Jovian dimensions. However, R_{σ_x} spans around an order of magnitude within each spectral type, and more than two orders of magnitude overall.

The results in Figure 3.15 are grouped by spectral type to examine the tradeoff between the smaller $R_\star$ but higher σ_x (see Section 3.5.5) of less massive stars. Smaller stellar disks imply deeper transit signals, but higher levels of stochastic fluctuations better hide these signals. From Figure 3.15, it appears stellar size trumps σ_x: the smallest stars also permit the smallest objects to produce detectable transits. However, this apparent trend is significantly weakened when the F stars, all post main-sequence giants or sub-giants, are removed.

Of the stars with data robustly sampling their stochastic fluctuations on transit timescales (mean flux over 5×10^{-16} erg s^{-1} cm^{-2} and total accumulated observations ≥ 3.5 h), Prox Cen has the most generous R_{σ_x} limits in each band. These are 1.8 ± 0.1 $R_\oplus$ in C II, < 1.5 $R_\oplus$ in Si III, 2.1 ± 0.1 $R_\oplus$ in Si IV and < 1.1 $R_\oplus$ in the FUV continuum. Interestingly, Prox Cen is classified as a flare star, and the chances that it could flare near or within a transit are significant.

Like Prox Cen, most of the stars in this sample have received flare, variable, or WTTS classifications. The sample is biased: The targets were preferentially selected for variability by the various individuals that commissioned the observations. It seems probable that a less-biased sample would produce detection limits clustered lower than those in Figure 3.15. Therefore, the prospects for FUV transit measurements of planets the size of Neptune or super-Earths seem promising. Furthermore, if the observed planet hosts an atmosphere inflated to several times the area of the solid disk, like HD209458b (Vidal-Madjar et al., 2003), then in an ideal case even an Earth-size planet might produce a detectable FUV signal within a few folded transits. These prospects are exciting, but it bears remembering that, to attain such limits, photometric noise must be suppressed to below the level of stochastic fluctuations.

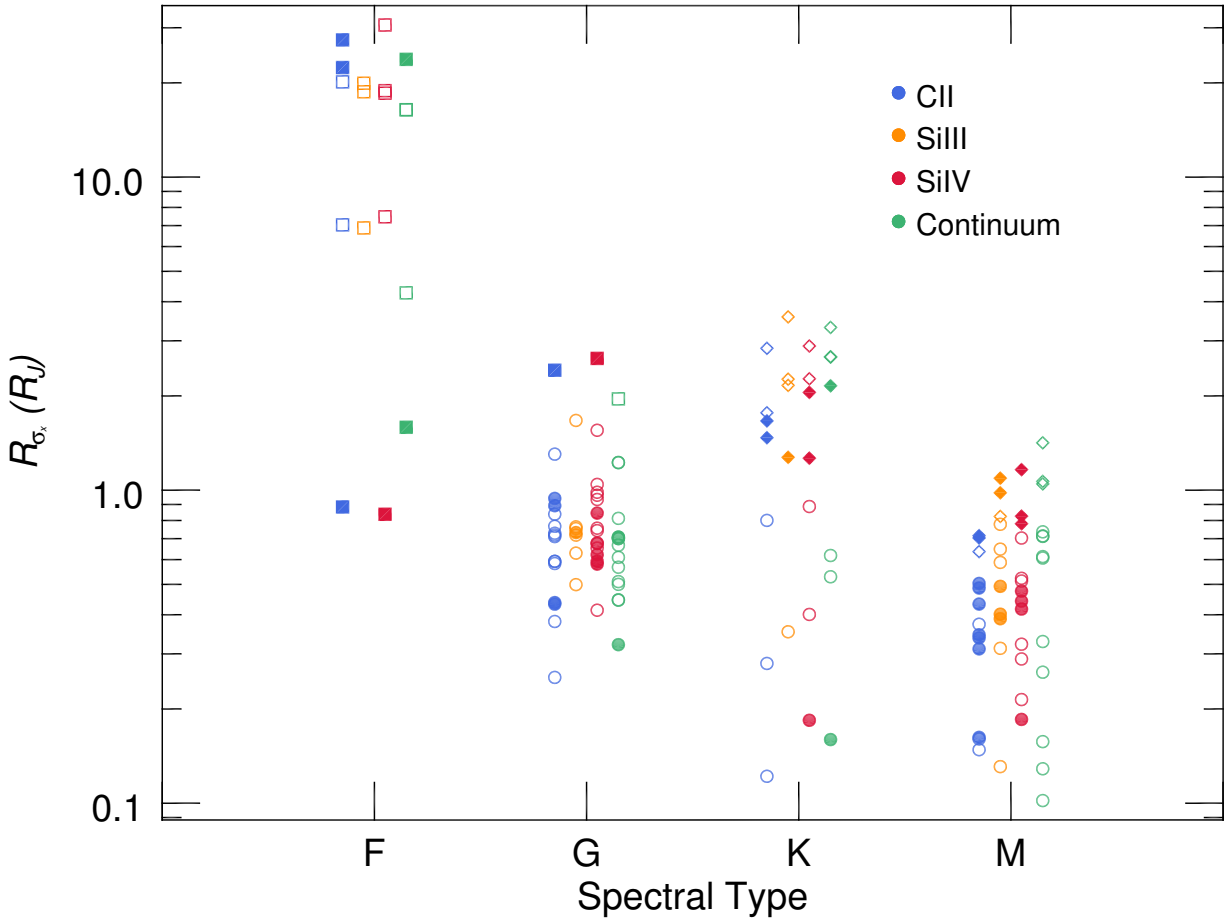

Figure 3.15 The size in Jupiter radii of an occulting disk that would cause a dip equivalent to the 1-σ scatter in the stellar flux at $\Delta t = 3.5$ h. Filled circles represent confident measurements of σ_x whereas open circles represent upper limits. Squares represent post-main-sequence stars, circles represent main sequence stars, and diamonds represent WTTS. I group values on the x-axis by spectral type (labels below axis), then by band (symbol color).

3.5.5 Correlations with Stellar Properties

I explored correlations between the mean-normalized excess noise measurements in C II and Si IV with properties of the sample stars (see Table 3.1). Excess noise values in the remaining bands, Si III and the FUV continuum, were too poorly constrained (essentially, there were too few detections and too many upper limits) to support correlations with any value. As a means of visualizing potential correlations, Figures 3.16 and 3.17 graph σ_x values (both detections, black, and upper limits, blue) against each of the stellar properties, excluding mass and luminosity, for the C II and Si IV bands respectively.

These figures show that the error bars of the mean-normalized excess noise values and stellar properties often overlap. Thus, changes in the point values even under the 1-σ error bars could change the Spearman Rank-Order correlation coefficient for the data and, more importantly, confidence that the correlation cannot be explained by randomly scattered points. To account for the uncertainty in how the true values of the points fall, I constructed a Monte-Carlo simulation, generating 10^4 possible arrangements of the data points given the uncertainties. For each trial in the Monte-Carlo simulation, I randomly drew stellar parameter (e.g., age, M, P_{rot}) values from Gaussians matching the means and 1-σ uncertainties. When there was no uncertainty accompanying the measurement I found in the literature, I assigned an uncertainty of 10%. For the mean-normalized excess noise values, I did not use Gaussians. Instead I randomly drew values from the actual likelihood distributions of σ_x for each star/band (Appendix A.3).

For each of the 10^4 such realizations of the data, I recorded probability to exceed (PTE) for the null hypothesis of randomly distributed points (i.e. no correlation) using the Spearman Rank-Order test. I multiplied the PTE by 10^{-4} to compute the joint probability of the data producing the correlation coefficient **and** such a correlation coefficient resulting from random point scatter. The integral of these values over the range of possible correlation coefficients (-1 to 1), provided the overall estimate of the PTE for random scatter in light of the data and uncertainties. I then recorded the significance of the correlation as $1-\text{PTE}$.

I carried out this process with and without the σ_x upper limits and, for both cases, quote the significance of the correlation in Figures 3.16 and 3.17. The σ_x upper limits provide useful constraints on correlations when they fall below the surrounding σ_x detections. As with the σ_x detections, when I included upper limits I generated σ_x values in the Monte-Carlo simulation from the likelihood distribution that produced each upper limit. For instance, an upper limit of 0.01 on σ_x for a point meant that I randomly drew a value between 0 and 0.01 with roughly uniform probability for each trial in the Monte-Carlo simulation.

The results computed without including the upper limits suggest weak correlations in all cases except σ_x-age and, in C II σ_x-P_{rot}. The σ_x upper limits further constrain these correlations, both quantitatively and by eye, and bring C II and Si IV into closer agreement. The subsections below address each of these in light of previous literature.

3.5.5.1 Temperature, Radius, Mass, and Luminosity

Possible correlations of excess noise with temperature and radius (as well as mass and luminosity, though these are left out of Figures 3.16 and 3.17) become strong when upper limits are included. This indicates a more general correlation between excess noise and spectral type: Stars of later spectral type typically exhibit higher σ_x. Correlations between stellar variability and spectral type were explored by McQuillan et al. (2012) for all *Kepler* stars save those with known eclipsing companions (stellar or planetary) and lightcurve discontinuities. They found that cooler, later type stars exhibited high levels of stochastic variability by their metric, in agreement with the findings. Similarly, Ciardi et al. (2011) found a relationship between variability and temperature in their analysis of *Kepler* field stars, in both dwarfs and giants. I note, however, that *Kepler* utilizes a broad optical bandpass (∼4000-9000 Å). Therefore, variability in the *Kepler* data reflects processes occurring in the photosphere, rather than the transition region, and there is no guarantee that the two are directly related.

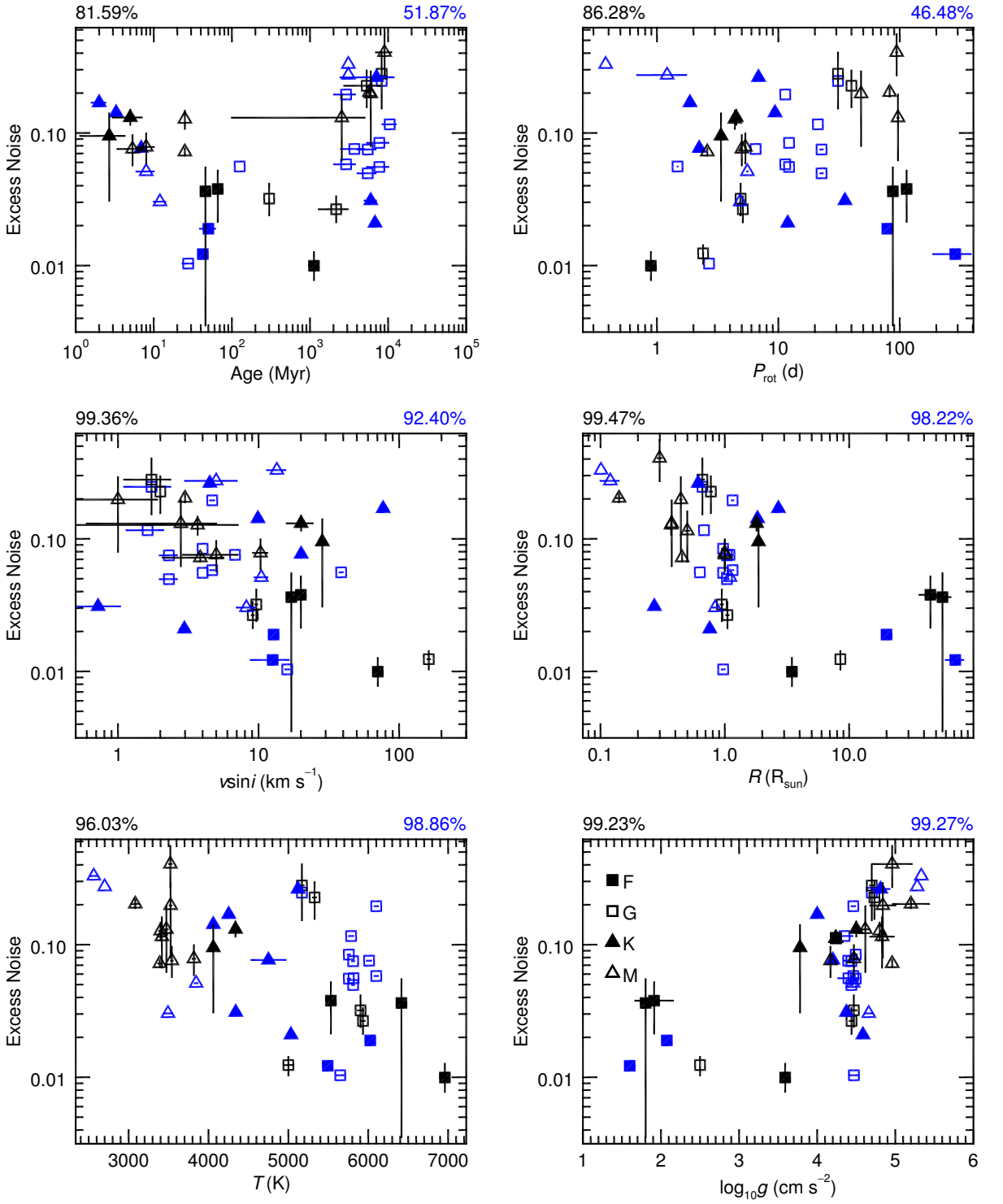

Figure 3.16 Excess noise versus stellar properties in the C II band. Symbols differentiate between spectral types (see legend in bottom right plot). Black symbols represent excess noise detections, while blue symbols represent upper limits. The black numbers above each plot give the significance of the correlation (probability it is not produced by uncorrelated points) using only excess noise detections while the blue number gives the significance including upper limits (see Section 3.5.5).

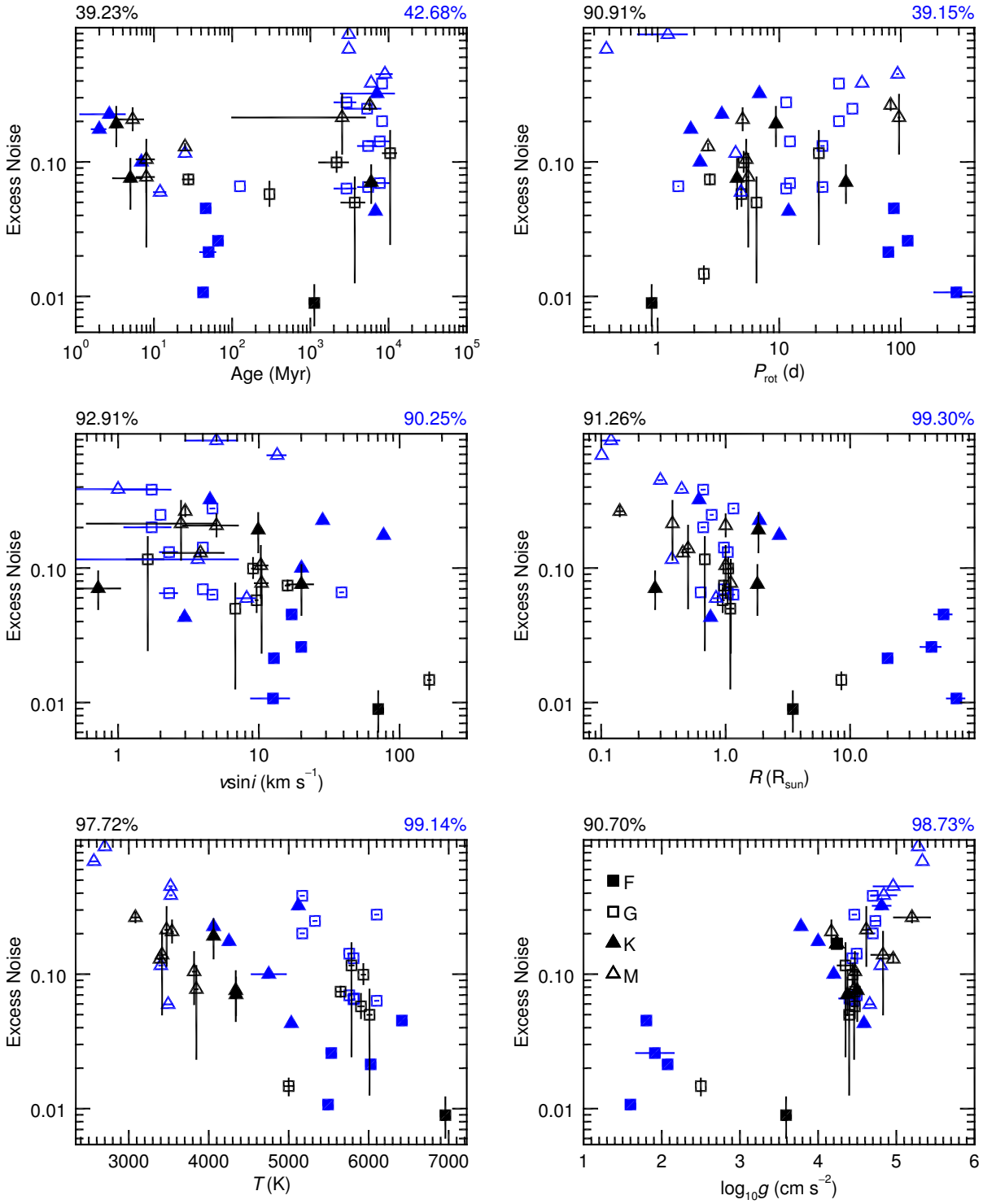

Figure 3.17 Excess noise versus stellar properties in the Si IV band, following the same format as Figure 3.16.

3.5.5.2 Rotation Period, Equatorial Velocity, and Age

Excess noise does not correlate with age, and the hint of a correlation between σ_x and rotation period is all but eliminated with the inclusion of σ_x upper limits. A possible anticorrelation seems to exist between σ_x and $v \sin i$; however, when σ_x upper limits are included, the anticorrelation is probably weak enough to dismiss outright. Furthermore, because $v = 2\pi R/P_{rot}$, the combination of a lack of a σ_x-P_{rot} correlation and the presence of a strong σ_x-R anticorrelation are capable of producing the σ_x-$v \sin i$ trend. Thus, it is the σ_x-R anticorrelation (or, rather, the relationship of σ_x to spectral type) that drives the σ_x-$v \sin i$ trend. Indeed, σ_x and the quotient R/P_{rot} (excluding the 8 stars for which I computed $P_{rot}/\sin i$ from $v \sin i$ and R) are anticorrelated to roughly the same confidences as σ_x-$v \sin i$.

Interpreting the lack of correlations with age and rotation in light of previous work is difficult, as I did not find any studies exploring correlations between these properties and stellar stochastic fluctuations. Both age and rotation, however, have been tied to stellar activity as quantified by chromospheric emission (e.g., Wilson 1963; Skumanich 1972; Noyes et al. 1984; Mamajek & Hillenbrand 2008). In turn, chromospheric emission likely has a direct relationship with stochastic fluctuations at visible wavelengths (Hall et al., 2009). This suggests that younger, faster rotating stars might exhibit higher levels of UV emission line variability.

Given these past results, the lack of σ_x-age and σ_x-P_{rot} correlations in this sample could be explained if either the age-rotation-activity or the variability-activity relationships do not hold for this sample. That either might not hold would not be particularly alarming given that this sample includes stars approaching, dwelling on, and departing the main sequence, whereas the above-mentioned studies only analyze stars on the main sequence. The pre and post main-sequence stars in this sample might exhibit magnetic behavior not in line with that of main-sequence stars, such that relationships between magnetic activity (chromospheric emission) and rotation, age, and/or variability for main-sequence stars are not extensible to this broader sample.

3.5.5.3 Surface Gravity

A strong correlation exists between excess noise and surface gravity in the sample, particularly in C II. This is in conflict with the recent results of Bastien et al. (2013), who find an inverse relationship between variability and surface gravity in *Kepler* field stars. However, compared to this work, the stellar sample employed by Bastien et al. (2013) is far more restrictive. They limit their study to stars with 4500 K $< T_{eff} <$ 6500 K, $2.5 < \log_{10} g < 4.5$ (cgs units), and relative brightness variations (measured using a 30 min cadence) of < 0.003. Applying the same cuts in T_{eff} and $\log_{10} g$ to this stellar sample eliminates any correlation (null hypothesis can produce the observed or stronger correlation with $\sim$50% probability). The strong correlation present in this data when all stars are included is driven primarily by the F giants, as these have both very low g and σ_x. However, high σ_x, high g M stars also promote the correlation.

3.5.6 Star-Planet Interactions

Close-in planets might interact with their host star magnetically and tidally, producing enhanced activity in the stellar upper atmosphere (Cuntz et al., 2000). Evidence for these interactions could be found by monitoring a single star with a transiting planet to search for signs of elevated activity near transit, when the portion of the star interacting with the planet is in view. Indeed, this has been attempted for two systems with transiting planets in this sample, HD209458 (Shkolnik, 2004) and HD189733 (Shkolnik et al., 2008; Fares et al., 2010). However, these studies found no clear evidence of enhanced activity correlated with orbital phase for either of these systems.

Alternatively, evidence for star-planet interactions might result from comparing the overall activity or variability of the stars with close-in planets to a sample of control stars. Shkolnik (2013) recommended investigations into star-planet interactions in the form of time-resolved observations of UV flux variability rather than activity (i.e. mean line flux), such as those presented in this paper. The small size and high diversity of the 32 stars in this sample that do not host planets make for a poor control. Nevertheless, I looked for increased σ_x in the six known planet hosts.

These hosts are identified in the σ_x detections and upper limits presented in Figures 3.12 and 3.12 as open points.

The hosts with σ_x detections in Figure 3.12 do appear clustered at higher σ_x. However, these are all M dwarfs, shown in the previous section to have the highest σ_x values in the sample. The M dwarf planet hosts do not stand out when grouped with the other M dwarfs in the sample. The G and K planet hosts (HD209458 and HD189733) have insufficient data for a σ_x detection, allowing only 95% upper limits. Because only upper limits are possible, these stars are not constrained to be more variable than other sample stars of the same spectral type. Thus, star-planet interactions, manifested as increased variability, are not supported by the limited volume of this data.

3.6 Summary

I have examined stellar luminosity fluctuations and stellar flares in a sample of 38 cool stars using 60 s cadence lightcurves constructed from narrow spectroscopic bands containing the Si III λ1206, C II $\lambda\lambda$1334,1335, and Si IV $\lambda\lambda$1393,1402 resonance lines and a combined 36.5 Å of interspersed FUV continuum bands. In the high pass filtered lightcurves, I detected 116 flares, occurring roughly once per 2.5 h. Flares commonly radiated more energy in Si IV, relative to quiescent levels, than the other bands. Shorter flares are more prevalent, with over half lasting 4 min or less. Most (90 of 116) of the detected flares could annihilate the signal of an Earth transit, while 7 of the 116 could annihilate the signal of a Jupiter transit. These results highlight the usefulness of minute-scale cadences for finding and removing flares prior to estimating transit depths.

To quantify stochastic fluctuations, I found the maximum-likelihood "excess noise" that, in addition to the photometric noise, accounts for the scatter of the high-pass filtered, mean-normalized lightcurves excluding flares. Values of the excess noise, relative to the mean flux, range from about 1-41% in C II, 8-18% in Si III, 0.9-26% in Si IV, and 1-22% in the FUV continuum. Where the likelihood distribution of the excess noise was one-sided, I instead quote a 95% upper limit on the excess noise. These upper limits on excess noise are often strong enough to be lower than the values

for stars where excess noise was detected.

I found significant anticorrelations of excess noise with mass, radius, temperature, and luminosity in C II and Si IV. An additional, weaker anticorrelation of excess noise with $v \sin i$ could be an artifact of the strong underlying correlation between radius and rotation rate in the sample. There was no correlation with age or rotation period.

The median levels of stochastic stellar fluctuations I estimated, integrated over a typical transit timescale of 3.5 h, would impose a rough 1-σ transit detection limit of ~ 1 R_J occulting disks for many of the stars in the sample. However, the range in these limits is broad, spanning from tenths of R_J to tens of R_J. M dwarfs might permit the FUV observation of transiting objects as small as Neptunes or even super-Earths in the absence of photometric noise. While the large fluctuations of some stars might stymie transit spectroscopy in the FUV for any but the largest planets, these results suggest that many planetary host stars might be found for which the limits of FUV transit spectroscopy can be pushed well below the hot Jupiters observed thus far.

Acknowledgments: The authors wish to acknowledge the anonymous referee, whose familiarity with the field and resulting thoughtful and constructive comments greatly improved this work. The authors also wish to thank Tom Ayres for his careful reading and helpful suggestions that similarly improved this work. Kevin France acknowledges support through a NASA Nancy Grace Roman Fellowship during a portion of this work. This research has made use of the Exoplanet Orbit Database and the Exoplanet Data Explorer at exoplanets.org (Wright et al., 2011a) as well as extensive use of the SIMBAD database and VizieR catalog access tool, operated at CDS, Strasbourg, France (Wenger et al. (2000), Ochsenbein et al. (2000)). The authors wish in particular to acknowledge Glebocki & Gnacinski (2005) for the excellent stellar rotation catalog that I used in this work. Some of the data presented in this paper were obtained from the Mikulski Archive for Space Telescopes (MAST). STScI is operated by the Association of Universities for Research in Astronomy, Inc., under NASA contract NAS5-26555. This work was supported by NASA grant NNX08AC146 to the University of Colorado at Boulder.

Chapter 4

A Panchromatic Spectral Atlas of 11 Exoplanet Host Stars

Preface

This chapter is a reproduction of the paper "The MUSCLES Treasury Survey III: X-ray to Infrared Spectra of 11 M and K Stars Hosting Planets," published in 2016 in *The Astrophysical Journal* (Loyd et al., 2016).

Abstract

I present a catalog of panchromatic spectral energy distributions (SEDs) for 7 M and 4 K dwarf stars that span X-ray to infrared wavelengths (5 Å – 5.5 μm). These SEDs are composites of *Chandra* or *XMM-Newton* data from 5 – ∼50 Å, a plasma emission model from ∼50 – 100 Å, broadband empirical estimates from 100 —1170 Å, *HST* data from 1170 — 5700 Å, including a reconstruction of stellar Lyα emission at 1215.67 Å, and a PHOENIX model spectrum from 5700 – 55000 Å. Using these SEDs, I computed the photodissociation rates of several molecules prevalent in planetary atmospheres when exposed to each star's unattenuated flux ("unshielded" photodissociation rates) and found that rates differ among stars by over an order of magnitude for most molecules. In general, the same spectral regions drive unshielded photodissociations both for the minimally and maximally FUV active stars. However, for O_3 visible flux drives dissociation for the M stars whereas NUV flux drives dissociation for the K stars. I also searched for an FUV continuum in the assembled SEDs and detected it in 5/11 stars, where it contributes around 10% of the flux in the range spanned by the continuum bands. An ultraviolet continuum shape is resolved

for the star ϵ Eri that shows an edge likely attributable to Si II recombination. The 11 SEDs presented in this paper, available online through the Mikulski Archive for Space Telescopes, will be valuable for vetting stellar upper-atmosphere emission models and simulating photochemistry in exoplanet atmospheres.

4.1 Introduction

Current stellar and planetary population statistics indicate that most rocky planets orbit low-mass stars. Low-mass stars, specifically spectral types M and K, greatly outnumber those of higher-mass, making up at least 91% of the stellar population within 10 pc of the Sun (Henry et al., 2006). On average, the low-mass stellar population exhibits a planetary occurrence rate of 0.1 – 0.6 habitable zone (HZ) terrestrial planets per star (Dressing & Charbonneau, 2013; Kopparapu, 2013; Dressing & Charbonneau, 2015). Further, the occurrence rate of rocky planets was found to decrease with increasing stellar mass by Howard et al. (2012) and no trend with stellar mass was found by Fressin et al. (2013). The above results collectively imply that, by numbers alone, low-mass stars are certain to be a cornerstone of exoplanet science and the search for other Earths.

The abundance of low-mass stars ensures that many are close enough to enable high-precision photometry and spectroscopy. In addition, their smaller sizes and lower masses yield deeper planetary transits and larger stellar reflex radial velocities when compared to a system with a higher stellar mass but identical planetary mass and orbital period. Furthermore, orbits around cooler, less-luminous stars must have shorter periods than those around Sun-like stars to achieve the same planetary effective temperature, making transits more likely and frequent and enhancing reflex velocities for radial velocity detection. These advantages facilitate the detection and bulk characterization (e.g. mass, radius) of planets orbiting nearby low-mass stars using radial velocity and transit techniques. They also facilitate atmospheric characterization through transmission spectroscopy, as has recently been performed for super-Earths orbiting the M4.5 star GJ 1214 and K1 star HD 97658 (Kreidberg et al., 2014; Knutson et al., 2014).

Upcoming exoplanet searches, such as the *Transiting Exoplanet Survey Satellite (TESS)*, will

focus on low-mass stars. In searching for planets as cool as Earth, *TESS* is biased by its short (1 – 12 month) monitoring of host stars (Ricker et al., 2014). Only around low-mass stars will cool planets orbit with short enough periods to transit several times during these monitoring programs. As a result, the *TESS* sample of potentially-habitable exoplanets will mostly be orbiting low-mass stars (Deming et al., 2009).

The prevalence of low-mass stars hosting planets makes a thorough knowledge of the typical planetary environment provided by such stars indispensable. However, the circumstellar environment of an M or K dwarf differs substantially from the well-studied environment of the Sun. Lower-mass stars have cooler photospheres that emit spectra peaking at redder wavelengths in comparison with Sun-like stars, but there are other important differences to address. As I discuss these differences and throughout this paper, I will refer to various ranges of the stellar spectral energy distributions using their established monikers. I adopt the definitions of X-ray $<$ 100 Å, EUV = [100 Å, 912 Å] (912 Å corresponds to the red edge of emission from H II recombination), XUV (X-ray + EUV) $<$ 912 Å, FUV = [912 Å, 1700 Å], NUV = [1700 Å, 3200 Å], visible = [3200 Å, 7000 Å], IR $>$ 7000 Å. Although emission from the stellar photosphere dominates the energy budget of emitted stellar radiation ($F(< 1700$ Å$)/F(> 1700$ Å$) \approx 10^{-4}$ for the stars in this paper), X-ray through UV emission that is emitted primarily from the stellar chromosphere and corona drives photochemistry, ionization, and mass loss in the atmospheres of orbiting planets. I briefly describe thee influences below.

FUV photons are able to dissociate molecules, both heating the atmosphere and directly modifying its composition. This affects many molecules common in planetary atmospheres, including O_2, H_2O, CO_2, and CH_4. If the fraction of FUV to bolometric flux is sufficiently large, photodissociation can push the atmosphere significantly out of thermochemical equilibrium (see, e.g., Moses 2014; Miguel & Kaltenegger 2014; Hu & Seager 2014). Photochemical reactions can produce a buildup of O_2 and O_3 at concentrations that, in the absence of radiative forcing, might be considered indicators of biological activity (Tian et al., 2014; Domagal-Goldman et al., 2014; Wordsworth & Pierrehumbert, 2014; Harman et al., 2015). It is also possible that these atmospheric

effects, besides just interfering with the detection (or exclusion) of existing life, might also influence the emergence and evolution of life. UV radiation can both damage (Voet et al., 1963; Matsunaga et al., 1991; Tevini, 1993; Kerwin & Remmele, 2007) and aid in synthesizing (Senanayake & Idriss, 2006; Barks et al., 2010; Ritson & Sutherland, 2012; Patel et al., 2015) many molecules critical to the function of Earth's life.

At higher photon energies, stellar extreme ultraviolet (EUV) and X-ray photons (often termed XUV in conjunction with the EUV) can eject electrons from atoms, ionizing and heating the upper atmospheres of planets. This heating can drive significant atmospheric escape for close-in planets (Lammer et al., 2003; Yelle, 2004; Tian et al., 2005; Murray-Clay et al., 2009). In addition, the development of an ionosphere through ionization by EUV flux will influence the interaction (and associated atmospheric escape) of the planetary magnetosphere with the stellar wind (e.g. Cohen et al. 2014). Indeed, atmospheric escape has been observed on the hot Jupiters HD 209458b (Vidal-Madjar et al., 2003; Linsky et al., 2010), HD 189733b (Lecavelier Des Etangs et al., 2010), and WASP-12b (Fossati et al., 2010, 2013) and the hot Neptune GJ 436b (Kulow et al., 2014; Ehrenreich et al., 2015).

The effects of stellar radiation on planetary atmospheres warrant the spectroscopic characterization of low-mass stars at short wavelengths. Yet these observations are rare compared to visible-IR observations and model-synthesized spectra. To address this scarcity, France et al. (2013) conducted a pilot program collecting UV spectra of 6 M dwarfs, a project termed Measurements of the Ultraviolet Spectral Characteristics of Low-Mass Exoplanetary Systems (MUSCLES).

Responding to the success of the pilot survey and continued urging of the community (e.g. Segura et al. 2005; Domagal-Goldman et al. 2014; Tian et al. 2014; Cowan et al. 2015; Rugheimer et al. 2015), I have completed the MUSCLES Treasury Survey, doubling the stellar sample and expanding the spectral coverage from $\Delta\lambda \approx 2000$ Å in the ultraviolet to a span of four orders of magnitude in wavelength (5 Å – 5.5 μm). I have combined observations in the X-ray, UV, and blue-visible; reconstructions of the ISM-absorbed Lyα and EUV flux; and spectral output of the PHOENIX photospheric models (Husser et al. 2013; 5700 Å – 5.5 μm) and APEC coronal

models (Smith et al. 2001; ∼50 – 100 Å) to create panchromatic spectra for all targets. The fully reduced and co-added spectral catalog is publicly available through the Mikulski Archive for Space Telescopes (MAST).[1]

I present the initial results of the MUSCLES Treasury Survey in three parts: France et al. (2016a; hereafter "Paper I") gives the overview of this MUSCLES Treasury program including an investigation of the dependence of total UV and X-ray luminosities and individual line fluxes on stellar and planetary parameters that reveals a tantalizing suggestion of star-planet-interactions. Youngblood et al. (2016a; hereafter "Paper II") supplies the details of the Lyα reconstruction and EUV modeling and explores the possibility of estimating EUV and Lyα fluxes from other, more readily observed emission lines and the correlation of these fluxes with stellar rotation. This paper, the third in the series, discusses the details of assembling the panchromatic spectral energy distributions (SEDs) that are the primary data product of the MUSCLES Treasury Survey, with a report on the detection of FUV continua in the targets, a computation of "unshielded" dissociation rates for important molecules in planetary atmospheres, and a comparison to purely photospheric PHOENIX spectra.

This paper is structured as follows: Section 4.2 describes the data reduction process, separately addressing each of the sources of the spectra that are combined into the composite SEDs, the process for this combination, special cases, and overall data quality. Section 4.3 explores the SED catalog and discusses its use. There I examine the FUV continuum, make suggestions for estimating the SEDs of non-MUSCLES stars, compute and compare unattenuated photodissociation rates, and illustrate the importance of accounting for emission from stellar upper atmospheres in SEDs. Section 4.4 then summarizes the data products and results.

4.2 The Data

Assembling panchromatic SEDs for the MUSCLES spectral catalog requires data from many sources, including both observations and models. Observational data was obtained using the space

[1] https://archive.stsci.edu/prepds/muscles/

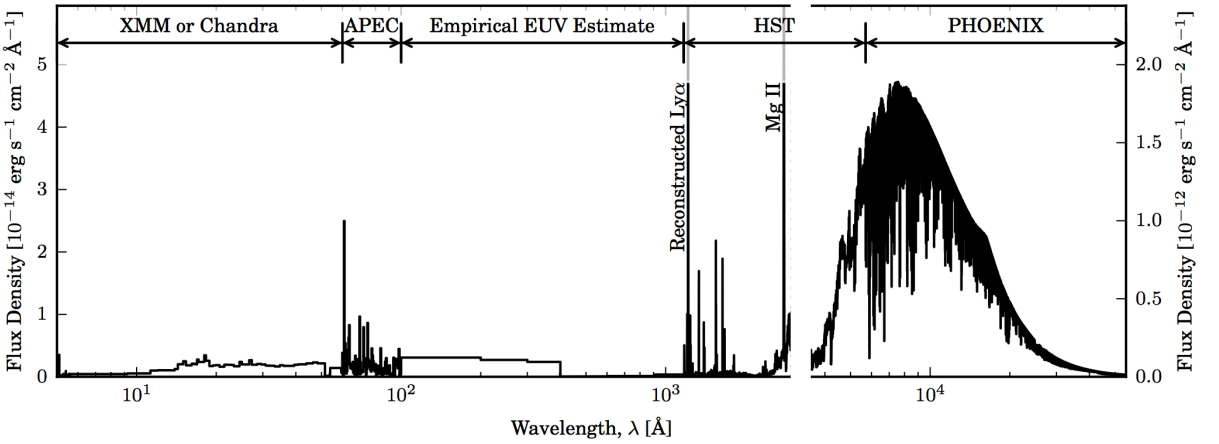

Figure 4.1 Source data ranges for the MUSCLES composite panchromatic SEDs shown with the GJ 832 spectrum for reference.The gap in the axes indicates a change in the vertical plot scale. Both the Lyα and Mg II lines extend beyond the vertical range of the plot.

telescopes *HST*, *Chandra*, and *XMM-Newton* through dedicated observing programs. Model output was obtained from APEC plasma models (Smith et al., 2001), empirical EUV predictions (Paper II), Lyα reconstructions (Paper II), and PHOENIX atmospheric models (Husser et al., 2013). The approximate wavelength range covered by each source is illustrated in Figure 4.1. I describe each data source and the associated reduction process in order of increasing wavelength below, followed by a discussion of how these sources were joined to create panchromatic SEDs. Paper I includes further details on the rationale and motivation for the various sources.

Two versions of the SED data product, one that retains the native source resolutions and another rebinned to a constant 1 Å resolution, are available for download through the MAST High Level Science Product (HLSP) Archive[2] . I made one exception to retaining native source resolutions by upsampling the broad (100 Å) bands of the EUV estimates to 1 Å binning to ensure accuracy for users that numerically integrate the spectra using the bin midpoints. I note, however, that the most precise integration over any portion of the SED is obtained through multiplying bin widths by bin flux densities and summing.

The detailed format of this data product is described in the readme file included in the archive, permitting small improvements to be made over time and reflected in the living readme

[2] https://archive.stsci.edu/prepds/muscles/

document. The spectral data products retain several types of relevant information, beyond just the flux density in each bin. This information is propagated through the data reduction pipeline at each step. As a result, every spectral bin of the final SEDs provides (at the time of publication) information on the

- Bin: wavelength of the edges and midpoint [Å].
- Flux Density: measurement and error of the absolute value [erg s^{-1} cm^{-2} $Å^{-1}$] along with the value normalized by the estimated bolometric flux [$Å^{-1}$] (this estimate is discussed in Section 4.2.7.4).
- Exposure: Modified Julian Day of the start of the first contributing exposure, end of the last contributing exposure, and the cumulative exposure time [s].
- Normalization: any normalization factor applied to the data prior to splicing into the composite SED (applies only to PHOENIX model and *HST*-STIS data, see Sections 4.2.3 and 4.2.4).
- Data source: a bit-wise flag identifying the source of the flux data for the bin.
- Data quality: bit-wise flags of data quality issues (*HST* data only).

4.2.1 X-ray data

I obtained X-ray data with *XMM-Newton* for GJ 832, HD 85512, HD 40307, and ϵ Eri and with *Chandra* for GJ 1214, GJ 876, GJ 581, GJ 436, and GJ 176. Complete details of the X-ray data reduction and an analysis of the results will be presented in a follow-on paper (Brown et al. 2016; in prep.). Here I provide a brief outline of the reduction process. The technique used to observe X-ray photons imposes some challenges to extracting the source spectrum from the observational data. The X-ray emission was observed using CCD detectors that have much lower spectral resolution ($\lambda/\Delta\lambda \sim$ 10-15 for the typical 1 keV photons observed from the MUSCLES stars) than the spectrographs used to measure the UV and visible spectra. The data were recorded in instrumental

modes designed to allow the efficient rejection of particle and background photon events. CCD X-ray detectors have very complex instrumental characteristics that are energy-dependent and also depend critically on where on the detector a source is observed. Broad, asymmetric photon energy contribution functions result from these effects, and it is nontrivial to associate a measured event energy to the incident photon energy. Consequently, simply assigning to each detection the most likely energy of the photon that created the detected event and binning in energy does not accurately reproduce the source spectrum.

To estimate the true source spectrum, I used the XSPEC software package (Arnaud, 1996) to forward model and parameterize the observed event list, using model spectra generated by APEC (Astrophysical Plasma Emission Code; Smith et al. 2001). For each spectrum, I experimented with fits to plasma models containing one to three temperature components and with elemental abundance mixes that were either fixed to solar values or free to vary (but normally only varying the Fe abundance, because it is the dominant emission line contributor) until I achieved the most reasonable statistical fit. The complexity of the model fit is strongly controlled by the number of detected X-ray events. The resulting model parameters are listed in Table 4.1.

I then computed the ratio of the number of photons incident in each energy bin to the number actually recorded, and corrected the measured photon counts accordingly. The spectral bin widths are variable because the data were binned to contain an equal number of counts per energy bin.

The X-ray data do not extend to the start of the EUV region, and this results in an energy distribution gap that, depending on the S/N of the X-ray observations, starts at 30 – 60 Å and ends where the empirical EUV flux estimates (see Section 4.2.2) begin at 100 Å. I filled this gap with the output of the same best-fit APEC model that yielded the count-rate corrections for the measured X-ray spectrum.

4.2.2 EUV and Lyα

Much of the EUV radiation emitted by a star, along with the core of the Lyα line, cannot be observed because of absorption and scattering by hydrogen in the interstellar medium. However,

Table 4.1. Parameters of the APEC model fits to the X-ray data.

Star	kT[a] [keV]	EM_i/EM_1[b]	F_X[c] [10^{-14} erg s^{-1} cm^{-2}]
GJ 1214	0.2[d]		≤ 0.11
GJ 876	0.80 ± 0.14		9.1 ± 0.8
	0.14 ± 0.04	3.5 ± 4.6	
GJ 436	0.39 ± 0.03		1.2 ± 0.1
GJ 581	0.26 ± 0.02		1.8 ± 0.2
GJ 667C	0.41 ± 0.03		3.9 ± 0.3
GJ 176	0.31 ± 0.02		4.8 ± 0.3
GJ 832	$0.38^{+0.11}_{-0.07}$		$6.2^{+0.8}_{-0.7}$
	$0.09^{+0.02}_{-0.09}$	$4.8^{+2.6}_{-2.9}$	
HD 85512	$0.25^{+0.04}_{-0.03}$		$1.9^{+0.4}_{-0.3}$
HD 40307	0.15 ± 0.06		1.0 ± 0.2
HD 97658[e]	...	...	...
ϵ Eri	$0.70^{+0.04}_{-0.07}$		940 ± 10
	0.32 ± 0.01	$3.6^{+0.7}_{-0.9}$	
	$0.12^{+0.09}_{-0.02}$	$2.4^{+2.0}_{-1.0}$	

[a]Plasma temperature. Multiple values for an entry represent multiple plasma components in the model.

[b]For multi-component plasmas, this represents the ratio of the emission measure of the i^{th} component to the first component according to the order listed in the kT column.

[c]Flux integrated over full instrument bandpass.

[d]Estimate is not well constrained and is based on an earlier *XMM-Newton* observation. See Section 4.2.6.

[e]No observations. See Section 4.2.6.

emission in the wings of the Lyα line does reach Earth because multiple scatterings in the stellar atmosphere produce broad emission wings that are not affected by the narrower absorption profile produced by H I and D I in the ISM. This allows the full line to be reconstructed by modeling these processes.

Youngblood et al. (2016a; Paper II) have reconstructed the intrinsic Lyα profile from observations made with *HST* STIS G140M and (for bright sources) E140M data. The narrow slits used to collect these data (52x0.1″ for G140M and 0.2x0.06″ for E140M) produce a spectrum where the diffuse geocoronal Lyα "airglow" emission is spatially extended beyond the target spectrum and spectrally resolved. This allows the geocoronal spectrum to be measured and subtracted from the observed spectrum, leaving only the target flux. The modeling procedure used to reconstruct the intrinsic Lyα line from the airglow-subtracted data is described in detail in Paper II. This reconstruction covers 1209.5 to 1222.0 Å in the MUSCLES spectra.

The EUV is estimated from the intrinsic Lyα flux for each source using the empirical fits of Linsky et al. (2014). This also is detailed in Paper II. I use these estimates to fill all of the EUV as well as the portion of the FUV below 1170 Å where the reflectivity of the Al+MgF_2 coatings in the *HST* spectrograph optics rapidly declines.

4.2.3 FUV through Blue-Visible

Currently, *HST* is the only observatory that can obtain spectra at UV wavelengths. I used *HST* with the COS and STIS spectrographs to obtain UV data of all 11 sources. Obtaining full coverage of the UV required multiple observations using complementary COS and STIS gratings. The choice of gratings depended on the target brightness. Figure 4.2 illustrates these configurations, depicting which instrument and which grating provided the data for the different pieces of each star's UV dataset. Along with the UV observations, I also obtained a visible spectrum with STIS G430L covering visible wavelengths up to 5700 Å (with the exception of ϵ Eri, for which instrument brightness limits required the use of STIS G430M covering $\sim$3800 – 4075 Å) since the required observing time once the telescope was already pointed was negligible.

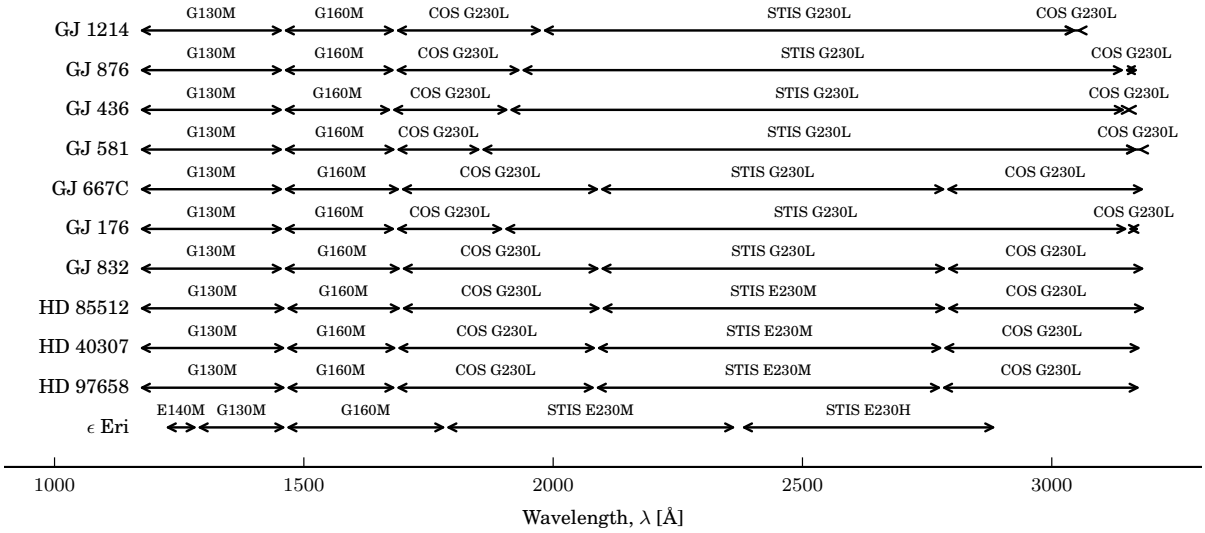

Figure 4.2 Sources of the UV data for the composite SED of each MUSCLES star. Due to space constraints, the labels E140M, G130M, and G160M are used in place of STIS E140M, COS G130M, and COS G160M. Note that the STIS G140M or E140M data obtained for each star do not appear on this figure because they were only used to reconstruct the Lyα emission (Section 4.2.2) and fill small gaps left by airglow removal (Section 4.2.3).

For observations with multiple exposures, I coadded data from each exposure. I did the same for the (overlapping) orders of echelle spectra. This produced a single spectrum for each instrument configuration.

I inspected all the coadded spectra and culled any data suspected of detector edge effects. I also removed emission from the geocoronal airglow present in the COS G130M spectra if the airglow line was visible in the spectrum of at least one MUSCLES source. The wavelengths at which I inspected the MUSCLES data for this emission are those listed in the MAST database of airglow lines[3] compiled from airglow-only observations. The removed lines were N I λ1134, He I λ584 at second order (1168 Å), N I λ1200, O I λ1305, and O I λ1356. The resulting gaps were later filled with STIS data where there was overlap and a quadratic fit to the nearby continuum where there was not.

4.2.3.1 A Discrepancy in the Absolute Level of Flux Measurements by COS and STIS

Several instrument configurations of the *HST* data have overlapping wavelength ranges. This allowed us to compare the fluxes from these configurations prior to stitching the spectra into the final panchromatic SED. Where there was sufficient signal for a meaningful comparison, STIS always measured lower fluxes than COS by factors of 1.1 – 2.4. The cause of this discrepancy could be a systematic inaccuracy in the STIS data, the COS data, or both.

The STIS G430L data can be compared against external data in search of a systematic trend because the grating bandpass overlaps with the standard B band for which many ground-based photometric measurements are available. Carrying out this comparison showed that the fluxes measured with the STIS G430L grating were lower than ground based B-band photometry for every star. The magnitude of these discrepancies varied from the discrepancies between STIS and COS data, but not beyond what is reasonable given uncertainties in the B-band photometry. A plausible cause of systematically low flux measurements by STIS could be imperfect alignment of

[3] http://www.stsci.edu/hst/cos/calibration/airglow_table.html

the spectrograph slit on the target. This can produce significant flux losses when a narrow slit is used (Biretta et al. 2015; see Section 13.7.1). No such comparison with external data was possible for the COS data. While there is overlap of COS data with *GALEX* bands, *GALEX* photometry is only available for roughly half the targets and uncertainties are very large.

Given the low STIS fluxes relative to ground-based photometry, the plausible explanation of such low fluxes, and the lack of an external check for the COS absolute flux accuracy, I chose to treat the absolute flux levels to be accurate for COS and inaccurate for STIS. Thus, for each STIS spectrum, I normalized to overlapping COS data whenever the difference in flux in regions of high signal was sufficiently large to admit a $< 5\%$ false alarm probability. This condition was met for all of the G230L and E230M spectra (excepting ϵ Eri for which comparable COS NUV data could not be collected due to overlight concerns), a few G140M spectra, and the E140M spectrum of ϵ Eri. The normalization factor was simply computed as the ratio of the integrated fluxes in the chosen region. I normalized data from each instrumental configuration separately, rather than normalizing all STIS data by the same factor, to allow for potential variations in throughput between instrument configurations. An example of this normalization is displayed in Figure 4.3.

The STIS G430L spectra have a small amount of overlap with COS G230L near 3100 Å that could be used for normalization. However, the G430L data are of poor quality in this region, making normalization factors very uncertain and heavily dependent on the wavelength range used. Thus, I normalized the G430L data to all available non-MUSCLES photometry via a PHOENIX model fit, detailed in the following section.

The normalization factors applied are recorded pixel-by-pixel as a separate column in the final data files.

4.2.4 Visible through IR

I used synthetic spectra generated by Husser et al. (2013) from a PHOENIX stellar atmosphere model to fill the range from the blue visible at ∼5700 Å out to 5.5 μm where their model spectra truncate. The choice to use model output instead of observations enabled greater consis-

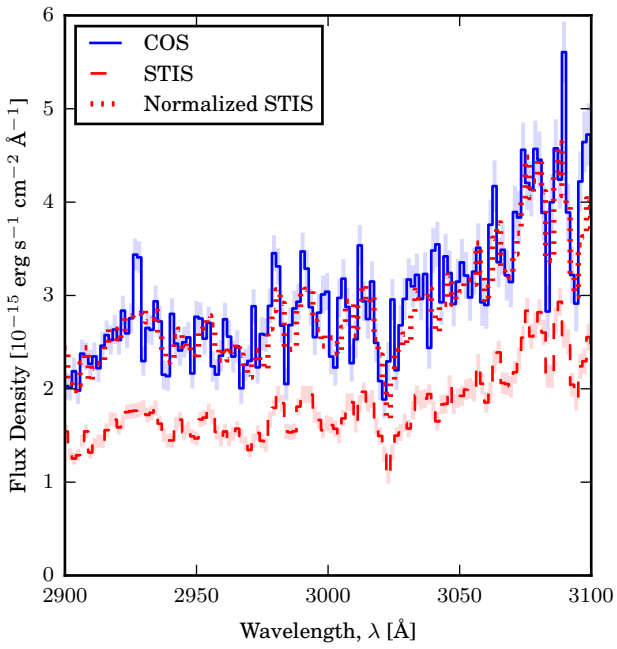

Figure 4.3 An example of normalizing STIS to COS data. The figure shows a portion of the NUV data for GJ 436 from the STIS G230L and COS G230L observations, identically binned for comparison. The COS flux exceeds the STIS flux by a wide margin. Normalizing the STIS data in lieu of possible slit losses produces good agreement.

Table 4.2. Selected properties of the stars in the sample.

Star	Type	d [pc]	V	ref	MUSCLES T_{eff} [K]	Literature T_{eff} [K]	ref	$\log g$ [[cm s^{-2}]	ref	$[Fe/H]$	ref
GJ 1214	M4.5	14.6	14.68 ± 0.02	1	2935 ± 100	2817 ± 110	2	5.06 ± 0.52	3	0.05 ± 0.09	2
GJ 876	M5	4.7	10.192 ± 0.002	4	3062^{+120}_{-130}	3129 ± 19	5	4.93 ± 0.22	3	0.14 ± 0.09	2
GJ 436	M3.5	10.1	10.59 ± 0.08	6	3281 ± 110	3416^{+54}_{-61}	7	4.84 ± 0.16	3	-0.03 ± 0.09	2
GJ 581	M5	6.2	10.61 ± 0.08	6	3295 ± 140	3442 ± 54	8	4.96 ± 0.25	3	-0.20 ± 0.09	2
GJ 667C	M1.5	6.8	10.2	9	3327 ± 120	3445 ± 110	2	4.96 ± 0.25	3	-0.50 ± 0.09	2
GJ 176	M2.5	9.3	10.0	10	3416 ± 100	3679 ± 77	5	4.79 ± 0.13	3	-0.01 ± 0.09	2
GJ 832	M1.5	5.0	8.7	10	3816 ± 250	3416 ± 50	11	4.83 ± 0.15	3	-0.17 ± 0.09	2
HD 85512	K6	11.2	7.7	10	4305^{+120}_{-110}	4400 ± 45	12	4.4 ± 0.1	12	-0.26 ± 0.14	12
HD 40307	K2.5	13.0	7.1	10	4783 ± 110	4783 ± 77	12	4.42 ± 0.16	12	-0.36 ± 0.02	12
HD 97658	K1	21.1	7.7	10	5156 ± 100	5170 ± 50	13	4.65 ± 0.06	14	-0.26 ± 0.03	14
ϵ Eri	K2.0	3.2	3.7	15	5162 ± 100	5049 ± 48	12	4.45 ± 0.09	12	-0.15 ± 0.03	12

References. — (1) Weis 1996; (2) Neves et al. 2014; (3) Santos et al. 2013a; (4) Landolt 2009; (5) von Braun et al. 2014; (6) Høg et al. 2000; (7) von Braun et al. 2012; (8) Boyajian et al. 2012; (9) Mermilliod 1986; (10) Koen et al. 2010; (11) Houdebine 2010; (12) Tsantaki et al. 2013; (13) Van Grootel et al. 2014; (14) Valenti & Fischer 2005; (15) Ducati 2002

Note. — I located many of these parameters through the PASTEL (Soubiran et al., 2010a) catalog, but have provided primary references in this table.

tency in the treatment of the visible and IR between sources, given that for some sources I was unable to acquire optical and IR spectra within the same time window as the X-ray and UV observations. The visible and IR emission of low-mass stars is well reproduced by PHOENIX models. The Husser et al. (2013) PHOENIX spectra cover a grid in effective temperature ($T_{\rm eff}$), surface gravity ($\log_{10} g$), metallicity ([Fe/H]), and α metallicity. The α metallicity is used to specify the abundance of the elements O, Ne, Mg, Si, S, Ar, Ca, and Ti relative to Fe. However, I found no data on α metallicity for the target stars, so I treated each as having the solar value. For $T_{\rm eff}$, $\log_{10} g$, and [Fe/H], I found literature values for all stars, as listed in Table 4.2.

The PHOENIX model output provided by Husser et al. (2013) has an arbitrary scale. Thus, the output must be normalized to match the absolute flux level of the star. To constrain this normalization using data on the star, I collected all external photometry for the star returned by the VizieR Photometry Viewer[4] within a 10" search radius. An exception was GJ 667C, where companion stars A and B prevented a position-based search. Instead, I collected photometry specifically associated with the object from the Denis catalog, the UCAC4 catalog, and the HARPS survey. For all other stars, I verified that no other sources fell within the search radius in 2MASS imagery. References for the photometry I collected are given in Table 4.3.

For several stars, simply retrieving a PHOENIX spectrum from the Husser et al. (2013) grid using stellar parameters found in the literature produced a spectrum with an overall shape that did not match the collected photometry. The overall spectral shape is primarily driven by $T_{\rm eff}$, so, to correct this mismatch, I wrote an algorithm to search the Husser et al. (2013) grid of PHOENIX spectra for the best-fit $T_{\rm eff}$. The fitting algorithm operated by taking a supplied $T_{\rm eff}$ and the literature values for $\log_{10} g$ and [Fe/H] and tri-linearly interpolating a spectrum from the Husser et al. (2013) grid. It then computed the best-fit normalization factor that matched the spectrum to stellar photometry. The normalization factor was computed analytically via a min-χ^2 fit to the photometry under the assumption of identical S/N for each point. I estimated the S/N as the RMS

[4] http://vizier.u-strasbg.fr/vizier/sed/

of the normalized residuals, that is

$$\frac{F_{o,i}}{\sigma_i} = \left[\frac{1}{N}\sum_i \frac{\left(F_{o,i} - F_{c,i}\right)^2}{F_{o,i}^2}\right]^{-1/2}, \tag{4.1}$$

where σ_i is the uncertainty on the observed flux $F_{o,i}$, $F_{c,i}$ is the synthetic flux computed by applying the transmission curve of the filter used to measure $F_{o,i}$ to the PHOENIX model, and i indexes the N available flux measurements. Estimating measurement uncertainties permits the inclusion of data lacking quoted uncertainties and mitigates possible underestimation of uncertainties in those data for which they are given. Uncertainties on the best-fit normalization factors span 0.007% (ϵ Eri) to 6% (GJ 1214) with a median uncertainty of 0.4%, and the uncertainty in normalization correlates well with the target V magnitude.

After normalization, the algorithm checked for outlying photometry by computing the deviation for which the false alarm probability of a point occurring beyond the deviation was < 10 %. Points beyond that deviation were culled and the fit recomputed to convergence. Once converged, the algorithm computed the likelihood of the model given the data. This then permitted a numerical search for the maximum-likelihood $T_{\rm eff}$.

Once the best-fit $T_{\rm eff}$ was found, the algorithm sampled the likelihood function to find the 68.3% confidence interval on $T_{\rm eff}$. For this search, the photometry was fixed to the outlier-culled list and associated S/N estimate from the best fit. This confidence interval provides a statistical uncertainty estimate, but the assumptions made in the fitting process (PHOENIX model, constant S/N estimated from residuals) introduces a further, systematic uncertainty. I estimated this systematic uncertainty to be 100 K and added it in quadrature to the statistical uncertainty to produce a final uncertainty estimate for the $T_{\rm eff}$ values I computed for each star.

The best-fit $T_{\rm eff}$ values and corresponding literature values are listed in Table 4.2. Figure 4.4 illustrates the discrepancy between the literature $T_{\rm eff}$ values and the photometry for the worst case. The figure includes one fit computed with $T_{\rm eff}$ as a free parameter and another with $T_{\rm eff}$ fixed to the literature value. The shape of the PHOENIX spectrum interpolated at the literature value

Table 4.3. References for stellar photometric measurements.

Star	Photometry References
GJ 1214	1,2,3,4,5,6,7,8,9
GJ 876	10,11,12,7,13,6,14,15,16,3,17,18,19,20,9
GJ 436	21,22,12,2,7,13,14,3,17,6,19,23,9
GJ 581	10,21,1,24,7,13,17,12,14,19,23,9
GJ 667C	25,26,27
GJ 176	11,22,7,13,6,14,15,16,12,18,19,9
GJ 832	28,10,29,30,7,13,14,16,31,32,23,19,33,8,9
HD 85512	28,34,35,36,37,30,23,13,14,31,18,32,33,8,9
HD 40307	28,34,35,11,37,30,23,13,9,3,18,32,33,8,38
HD 97658	11,37,30,3,13,39,31,18,32,33,8,9
ϵ Eri	35,37,30,40,41,13,14,42,9,18,32,33,8,43

References. — (1) Zacharias et al. 2004a; (2) Triaud et al. 2014; (3) Santos et al. 2013b; (4) Wright et al. 2011b; (5) Cutri & et al. 2014; (6) Rojas-Ayala et al. 2012; (7) Lépine & Gaidos 2011; (8) Cutri & et al. 2012; (9) Cutri et al. 2003; (10) Winters et al. 2015; (11) Ammons et al. 2006; (12) de Bruijne & Eilers 2012; (13) Röser et al. 2008; (14) Salim & Gould 2003; (15) Zacharias et al. 2004b; (16) Bonfils et al. 2013; (17) Jenkins et al. 2009b; (18) Pickles & Depagne 2010; (19) Gaidos et al. 2014; (20) Finch et al. 2014; (21) Roeser et al. 2010; (22) Reid et al. 2004; (23) Abrahamyan et al. 2015; (24) Bryden et al. 2009; (25) Consortium 2005; (26) Delfosse et al. 2013; (27) Zacharias et al. 2012; (28) Girard et al. 2011; (29) Neves et al. 2013; (30) van Leeuwen 2007a; (31) Myers et al. 2015; (32) Anderson & Francis 2012; (33) Kharchenko 2001; (34) Lawler et al. 2009; (35) Holmberg et al. 2009b; (36) Anglada-Escudé & Butler 2012; (37) Soubiran et al. 2010b; (38) Eiroa et al. 2013; (39) Bailer-Jones 2011; (40) Fabricius et al. 2002; (41) Haakonsen & Rutledge 2009; (42) Aparicio Villegas et al. 2010; (43) Gould 1879

does not conform to the photometry.

After finding the best-fit PHOENIX spectrum, I used it to normalize the STIS G430L data according to the ratio of integrated fluxes in the overlap redward of 3500 Å.

4.2.5 Creating Composite Spectra

I spliced together the spectra from each source to create the final spectrum. When splicing, observations were always (with a few exceptions mentioned in the next section) given preference over the APEC or PHOENIX models. When two observations were spliced, I chose the splice wavelength to minimize the error on the integrated flux in the overlapping region. This causes the splice locations to vary somewhat from star to star (see Figure 4.2). Once all of the spectra were joined, I filled the remaining small gaps that resulted from removing telluric lines (along with a slight separation between the E230M and E230H spectra in ϵ Eri) with a quadratic fit to the continuum in a region 20 times the width of the gap. Throughout the process, I propagated exposure times, start date of first exposure, end date of last exposure, normalization factors, data sources, and data quality flags on a pixel-by-pixel basis into the final data product.

4.2.6 Special Cases

The diversity of targets and data sources included in this project necessitated individual attention in the data reduction process. In all cases, spectra were separately examined and suspect data, particularly data near the detector edges, were culled. In a variety of cases, detailed below, I tweaked the data reduction process.

The *HST* STIS G430L data for all stars show large scatter with many negative flux bins at the short-wavelength end of the spectrum. For most stars, this region is small enough to be significantly overlapped by COS G230L data that I have used in the composite SED. However, for **GJ 667C** and **GJ 1214** this region is much larger than the COS G230L overlap. In these cases, I culled the STIS G430L data from the long-wavelength edge of the COS G230L spectra to ∼3850 Å, roughly where the negative-flux pixels of the STIS G430L data cease, and filled the gap

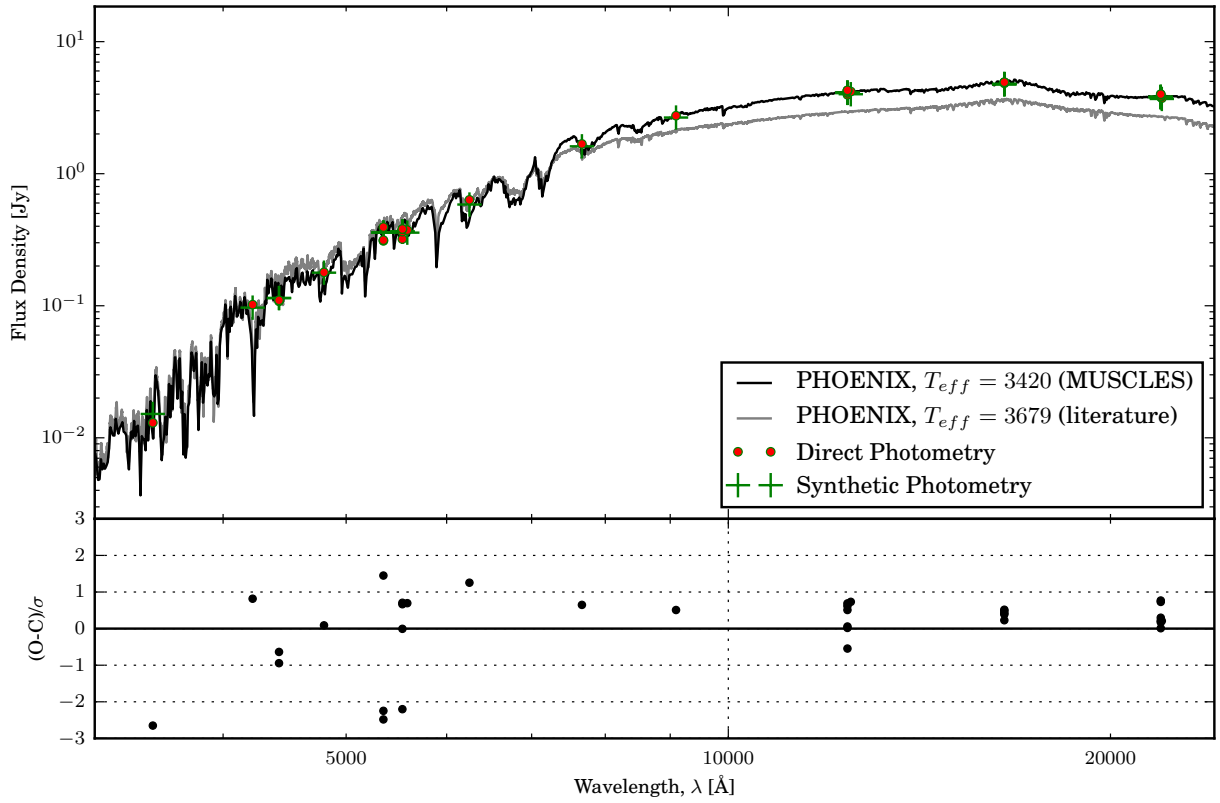

Figure 4.4 The normalization and $T_{\rm eff}$ fit of PHOENIX model output to non-MUSCLES photometry for GJ 176. Synthetic photometry (green crosses) computed from the PHOENIX spectrum with best-fit $T_{\rm eff}$ (black line) agrees well with all photometric data (red dots). In contrast, the PHOENIX spectrum where $T_{\rm eff}$ is fixed to the literature value (gray line) produces a noticeably poor fit to the photometry. Photometric data are plotted at the mean filter wavelength.

with the PHOENIX model. While the PHOENIX models used here omit emission from the stellar upper atmosphere that dominates short-wavelength flux (see Section 4.3.4), this omission does not begin to have a substantial effect until shortward of where the COS G230L coverage begins in other targets.

GJ 667C showed fluxes for all STIS data several times below that of the COS data. Inspection of the acquisition images revealed the spectrograph slit was very poorly centered on the source. I did not alter the reduction process for this star, but I note that the STIS data were normalized upward by large factors in this case. Specifically, I computed normalization factors of 3.5 for the STIS G140M data, 5.1 for the STIS G230L data, and 4.2 for the STIS G430L data.

The STIS G140M spectra of **GJ 1214, GJ 832, GJ 581** and **GJ 436** and the STIS G230L spectrum of GJ 1214 were improperly extracted by the CalSTIS pipeline because the pipeline algorithm could not locate the spectral trace on the detector. However, the spectral data were present in the fluxed 2D image of the spectrum (the .x2d files). I extracted spectra for these targets by summing along the spatial axis in a region of pixels centered on the signal in the spectral images with a proper background subtraction and correction for excluded portions of the PSF. I checked the method using stars where CalSTIS succeeded in locating and extracting the spectrum and found good agreement.

The *Chandra* data for **GJ 1214** provided only an upper limit on the X-ray flux. As a result, I decided to use a previous model fit to *XMM-Newton* data (Lalitha et al., 2014) to fill the X-ray portion of GJ 1214's spectrum.

I did not acquire X-ray data for **HD 97658**. To fill this region of the spectrum, I use data from HD 85512 scaled by the ratio of the bolometric fluxes of the two stars. These stars have nearly identical Fe XII λ1242 emission relative to their bolometric flux. The Fe XII ion has a peak formation temperature above 10^6 K (Dere et al., 2009), associating it with coronal emission. Thus, the similarity in Fe XII emission between HD 97658 and HD 85512 suggests similar levels of coronal activity. This conclusion is further supported by the similar ages estimated by Bonfanti et al. (2016) of 9.70 ± 2.8 Gyr for HD 97658 and 8.2 ± 3.0 Gyr for HD 85512.

Both **GJ 581** and **GJ 876** were observed by *Chandra* at two markedly different levels of X-ray activity. I include in the panchromatic SEDs the observations taken when the stars were less active.

Finally, the spectral image of the STIS G230L exposure of **GJ 436** shows a faint secondary spectrum separated by about 80 mas from the primary. It is very similar in spectral character, if not identical, to the GJ 436 spectrum. An identical exposure from 2012 does not show the same feature, but this is unsurprising given the high proper motion of GJ 436 (van Leeuwen, 2007b). If a second source is a significant contributor, this could impart an upward bias to the GJ 436 flux.

4.2.7 Notes on Data Quality

Users should keep several important characteristics of the panchromatic SEDs in mind when using them.

4.2.7.1 Flares

These stars exhibited flares in the UV, some very large (see Paper I), during the observations. The rates of such flares on these stars is mostly unconstrained: there is little or no previous data that could provide a good estimate of whether the observed flares were typical or atypical for the target. Thus, the safest assumption is to treat the MUSCLES observations as typical. As such, I did not attempt to separate the data into times of flare and quiescence. These observations should thus be treated as roughly typical of any average of one to a few hours of UV data for a given star. These flares will be the subject of a future publication (Loyd et al. 2017b; in prep).

4.2.7.2 Wavelength Calibration

I observed some mismatches in the wavelengths of spectral features in the NUV data from COS and STIS. This mismatch is most pronounced at the Si II $\lambda\lambda 1808, 1816$ lines, where the line centers in the STIS E230M data for ϵ Eri (the only STIS observation that resolves the lines) match the true line wavelengths, but the COS G230L data of all other targets show the lines shifted $\sim$4 Å

(∼660 km s^{-1}) blueward. This shift in the COS G230L wavelength solution is not present at the next recognizable spectral feature redward of Si II, Mg II. Flux from Si II and Mg II is captured on different spectral "stripes" on the COS G230L detector, suggesting that the entire stripe capturing Si II flux might be poorly calibrated in comparison to the stripe capturing Mg II flux. The Mg II $\lambda\lambda$ 2796, 2803 lines are in an area of overlap between the COS G230L data and STIS E230M (K stars) and G230L (M stars) data, enabling a direct comparison of the wavelength solutions for these spectra at Mg II. Making this comparison reveals that STIS E230H and COS G230L data agree to within 1 Å, while STIS G230L and COS G230L data can disagree by up to 2 Å (∼330 km s^{-1}). In the latter cases, the COS data more closely match the true wavelength of the Mg II lines.

The NUV discrepancy for the narrow-slit STIS G230L observations at Mg II could result from the same target centering issues that may cause the flux discrepancies discussed in Section 4.2.3.1. I do not understand the source of the erroneous COS wavelength solution at the Si II lines.

In the FUV, wavelength calibrations between COS G130M and STIS G140M data at the N V $\lambda\lambda$1238,1242 lines typically agree to within a single pixel width of the STIS G140M data (∼0.05 Å, 10 km s^{-1}).

I did not alter the wavelength calibration of any spectra. Neither do I attempt to shift the spectra to the rest frame of the star. Such a shift would be <0.05% for any target (< 0.5 Å at 1000 Å). To place the wavelength miscalibrations and target redshifts in context, I note that the molecular cross section spectra used in Section 4.3.3 have a resolution of 1 Å.

4.2.7.3 Negative Flux

Users will notice bins with negative flux density in many low-flux regions in the UV. This is a result of subtracting a smoothed background count rate from regions where noise dominates the signal (Section 3.4[5] of the STIS Data Handbook, Bostroem & Proffitt, 2011 and Section 3.4[6] of the COS Data Handbook, Fox et al. 2017). While a negative flux is unphysical, the background

[5] http://www.stsci.edu/hst/stis/documents/handbooks/currentDHB/ch3_stis_calib5.html
[6] http://www.stsci.edu/hst/cos/documents/handbooks/datahandbook/ch3_cos_calib5.html

subtraction serves to produce an unbiased estimate of the flux when low-flux regions are integrated. Thus, I left the negative bins in the low-flux regions unaltered.

4.2.7.4 The Rayleigh-Jeans Tail

The truncation of the PHOENIX spectra at 5.5 μm results in the omission of flux that contributes a few percent to the bolometric flux of the stars. The bolometric flux estimate determines the relative level at which each wavelength regime contributes to the stellar SED, so accuracy is important. I therefore compute and include in the data product a bolometric flux value for each target that incorporates the integral of a blackbody fit to the PHOENIX spectrum from the red end of the PHOENIX range at 5.5 μm to ∞. Whenever I present bolometrically normalized fluxes, I use this more accurate value as opposed to the integral of the MUSCLES SED alone.

4.2.7.5 ϵ Eri STIS E230M/E230H Data Compared with PHOENIX Output

Unlike the other targets, ϵ Eri was too bright to permit the collection of *HST* COS observations in the NUV, so only *HST* STIS data, specifically using the E230M and E230H gratings, were collected. Because of the lack of COS data that was used to correct systematically lower flux levels in the STIS NUV data of other stars (Section 4.2.3.1), I examined the ϵ Eri STIS NUV data closely. This star has a high enough $T_{\rm eff}$ for photospheric flux to contribute significantly in the NUV. Thus, the PHOENIX spectrum for ϵ Eri can be meaningfully compared to the observation data in this regime.

The lower envelope of the PHOENIX spectrum matches very well with that of the E230M and E230H data. However, some portions of the PHOENIX spectrum show emission features well above that seen in the E230M and E230H spectra. This results in the integrated flux of the PHOENIX spectrum exceeding that of the observations by 28% for E230M and 43% for E230H. Because of the agreement in the lower envelopes of the spectra, I conclude that this mismatch is likely caused by inaccuracy in the PHOENIX spectrum rather than in the observations. At longer wavelengths, the *HST* STIS G430M observation of ϵ Eri covering $\sim$3800 – 4100 Å agrees with the PHOENIX

spectrum to 0.2%, suggesting the accuracy of both the observations and PHOENIX output is good in that regime.

4.2.7.6 Transits

I did not attempt to avoid planet transits during observations of the MUSCLES targets to facilitate the observatory scheduling process. As a result, some observations overlap with planet transits. I checked for overlap by acquiring transit ephemerides for all hosts where these ephemerides were well established from the NASA Transit and Ephemeris Service[7] and comparing these in-transit time ranges to the time ranges of *HST* observations.

GJ 1214b transited during one of the *HST* observations: one of the three COS G160M exposures is almost fully within GJ 1214 b's geometric transit. However, the $\sim 1\%$ transit depth of GJ 1214b (Carter et al., 2011), is insignificant in comparison to the 34% uncertainty on the integrated G160M flux.

GJ 436b was undergoing geometric transit ingress at the end of the third COS G130M exposure and transit egress at the start of the fourth, according to the Knutson et al. (2011) ephemeris. The G130M exposures were sequential, broken up only by Earth occultations. Consequently, the last four of the five G130M exposures fall within the range of the extended Lyα transit that begins two hours prior and lasts at least three hours following the geometric transit and absorbs 56% of the stellar Lyα emission (Kulow et al., 2014; Ehrenreich et al., 2015). Thus, these observations should be treated as lower limits to the out-of-transit emission of GJ 436 from ions that might be present in the planet's extended escaping cloud. The geometric transit depth of GJ 436 is under 1% (Torres et al., 2008), so only an extended cloud of ions could effect the G130M spectra by an amount that is significant relative to uncertainties. I inspected the G130M data for evidence of transit absorption by measuring the flux of the strongest emission lines as a function of time and found no such evidence. However, because all exposures may be affected by an extended cloud, the lack of a clear transit dip might not be conclusive. I intend to explore the COS G130M transit

[7] `http://exoplanetarchive.ipac.caltech.edu/cgi-bin/TransitView/nph-visibletbls?dataset=transits`

data in greater depth in a future work (Loyd et al. 2017a). The reconstructed Lyα flux stitched into the panchromatic SEDs is not affected. It was created from separate STIS observations that occurred outside of transit.

4.3 Discussion

I display the primary data product of the MUSCLES survey, the panchromatic SEDs for each target, in Figures 4.5 and 4.6. I also include a spectrum of the Sun for comparison to the MUSCLES stars. The solar spectrum I present in these figures and in the discussion following is that assembled by Woods et al. (2009) from several contemporaneous datasets covering a few days of "moderately active" solar emission. I adopt a value of 1.361×10^6 erg s^{-1} cm^{-2} for the bolometric solar flux at Earth, i.e. Earth's insolation, per resolution B3 of IAU General Assembly XXIX (2015).

For a detailed discussion of emission line strengths and the correlation of fluxes from lines with different formation temperatures, see Paper I. Here I will examine the UV continuum, the degree of deviation from purely photospheric models, and photodissociation rates on orbiting planets.

4.3.1 The FUV Continuum

Hitherto, the sensitivities of FUV instruments, such as the *International Ultraviolet Explorer* and *HST* STIS, have rendered observations of anything but isolated emission lines in spectra from low-mass stars challenging. The greater effective area and lower background rate of *HST* COS facilitates observations of less prominent spectral features. Linsky et al. (2012a) used this advantage to study the FUV continua of solar-mass stars, finding that more rapidly rotating stars showed higher levels of FUV surface flux and corresponding brightness temperature.

In a similar vein, I searched for evidence of an FUV continuum in the spectra of the MUSCLES stars. Continuum regions were identified by eye through careful examination of the spectra of all 11 targets, similar to the methodology of France et al. (2014), and typically range from 0.7 to 1 Å in width. The selected regions constitute 157.9 Å of continuum spanning 1307 – 1700 Å. These

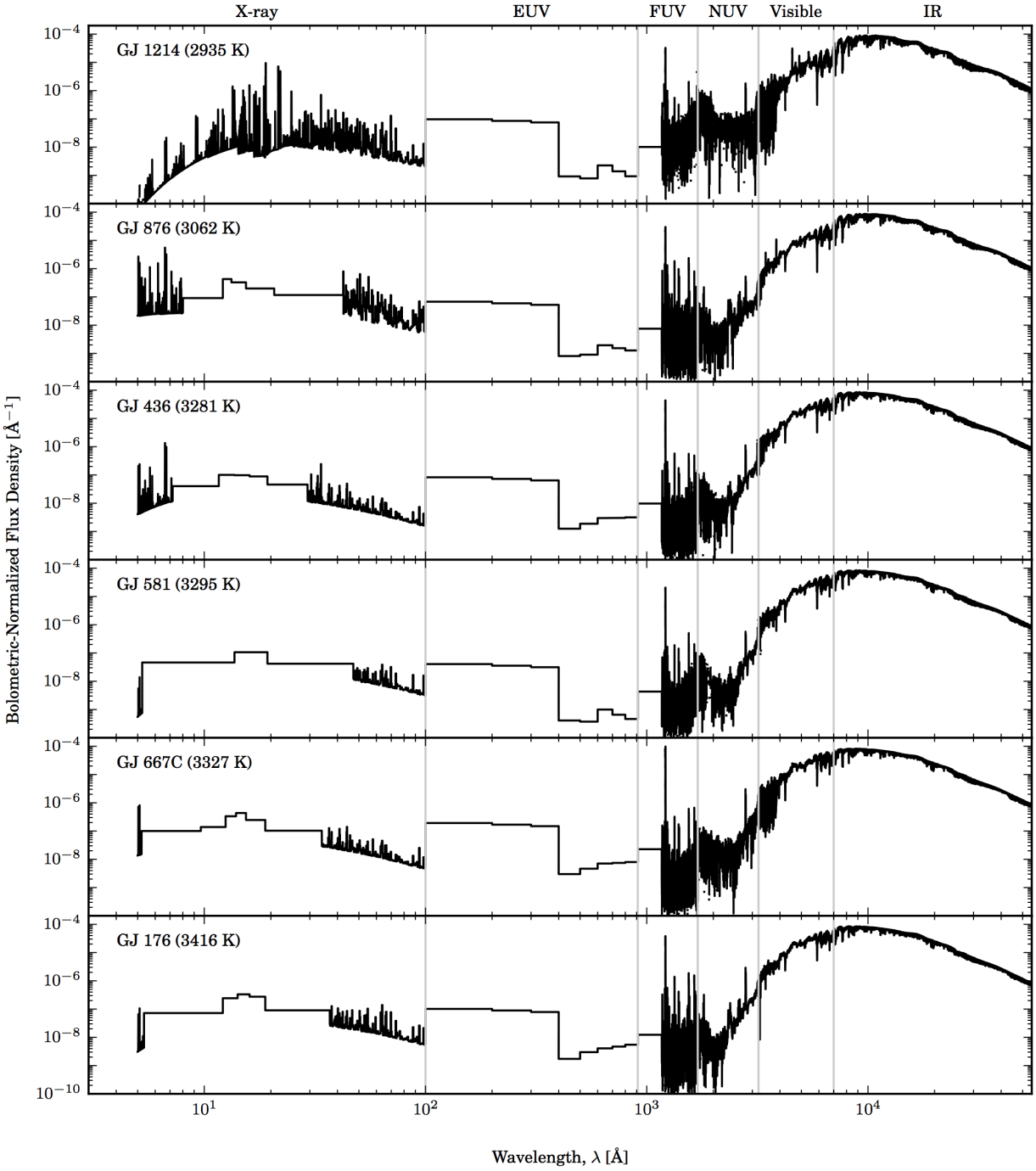

Figure 4.5 Spectral energy distributions of the MUSCLES stars, normalized by their bolometric flux such that they integrate to unity. Axes have identical ranges to facilitate comparisons, each spanning 3 – 55000 Å in wavelength and 10^{-10} – 2×10^{-4} Å^{-1} in flux density. Light gray vertical lines show the division between the spectral regions labeled at the top of the plot. The best-fit effective temperature of each star computed via the PHOENIX model grid search (Section 4.2.4) is listed in parenthesis next to its name. The normalization enables easy scaling to any star-planet distance; e.g. for an Earth-like planet, multiply by Earth's insolation, 1361 W m^{-2}.

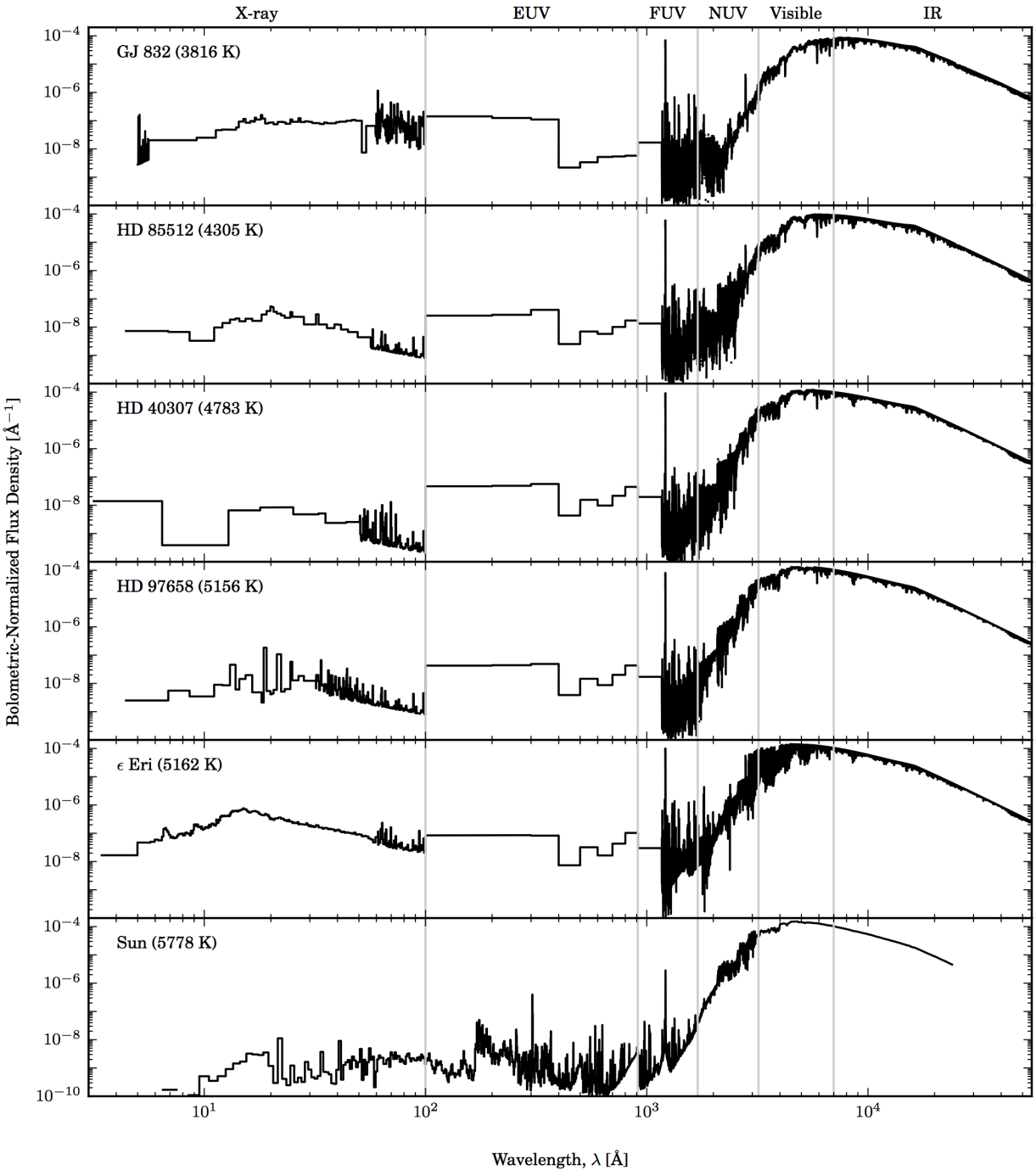

Figure 4.6 Spectral energy distributions of the MUSCLES stars, continued from Figure 4.5.

regions have a bandwidth-weighted mean wavelength of 1474.3 Å. I integrated the flux in each of these bands to create continuum spectra for the targets.

The continuum spectrum of the brightest target, ϵ Eri, is displayed in Figure 4.7. This continuum shows a shape that strongly suggests a recombination edge occurring between 1500 and 1550 Å. This is consistent with the ∼1521 Å limit of Si II recombination to Si I. Models of the solar chromosphere have predicted this edge, but it is not observed in the solar FUV spectrum (Fontenla et al., 2009), nor was it observed in the continua of solar-mass stars studied by Linsky et al. (2012a).

Data from other targets did not have sufficient S/N to show a clear continuum shape. However, by integrating the flux in all 157.9 Å of continuum bands, some level of continuum was detected at $> 3\sigma$ significance for 5/11 targets. Note that the negative values in Table 4.4 are not concerning given their large error bars. A simple detection of continuum emission does not indicate whether this emission is significant relative to line emission in the FUV. To quantify this significance, I compute the fractional contribution of the flux in the continuum bands to the total FUV flux over the full range containing the continuum bands (1307 – 1700 Å) and present the results in the last column of Table 4.4. This fraction does not account for the continuum flux present within emission line regions. Therefore, it serves as a lower limit on the total contribution of continuum within the 1307 – 1700 Å range. This contribution is at least on the order of 10% for the stars where it is detected, and where it is not detected the uncertainties do not rule out similar levels.

4.3.2 Estimating SEDs for Stars not in the MUSCLES Catalog

A means of estimating the UV SED for any star without *HST* observations would be very useful. I investigated the potential for using photometry in the GALEX FUV and NUV bands to empirically predict fluxes in other UV bands. However, the GALEX All-sky Survey (AIS; Bianchi et al. 2011) contains magnitudes for only half of the MUSCLES sample. The MUSCLES stars represent the brightest known M and K dwarf hosts. Therefore, they will be better represented than a volume-limited sample of such stars in the GALEX AIS catalog. That half do not appear

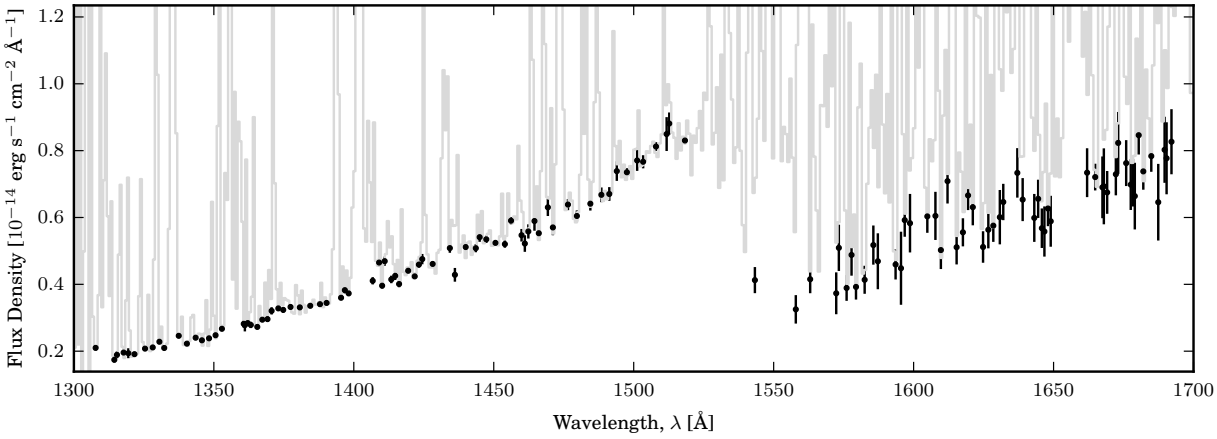

Figure 4.7 Continuum of ϵ Eri, the brightest source with the clearest continuum. Each black point is the average flux density in a continuum band. The width of each band is roughly the size of the point or smaller. The full spectrum (i.e. non-continuum) is plotted in gray in the background, rebinned to $R = 2000$ for display. The edge occurring between 1500 – 1550 Å is consistent with recombination of Si II to Si I at ∼1521 Å.

Table 4.4. FUV continuum measurements

Star	FUV Continuum Flux [erg s^{-1} cm^{-2} Å^{-1}]	Detection Significance σ	Fraction of Flux[a]
GJ 1214	$-1.2 \pm 1.1 \times 10^{-15}$	···	-0.753
GJ 876	$6.7 \pm 1.2 \times 10^{-15}$	5.7	0.080
GJ 436	$1.1 \pm 1.4 \times 10^{-15}$	···	0.082
GJ 581	$-8 \pm 13 \times 10^{-16}$	···	-0.201
GJ 667C	$1.1 \pm 1.1 \times 10^{-15}$	···	0.088
GJ 176	$4.1 \pm 1.2 \times 10^{-15}$	3.5	0.070
GJ 832	$6.4 \pm 1.1 \times 10^{-15}$	6.1	0.122
HD 85512	$6.4 \pm 5.4 \times 10^{-15}$	···	0.114
HD 40307	$8.2 \pm 4.8 \times 10^{-15}$	···	0.147
HD 97658	$1.13 \pm 0.18 \times 10^{-14}$	6.3	0.201
ϵ Eri	$8.128 \pm 0.038 \times 10^{-13}$	215.9	0.128

[a]Integral of flux within continuum bands divided by the integral of all flux over the range containing those bands.

in the catalog suggests the GALEX AIS catalog, while an excellent tool for population studies with few restrictions on sample selection, is not a generally useful tool for studies involving one or a few preselected targets. Nonetheless, I checked for a correlation of GALEX FUV magnitudes for the 6 targets in the AIS catalog with their integrated FUV flux from *HST* data and found no correlation. It bears mentioning that while most M and K dwarf planet hosts may not appear in GALEX catalogs, the GALEX survey data have proved useful both for prospecting for low-mass stars (Shkolnik et al., 2011) and population studies of these stars (Shkolnik & Barman, 2014; Jones & West, 2016).

There are other means, besides GALEX data, of estimating broadband and line fluxes for a low-mass star without complete knowledge of its SED. To this end, Paper I provides useful relations between broadband fluxes and emission line fluxes. Paper I also quantifies levels of FUV activity, taken as the ratio of the integrated FUV flux to the bolometric flux, and shows that they are roughly constant. This consistency suggests that the median ratio of FUV to bolometric flux of the MUSCLES sample would be appropriate as a first-order estimate of that same ratio for any similar low-mass star. Further, the MUSCLES spectra, normalized by their bolometric flux, can serve as rough template spectra for a low-mass star with no available spectral observations. If the star's bolometric flux is known, this can be multiplied with the template normalized spectrum to provide absolute flux estimates.

However, age is likely a factor in the consistency in FUV activity among MUSCLES targets. Age estimates are not presently available for the full MUSCLES sample; however, ages of the MUSCLES stars are likely to be consistent with other nearby field stars of similarly weak Ca II H and K flux (see Paper I). These have ages of several Gyr (Mamajek & Hillenbrand, 2008). Stars with ages under a Gyr are likely to have higher levels of FUV and NUV activity compared to the MUSCLES sample. This conclusion follows from the recent work of Shkolnik & Barman (2014) that demonstrated a dependence of excess (i.e. non-photospheric) FUV and NUV flux on stellar age for early M dwarfs. Shkolnik & Barman (2014) found that the excess FUV and NUV flux of their stellar samples remained roughly constant at a saturated level until an age of a few hundred

Myr. After this age, the excess flux declines by over an order of magnitude as the stars reach ages of several Gyr. Because of this age dependence in FUV flux, the consistency in FUV activity of the MUSCLES stars should not be taken to be representative of stars with ages under a Gyr.

4.3.3 Photodissociation

The composition of a planetary atmosphere depends on a complex array of factors including mass transport, geologic sources and sinks, biological activity, impacts, aqueous chemistry, stellar wind, and incident radiation (e.g. Matsui & Abe 1986; Lammer et al. 2007; Seager & Deming 2010; Hu et al. 2012; Kaltenegger et al. 2013). Many of these factors require assumptions weakly constrained by what is known of solar system planets. However, the MUSCLES data directly characterize the radiation field incident upon planets around the 11 host stars. This allows the use of MUSCLES data to address two top-level questions regarding atmospheric photochemistry without detailed modeling of specific atmospheres: (1) What is the relative importance of various spectral features to the photodissociation of important molecules, and (2) how does this differ between stars?

To quantitatively answer these questions, I examined the photodissociation rates of various molecules as a function of wavelength resulting from the radiative input of differing stars. Because I leave atmospheric modeling to future work, I did not introduce any attenuation of the stellar SED by intervening material. In other words, I assumed direct exposure of the molecules to the stellar flux. However, for wavelengths shortward of the ionization threshold of the molecule, I assumed that all photon absorptions result in ionization rather than dissociation. Consequently, for each molecule I ignore stellar flux shortward of that molecule's ionization threshold. Because I assumed direct exposure to the stellar flux, I refer to the photodissociation rates I have computed as "unshielded."

4.3.3.1 Method of Computing "Spectral" Photodissociation Rates

To determine "spectral" photodissociation rates, $j(\lambda)$, I multiplied the wavelength-dependent cross sections, $\sigma(\lambda)$, by the photon flux density, $F_p(\lambda)$, and the sum of the quantum yields for all dissociation pathways, $q(\lambda)$. The quantum yield of a pathway expresses the probability that the molecule will dissociate through that pathway if it absorbs a photon with wavelength λ. To wit,

$$j(\lambda) = F_p(\lambda)\sigma(\lambda)\sum_i q_i(\lambda). \tag{4.2}$$

Note that the stellar spectrum must be specified in **photon** flux density [s^{-1} cm^{-2} $Å^{-1}$] rather than energy flux density [erg s^{-1} cm^{-2} $Å^{-1}$] ($F_p = F/(hc/\lambda)$).

The photodissociation cross sections and quantum yields I used come from the data gathered by Hu et al. (2012) and presented in their Table 2, updated to include the high-resolution cross section measurements of O_2 in the Schumann-Runge bands from Yoshino et al. (1992). I extrapolated the H_2O cross section data, as is conventional, from ∼2000 Å to the dissociation limit at 2400 Å using a power-law fit to the final two available data points. The cross sections only apply to photodissociation from the ground state. I also do not include H_2 dissociation by excitation of the Lyman and Werner bands. Physically, j in Eq. 4.2 represents the rate at which unshielded molecules are photodissociated by stellar photons per spectral element at λ. Thus the units of j are $s^{-1}Å^{-1}$.

The absolute level of j is tied to a specific distance from the star since F_p drops with the inverse square of distance. For the values I present in the remainder of Section 4.3.3, I set the F_p level of each star's spectrum such that the bolometric **energy** flux ("instellation"), $I = \int_0^\infty F(\lambda)d\lambda$, was equivalent to Earth's insolation.

The dissociation rate, J [s^{-1}], due to radiation in the wavelength range (λ_a, λ_b) is then given by

$$J = \int_{\lambda_a}^{\lambda_b} F_p(\lambda)\sigma(\lambda)\sum_i q_i(\lambda)d\lambda. \tag{4.3}$$

Integrating from the molecule's ionization threshold wavelength, λ_{ion}, to ∞ gives the total dissociation rate due to irradiation from stellar photons (neglecting any dissociations from photons with

Table 4.5. Dissociation rates [s^{-1}] for unshielded molecules receiving bolometric flux equivalent to Earth's insolation.

Star	H_2 $\times10^{-7}$	N_2 $\times10^{-6}$	O_2 $\times10^{-6}$	O_3 $\times10^{-4}$	H_2O $\times10^{-5}$	CO $\times10^{-6}$	CO_2 $\times10^{-5}$	CH_4 $\times10^{-5}$	N_2O $\times10^{-7}$	O_2/O_3[a]
GJ 1214	0.36	3.3	0.86	1.2	3.2	2.6	0.7	4.2	0.82	0.0069
GJ 876	0.49	2.6	4.2	1.4	3.0	2.0	0.54	4.1	2.4	0.031
GJ 436	1.2	3.7	1.2	1.9	3.3	2.6	0.69	4.5	0.85	0.0065
GJ 581	0.18	1.4	0.59	1.5	1.6	1.1	0.3	2.2	0.34	0.0039
GJ 667C	3.1	8.9	1.6	3.0	7.6	6.2	1.6	10	1.1	0.0052
GJ 176	2.1	5.1	3.4	2.6	4.2	3.4	0.89	5.6	2.2	0.013
GJ 832	2.2	6.5	2.1	3.7	5.7	4.6	1.2	7.8	1.6	0.0057
HD 85512	6.6	8.1	1.1	5.6	3.9	4.5	1.0	5.4	1.1	0.002
HD 40307	17	17	1.1	15	5.5	8.0	1.6	7.5	1.4	0.00075
HD 97658	17	15	1.8	34	4.9	7.2	1.4	6.6	3.6	0.00052
ϵ Eri	40	33	5.0	29	8.4	15	2.7	11	5.4	0.0017
Sun	0.56	1.1	2.5	81	1.1	0.67	0.13	0.88	13	0.0003

[b]Ratio of the O_3 to O_2 dissociation rates.

sufficient energy to ionize the molecule).

To examine the importance of various spectral regions and features to dissociating a given molecule, a useful quantity is the "cumulative distribution" of j, normalized by the total dissociation rate, i.e.

$$\tilde{j} = \frac{\int_{\lambda_{\rm ion}}^{\lambda} j(\lambda')d\lambda'}{\int_{\lambda_{\rm ion}}^{\infty} j(\lambda')d\lambda'}. \tag{4.4}$$

where $\lambda_{\rm ion}$ is the ionization threshold of the molecule. Physically, $\tilde{j}$ expresses the fraction of the total photodissociation rate of a molecule that is due to photons with wavelengths between the molecule's ionization threshold and λ. This permits easy visual interpretation from plotted $\tilde{j}$ values of the degree to which a portion of the stellar spectrum is driving photodissociation of a molecule. The change in $\tilde{j}$ over a given wavelength range gives the fraction of all dissociations attributable to photons in that range. Thus, ranges where $\tilde{j}$ rapidly rises by a large amount indicate that stellar radiation with wavelengths in that range contribute disproportionately to the overall rate of photodissociation.

4.3.3.2 Comparison of Unshielded Photodissociation Rates of H_2, N_2, O_2, O_3, H_2O, CO, CO_2, CH_4, and N_2O Among the MUSCLES Stars

For all 11 MUSCLES hosts and the Sun, I have tabulated the total unshielded dissociation rate, J, of the molecules H_2, N_2, O_2, O_3, H_2O, CO, CO_2, CH_4, and N_2O in Table 4.5. I considered these molecules because of their ubiquity and biological relevance. Among the MUSCLES stars, unshielded photodissociation rates of most of these molecules range over roughly an order of magnitude. Exceptions are H_2, for which J values vary by over two orders of magnitude, and H_2O and CH_4, for which J values vary by about a factor of 5. Confining the comparison to only the 4 K stars or only the 7 M stars reduces the spread in J values, but the values still vary by a factor of a few or more. This variability between stars emphasizes the importance of spectral observations of individual exoplanet host stars to photochemical modeling.

Median unshielded photodissociation rates for the MUSCLES stars are generally a factor of a few higher than the Sun. However, one key exception to this is O_3, for which the Sun's relatively high level of photospheric flux in the NUV makes it the strongest dissociator by a factor of a few to nearly two orders of magnitude. I reserve further discussion of this molecule for Section 4.3.3.3.

To examine the wavelength dependence of unshielded photodissociation rates, I computed $\tilde{j}$ curves for three representative stars: the most active star in the MUSCLES sample, ϵ Eri; the least active star, GJ 581; and the Sun, where I define activity as the ratio of the integrated FUV flux to the bolometric flux. Before presenting plots of the computed $\tilde{j}$ curves, I first plot in Figure 4.8 the photodissociation cross sections incorporating quantum yields, $\sigma \sum_i q_i(\lambda)$, and the stellar photon flux density, $F_p(\lambda)$. The spectrum of GJ 581 had very low S/N in some areas, resulting in many spectral bins with negative flux density values due to the subtraction of background count rate estimates. Thus, for all stars I merged any negative-flux bins with their neighbors until the summed flux was above zero. This amounts to sacrificing resolution for S/N in these areas. The integrated and normalized product of the two curves in Figure 4.8 then gives the $\tilde{j}$ curves plotted in Figure 4.9. Because $\tilde{j}$ values are normalized by the overall photodissociation rate, J, for a given

input SED, Figure 4.9 does not show how J varies between stars. However, this information is available in Table 4.5.

From Figure 4.9 it is clear that, with the exception of H_2O and N_2O, the same portions of the stellar spectra drive unshielded photodissociations of each molecule. This results from the relatively small differences in the reference star SED shapes over the range of photon wavelengths capable of photodissociating these molecules.

Although similar between stars for most molecules, the $\tilde{j}$ curves reveal some intriguing structure. The dissociation of H_2, N_2, CO, and CO_2 is primarily due to flux shortward of the 1170 Å cutoff of the COS data. There is an apparent difference between the curves for the Sun versus GJ 581 and ϵ Eri in this region: The curve for the Sun shows jumps not present in the curves of GJ 581 and ϵ Eri. The jumps are caused by solar line emission that significantly dissociates these molecules. The jumps are not present in the curves for GJ 581 and ϵ Eri because these stars were not directly observed at those wavelengths. Flux in this region is instead given by the broadband estimates described in Section 4.2.2 that lack any individual spectral lines. However, it is probable that line emission from GJ 581 and ϵ Eri in these ranges will, like the Sun, be important to the photodissociation of H_2, N_2, CO, and CO_2. Similarly, note that while the CO_2 $\tilde{j}$ curves of ϵ Eri and GJ 581 show some jumps, these are due to spikes in the photodissociation cross section of CO_2 rather than structure in the ϵ Eri and GJ 581 SEDs.

For O_2, the photodissociation cross section has a narrow peak near Lyα and a broad, highly asymmetric peak at ∼1400 Å. Thus, for the low-mass stars, emission from the Lyα; Si IV $\lambda\lambda$ 1393,1402; and C IV $\lambda\lambda$ 1548,1550 lines contributes significantly to the overall photodissociation of O_2. These are weaker relative to the FUV continuum in the Sun, so instead the solar FUV continuum dominates photodissociation.

Unshielded photodissociation of H_2O is dominated by Lyα in ϵ Eri and GJ 581 and unshielded photodissociation of CH_4 is dominated by Lyα for all three reference stars. For the Sun, dissociation of H_2O is roughly evenly shared between Lyα and the 1600 – 1800 Å FUV because of weaker Lyα emission and stronger FUV continuum emission. However, when interpreting the effect of

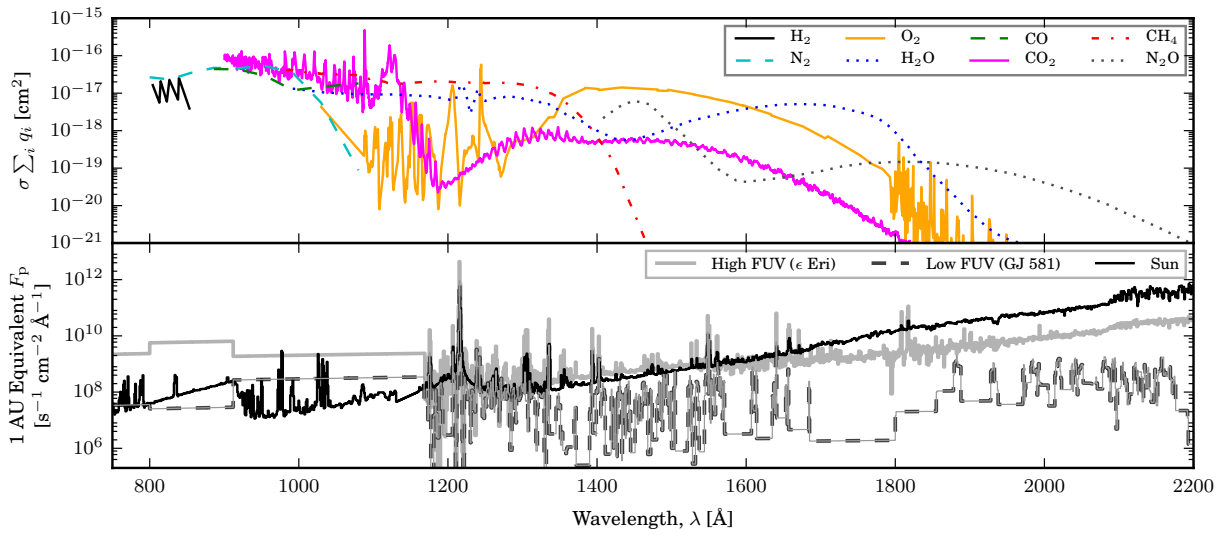

Figure 4.8 Top: Photodissociation cross sections of the examined molecules. Bottom: SEDs of the reference stars: the most active MUSCLES star (as defined by the ratio of FUV to bolometric flux), least active MUSCLES star, and the Sun, converted to photon flux density instead of energy flux density and scaled such that the bolometric energy flux is equivalent to Earth's insolation.

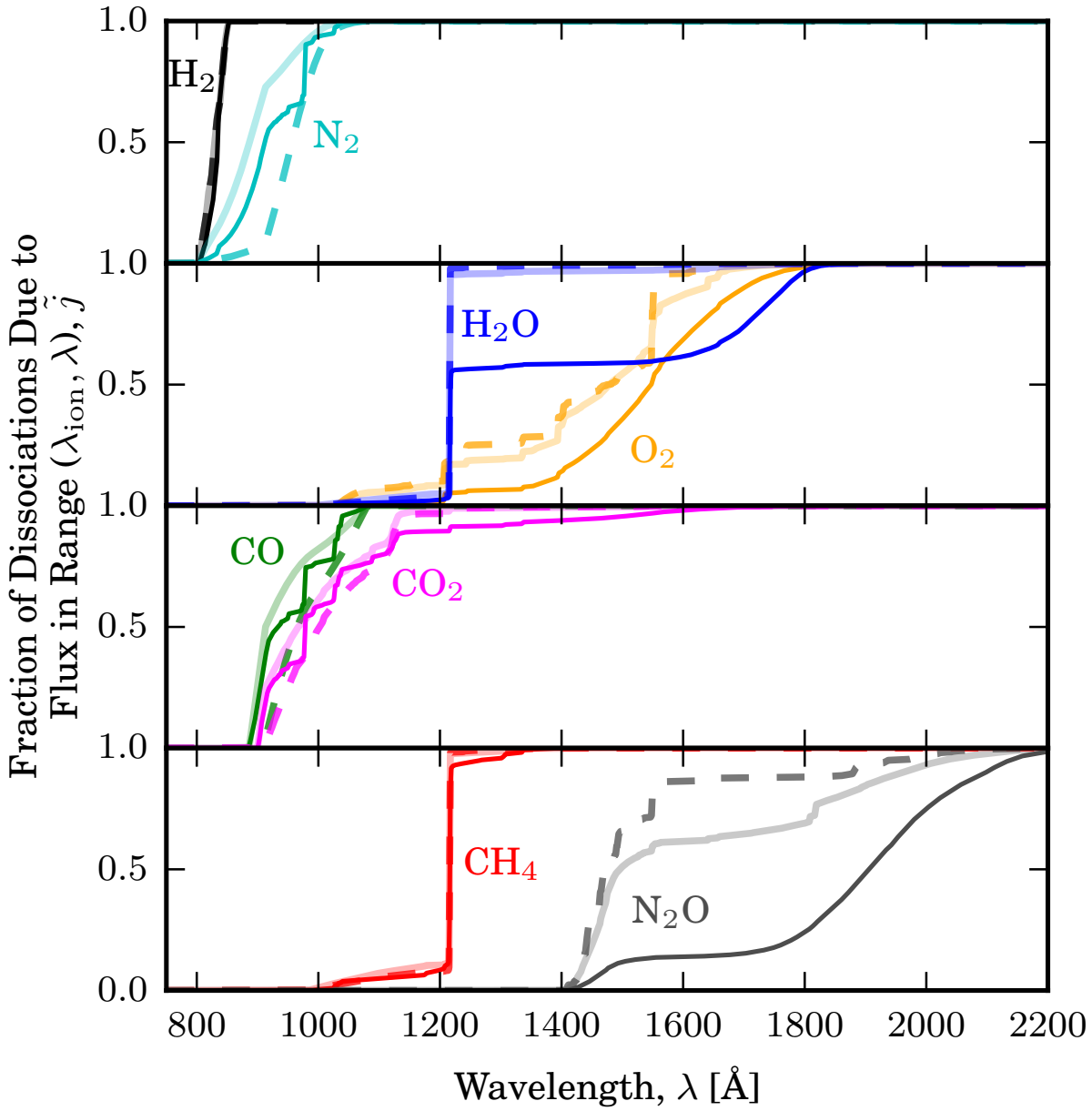

Figure 4.9 Cumulative photodissociation spectra. The curves show what fraction of the dissociation is due to photons with wavelengths from the molecule's ionization threshold (λ_{ion}) to λ. This corresponds to the product of the curves in Figure 4.8 integrated from λ_{ion} to λ and normalized by the full integral. The curve's rate of growth indicates the importance of that region of the spectrum to photodissociation of the molecule. Each molecule has three curves corresponding to the three reference stars whose spectra are plotted in the bottom panel of Figure 4.8 using the same line styles. Groups of curves are labeled by molecule and colored to match the top panel of Figure 4.8.

Lyα emission on photodissociation rates, it is especially important to consider the assumption of unshielded molecules. Lyα is significantly attenuated by only small amounts of intervening H I, H_2, H_2O, or CH_4. These species scatter and absorb Lyα so readily that their presence limits Lyα dissociation to the uppermost reaches of an atmosphere. For reference, unity optical depth for the center of the Lyα line occurs at a column density of 3×10^{17} cm^{-2} of H_2 from scattering and column densities of 7×10^{16} cm^{-2} of H_2O or 5×10^{16} cm^{-2} of CH_4 from absorption. These densities correspond to pressures of order 10^{-9} bar for planets with surface gravities close to Earth's. For an investigation of the effect of Lyα on mini-Neptune atmospheres, see Miguel et al. (2015).

Like H_2O, N_2O dissociation is driven by differing wavelength ranges when comparing the SED of the Sun with that of ϵ Eri and GJ 581. While the photodissociation cross section of N_2O peaks in the FUV at around 1450 Å, a secondary peak that is several times broader and some two orders of magnitude lower occurs in the NUV near 1800 Å. For ϵ Eri and GJ 581, flux levels are slow to rise across the region encompassing these peaks, so radiation at the 1450 Å primary peak dominates dissociations. In contrast, the solar spectrum rises very rapidly over the same range and beyond. Consequently, solar radiation from ∼1800-2100 Å dominates the dissociation of N_2O.

Overlying material will attenuate the stellar flux density at all wavelengths within an atmosphere, but the degree of attenuation varies by many orders of magnitude across the spectrum. This modifies both the overall level and the spectral content of the ambient radiation field with atmospheric depth. In turn, the shapes of the $\tilde{j}$ curves in Figure 4.9 change and values of J diminish as atmospheric depth is increased. Many atmospheric models incorporate a treatment of radiative transfer in order to address the change in the ambient radiation field with atmospheric depth and accurately incorporate photochemistry (see, e.g., Segura et al. 2005; Hu et al. 2012; Grenfell et al. 2014; Rugheimer et al. 2015). Although inapplicable within an atmosphere, the unshielded photodissociation rates I present allow a physical comparison of "top of the atmosphere" photochemical forcing as a function of stellar host and wavelength.

4.3.3.3 Abiotic O_2 and O_3 Production and the Significance of Visible Radiation in O_3 Photodissociation

The photodissociation of O_2 and O_3 is of special interest because of the potential use of these molecules as biomarkers (e.g. Lovelock 1965; Selsis et al. 2002; Tian et al. 2014; Harman et al. 2015). Significant abiotic production of these molecules is possible in CO_2-rich atmospheres through CO_2 dissociation that liberates free O atoms to combine with O and O_2, creating O_2 and O_3 (Selsis et al., 2002; Hu et al., 2012; Tian et al., 2014; Domagal-Goldman et al., 2014; Harman et al., 2015). Abiotic O_2 and O_3 generation is also possible in water dominated atmospheres from H_2O photolysis and subsequent H loss (Wordsworth & Pierrehumbert, 2014). Further, O_2 and O_3 buildup by water photolysis is especially important early in the life of a low-mass star when XUV and UV fluxes are higher (Luger & Barnes, 2015). Hu et al. (2012) found that the strongest factor controlling abiotic O_2 levels is the presence of reducing species (such as outgassed H_2 and CH_4), extending the previous work by Segura et al. (2007) to planetary scenarios with very low volcanic outgassing rates. In addition Tian et al. (2014) and Harman et al. (2015) found that the ratio of FUV to NUV flux positively correlates with abiotic O_2 and O_3 abundances. This ratio is tabulated for the MUSCLES stars in Paper I. Tian et al. (2014) and Harman et al. (2015) suggest that the dependence of abiotic O_2 abundance on the FUV/NUV ratio results from a variety indirect pathways according to the various atmospheric compositions considered.

In contrast to the indirect effect the FUV/NUV ratio has on O_2 levels, it has a direct impact on the production of O_3 in CO_2-rich or O_2-rich atmospheres. NUV photons dissociate O_3, whereas FUV photons liberate free O atoms from O_2 and CO_2 that can then combine in a three-body reaction with O_2 to create O_3.

Photodissociation rates vary among MUSCLES stars by over an order of magnitude for O_2 and O_3 (Table 4.5). As a proxy for the relative forcing to higher O_3 populations in an O_2 - rich atmosphere, I give the ratio of the unshielded dissociation rate of O_2 to O_3 in Table 4.5. Higher ratios indicate photochemical forcing towards larger O_3 concentrations through more rapid

dissociation of O_2 or less rapid dissociation of O_3. These ratios vary by factors of a few in the MUSCLES stars, with ϵ Eri standing out as having a ratio roughly an order of magnitude below the median. The Sun has comparatively weak O_3 forcing – two orders of magnitude below the median.

Interestingly, NUV flux does not dominate the dissociation of O_3 in all stars. For those with weak levels of NUV flux, visible light can play a roughly equal role. This is apparent when examining photodissociation of O_3 by the unattenuated radiation of ϵ Eri and GJ 581. Figure 4.10 shows this, plotting the photodissociation cross section of O_3, photon flux density of the reference stars, and the resulting $\tilde{j}$ curves for O_3 (akin to Figures 4.8 and 4.9). For ϵ Eri and the Sun, 2500 – 3200 Å NUV flux is responsible for the bulk of O_3 dissociation. In stark contrast, for GJ 581 about 20% of the dissociation is a result of Lyα, and visible photons are responsible for most of the remainder. The NUV flux of GJ 581, at roughly two orders of magnitude below that of the Sun and ϵ Eri, provides a minimal contribution, about 10%, to the photolysis of O_3.

Indeed, visible radiation plays an important role in unshielded photodissociation of O_3 for all of the MUSCLES M dwarfs. This pattern is depicted in Figure 4.11, comparing the ratio of O_3 photolysis from NUV flux to visible flux with the stellar effective temperature. For the M dwarfs, photospheric continuum flux is no longer a significant contributor in the NUV and visible radiation contributes as much or more than NUV flux to the photolysis of O_3. This suggests that, among M dwarf hosts, the ratio of FUV to visible flux might prove a better predictor of relative O_3 populations in planetary atmospheres than the FUV/NUV ratio.

4.3.4 A Note on Models of Stellar Atmospheres

Section 4.3.3 demonstrates the importance of including accurate levels of the stellar FUV flux in the SEDs used as input to photochemical models. When such models involve a system lacking observations of the host star, the modeler must draw from other sources to provide the necessary input SED. One such source is the several existing codes that can synthesize a stellar SED by modeling the stellar atmosphere, most notably the PHOENIX code (Hauschildt & Baron, 1999).

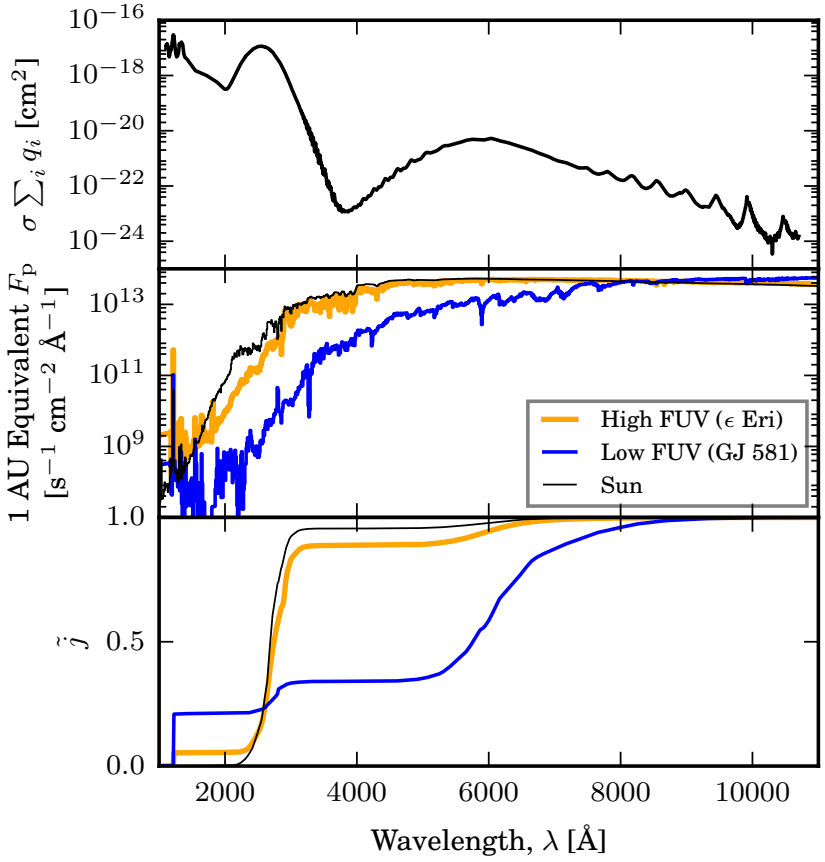

Figure 4.10 Same as Figures 4.8 and 4.9 for O_3. Top: Photodissociation cross section of O_3. Middle: Photon flux density spectra of ϵ Eri, GJ 581, and the Sun scaled such that the bolometric energy flux is equivalent to Earth's insolation. Bottom: Fraction of O_3 dissociations due to photons with wavelengths between λ_{ion} and λ if exposed to the spectra in the middle panel.

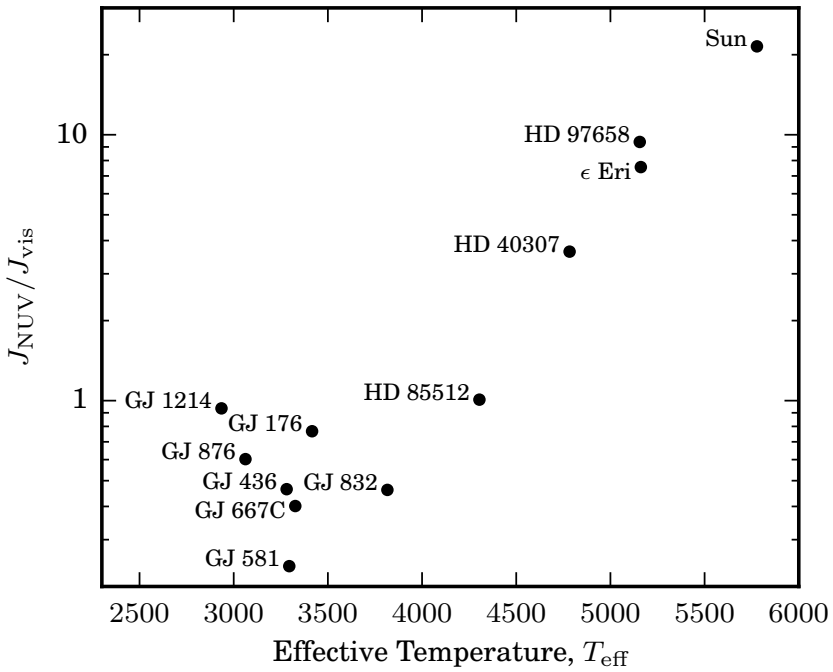

Figure 4.11 Ratio of dissociations of O_3 from NUV photons to those from visible photons if exposed to the unattenuated flux of the MUSCLES stars versus the stellar effective temperatures I estimated. Visible flux is important for all stars with $T_{\rm eff}$ under 4500 K, but this importance diminishes with increasing $T_{\rm eff}$ above 4500 K.

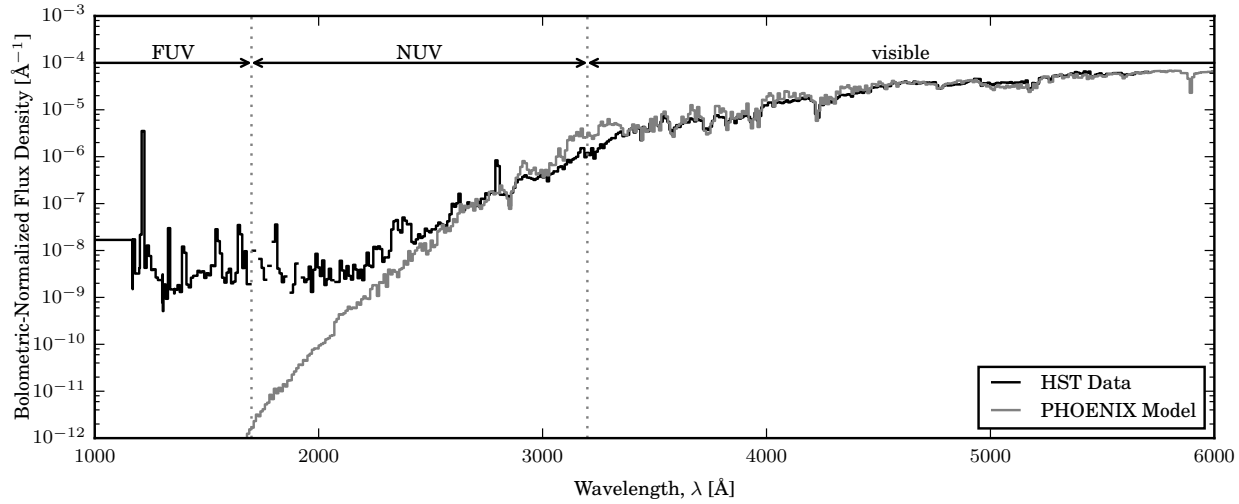

Figure 4.12 Fit of the PHOENIX model spectrum for GJ 832. The spectra are identically binned to facilitate comparison. The PHOENIX models closely track the visible spectrum measured by *HST*, but poorly predict the flux in the FUV and NUV. The discrepancy near 3200 Å dominates the integrated NUV flux, causing a factor ~ 2 overprediction of the NUV by the PHOENIX models. The PHOENIX FUV flux is negligible compared to that measured by *HST*.

However, most implementations of these codes truncate the stellar atmosphere above the photosphere. This includes the Husser et al. (2013) code that generated the spectra covering the visible and IR portions of the MUSCLES SEDs. Such photosphere-only models greatly underestimate levels of FUV flux emitted by low-mass, cool stars.

The extremity of this underestimate is illustrated in Figure 4.12 by plotting the panchromatic SED of GJ 832, incorporating the UV observations by *HST*, against the photosphere-only PHOENIX spectrum interpolated from the Husser et al. (2013) catalog. Comparing the two spectra shows that the Husser et al. (2013) PHOENIX spectrum predicts a flux lower than the observed value by three orders of magnitude or greater throughout the FUV. A similar discrepancy has been noted before for stars of mass equal to or less than that of the Sun (Franchini et al., 1998; Seager et al., 2013; Shkolnik & Barman, 2014; Rugheimer et al., 2015). Because the FUV is where the photodissociation cross sections of many molecules peak, the use of inaccurately low FUV flux levels could underpredict rates of photodissociations if, like the MUSCLES stars, most low-mass stars show levels of UV emission exceeding that predicted by photosphere-only models. Similarly, photosphere-only models are likely to underpredict EUV levels and associated heating rates in planetary thermospheres by many orders of magnitude.

The prediction of lower than observed levels of short-wavelength flux is not a oversight of the Husser et al. (2013) PHOENIX model. Rather, the Husser et al. (2013) models and most others omit the stellar upper atmosphere by design. While not common, models that attempt to reproduce emission from the stellar upper atmosphere do exist. The same PHOENIX code often used for modeling photospheric emission has also been adapted for chromospheric emission from five M dwarfs (Fuhrmeister et al., 2005) and for CN Leonis during a flare (Fuhrmeister et al., 2010). In addition, much work on chromospheric modeling has been done by the Houdebine group, beginning with Houdebine & Doyle (1994). These works focused on ground-observable NUV and visible emission, rather than the FUV emission most important to photochemistry. Alternatively, a model by Fontenla et al. (2016; submitted) reproduces much of the spectral structure of the X-ray, UV, and visible emission of the M1.5V star GJ 832, and work underway by Peacock et al. (2015)

seeks to model the same emission for a variety of M dwarf stars. Generalized to a broader range of stellar types, I expect models like this will be indispensable for the simulation of photochemistry in the atmospheres of planets orbiting stars lacking detailed observations. These models require a sample of stars with detailed UV observations for validation. The MUSCLES Treasury Survey provides this sample.

4.4 Summary

I have presented a catalog of SEDs spanning X-ray to IR wavelengths for 11 nearby, low-mass exoplanet host stars. Using these spectra, I examined the line versus continuum emission energy budget in the FUV, detecting an inter-line continuum at $> 3\sigma$ confidence for 5 stars. This revealed a likely ionization edge structure in the FUV continuum of ϵ Eri that could represent the Si II recombination continuum. I found that, when it was detected, the continuum contributed around 10% of the flux in the range spanned by the continuum bands. Uncertainties on nondetections were also consistent with this level.

Additionally, I examined photodissociation rates of the molecules H_2, N_2, O_2, O_3, H_2O, CO, CO_2, CH_4, and N_2O assuming that these species were exposed directly to the unattenuated stellar flux. I found total dissociation rates driven by different stars in the sample varied by over an order of magnitude for the majority of these molecules. By comparison, the photodissociation rates for the solar spectrum are near or below the lowest values for MUSCLES stars, except for O_3 where the solar photospheric NUV flux produces dissociation rates several times larger than the median value for MUSCLES stars. I also examined the relative importance of different spectral regions to the photodissociation of unshielded molecules driven by the SEDs of the most active host star (ϵ Eri), least active host star (GJ 581), and the Sun. There is little variation among these stars in which portion of the stellar emission is responsible for the bulk of unshielded photodissociations for most of the molecules examined. However, for O_3 I found that the dominant dissociative wavelength range can move from the NUV to the visible for low-mass stars with little NUV flux.

The spectral atlas presented in this paper, archived with MAST[8] , provides critical data for vetting stellar models and simulating photochemistry in planetary atmospheres.

[8] https://archive.stsci.edu/prepds/muscles/

Chapter 5

C II and Si III Transit Observations and Modeling of the Evaporating Atmosphere of GJ436b

Preface

In 2014, I coauthored the discovery paper of the deep Lyα transit and associated evaporating atmosphere of the hot Neptune GJ 436b (Kulow et al., 2014). This discovery was confirmed a year later with additional observations by Ehrenreich et al. (2015). As part of the Kulow et al. (2014) work, I shored up a method of approximating the escape rate of the planet based solely on a measurement of the Lyα transit depth and an estimate of the outflow velocity that was originally proposed by Linsky et al. (2010). As this derivation could be of use to future research, I have included a more detailed derivation and discussion as Chapter 5.6. However, to provide context to that derivation, I first include in this chapter my publication concerning later COS data constraining the C II and Si II transit of GJ 436b.

Abstract

Hydrogen gas evaporating from the atmosphere of the hot-Neptune GJ436b absorbs over 50% of the stellar Lyα emission during transit. Given the planet's atmospheric composition and energy-limited escape rate, this hydrogen outflow is expected to entrain heavier atoms such as C and O. I searched for C and Si in the escaping atmosphere of GJ436b using far-ultraviolet *HST* COS G130M observations made during the planet's extended H I transit. These observations show no transit absorption in the C II 1334,1335 Å and Si III 1206 Å lines integrated over [-100, 100]

km s^{-1}, imposing 95% (2σ) upper limits of 14% (C II) and 60% (Si III) depth on the transit of an opaque disk and 22% (C II) and 49% (Si III) depth on an extended, highly asymmetric transit similar to that of H I Lyα. C^+ is likely present in the outflow according to a simulation carried out using a spherically-symmetric, photochemical-hydrodynamical model. This simulation predicts a $\sim$2% transit over the integrated bandpass, consistent with the data. At line center, I predict the C II transit depth to be as high as 19%. Our model predicts a neutral hydrogen escape rate of 1.6×10^9 g s^{-1} (3.1×10^9 g s^{-1} for all species) for an upper atmosphere composed of hydrogen and helium.

5.1 Introduction

The hot Neptune GJ436b was recently found to have an escaping atmosphere producing an extended transit that absorbs 56.3% of its host star's Lyα (H I) emission (Kulow et al. 2014; Ehrenreich et al. 2015, hereafter E15; Bourrier et al. 2016, hereafter B16). This discovery classifies GJ436b as the only Neptune-mass planet among the three planets for which atmospheric escape has been observed in H I. The others, HD209458b (Vidal-Madjar et al., 2003) and HD189733b (Lecavelier Des Etangs et al., 2010) (note also a tentative detection for 55 Cnc b; Ehrenreich et al. 2012), have masses similar to Jupiter. For these two planets, atoms and ions more massive than H are also entrained in the escaping gas, specifically O I and C II, and Si III in the outflow of HD209458b (Vidal-Madjar et al. 2004; Linsky et al. 2010, though see also Ballester & Ben-Jaffel 2015 regarding Si III) and O I in the outflow of HD189733b (Ben-Jaffel & Ballester, 2013). These species produce transit depths within a factor of two of the H I transits of those planets. The escape of heavier species implies that some combination of turbulence (eddy diffusion) and "drag" exerted on the heavier species by the escaping hydrogen must be at work (e.g. Vidal-Madjar et al. 2003, 2004; Koskinen et al. 2010).

This letter presents a search for transit absorption by C II, Si III, Si IV, and N V in the escaping atmosphere of GJ436b with the G130M grating of the Cosmic Origins Spectrograph (COS) onboard the *Hubble Space Telescope (HST)*. I analyzed these data to place upper limits on transit

depths, examining simultaneous X-ray data from *Chandra* for information on stellar activity during transit. Tommi Koskinen constructed an updated 1D hydrodynamic-photochemical model of GJ436b's thermosphere that predicts H, He, C, and O escape from first principles and compared estimated transit depths with the data upper limits.

5.2 Transit Data and Analysis

5.2.1 *HST* Data

The MUSCLES Treasury Survey (France et al., 2016b) recently obtained HST observations of GJ436. Scheduling constraints, including coordinated observations by X-ray observatories, precluded any effort to time the MUSCLES observations with a transit of the star's hot Neptune. Nonetheless, three of five HST COS G130M exposures took place during the planet's extended H I transit. The broadband visible-IR (i.e. not extended) transit occurred during the portion of *HST*'s orbit when Earth occulted the target, so it was not captured. I extracted lightcurves from the time-tagged photon lists provided for each exposure with an ∼500 s cadence (adjusted to evenly divide each exposure) using the procedure outlined in Loyd & France (2014). In brief, this entailed counting weighted detector "events" in the appropriate regions of the spectrum and subtracting an estimate of background counts based on regions offset from the spectral signal trace. The event weights adjust for fixed pattern noise and detector dead time.

I created lightcurves for every strong line in the COS G130M bandpass that is not contaminated by geocoronal emission: C II 1334,1335 Å; Si III 1206 Å; Si IV 1393,1402 Å; and N V 1238,1242 Å. Si IV and N V are included for completeness, though absorption by these species is not expected due to their high formation temperatures. In creating lightcurves, I employed two separate velocity ranges over which I integrated emission line flux: The "blue integration", [-100, 30] km s^{-1}, includes the velocities predicted by the outflow model of E15, shifted to the heliocentric frame, and the "full integration", [-100, 100] km s^{-1}, includes all appreciable line flux.

Figure 5.1 displays the lightcurves, with the extended H I transit fit of E15 overplotted

for comparison. Note that the same group has presented forward modeling with separate fits for each epoch of H I transit data in B16. I computed the transit phase of the observations using the ephemeris of Knutson et al. (2011). In addition to integrated time-series, I also searched for velocity-dependent absorption by comparing a spectrum coadded from the first two exposures (pre-transit) to one coadded from the last two exposures (extended H I transit; Figure 5.2).

5.2.1.1 Correction of a Systematic Wavelength Offset

Due to the instrument configuration, *HST* COS far-ultraviolet spectra have a small gap near their midpoint. To eliminate this gap, the MUSCLES survey observations employed two central wavelength (CENWAVE) settings, shifting from CENWAVE 1291 to 1318 between orbits 2 and 3. This spuriously shifted the measured wavelength of the lines for all 10 of the other MUSCLES targets. Left unaddressed, for these observations this shift produces an artificial transit signal at blueward wavelengths for C II and Si III. To correct for this effect, I applied wavelength offsets that produced the minimum χ^2 agreement between line profiles generated before and after the shift. These values are -9 (C II), -6 (Si III), 5 (Si IV), and -6 (N V) km s^{-1}.

The CENWAVE change did not significantly influence the measured line flux relative to the statistical noise. The absolute flux accuracy of the detector is estimated to be 5% (mainly due to fixed pattern noise; Debes et al. 2016). This is reduced to the 1% level when integrating a line.

5.2.2 *Chandra* Data

Data from the Chandra X-ray Observatory was obtained in tandem with the *HST* data, providing information on stellar activity. From this data, I created a light curve of the 300 – 2000 eV photon flux (Figure 5.3). The observation was performed with the ACIS-S detector on board *Chandra*. Source photons were extracted within a circle of radius 2 arcsec and I chose a large, nearby, source-free region to correct for the detector background.

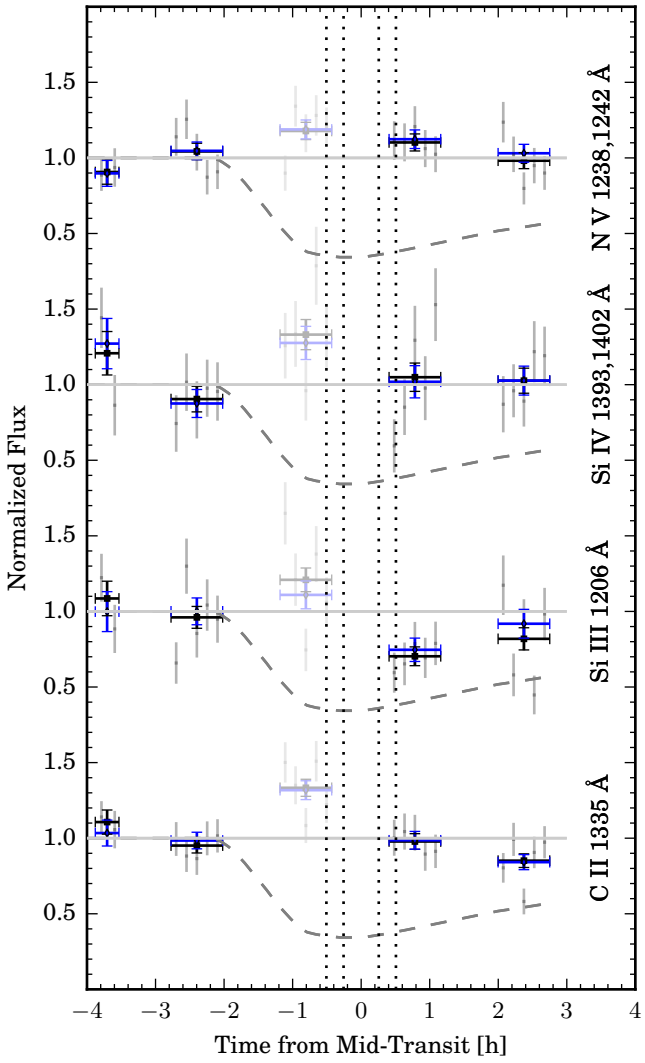

Figure 5.1 Lightcurves of line flux, normalized to the average flux from the first two exposures. Blue points represent flux integrated over [-100, 30] km s^{-1}, black over [-100, 100] km s^{-1}. Small points integrate flux over ∼500 s intervals and large points integrate the full exposures, with horizontal bars showing the exposure duration. Dashed gray lines show the E15 H I transit model. Dotted vertical lines delimit the contact points of the broadband visible-IR transit. The third exposure is faint to emphasize that I discarded it from the analysis (Section 5.2.3).

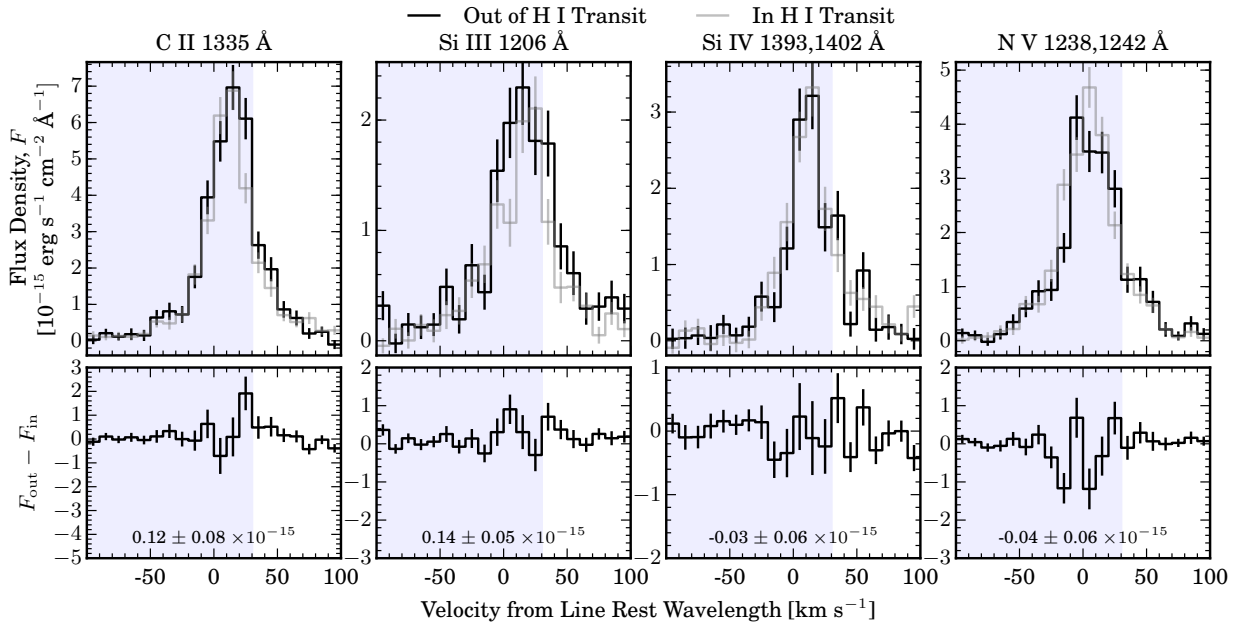

Figure 5.2 Comparison of line profiles prior to (first two exposures) and during the H I transit (final two exposures). Line wavelengths are listed above each panel, with multiple values indicating coadded lines. The spectra have been binned to 10 km s^{-1} per bin for display. The plotted wavelength range and the blue shaded area show the full and blue integration ranges used to create lightcurves. Numbers at the bottom of the lower plot give the flux difference of the full integrations.

5.2.3 Accounting for Activity-induced Variability

Limb brightening (Schlawin et al., 2010), stellar active regions (Llama & Shkolnik, 2015), or any other spatial inhomogeneities in the stellar emission can modify the shape and overall depth of a transit curve. However, for GJ436b the depth and duration of the H I transit requires a cloud that covers a large fraction of the stellar disk, diluting effects on the transit from spatial inhomogeneities in stellar emission.

Temporal fluctuations in stellar emission on short timescales contribute to lightcurve scatter. These are constrained by two orbits of archival *HST* COS-G130M data (acquired ∼14 h before transit and predating the present observations by about 2 years) to C II 3^{+1}_{-2}%, Si III <7%, and Si IV < 6% at the exposure timescale of ∼45 min (Loyd & France 2014; N V omitted in that work). I used these values to augment the lightcurve errors when exploring the parameter space of the transit models (Section 5.3).

I examined lightcurves for each line at high cadence and discovered a possible flare at ∼700 s in the first exposure, visible in C II and Si III flux. Consequently, I excised the data from 650 – 800 s for all lines.

Stellar activity is also likely responsible for an enhancement in flux from all four lines throughout the third exposure. The simultaneity of these enhancements implies a common, physical source. One possible explanation is a flare, but this signal does not exhibit sharp, closely-aligned peaks in C II, Si III, and Si IV flux like flares observed on AD Leo and other M stars (Hawley et al. 2003; Loyd & France 2014; France et al. 2016b; Loyd et al. 2017b in prep). Those flares also show responses in Si III and Si IV many times greater than in N V, unlike this instance. No clear signal is seen in the stellar X-ray emission (Figure 5.3), though a slight enhancement peaking 1 – 2 h after the FUV lines might be present. Regardless of the origin, this signal could mask the beginning of a transit absorption signal, and because it cannot be accurately disentangled from superimposed transit absorption, I omitted it from further analysis.

I speculate that this activity enhancement could result from a star-planet interaction (SPI),

such as an accretion stream from the planet. The N V flux, in particular, is well fit by a model wherein a hot-spot traverses the stellar disk at the sub-planetary point, but this fit is not significantly better than constant flux. In the full MUSCLES sample of stars, N V emission is strongly correlated with the ratio of planet mass to semi-major axis, suggesting N V might be a good tracer of SPIs (France et al., 2016b). The hot spot hypothesis could be tested by additional *HST* G130M observations spanning a face-on view of the putative spot (near transit) through its disappearance behind the viewable stellar hemisphere (quadrature).

5.3 Constraints on Transit Signals

The lightcurves (Figure 5.1) and spectra (Figure 5.2) show no apparent transit signals. In order to derive upper limits, I explored the parameter space of two transit models that represent contrasting cases from the zoo of transit shapes that could arise from the many possible ion outflow geometries (e.g. tails, bow shocks, and accretion streams; Ness 1965; Matsakos et al. 2015; Cauley et al. 2015, 2016). As one model I chose the symmetric signal produced by an opaque disk transiting a uniformly illuminated stellar disk, representing scenarios where the ions are decoupled from the H I outflow and symmetric about the projected planetary disk. At another extreme, I chose to scale the highly asymmetric H I Lyα transit curve of E15, representing scenarios where ions trail the planet in its orbit, as they would if they were coupled to the H I outflow.

The parameters of the opaque disk model are the baseline flux level and disk radius. To these I applied uniform priors for all positive values. While the data do not sample the transit of a disk equivalent to GJ436b's broadband visible-IR radius very well (contact points shown as dotted lines in Figure 5.1), the geometry of the transit is such that the disk diameter is a substantial fraction of the path of the transit across the stellar disk. Consequently, increases in transiting disk radius significantly increase transit duration as well as depth, causing the transit dip to overlap with exposure 4 and allowing that exposure to constrain the model. I account for the fact that the transit becomes grazing for radii $>1.8\ R_p$.

The parameters of the H-like model are the baseline flux, ingress time (equivalently transit

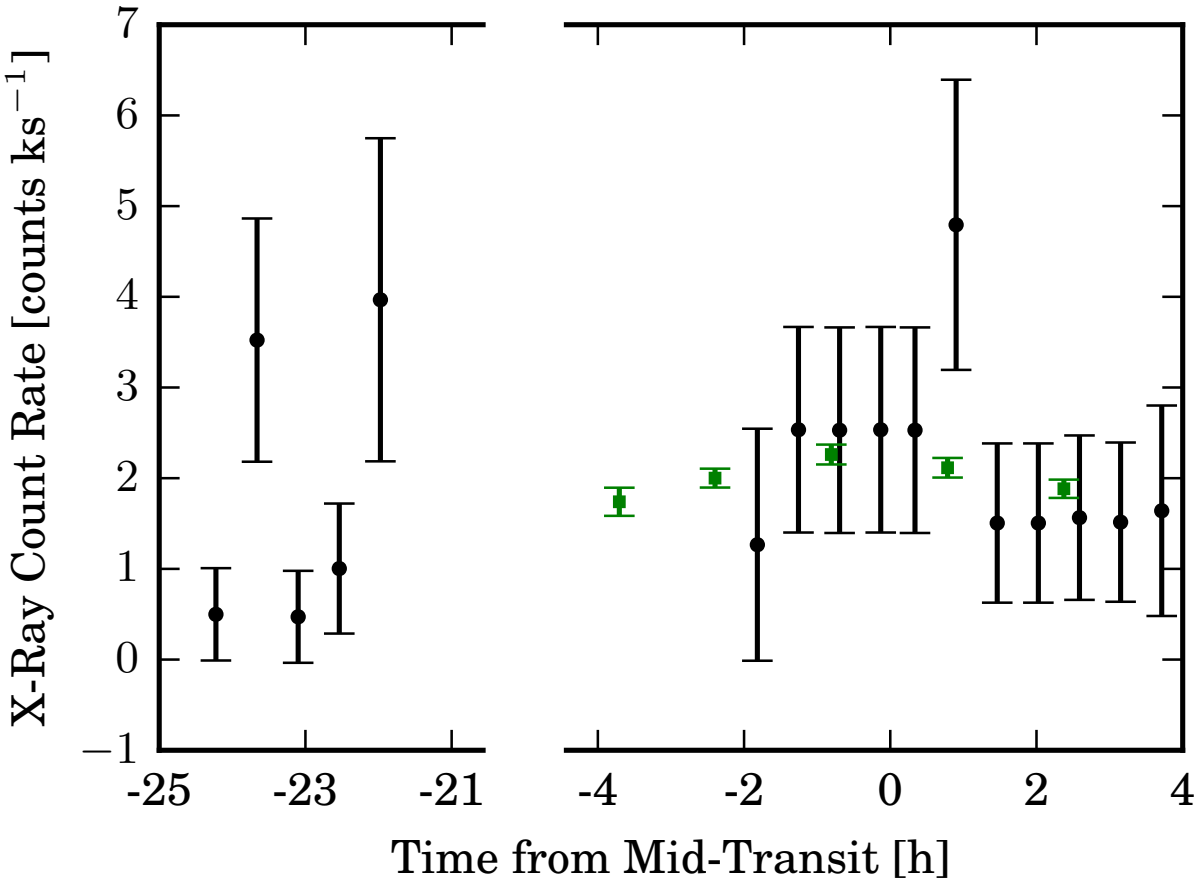

Figure 5.3 Lightcurve of the *Chandra* X-ray observations of GJ436, performed coincident with the *HST* observations. Green squares are the N V lightcurve normalized to 2 counts ks^{-1}, included for reference.

Table 5.1. Upper limit estimates on transit depth.

	Occulting Disk		H-like	
Line	Blue[a]	Full[b]	Blue	Full
C II	<14%	<14%	<23%	<22%
Si III[c]	<58%	<60%	<44%	<49%
Si IV	<51%	<43%	<31%	<25%
N V	<13%	<12%	<10%	<10%

[a]Based on blue integration ([-100, 30] km s^{-1}) lightcurve. See Section 5.2.

[b]Based on full integration ([-100, 100] km s^{-1}) lightcurve.

duration), and depth. I applied a uniform prior to all positive baseline flux values and all transit depths between zero and unity. For ingress time, I use a uniform prior that begins at the end of the first exposure to avoid hyper-extended transits that the data cannot constrain, and ends at the ingress of an equivalent opaque disk to avoid invoking contrived geometries for the absorbing cloud.

I used a Python implementation of the Markov-Chain Monte Carlo (MCMC) method, *emcee* (Foreman-Mackey et al., 2013), to sample the parameter space of these models. For all model and light curve combinations, no transit is detected. I report 95% (2σ) upper limits for each case in Table 5.1. A subset of the H-like models of particular interest consists of transits with duration fixed to that of the H I transit. I sampled this subset of models separately and found upper limits on H-like transit depth decreased by $\lesssim$2%.

The broad integration ranges I used could dilute transit absorption in narrow velocity ranges, so I searched all possible velocity ranges 5 – 100 km s^{-1} in width for absorption. To assess the significance of the absorption signals this revealed, I applied the same methodology to 10^6 trials of data simulated assuming the null hypothesis of no true absorption, only white noise fluctuations. None of the absorption signals I found were sufficient to reject the null hypothesis at $> 2\sigma$ confidence.

5.4 Model Thermosphere

5.4.1 Model Description

To interpret the upper limits on transit depth and place constraints on the mass loss rates, Tommi Koskinen simulated the thermosphere of GJ436b using an updated version of the 1D escape model of Koskinen et al. (2013b). This model solves the radial time-dependent equations of continuum, momentum, and energy simultaneously, with the ability to include several ion and neutral species. The model treats ionization, recombination, and basic photochemistry of H_2, H, He, C, O, H^+, H_2^+, H_3^+, HeH^+, C^+, O^+ and electrons. The related molecules H_2O, CO, and CH_4 and their chemistry were excluded, limiting C and O reactions to ionization, recombination, and charge exchange (excluding reactions with H_3^+ that create molecular ions). The energy equation includes heating by the absorbed stellar XUV radiation, heat conduction, adiabatic cooling and heating, vertical advection, viscous heating and radiative cooling by H_3^+ infrared emission and H recombination. Stellar gravity in the calculations to account for Roche lobe overflow effects along the substellar streamline, although these do not significantly affect mass loss from GJ436b. Magnetic fields are not considered. Though such fields would influence the flow of ions like C^+, no measurements exist for exoplanetary magnetic fields.

The lower boundary conditions for the model are pressure, temperature, altitude, and composition. Koskinen adopted 1 μbar as the lower boundary pressure. At this pressure level the T-P profile derived from secondary eclipse data (Line et al., 2014) gives a temperature of 583 K and an altitude of 3120 km. The lower boundary abundances of H_2, H, He, C and O are based on solar composition (Lodders 2003; see Section 5.4.3 for discussion) and a thermal equilibrium ratio of 0.032 for H/H_2.

The upper boundary of the model was placed at 10 R_p, well above the L1 point distance (5.8 R_p). The flow is collisional throughout the simulated range of altitudes, as verified using the Knudsen number. Linearly extrapolated upper boundary conditions on densities, velocity, and temperature that are valid above the Roche lobe and the sonic point were imposed. Koskinen

ran the model with the stellar spectrum compiled by the MUSCLES survey (France et al., 2016b; Youngblood et al., 2016a; Loyd et al., 2016) with effective energies ranging from X-rays to the dissociation threshold of H_2 near 10 eV. This spectrum has an integrated EUV flux (100-911 Å) of 870 erg s^{-1} cm^{-2} at the 0.0308 AU semi-major axis of GJ436b (Lanotte et al., 2014).

5.4.2 Model Predictions for Outflow Rate, Composition, and Transit Depths

Our model predicts an escape rate of 1.6×10^9 g s^{-1} for neutral hydrogen and 3.1×10^9 g s^{-1} for all species. This exceeds the values of 10^8 – 10^9 g s^{-1} and $2.5 \pm 1 \times 10^8$ g s^{-1} estimated by E15 and B16 from model fits to the H I transit data. Their lower escape rate estimates correspond to heating efficiencies below the 11% efficiency derived from the simulation. The escape estimate of the B16 model increases to a value agreeing with ours if they impose a fast stellar wind. However, B16 note that doing so produces a problematic fit to the transit data.

Figure 5.4 gives the temperature, outflow velocity, and composition profiles predicted by the model. The outflow velocity reaches 12 km s^{-1} at the upper boundary, consistent with other simulations of escaping atmospheres (Murray-Clay et al., 2009). This value is below the 40 – 70 km s^{-1} required by the B16 model to produce reasonable H I transit fits. B16 do not give the flow density at their lower boundary (near the Roche lobe), but Bourrier et al. (2015a) quote a density of 0.4 cm^{-3} at 4 R_p when describing the precursor to the B16 model, a value that is significantly below the calculations (see Figure 5.4).

From the density profiles provided by the simulation, rough predictions of transit depth (at mid-transit) for a given line are possible. For altitudes sampled by the stellar disk at mid-transit but beyond the model boundary, I extrapolate the outflow density profile with an inverse square law. Alternatively, applying zero density or constant density extrapolations produced roughly a factor of two difference in predicted transit depths. Beyond the planet's Roche lobe ($\sim$5.8 R_p), orbital dynamics, stellar winds, and radiation pressure influence the outflow, producing a broad and asymmetric absorption profile (see E15 and B16). To approximate modified flows, I explored a parameter space of broadened and shifted Voigt absorption profiles applied to the spherically-

symmetric density profile.

Using this procedure to investigate H I Lyα absorption, I found that absorption profiles blueshited by 20 – 40 km s^{-1} and given a FWHM of 30 – 50 km s^{-1} reproduced the ∼50% absorption observed in the [-120, -40] km s^{-1} range by E15. For C II, FWHMs of 20 – 80 km s^{-1} and no velocity shift yielded transit depths in the 1334.5 and 1335.7 Å lines of ∼2%, well below the data-imposed upper limits (Table 5.1). At the line centers, the C II transit depth could be as high as ∼19% if the absorption is narrow (10 km s^{-1}). Unlike Lyα absorption, absorption at line center for ion lines like C II is not prevented by ISM absorption. This permits observations that probe lower levels of planetary outflows than Lyα, before the flow is accelerated to velocities outside the ISM absorption profile. However, neither the S/N nor the spectral resolution of the present data is sufficient to measure an ∼19% transit over a band as narrow as 10 km s^{-1}.

An unexpected result of the model is the prediction of significant quantities of neutrals and H_2 in the outflow. H_2 at the predicted temperatures would have substantial populations in the $v = 1$ and 2 vibrational levels that have a dense forest of electronic transition lines in the FUV. This absorption could be measured against strong stellar emission lines, like Lyα, O VI 1032 Å, and C III 977 and 1175 Å by future missions with enhanced resolution and sensitivity in the FUV.

5.4.3 Limitations of the Model

The model's omission of H_2O, CO, and CH_4 could be important for GJ436b, as radiative cooling by these molecules could significantly reduce the mass loss heating efficiency of the atmosphere and thus lower the mass loss rate. This simplification was justified when applying the same model to hot Jupiters, such as HD209458b (Koskinen et al., 2013b), because detailed photochemical models predicted these molecules dissociate before reaching outflow altitudes (Moses et al., 2011; Lavvas et al., 2014), but this might not be the case for GJ436b (Moses et al., 2013). If substantial populations of these molecules are present, they could be transported into the thermosphere through turbulent mixing or collisional "drag" by rapidly escaping hydrogen, as is shown in the following paragraphs.

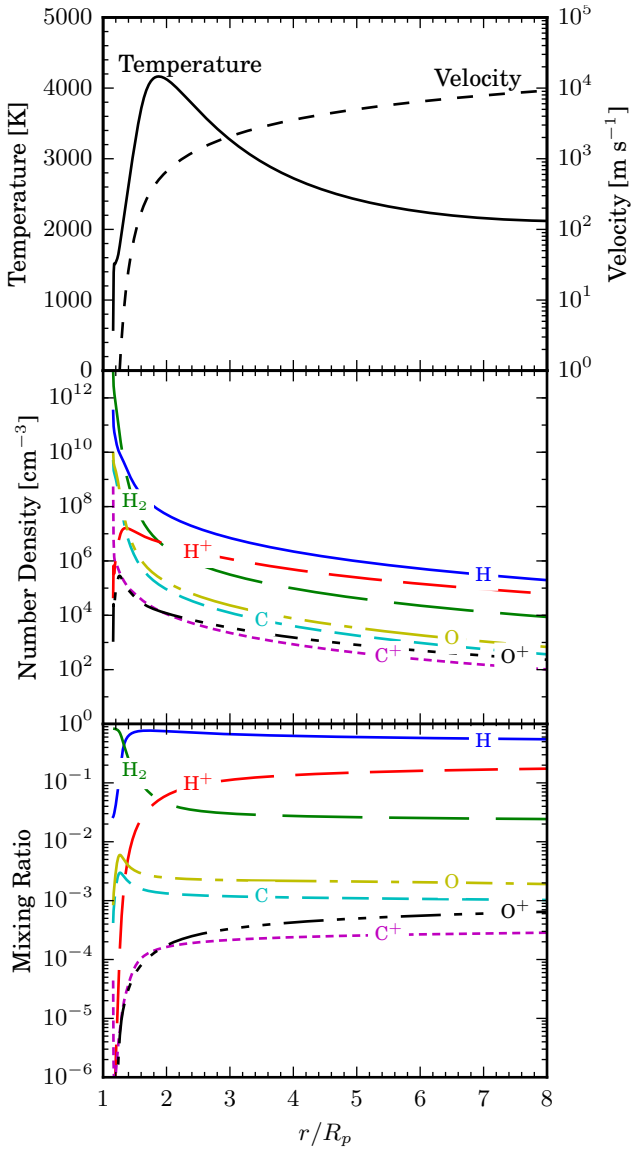

Figure 5.4 Outflow velocity, temperature, and composition of the model thermosphere as a function of height.

Turbulent mixing can be parameterized in the form of an eddy diffusion coefficient, K_{zz}. In this model, if $K_{zz} \gtrsim 10^8$ cm^2 s^{-1}, H_2O can be transported above the 1 μbar level. Estimates of K_{zz} for hot Jupiters (e.g. Moses et al. 2013) exceed this value. If similar values apply to GJ436b, then turbulence will transport molecules into the upper atmosphere.

Collisional drag can effectively transport any species with a mass below the crossover mass,

$$m_{xo} = m_H + \frac{kT\dot{M}}{4\pi nDGM_p\mu}, \tag{5.1}$$

where the quantities involved are the mass of hydrogen, m_H; Boltzmann constant, k; gas temperature, T; mass loss rate, $\dot{M}$; coefficient of diffusion between the particle and hydrogen, nD; gravitational constant, G; planet mass M_p; and mean molecular weight, μ (Hunten et al., 1987). Using the properties of the simulated outflow and the approximation

$$nD = 1.52 \times 10^{18} \sqrt{\frac{T}{\mathrm{K}} \left(\frac{1}{m_{xo}/\mathrm{amu}} + 1 \right)} \ \mathrm{cm^{-1}s^{-1}} \tag{5.2}$$

(Koskinen et al., 2013a), I find a crossover mass of 28 amu, well above the mass of H_2O and CH_4. Therefore, these molecules could be dragged along with the outflow.

The presence of molecules could be enhanced by super-solar abundances of C and O. A super-solar metallicity is necessary to explain the ratio of 3.8 μm to 4.5 μm planetary emission measured via secondary eclipse (Stevenson et al., 2010; Madhusudhan & Seager, 2011; Moses et al., 2013; Lanotte et al., 2014). However, for this work solar metallicity was used. The enhanced molecular cooling at higher metallicities could produce a shallower C II transit if it reduces the escape rate by an amount that overcomes the increased mixing ratio of C^+, producing lower C^+ column densities at a given altitude.

The addition of H_2O, CO, and CH_4 to the model and the exploration of higher metallicities is beyond the scope of this Letter, but provides motivation for future work.

5.5 Discussion and Conclusions

I found no evidence of transit absorption by C II or Si III in *HST* COS G130M observations of GJ436b. The non-detection of a Si III transit is likely due to blockage of upward Si transport by

condensation traps, namely clouds of forsterite (Mg_2SiO_4) and enstatite ($MgSiO_3$). These species have condensation curves (Fortney, 2005) that cross the T-P profile for GJ436b retrieved by Line et al. (2014). Further, Si bearing molecules are too heavy to be dragged into the upper atmosphere by escaping H. By these same arguments, Mg, another species observed in extended hot-Jupiter atmospheres (HD209458b and WASP-12b; Fossati et al. 2010; Vidal-Madjar et al. 2013; Bourrier et al. 2014, 2015b), is unlikely to be present in the upper atmosphere of GJ436b.

The data impose upper limits on C II transit depth that are well below the H I Lyα transit, unlike the hot Jupiter HD209458b (Vidal-Madjar et al., 2004; Linsky et al., 2010). To test this result, Tommi Koskinen created a simulation of GJ436b's thermosphere to predict C II populations and found them significant, yet too low to produce sufficient transit absorption for detection with the present dataset: The data-imposed upper-limits of 14% (occulting disk transit) and 22% (H-like transit) substantially exceed the model-predicted transit depth of $\sim$2%. The simulation further predicted densities of H I capable of producing the $\gtrsim$50% transit observed in previous data (E15) and an escape rate of 3.1×10^9 g s^{-1} (all species) that implies a mass loss efficiency of 11%.

The escape rate estimated exceeds the $2.5 \pm 1 \times 10^8$ g s^{-1} estimate of B16. Further, the predicted densities and outflow velocities of these models differ significantly. Future work is needed to resolve the discrepancy between the Monte-Carlo forward modeling ("top-down") approach of B16 and the photochemical-hydrodynamical ("bottom-up") approach. A thorough understanding of escape from GJ436b is of particular importance given that it is currently the sole Neptune-mass planet with a known escaping atmosphere.

5.6 Addendum: The Thin Wind Mass Loss Rate Approximation

One of the critical questions that arose when hydrodynamic escape from hot Jupiters was first observed (e.g. Vidal-Madjar et al. 2003) was whether these atmospheres were "stable" against escape. In other words, was the escape rapid enough to significantly deplete the planet's atmospheric mass over its lifetime. A clever means of estimating the order of magnitude of the mass loss rate based only on the transit depth and a spectroscopic or theoretical estimate of the outflow

velocity was suggested by Linsky et al. (2010). However, the initial derivation contained some inconsistencies, most notably an integration over the line of sight where instead an integration over the stellar disk was appropriate. I rederived this procedure with these inconsistencies corrected for use in Kulow et al. (2014). I provide the complete derivation here.

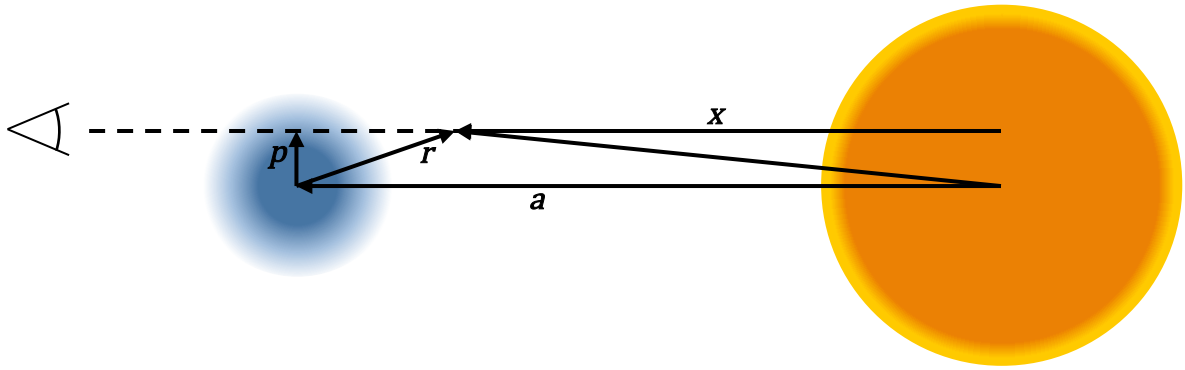

Figure 5.5 Geometry of the planetary thin wind approximation.

Assuming a spherically symmetric outflow, the mass loss rate of a gas with mean particle weight m through a shell of radius r is

$$\dot{M} = 4\pi r^2 vnm, \tag{5.3}$$

where n is the number density and v the radial velocity of the flow at r. For a basic outflow estimate, n and v must be constrained for some value of r. The route to this constraint is somewhat roundabout. To begin with, consider that the optical depth along a line of sight (LOS) to the star though the planetary atmosphere is simply

$$\tau = \sigma \int_0^\infty n(x)dx, \tag{5.4}$$

where σ is the cross section for absorption (taken to be constant over the LOS, though this is not necessarily the case) and x is the path length along the LOS. The geometry of the problem is sketched in Figure 5.5.

Combining Equations 5.3 and 5.4 yields

$$\dot{M} = \frac{4\pi m\tau}{\sigma}\left[\int_0^\infty \frac{dx}{vr^2}\right]^{-1}. \tag{5.5}$$

In the LOS integral on the right hand side, the values of v where r is smallest receive the most weight. Therefore, for an order-of-magnitude estimate, v can be taken to be constant at a value representative of its value near $r = p$, the closest approach of the LOS to the planet. This enables an analytical solution to the integral. Noting from the sketch of the geometry that $r^2 = (x-a)^2 + p^2$, where a is the star-planet separation,

$$\int_0^\infty \frac{dx}{r^2} = \frac{\pi}{2p} + \frac{1}{p}\arctan(a/p). \tag{5.6}$$

Assuming $a/p > a/R_\star \gtrsim 5$, $\arctan(a/p)$ can be taken to be $\pi/2$ to good accuracy. Thus,

$$\int_0^\infty \frac{dx}{r^2} \approx \frac{\pi}{p} \tag{5.7}$$

and

$$\dot{M} \approx \frac{4pvm\tau}{\sigma}. \tag{5.8}$$

This has recast the problem such that an estimate of the optical depth and outflow velocity at some characteristic distance are needed. The absorption cross section will be known, at least roughly, for the absorption line being observed. For example, for Lyα Doppler broadened with $b = 50$ km s^{-1} in

$$\Delta\nu_D = \frac{b}{\lambda} = \frac{\nu_0}{c}\sqrt{\frac{2kT}{m_H} + v_{\rm turb}^2}, \tag{5.9}$$

σ at -50 km s^{-1} from line center is 6×10^{-15} cm^2.

The final piece of the puzzle is to relate Equation 5.8 to the transit depth. The transit depth for a planet centered on the stellar disk is given by

$$\delta = \frac{2}{R_\star^2}\int_0^{R_\star} p(1 - e^{-\tau(p)})dp. \tag{5.10}$$

If the planet is significantly offset from the stellar center at mid-transit (i.e. it has a high impact parameter), then this integral must be done more carefully. Assuming that the transition from an

optically thick to thin cloud is abrupt relative to the size of the stellar disk (a shaky but necessary assumption), the integral can be split piecewise into an integrals over the areas in which $\tau \gg 1$ and $\tau \ll 1$. Then

$$\delta = \frac{2}{R_\star^2} \int_0^{R_{\rm opaque}} p dp + \frac{2}{R_\star^2} \int_{R_{\rm opaque}}^{R_\star} p\tau dp. \tag{5.11}$$

In the simulations of Murray-Clay et al. (2009), the optically-thick portion of the escaping cloud makes up just a fraction of the total transit depth. Therefore, as an order-of-magnitude estimate the integral can simply be replaced with

$$\delta \approx \frac{2}{R_\star^2} \int_0^{R_\star} p\tau dp, \tag{5.12}$$

which I call the "thin wind" approximation. Substituting Equation 5.8 yields

$$\delta \approx \frac{1}{R_\star^2} \frac{\dot{M}\sigma}{2m} \int_0^{R_\star} \frac{dp}{v}. \tag{5.13}$$

Again referring to the simulations of Murray-Clay et al. (2009), v is constant over most radii covering the stellar disk (and is of order 10 km s^{-1}). Therefore, v can be taken as independent of p to compute the integral, yielding

$$\dot{M} = \frac{2\delta R_\star m v}{\sigma}. \tag{5.14}$$

Chapter 6

FUV Flares on M Dwarfs

Preface

The following chapter is in preparation for submission to *The Astrophysical Journal* under the title "The MUSCLES Treasury Survey V: FUV Flares on Active and Inactive M Dwarfs."

Abstract

M Dwarfs stars are known for their elevated rate of flaring in comparison to earlier spectral types. High energy radiation from these flares will impact the climate of orbiting planets through atmospheric chemistry and escape. Therefore, it is important to determine the flare behavior of M dwarfs at short wavelengths, particularly for "typical" exoplanet hosts that do not exhibit anomalous activity indicators. I have conducted a flare survey of 7 such M dwarfs from the recent MUSCLES survey, as well as 4 highly active M dwarfs with archival data. I found that 6/7 of the "inactive" stars flared, with some exhibiting flux increases and relative integrated energies (equivalent durations) matching or exceeding those of the active star sample. When these flares were aggregated to create a flare frequency distribution, inactive star flare rates in absolute energy were about an order of magnitude below the active stars, but in relative energy the two distributions are statistically identical. A power-law fit yields an index of -0.7 for the cumulative distribution of the equivalent duration of all flares. This fit suggests that flares likely dominate the FUV energy budget of M dwarfs, assuming it can be extrapolated to flare energies that have been observed in more comprehensive broadband surveys. I used the flare sample to create a fiducial flare energy

budget for use in atmospheric simulations that I make available to the community. Applied to our own simulation of impulsive photochemistry, I find that the observed flares have little effect on an Earth-like atmosphere, but at energies a factor of 10^2 beyond the observed flares ozone depletion becomes significant and at a factor of 10^4 beyond the observed flares ozone is almost fully dissociated. However, I estimate that recombination rates are likely high enough to rapidly re-equilibrate the atmosphere in the absence of other chemical factors.

6.1 Introduction

Exoplanet science is swiftly advancing toward an answer to the question "How (a)typical is Earth?" Results from the *Kepler* mission have shown that roughly 10-60% of F – M stars harbor a planet orbiting in the liquid-water habitable zone (e.g. Traub 2012; Gaidos & Mann 2013; Dressing & Charbonneau 2015). Planets the size, mass, and effective temperature of Earth are, therefore, common. What remains to be learned is whether Earth's climate is common as well.

The climactic evolution of a planet depends, ultimately, on its space environment. If most terrestrial planets in the habitable zone (hereafter "temperate" planets) orbited Sun-like stars, there might be little doubt about their clemency. However, most temperate planets do not orbit such stars. Rather, they orbit M dwarfs – a consequence of the plurality of M dwarfs (Henry et al., 2006; Bochanski et al., 2010) and the weak, possibly inverse, relationship between planet occurrence rates and stellar mass (Howard et al., 2012; Fressin et al., 2013).

The prevalence of M dwarfs, in concert with several detection biases favoring their planets, places them in the limelight of exoplanet science now and through the next decade (Shields et al., 2016). Recent work has sought to characterize the space environment provided by these stars. Shkolnik & Barman (2014) used *GALEX* survey data to explore the evolution of M dwarf ultraviolet activity with age, finding saturated activity to 0.1 – 1 Gyr followed by a t^{-1} decline. The MUSCLES Treasury Survey (France et al., 2016b) used X-ray and UV observations of known M dwarf planet hosts combined with reconstructions of the unobservable EUV and Lyα wavelengths (Youngblood et al., 2016b) and model photosphere spectra to create a library of panchromatic

SEDs for use in atmospheric modeling (Loyd et al., 2016). Prominent among the potential barriers to habitability for temperate planets orbiting M dwarfs is the vigorous flaring of these stars relative to the Sun (Segura et al., 2010; Airapetian et al., 2017). These works have characterized the long-term evolution and present state of the high-energy radiation environment provided by M dwarfs to their orbiting planets. A remaining unknown is the short-timescale volatility of this radiation, i.e. stellar X-ray and UV flares.

The UV contributes only negligibly to a star's radiative energy budget, but it has a vastly disproportionate impact on a planetary atmosphere. The extreme UV (EUV, 100 – 912 Å) ionizes and heats atmospheric gas down to roughly the nanobar level, powering thermal atmospheric escape (e.g. Koskinen et al. 2013a; Murray-Clay et al. 2009). For close-in planets, the rate of energy deposition can be sufficient to power "planetary winds" that eject enough gas as to be easily observed (e.g. the hot-Neptune orbiting the M dwarf GJ 436; Kulow et al. 2014; Ehrenreich et al. 2015). At longer wavelengths than the EUV, the far and near ultraviolet (FUV and NUV) dissociate and heat atmospheric gas down to roughly the millibar level, resulting in nonthermal chemistry (i.e. photochemistry) such as produces the stratospheric ozone of Earth.

The direct effects of the UV on the evolution and current state of a planet's atmosphere make observations of flares in the UV critically important. However, the EUV is inaccessible from Earth due to absorption by the ISM and the FUV and NUV are accessible only above Earth's atmosphere, presently with *HST* alone. As such, most UV flare observations have been limited to single targets that are known for exhibiting spectacular flares. These have made invaluable contributions, including panchromatic flare data for the M dwarfs AD Leo and EV Lac (Hawley et al., 2003; Osten et al., 2005). Other wavelength regimes, namely the visible and infrared, have recently benefited from time-domain survey missions, such as *MOST* and *Kepler*. The massive statistical sample provided by *Kepler* has confirmed that a greater fraction of M dwarfs exhibit flares detectable in the broadband visible than sun-like stars (Davenport, 2016).

In this work, I use the data from the Measurements of the Ultraviolet Spectral Characteristics of Low-Mass Exoplanet host Stars (MUSCLES) Treasury Survey to provide the first statistical

constraints on the ultraviolet and X-ray flaring behavior of a sample of M dwarf exoplanet host stars. I begin by describing the dataset and methods for detecting and characterizing flares in Section 6.2. I then describe the population of observed flares, including their frequency-energy distribution, in Section 6.3. The flares are then brought to bear upon planets in Section 6.4, with estimates and discussion of their photodissociative and photoevaporative power as regards planetary atmospheres. The conclusions of the work are summarized in Section 6.5.

6.2 Data and Reduction

6.2.1 Observations

I conducted the flare analysis primarily on two stellar populations, the MUSCLES M dwarfs and the well-known M dwarf flare stars AD Leo, Prox Cen, EV Lac, and AU Mic. I included the MUSCLES K stars (only one of which shows clear flares) as well, but primarily for comparison purposes, and they are not extensively discussed. The sample stars and selected properties are given in Table 6.1.

The MUSCLES Treasury Survey, *HST* observing program 13650, obtained photon-counting (TIME-TAG mode) FUV data using the COS G130M spectrograph for 5 *HST* orbits per target ($\sim$3.5 h of exposure within a span of $\sim$8 h), with the specific intent of monitoring stellar variability. I augmented these data with all available FUV COS and STIS TIME-TAG data in the *HST* archive on the MUSCLES targets. However, I discarded exposures where lines in the integrated spectrum were indistinguishable from noise, such as the archival STIS E140M data of GJ 581. These data were obtained by observing programs 12034, 12035, 12464, and 13020.

The MUSCLES survey also obtained contemporaneous and occasionally simultaneous X-ray data for the targets. For GJ 176, GJ 436, GJ 581, GJ 667C, and GJ 876, these observations were made with *Chandra X-ray Observatory* (*CXO*; proposal 16200943) using the ACIS-S instrument. For GJ 832, ϵ Eri, HD 85512, and HD 40307 the survey employed *XMM-Newton* (observation 0748010201) with the EPIC instrument instead. These observations varied from 2.8 to 5.6 h. No

Table 6.1. Selected properties of the stars in the sample.

Star	Type[a]	$T_{\rm eff}$ [K]	ref	$P_{\rm rot}$ [day]	ref	W_λ Ca II K [b] [Å]	Known[c] Planets
GJ 876	M5.0	3129 ± 19	1	87.3 ± 5.7	2	0.82 ± 0.15	4
GJ 581	M5.0	3442 ± 54	3	132.5 ± 6.3	2	0.36 ± 0.08	3
GJ 1214	M4.5	2817 ± 110	4	54.9	5	1.2 ± 0.2	1
GJ 436	M3.5	3416^{+54}_{-61}	6	39.9 ± 0.8	2	0.58 ± 0.07	1
GJ 176	M2.5	3679 ± 77	1	39.3 ± 0.1	2	1.76 ± 0.27	1
GJ 832	M1.5	3416 ± 50	7	45.7 ± 9.3	2	0.88 ± 0.09	2
GJ 667C	M1.5	3445 ± 110	4	103.9 ± 0.7	2	0.44 ± 0.11	5
HD 85512	K6.0	4400 ± 45	8	45.9 ± 0.4	2	···	1
HD 40307	K2.5	4783 ± 77	8	31.8 ± 6.7	2	···	5
ϵ Eri	K2.0	5049 ± 48	8	11.7	9	···	1
HD 97658	K1.0	5170 ± 50	10	38.5 ± 1.0	11	···	1
Prox Cen	M5.5	3098 ± 56	12	82.5	13	13.7 ± 5.9	1
EV Lac	M4.0	3325 ± 100	14	4.4	15	14.9 ± 2.5	0
AD Leo	M3.0	3414 ± 100	14	2.6	15	11.6 ± 1.6	0
AU Mic[e]	M1	3650	16	4.85 ± 0.02	17	12.1 ± 2.2	0
HD 103095	K1	4950 ± 44	18	$32.2^{+0.8}_{-0.4}$	18	···	0

[a]Spectral types taken from SIMBAD, `http://simbad.u-strasbg.fr/simbad/`.

[b]All Ca II K equivalent widths from (Youngblood et al., 2017).

[c]Planet count retrieved from NASA Exoplanet Archive, `https://exoplanetarchive.ipac.caltech.edu`.

[d]As categorized in SIMBAD. Data from these stars is archival; they were not included in the MUSCLES survey.

[e]Pre main-sequence star.

References. — (1) von Braun et al. 2014; (2) Suárez Mascareño et al. 2015; (3) Boyajian et al. 2012; (4) Neves et al. 2014; (5) Newton et al. 2016; (6) von Braun et al. 2012; (7) Houdebine 2010; (8) Tsantaki et al. 2013; (9) Donahue et al. 1996; (10) Van Grootel et al. 2014; (11) Henry et al. 2011; (12) Demory et al. 2009; (13) Kiraga & Stepien 2007; (14) Houdebine et al. 2016; (15) Hempelmann et al. 1995; (16) McCarthy & White 2012; (17) Messina et al. 2011; (18) Marsden et al. 2014

observations of GJ 1214 or HD 97658 were obtained.

For the flare stars, all FUV data are archival, and I did not retrieve any archival X-ray data. A previous survey of flares in the archival *HST* FUV data exists (Loyd & France, 2014). That work focused on constraining variability in the FUV to assess their impact on transit observations. In comparison, the present work is devoted to the flares themselves and their contribution to the space environment to which planets are exposed. I have reanalyzed the archival data using the methods presented here to ensure homogeneity. The retrieved data were obtained by observing programs 7556, 8040, 8613, 8880, and 9271.

6.2.2 UV Lightcurve Creation

For the COS and STIS UV data, I created lightcurves over a given bandpass using the process described in (Loyd & France, 2014). In brief, this involves binning detector events within a ribbon covering the signal trace over the desired wavelengths. Regions offset from the signal trace at the same spectral location are used to make an estimate of the background count rate that is then scaled according to area and subtracted from the signal count rate. The flux calibration from the full exposure is then applied to the sub-exposure count tallies to create a fluxed lightcurve. I did not attempt a subtraction of the continuum because it is negligible for these cool stars in the FUV. The lightcurves all contain $\sim$45 min gaps between sequences of exposures due to regular occultations of the target by Earth during *HST's* orbit. These are noteworthy because they frequently truncate the beginning or end of a flare.

The photon-counting data allow lightcurve bandpasses to be defined arbitrarily within the limits of the spectrograph bandpass and resolution. Wavelength uncertainties are well below the bandpass width for medium-resolution gratings used for the bulk of this work. For each exposure, I adjusted the count wavelengths by using strong emission lines to define a wavelength offset that was a linear function of wavelength (or a constant offset when only a single reference line could be used), thus removing the stellar radial velocity and mitigating some systematic errors in the instrumental wavelength solution.

For emission lines, I used bandpasses of 400 km s^{-1} intended to capture all of the line flux with limited contamination from the surrounding continuum and adjacent lines. I also defined broad bandpasses encompassing all flux captured by various instrument configurations, omitting regions contaminated by airglow and detector edges that are inconsistently covered due to instrument dithering. Of these, the band covered by the greatest quantity of exposure time is the COS G130M bandpass, which is a subset of the STIS E140M bandpass. This extends from ∼1170 – 1425 Å, and I label it FUV$_{130}$. When I wished to include ϵ Eri in broadband FUV measurements I further restricted this bandpass to the ∼1330 – 1425 Å range, labeled FUV$_{140}$. This is necessary because segment B of the COS G130M spectrograph that covers shorter wavelengths was held at a lower high-voltage setting and did not record data during the ϵ Eri observations, a necessary step to ensure detector safety against that star's bright Lyα emission.

6.2.2.1 "Count-binned" Lightcurves

Because the STIS and COS detectors are photon counters, there is great flexibility in the spectral and temporal binning of the data. I have utilized this flexibility to create lightcurves where the time-binning changes in accordance with the flux to maintain a roughly constant S/N. I do this by measuring the time taken for a set number of events to occur rather than counting the number of events during a set interval, leading us to call these "count-binned" lightcurves. These lightcurves are useful for visually examining flares and measuring their peak flux and FWHM. However, the statistical distribution this method produces has a greater skew than the corresponding Poisson distribution, so I do not use these lightcurves for identifying or integrating flares.

6.2.3 X-ray Lightcurve Creation

Similar to the UV lightcurve creation, X-ray lightcurves were created by integrating all detector events within a signal region and subtracting area-corrected event counts from a nearby background region, chosen to be devoid of other sources. Events of all recorded energies within the detector bandpass were integrated. The *CXO* ASIS-S bandpass is roughly 1 – 40 Å and the

XMM-Newton EPIC bandpass is roughly 1 – 80 Å. In keeping with convention, I did not flux these count rates, due uncertainties and possible confusion in the energy of the photon(s) causing a given detector event.

6.2.3.1 Flare Identification

I developed an automated process for identifying flares. Although the data are few enough to permit a by-eye search for flares, I desired consistency in the treatment of all datasets and the ability to rapidly reanalyze the data following upstream changes to the pipeline.

Many of the largest, clearest flares have complex shapes that differ substantially from the canonical shape of an impulsive rise followed by exponential decay. Therefore, I specifically designed our pipeline to be agnostic to the flare shape. The pipeline identified flares based on the area of "runs," consecutive points above and below a smoothed version of the lightcurve. The median area of the negative runs was taken to represent the expected area of a run caused by statistical and astrophysical noise. Positive runs with areas significantly above (usually about 10×) this value were then identified as flares. The process was iterated, excluding the identified flares from the lightcurve smoothing, until no further flares were identified. Figure 6.1 shows the end result of applying this algorithm on the final three exposures of the GJ 876 data. More details on the flare identification are provided in Appendix B.1.

6.2.4 Flare Metrics

For the purpose of looking for trends, I compute several metrics for each flare. Though mostly straightforward, there are some subtleties to their computation. Characterizing the flare requires an estimate of the contribution of the star's quiescent flux throughout the flare. I estimate this by rectifying the final version of the lightcurve smoothed without the flares (see Section 6.2.3.1) onto the locations of the lightcurve points within the flares.

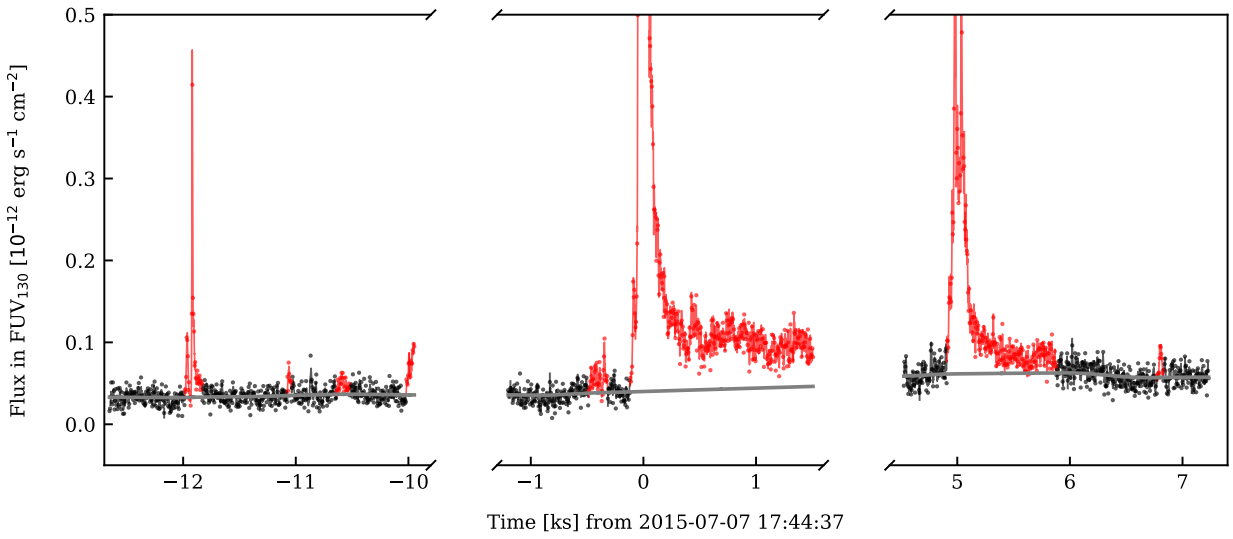

Figure 6.1 Example identification of flares in three exposures of the GJ 876 data using the FUV_{130} bandpass. Points show the lightcurve binning used in the identification process (Section 6.2.3.1). The thin underlying line is a "count-binned" lightcurve (see Section 6.2.2.1). The thick overlying gray line shows the estimate of quiescent flux created by smoothing the quiescent points.

6.2.4.1 Peak Flux

I use lightcurves count-binned to 100 counts to measure the flare peak. This mitigates the chances that the peak flux will be underestimated because it was not temporally resolved. In some cases, the count rate is too low for the count-binned lightcurve to adequately sample the flare. When this occurs, I use the same time-binned lightcurve used to identify the flare to compute the peak flux. The STIS data show a high-frequency signal with a period of a few tenths of a second that I believe is instrumental. Therefore, I do not allow bins less than 1 s for these data. X-ray data were not count binned; time-binned lightcurves were used for all X-ray flare characterization.

6.2.4.2 Full Width at Half-Maximum (FWHM) and Multipeaked Classification

As with the peak flux, I again use a count-binned lightcurve to compute the FWHM of the FUV flares. Measuring the FWHM is complicated by noise and secondary peaks that cause the lightcurve to cross the half-max flux value many times. To mitigate this, I take the FWHM to be the sum of all time spans in which flux was above the half-maximum value during the flare, including secondary peaks.

6.2.4.3 Absolute Energy and Equivalent Duration

I computed the absolute energy of the flare, E, as

$$E = 4\pi d^2 \int_{\text{flare}} (F - F_q) dt, \tag{6.1}$$

where d is the distance to the star, F is the measured flux, and F_q is the estimated quiescent flux. I do not estimate bolometric flare energies in this work, so all discussions of energy are tied to specific bandpasses. The equivalent duration, δ, of a flare is essentially a measure of this energy normalized by the quiescent luminosity of the star in the same bandpass. It is analogous to the equivalent width of a spectral line, occasioning the use of the term "photometric equivalent width." In this analogy, the flare substitutes for an emission line and the quiescent lightcurve substitutes

for the the spectral continuum. Mathematically,

$$\delta = \int_{\text{flare}} \frac{F - F_q}{F_q} dt. \tag{6.2}$$

Hawley et al. (2014) include a useful schematic of this value as their Figure 6. For the X-ray data, I did not compute absolute energies since I did not create fluxed lightcurves.

6.3 The Flares, Characterized

6.3.1 Catalog of FUV Flares

All but one M dwarf observed as part of the MUSCLES program flared during the observations. The one exception, GJ 1214, was too dim to enable the detection of minute-timescale flares like those observed on the other targets. Of the four K dwarfs, only ϵ Eri flared. I have created a catalog of all the flares observed in the FUV_{130} band and present the 20 flares with the largest δ_{130} in Table 6.2. The total number of flares detected and fraction of energy emitted in flares versus quiescence are tabulated by star in Table 6.3. I have plotted two example flares with large equivalent durations and high S/N in Figures 6.2, 6.3, and 6.4, showing the evolution of the flare in the broad FUV_{130} band, all major lines, and a compendium of narrow continuum bands hand-picked from the high S/N ϵ Eri spectrum.

As context for these flares, I compare the largest to the Great Flare of 1985 on AD Leo (Hawley & Pettersen, 1991). I estimate that this flare produced equivalent durations in C II and C IV during its impulsive phase (start of the flare to the start of its gradual decay) on the order of 40 ks (C II) and 70 ks (C IV). The comparable equivalent durations (also taken only over the impulsive phase) for the flares of AD Leo and GJ 876 with largest FUV_{130} equivalent durations in the data I analyzed are 0.4 ks (AD Leo, C II), 0.9 (AD Leo, C IV), and 3 ks (GJ 876, C II, no C IV data). The 5-10$\times$ greater equivalent duration of the 1985 flare is predominantly due to its 10-100$\times$ longer impulsive phase; the flux enhancements of these flares were similar.

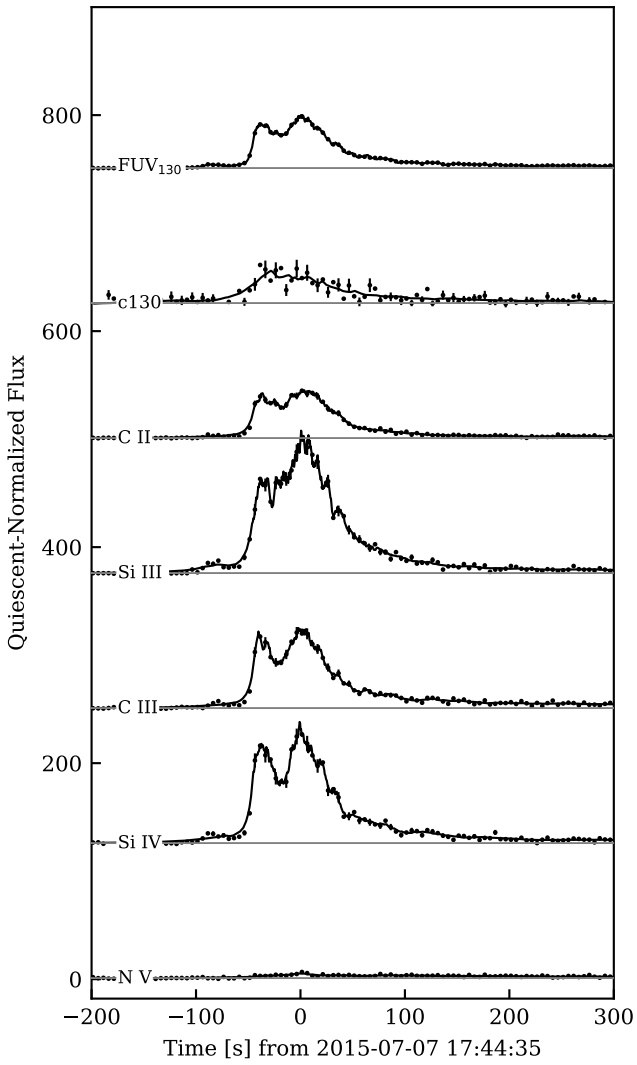

Figure 6.2 Spectrophotometry of the most energetic flare observed on GJ 876. Lightcurves have been normalized by the quiescent flux. Underlying lines are "count-binned" (see Section 6.2.2.1) to provide adaptive time resolution. The points are time-binned with a cadence chosen to provide a median S/N of roughly 5.

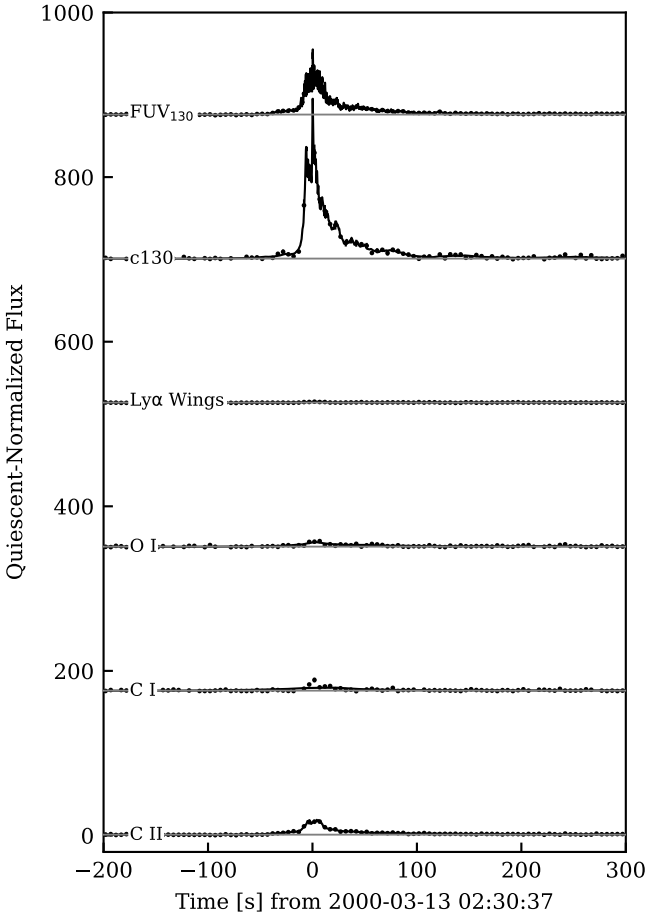

Figure 6.3 Same as Figure 6.2, showing the most energetic flare observed on AD Leo (continued in Figure 6.4).

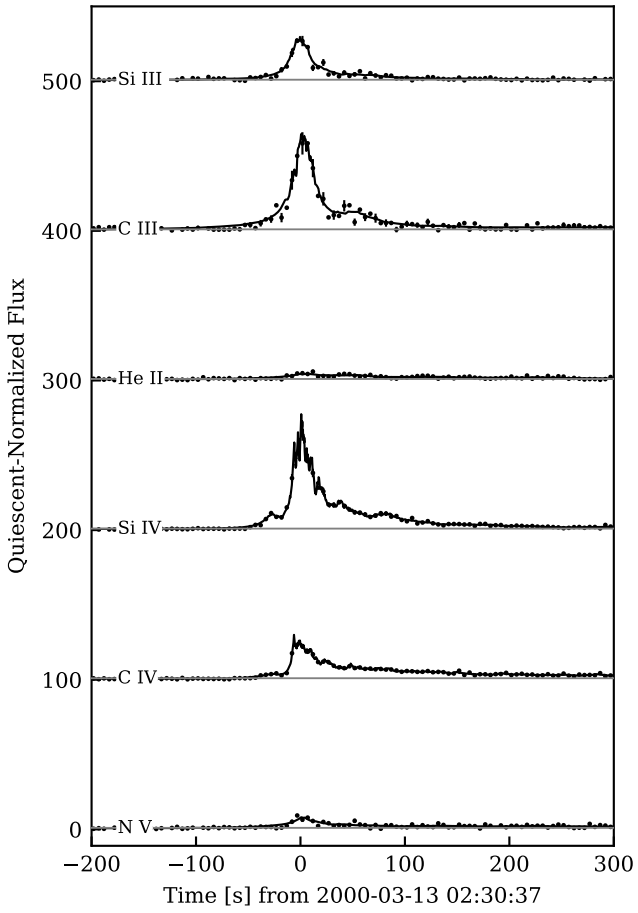

Figure 6.4 Continuation of Figure 6.3.

Table 6.2. Selected measurements from the 20 flares with greatest δ.

δ_{130} s	E_{130} 10^{27} erg	$t_{\rm peak}$ MJD	$F_{130,\rm peak}$ 10^{-13} $\frac{\rm erg}{\rm cm^2 s\ \mathring{A}}$	$\frac{F_{130,\rm peak}}{F_{130,q}}$	FWHM$_{130}$ s	Star
8266 ± 163[a]	295.7 ± 5.8	51673.1049	283 ± 73	160 ± 42	0.34	Prox Cen
5975 ± 42[a]	645.0 ± 4.6	57210.7393	22.5 ± 4.8	56 ± 12	37.27	GJ 876
3604 ± 38[a]	270.0 ± 2.9	56941.5122	5.7 ± 1.3	22.5 ± 5.3	31.80	GJ 832
3443 ± 44[a]	200.6 ± 2.6	55931.1242	10.7 ± 2.3	48 ± 11	7.81	GJ 876
1923 ± 30[b]	5041 ± 80	51616.1046	1420 ± 372	145 ± 38	0.06	AD Leo
1186 ± 120[a]	24.7 ± 2.5	51672.0826	96 ± 28	93 ± 27	0.81	Prox Cen
1048 ± 18[b]	170.7 ± 2.9	57210.7969	8.4 ± 2.0	13.6 ± 3.2	5.65	GJ 876
940 ± 22[b]	2397 ± 57	51614.4264	537 ± 162	56 ± 17	0.12	AD Leo
891 ± 22[b]	2549 ± 64	51614.2141	245 ± 77	23.2 ± 7.3	0.27	AD Leo
847 ± 100[b]	18.0 ± 2.1	51672.0746	30 ± 11	29 ± 11	0.91	Prox Cen
838 ± 81[b]	24.6 ± 2.4	51673.0719	38 ± 14	26.9 ± 9.9	0.84	Prox Cen
705 ± 21[b]	1483 ± 45	51615.1697	186 ± 66	23.4 ± 8.3	0.32	AD Leo
609 ± 78	10.4 ± 1.3	57245.8531	0.54 ± 0.16	14.5 ± 4.3	16.17	GJ 581
494 ± 17[b]	1490 ± 52	51615.2245	109 ± 37	9.5 ± 3.2	0.38	AD Leo
401 ± 38[b]	18.2 ± 1.7	57241.8025	0.48 ± 0.13	5.9 ± 1.6	4.19	GJ 667C
308 ± 43[b]	10.4 ± 1.5	51673.0910	25 ± 10	15.0 ± 6.2	1.72	Prox Cen
277 ± 44[b]	9.1 ± 1.5	51673.2301	18.0 ± 6.3	11.1 ± 3.9	2.40	Prox Cen
243 ± 50[b]	7.1 ± 1.5	51673.2494	19.4 ± 5.8	13.3 ± 4.0	1.80	Prox Cen
207 ± 16[b]	479 ± 38	51615.3689	45 ± 19	5.1 ± 2.1	0.82	AD Leo
206 ± 11	17.86 ± 0.93	57210.6014	5.4 ± 1.3	16.5 ± 4.0	4.76	GJ 876

[a]Flare cut off by the start or end of an exposure.

[b]Flare exhibits multiple distinct peaks. Time, FWHM, and flux measured only for the highest peak.

Note. — Uncertainties are statistical and do not reflect systematic effects due to choices made in the flare identification and measurement algorithm. I expect the effect of these choices on the flux and energy measurements to be at the 10% level.

Table 6.3. Simple flare statistics by star.

Star	$N_{\rm flares}$	E_{130}/E_q[a]	Flare Rate[b] $\rm d^{-1}$
GJ 876	11	73.9%	64
GJ 581	1	4.4%	6
GJ 436	1	1.1%	6
GJ 176	7	4.9%	48
GJ 832	4	24.6%	23
GJ 667C	2	4.0%	14
Prox Cen	7	45.9%	23
EV Lac	4	4.8%	32
AD Leo	40	10.5%	52
AU Mic	3	1.5%	26

[a]Ratio of flare to quiescent energy emitted, including quiescent emission during flares.

[b]Values not referenced to a common flare detection threshold, simply the number of detected flares divided by the exposure time.

Table 6.4. X-ray flares

δ s	$t_{\rm peak}$ MJD	$\frac{F_{\rm peak}}{F_q}$	FWHM s	Star
72995 ± 5512	56820.9147	21.0 ± 3.3	3600.00	GJ 581
33049 ± 1706[a]	57178.2578	8.1 ± 1.1	2881.01	GJ 876
2791 ± 637	56941.1683	1.4 ± 0.5	1654.75	GJ 832
1129 ± 84	57055.3596	0.499 ± 0.081	1166.07	ϵ Eri

[a]Could be interpreted as three separate events.

Note. — The ϵ Eri and GJ 581 flares are truncated by an exposure beginning and end near their peak flux, strongly affecting measurements of the flare properties.

6.3.2 X-ray Flares and Overlap

X-ray lightcurves in which I detected flares or that have overlapping FUV data are shown in Figure 6.5. The pipeline identified 4 flares in the X-ray data, cataloged in Table 6.4. There is only one case, a flare on ϵ Eri, in which a clear signal is detected in both the X-ray and FUV data. The X-ray observations captured only the declining phase of the flare, but they imply an equivalent duration at least several times as large as observed in FUV emission. This is also consistent with a comparison of the X-ray flares on GJ 876 and GJ 581 with the largest FUV flares I observed. The X-ray flares have equivalent durations of a few 10s of ks, whereas the largest FUV flares have equivalent durations of a few ks. This suggests that a given flare produces emission with an equivalent duration in the X-ray that is roughly an order of magnitude larger than FUV emission.

Such a relationship between the X-ray and FUV equivalent durations, however, is not consistent with the simultaneous FUV and X-ray coverage obtained during FUV flares on GJ 176 and GJ 667C. If the relationship held, then these flares would have produced enhancements several times in excess of the scatter in the quiescent X-ray lightcurve. However, these are not present, and re-reducing the data to produce lightcurves with finer time sampling during these flares did not reveal any hidden flux enhancements.

This implies that the flare energy budget between the FUV and the X-ray might not be consistent. If so, this suggests that different energy dissipation mechanisms could be operating in

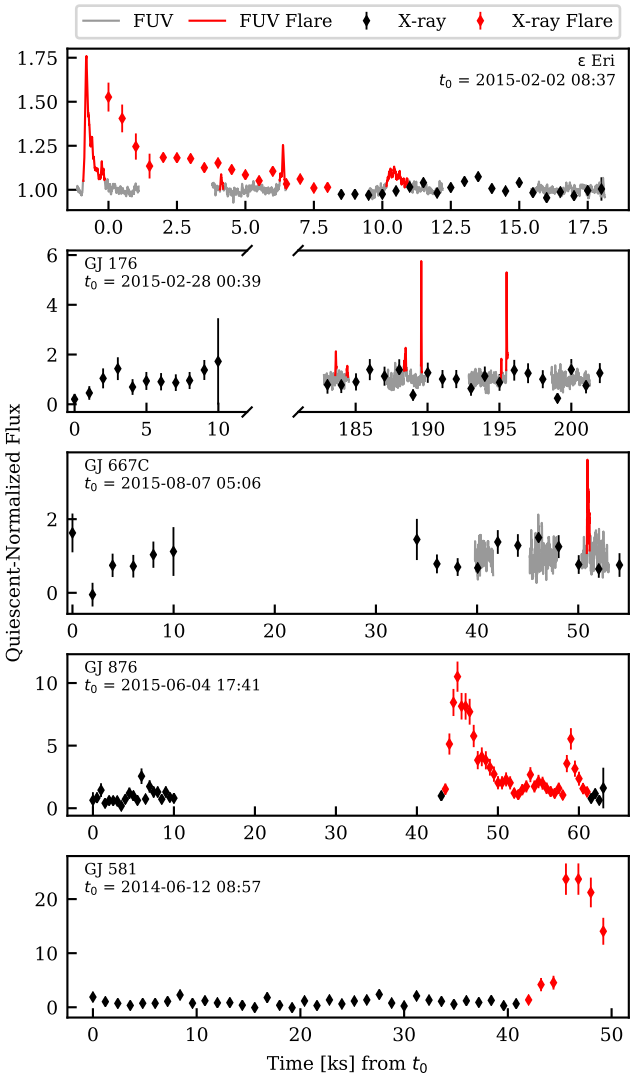

Figure 6.5 X-ray data of those stars with overlapping FUV data or where X-ray flares were observed. The GJ 176 and GJ 667C lightcurves are of FUV_{130} emission, whereas the ϵ Eri is of FUV_{140} emission due to necessary differences in observing configurations. X-ray data was also obtained for GJ 832, GJ 436, HD 40307, and HD 85512, but exhibited no flares and did not overlap any FUV observations.

different events, particularly in the brief FUV flares observed on GJ 581 and GJ 667C versus the more extended flare on ϵ Eri and the extended, highly energetic flares on GJ 876 and GJ 832. Such disparities are at odds with the generally good consistency in the relative responses of FUV energy budget (discussed further in Section 6.3.11), as well as observations by Hawley et al. (2003) of flares on AD Leo in the FUV and EUV. Simultaneous X-ray observations of M Dwarf FUV flares with equivalent durations at the 10 ks level are needed to determine if this inconsistency is real.

6.3.3 FUV Flare Frequency Distribution

I have aggregated the flares from two groups, the MUSCLES M dwarfs and the M dwarf flare stars, in order to examine the "typical" flare frequency distribution (FFD) of these populations. These will be particularly useful in estimating the volatility of high energy stellar radiation in the space environment inhabited by planets discovered after the era of *Chandra* and *HST*. FFDs of individual stars are not possible with the data, except for AD Leo, due to the lack of a sufficiently large flare sample for any individual star. For AD Leo, an FFD of FUV flares (from the same archival data) was published in Loyd & France 2014.

I created cumulative FFD curves using both absolute flare energy and equivalent duration. The detection limit varies for each target and sometimes for different observations of the same target. When creating histogrammed FFDs for plotting, I weight events according to the quantity of data with detection thresholds below the event's energy. I fit the FFDs with a power-law model of the form

$$\nu = \mu\delta^{-\alpha}, \tag{6.3}$$

where ν is the occurrence rate of flares with equivalent durations above δ (absolute energy, E, can be substituted for δ), μ is the rate constant, and α is the power-law index. The fit procedure is a maximum-likelihood method that works directly from the discrete flare events (i.e. does not fit the binned FFD curves) and accounts for the varying sensitivity of differing datasets. The free parameters are μ and α and their values are, as one would expect, nearly perfectly correlated in MCMC explorations of the parameter space. I used the MCMC Python code `emcee` (Foreman-

Mackey et al., 2013) to sample the posterior distributions of these parameters, taking the ±34% intervals of their marginalized distributions as the uncertainties on the values. In the following sections, I present FFDs for a variety of targets and bandpasses and discuss their implications.

6.3.4 M Dwarf Flares: Relatively the Same, Absolutely Different

Figure 6.6 shows the FFDs of the FUV_{130} flares of the MUSCLES and flare stars. When the flares are characterized by their absolute energy, the two distributions are clearly separated. For a given flare energy, the frequency of flares on the flare stars is about an order of magnitude larger than the MUSCLES stars. The power-law index of the fits to each distribution are statistically indistinguishable. Remarkably, when the flares are characterized in relative units by their equivalent durations, δ_{130}, the FFDs of the two populations become statistically indistinguishable in both flare rate and power-law index. The implication of this is clear: relative to their quiescent state, both the flare and MUSCLES stars show identical flare behavior. This is in spite of their substantial differences many properties typically associated with magnetic activity, such as chromospheric Ca II K flux and rotation period (see Section 6.3.9).

The consistency of FFDs in relative units means that their difference in absolute units is due simply to the differing levels of baseline FUV_{130} flux. This result is consistent with previous studies that have concluded that active stars have greater flare activity based on comparisons using absolute flare energies (Hilton, 2011; Hawley et al., 2014). I conclude that nearly all M dwarfs flare vigorously relative to their quiescent states, with the absolute energy of their flare emission determined by their quiescent state. Future flare surveys should determine if this result is robust against larger sample sizes and whether it extends to other sources of flare emission, such as the blackbody flux predominantly emitted in the NUV. In the meantime, this result has critical implications for exoplanets, as it confirms that even the relatively inactive stars preferentially selected for exoplanet surveys are likely to show relative flare increases akin to the most active stars.

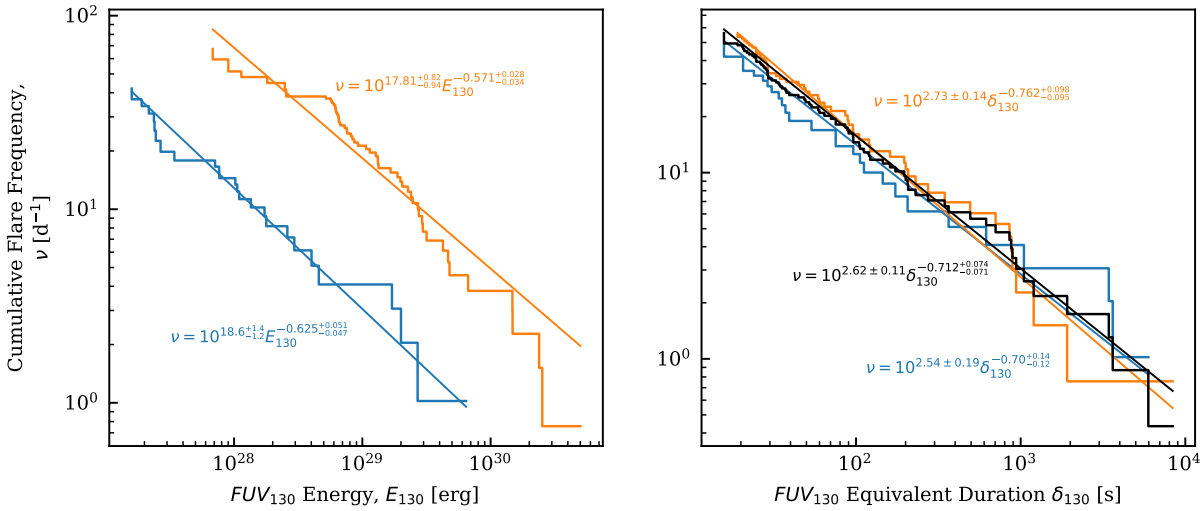

Figure 6.6 Flare frequency distributions and power-law fits of FUV_{130} flare in absolute energy, E_{130}, and relative energy δ_{130}. Observations are from two groups of stars, the "typical" M dwarfs of the MUSCLES survey and M dwarfs classified as flare stars. At a given absolute flare energy, the flare stars flare about an order of magnitude more frequently, but in relative units the two distributions are statistically indistinguishable.

6.3.5 Energy Emitted in the FUV Could be Dominated by Flares

As Table 6.3 shows, most of the FUV_{130} emission I observed from the targets was quiescent. However, these values do not accurately reflect the true quiescent/flare energy budget because of the limited data. An accurate estimate of the energy budget over timescales relevant to exoplanet climates would require knowledge of the FFD of each star to much more energetic, less frequent flares unlikely to be captured in observations lasting only hours or days. The contribution of these flares to the FUV energy budget could have critical implications for atmospheric photochemistry. This is also true of atmospheric escape, assuming the EUV is at least as volatile as the FUV. This assumption is well-founded given that the EUV is essentially a combination of emission from the corona (also responsible for most X-ray emission) and transition region (responsible for most FUV emission).

To obtain a sense of how likely it is that flares dominate the FUV_{130} emission of M dwarfs, I introduce a quantity for the critical energy at which the power laws I have estimated predict the cumulative energy from flares will exceed the energy from quiescent emission. Working from the power-law defined by Eq. 6.3, I obtain

$$\delta_{\rm crit} = \left(\frac{1-\alpha}{\mu\alpha}\right)^{1/(1-\alpha)}. \tag{6.4}$$

This quantity is very sensitive to uncertainty in α, so I used the MCMC procedure to determine its distribution given the combined MUSCLES and flare star FUV_{130} flares (black line of Figure 6.6). From the results, shown in Figure 6.7, I conclude that if the general M dwarf FFD power law extends 2-3 orders of magnitude beyond the largest flares detected in the present data, then the energy budget of M dwarf FUV_{130} emission is very likely dominated by flares. According to the power law, such energetic flares would occur about once per month to once per year.

6.3.5.1 How Big Do Flares Get?

Regardless of whether flares dominate the overall FUV energy budget, the energy budget of the flares themselves is dominated by the rare, energetic events. Since $\alpha < 1$, the integral of the

FFD is dominated by the upper integration limit. Yet what this important upper limit is is difficult to constrain, since these are the rarest events. Here, I explore observations and constrains on flares of higher energy than those I have characterized.

As previously mentioned, the great Flare of AD Leo in 1985 (Hawley & Pettersen, 1991) likely reached an FUV equivalent duration of no more than about 100 ks, about 10× that of the largest flares in this survey. Much more energetic M Dwarf flares have been observed in other bandpasses, such as a flare by EV Lac radiating 10^{34} erg in 0.3 – 10 keV X-rays observed by Osten et al. (2010) and two flares by DG CVn (a young M4 binary) radiating a few 10^{34} erg in the V band (10^{36} erg in 0.3 – 10 keV X-rays; Osten et al. 2016). Scaling to the FUV via the multiwavelength AD Leo flare observations of Hawley et al. (2003), these are likely 3-4 orders of magnitude more energetic than the most energetic flares of this survey.

More complete flare samples are accessible through surveys using U band and optical photometry. An analysis of *Kepler* observations by Hawley et al. (2014) detected M dwarf flares up to 2-3 orders of magnitude more energetic than the largest of this survey. Similar flares were observed earlier by a survey in the U band conducted by Hilton (2011). Both analyses found cumulative power law slopes of -0.5 – -0.7 (ignoring one -0.25 slope based on a 3-point fit). If U and *Kepler* band scalings remain linear through this range, it would imply that the FFD I have computed can be extrapolated to at least the critical duration described above. Consequently, it is reasonable to conclude that the FUV energy budget of M dwarfs is dominated by flares.

A different approach to estimating an upper limit is to scale FUV equivalent duration with flare covering fraction and compute the energy of a flare covering the entire visible hemisphere. The covering fraction of the largest AD Leo flares I characterized was estimated by Hawley et al. (2003) to be roughly 0.01%, and I estimate equivalent durations of $\sim$ 1 ks for these flares. This would imply, under the assumption that the FUV flare flux increases linearly with the flare covering fraction, an upper limit 4 orders of magnitude above the most energetic flares here characterized.

However, the assumption that FUV flare energy scales with covering fraction is dubious. The process underlying FUV emission during flares is not well-understood, so a non-linear relationship

with covering fraction is well within reason. Until this process is better understood and there are observations of M dwarf flares detecting a fall-off in the FFD, a firm upper limit is not possible.

The higher-energy tail of the FFD could be better characterized by staring observations of stars from the upcoming cubesat mission CUTE. Though these are NUV observations, NUV-FUV links could be established with the appropriate preparatory *HST* observations that could enable a rough scaling of the observed flares. This would have great value for the accurate modeling of exoplanetary atmospheric photochemistry and escape.

6.3.6 Microflares Probably Aren't the Energy Source for M dwarf Transition Region FUV Emission

It is worth revisiting the hypothesis of microflare heating as a resolution to the coronal heating problem (Gold, 1964; Parker, 1972). If flares continue to follow a power law distribution to very low energies and the power law index for the cumulative distribution (α in Eq. 6.3) is > 1, then the energy contributed by the smallest flares dominates. As the power law is extended to energies approaching zero, the total energy predicted by the power-law diverges. This is not the case for the FUV flares I have characterized. Since $\alpha < 1$ for these flares, the contribution of undetected flares to the energy budget is bounded. The energy emitted from flares below the detection threshold relative to the quiescent emission can be estimated from the flare power-law distribution, under the assumption that it extends to energies much smaller than the detection threshold, as

$$\frac{F_{\rm UF}}{F_q} = \frac{\mu\alpha}{1-\alpha}\delta_{\rm lim}^{1-\alpha}, \tag{6.5}$$

where $F_{\rm UF}$ is the time-averaged flux from undetected flares, F_q is the quiescent flux, and $\delta_{\rm lim}$ is the equivalent duration detection limit. This value is relatively insensitive to α and $\delta_{\rm lim}$ within the constraints of the fits and evaluates to $\sim$0.01. Therefore, flares too weak to be detected are a negligible contributor to quiescent FUV flux under the aforementioned assumptions. The further implication is that microflares are not heating the transition region. This is in line with results regarding coronal heating and solar EUV and X-ray flares (e.g. Hudson 1991).

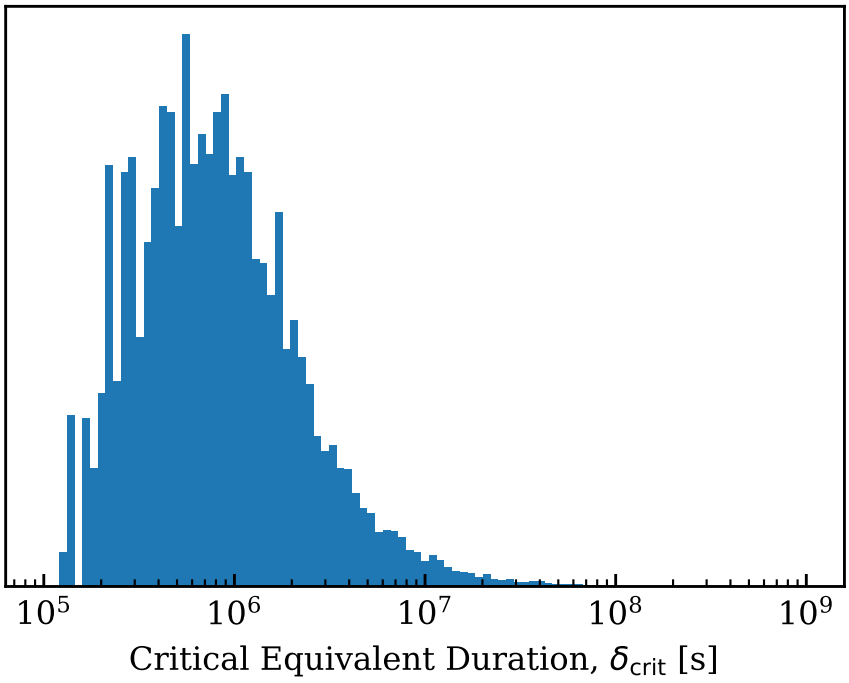

Figure 6.7 Possible values of δ_{crit} based on a power law fit to the FFD of FUV_{130} flares from the MUSCLES and flare star M dwarfs (black line, Figure 6.6). If the power law extends above δ_{crit}, then flares contribute more than quiescence to the FUV_{130} emission of these stars.

6.3.7 Comparison to Solar Flares

There is no solar dataset that is directly comparable to the spectrophotometric FUV data I have analyzed for M dwarfs. In the absence of directly comparable data, I have used the flare catalog from *SDO* EVE mission for comparison to M Dwarf flare data. This catalog contains measurements of flares in several EUV emission lines with formation temperatures similar to the FUV lines COS and STIS observe, all originating in the stellar transition region. The EVE flare catalog does not contain equivalent durations for the flares, so I estimated them by dividing the flare energy by the pre-flare flux estimate. Figure 6.8 shows the resulting cumulative FFDs for the solar C III 977 Å ($T_{\rm form} = 10^{4.8}$ K) and He II 304 Å ($T_{\rm form} = 10^{4.9}$ K) lines, compared to the M dwarf FFDs for Si III 1206 Å ($T_{\rm form} = 10^{4.7}$ K), Si IV 1393,1402 Å ($T_{\rm form} = 10^{4.9}$ K), and He II 1640 Å ($T_{\rm form} = 10^{4.9}$ K; though see Section 6.3.8) lines. The He II 1640 Å data come from the flare stars only. Because these lines have different quiescent fluxes, I use equivalent duration rather than absolute flare energy to provide a more consistent comparison. For all lines, the stellar photosphere does not contribute significant flux (though this would not be the case for observations of the Sun in the FUV lines if such were available).

The figure shows that transition-region flares occur ∼3 orders of magnitude more frequently on M Dwarfs than on the Sun for a given flare equivalent duration. The Sun and MUSCLES M Dwarfs have comparable quiescent fluxes in transition region FUV lines relative to their bolometric luminosity. Therefore, this comparison implies that for planets receiving similar instellations (e.g., planets in the habitable zone of both stellar types), those orbiting M dwarfs will experience ∼3 orders of magnitude more flare emission from these lines than those orbiting Sun-like stars.

These types of solar-stellar comparisons would be greatly facilitated by disk-integrated, spectrophotometric FUV data of the Sun. Though the EUV is an excellent tool for the study of solar magnetic activity, EUV emission from stars is inaccessible due to ISM absorption. Stellar X-ray emission can be observed, but X-ray observatories do not provide spectral and temporal resolution akin to the FUV. Thus, to strengthen the Sun-star connection, spectrophotometric FUV observa-

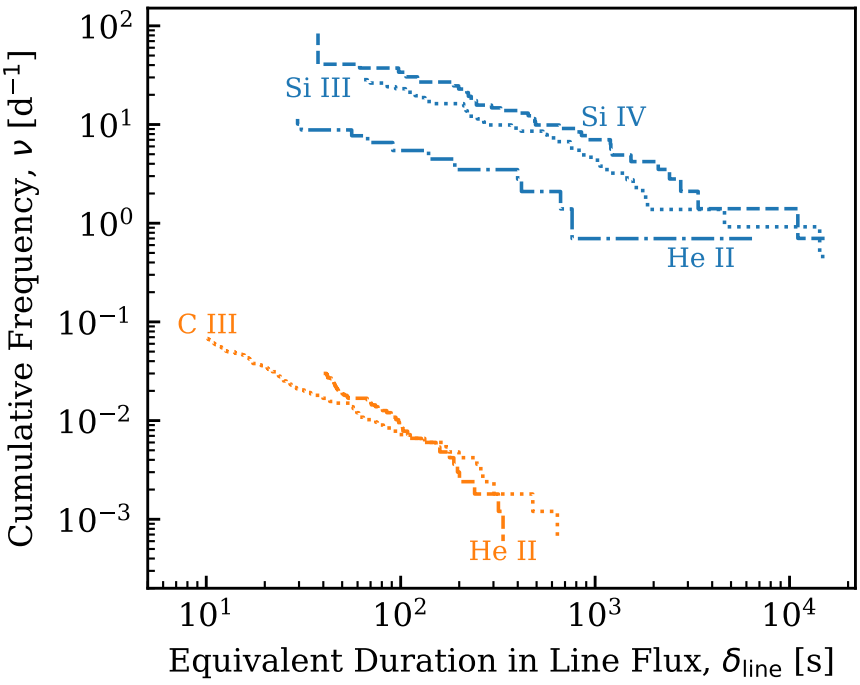

Figure 6.8 Comparison of solar (orange) and M Dwarf (blue) flare rates in transition region lines. Line wavelengths and formations temperatures are defined in the text. Transition-region flares of a given equivalent duration occur on M dwarfs ∼3 orders of magnitude more frequently than on the Sun.

tions of the Sun should be pursued.

6.3.8 Line FFDs

In Figure 6.9, I compare power-law fits to all major emission lines. There is no detectable relationship between the flare rate and power-law index for a given emission source. The same is true of correlations with line formation temperature (shown as point size in the figure). The differences in the rate of $\delta = 1$ ks flares span factors of a few between lines.

Uncertainty in these rates imply that they could mostly be consistent with a single value. However, the significant difference in the Si IV and He II lines is particularly intriguing. Individual flares illustrate the difference, sometimes quite dramatically, such as the AD Leo flare shown in Figures 6.3, and 6.4. Yet these lines have nearly identical peak formation temperatures in the CHIANTI models. A likely explanation is that the CHIANTI formation temperature is misleading and the regions of the stellar atmosphere in which He II and Si IV actually form do not significantly overlap. This is supported by nLTE modeling specifically of the formation of the He II 1640 Å multiplet in the solar atmosphere by Wahlstrom & Carlsson (1994), who found that radiative ionization and pumping lower in the atmosphere at the 7,000 – 10,000 K level dominates over the peak of collisional ionization and excitation at the 70,000 K level in generating the line intensity. This implies that peak formation temperatures cannot necessarily be relied upon as an indicator of the similarity of line formation mechanisms.

6.3.9 Ca II K Emission, $P_{\rm rot}$, and Flares: Even "Inactive," Slowly Rotating M Dwarfs Flare

A key result of the MUSCLES survey is the finding that FUV flares every few hours are the norm, rather than the exception, for M dwarfs. According to the conventional proxy for magnetic activity, the flux of the emission lines at the core of the Ca II H & K lines at 3933 and 3968 Å, the MUSCLES stars are not highly active, unlike the flare stars that I have included in this work. One might naively expect, then, that the MUSCLES stars would not flare with the same vigor. Yet

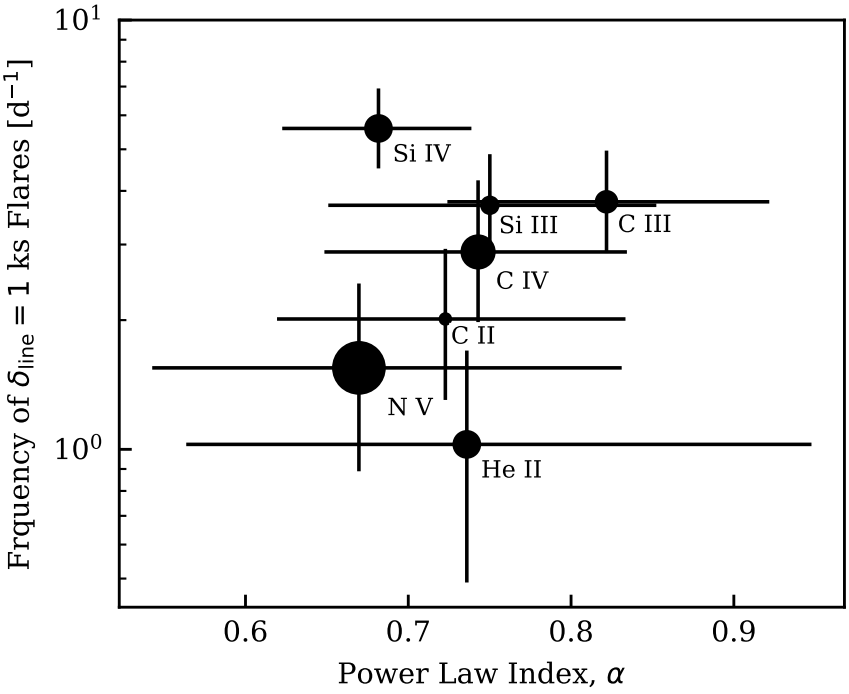

Figure 6.9 Results of power-law fits to independently identified flares in every major observed line. The area of the points is proportional to the peak line formation temperature. Not shown is the Si II 1264 Å line complex ($T_{\rm form} = 10^{4.5}$ K), a possible outlier with $\alpha = 1.2 \pm 0.3$. The figure demonstrates the lack of any detectable relationship between flare rate, power-law index, and formation temperature, but confirms that Si IV is the most "active" line, and therefore an excellent probe of M dwarf flares. Lyα and O I are not shown because too few flares were detected to enable a power-law fit.

such is not the case.

In Figure 6.10, I examine the relationship between the magnetic activity of a star measured as its temperature-corrected Ca II K equivalent width (from Youngblood et al. 2017) with both relative and absolute metrics of the star's flare activity. The temperature-correction to the equivalent width corrects for differences in the reference continuum used to define the equivalent width for stars of differing effective temperature (see Youngblood et al. 2017). K stars were not included in the analysis of Youngblood et al. (2017), so I have excluded them here as well. The relative metric of flare activity is simply the ratio of the energy emitted by flares to that emitted during quiescence over the course of the observations. The absolute metric of flare activity is the "surface flare flux:" the absolute energy of the star's flares spread over the time the star was observed and the surface area of the star.

The upper panel of Figure 6.10 makes it clear that no relationship exists between the chromospheric activity of a star and the relative intensity of its flaring in this sample. Therefore, Ca II K flux cannot be used to predict a star's likeliness to exhibit large flare enhancements over its quiescent FUV_{130} flux. This likely extends to other proxies for magnetic activity, such as H_α and Ca II H. Ca II K flux might correlate with flare emission measured in absolute units, such as the time-averaged surface flux from flares shown in the bottom panel of Figure 6.10. A Spearman Rank-Order correlation test conducted on the points in the lower panel yields a p-value of 0.2, i.e. no significant correlation. Removing GJ 876 as an outlier lowers this to 0.01, suggestive of a correlation though I would not consider it conclusive.

This result seemingly conflicts with the results of Hilton (2011); Hawley et al. (2014). These groups find higher rates of flaring for stars classified as active versus inactive based on H_α emission. This discrepancy can be explained by the difference in FFDs between the flare and MUSCLES stars when measured in absolute energy versus their similarity in equivalent duration (Figure 6.6). The results of Hilton (2011); Hawley et al. (2014) are based on absolute energy, so they are comparable to and consistent with the lower but not the upper panel of Figure 6.10.

Figure 6.11 makes the same comparisons with rotation period instead of Ca II K emission.

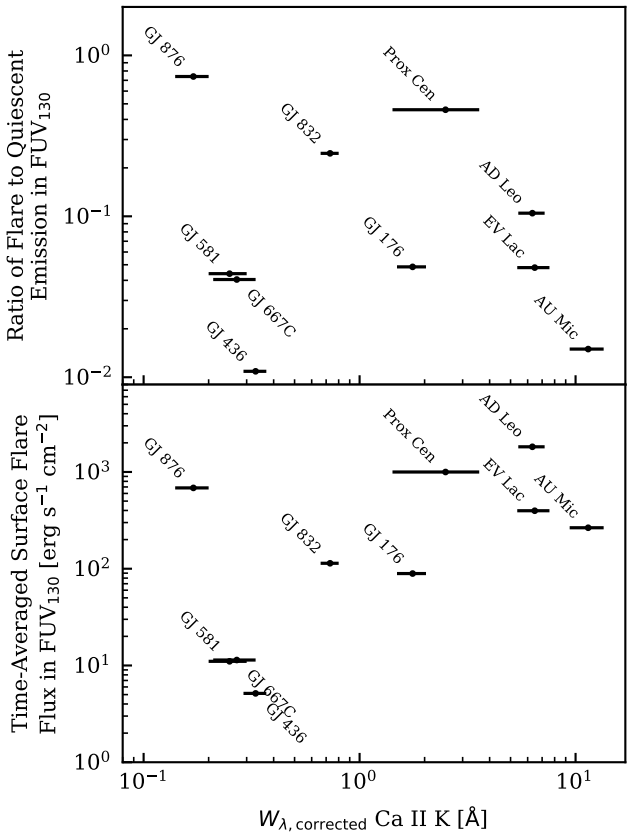

Figure 6.10 The flare activity of each star, using a relative (top) and an absolute (bottom) metric, as a function of chromospheric Ca II K line emission. In this sample, chromospheric Ca II K emission might correlate with flare emission in absolute units, but does not correlate when flare activity is measured relative to the star's quiescent activity.

Here, there is even less suggestion of any trend. It appears that rotation period does not predict flare emission.

The strength of the conclusions from this analysis is limited by the relatively short duration of observations for each target. Ideally, observations of sufficient duration to separately characterize the FFD for each star would be used. The analysis should be repeated with more extensive datasets when they are available. The ideal FUV survey would provide coarse spectra (sufficient to separate lines without resolving their profiles) over long temporal baselines of a sample of at least several dozen targets. Such a survey would require high-cadence time sampling to capture the minute-timescale flares that make up the bulk of the flares I observed.

6.3.9.1 What Predicts FUV Flare Activity?

In addition to examining the relationship of stellar flares with Ca II K flux and rotation rate, I also examined the relationship with effective temperature, and X-ray surface flux in a 10 – 25 Å band. For this, I used the FUV_{140} band so that the data from ϵ Eri could be included (see Section 6.2).

The limited sample size implies that only very strong relationships would be detectable. X-ray flux exhibits no suggestion of a relationship to a star's flare emission. However, the stellar effective temperature is negatively correlated with both the relative and absolute measures of a star's flare activity, shown in Figure 6.12. This correlation is tentative when only M stars are included (p-value $\sim$0.05 from a Spearman rank-order correlation test), but becomes very strong when K stars are included due to the lack of any detected flares on 2 of the 4 MUSCLES K stars (p-value 0.002 for flare surface flux, 6×10^{-5} for flare/quiescent ratio). Note that only a very weak flare was detected from HD 40307 in the FUV_{140} band, and it is not detected in the broader FUV_{130} band. This result is in line with the much larger surveys using *SDSS* and *2MASS* data on M dwarfs that found an increase in flare rates toward later spectral types (Kowalski et al., 2009; Hilton et al., 2010).

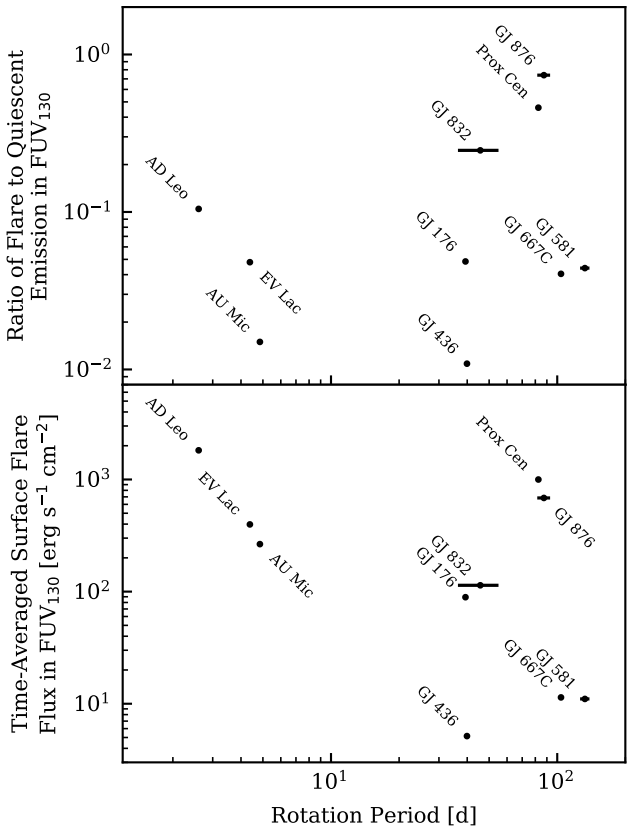

Figure 6.11 Same as 6.10, with rotation period as the independent variable. FUV flare activity does not correlate with rotation period in this sample.

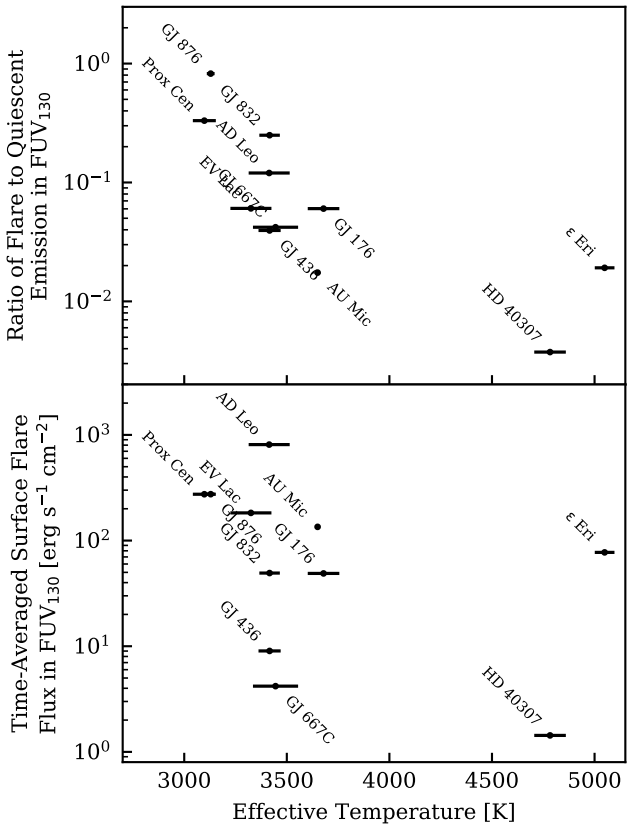

Figure 6.12 Same as 6.10, with effective temperature as the independent variable. FUV flare activity correlates well with effective temperature when K and M stars are included, tentatively when only M stars are included.

6.3.10 Comparison of Line Responses: Lyα is a Gentle Giant

The general line behavior observed in the AD Leo data by Hawley et al. (2003) holds for all the flares that I observed. This behavior is reflected in the relative ordering of the lines in Figure 6.9. For the lines not on the plot, namely O I, C I, and the wings of Lyα, flares induce such a minimal response that too few flares are identified to enable a power law fit. The flares plotted in Figures 6.2, 6.3, and 6.4 provide actual examples of the varying response of lines.

Of particular importance is the muted response of Lyα, the dominant source of flux in the FUV for M dwarfs (France et al., 2012b, 2013). In flares producing peak fluxes in Si IV 100$\times$ quiescence, flux in the Lyα wings increases by only a factor of a few. This result is directly relevant to the safety of instruments used to observe FUV flares. Estimates of the risk of brightness violations for these instruments can conservatively assume that relative increases in Lyα flux are an order of magnitude below Si IV. The core of the line, however, could behave differently, an important distinction for planets orbiting the star that are exposed to the flux of the line core. Because it is absorbed in the ISM, it cannot be directly observed. Photons in the core of the line originate, on average, higher in the stellar atmosphere than photons in the wings, which must undergo many inelastic scatterings to be shifted to the wing wavelengths. Therefore, flare heating is likely to affect emission in the core of the line more than the wings.

In integrated spectra, the core of the Lyα line can be reconstructed by fitting the wings with a model that parameterizes the ISM absorption (e.g. Youngblood et al. 2016a). However, these fits are not practical for time-series data. Therefore, the response of the Lyα core must be inferred from the activity of related sources of emission. In the COS G130M and STIS E140M bandpasses, the best such proxies are the resonance O I lines at 1305 Å and C I lines at 1657 Å. Thus, I compare the equivalent duration and peak flux ratio of these lines during flares identified in the FUV_{130} bandpass in Figure 6.13. The figure shows relative increases in the O I and C I lines during a flare that exceeds that of the Lyα wings by a factor of a few to ten, suggesting that the core of the Lyα line responds substantially more strongly during a flare than the wings. However, this response

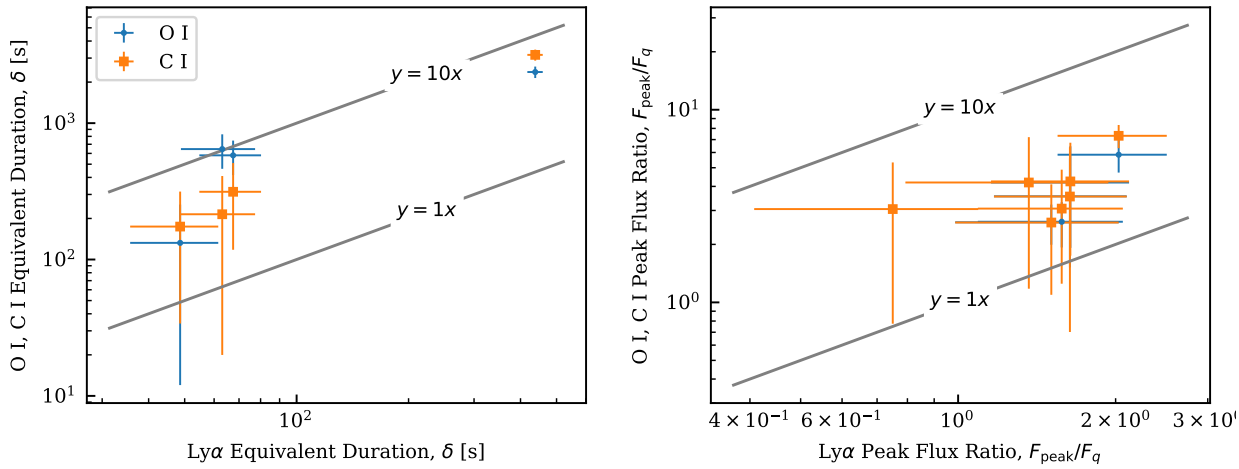

Figure 6.13 Comparison of equivalent duration and peak flux measurements of Lyα and resonance lines with comparable properties from flares identified in FUV_{130} emission. The comparison lines are the O I 1305 Å and C I 1657 Å multiplets. If O I and C I are taken as a proxy for the response in the core of the Lyα line to a flare, then the relative increase in core Lyα flux during a flare must exceed that of the wings by a factor of a few to ten.

would still be roughly an order of magnitude below that of Si IV.

6.3.11 Spectral Energy Budget

The sample flares are roughly uniform in their energy budget across the four orders of magnitude of flare energies observed. The energies emitted in each major emission line and the areas between are consistent with being linearly related to that emitted in FUV_{130}. For example, Figure 6.14 shows the relationship of energy emitted through Si IV to FUV_{130}. This is not terribly surprising given that $E_{\mathrm{Si\ IV}}$ typically contributes a few tens of percent to E_{130}, but it was not a forgone conclusion. A significantly non-linear relationship might have been observed if the emission processes differed between the smallest and largest observed flares, and this could still be the case for flares more energetic than I have observed. For example, a very energetic flare might eject emitting plasma from the higher temperature lines or produce continuum emission in FUV_{130} that would dominate over lines.

The linear relationships I found over the flare energies observed are convenient because they allow us to define a "typical" flare energy budget that is valid across the roughly four orders of

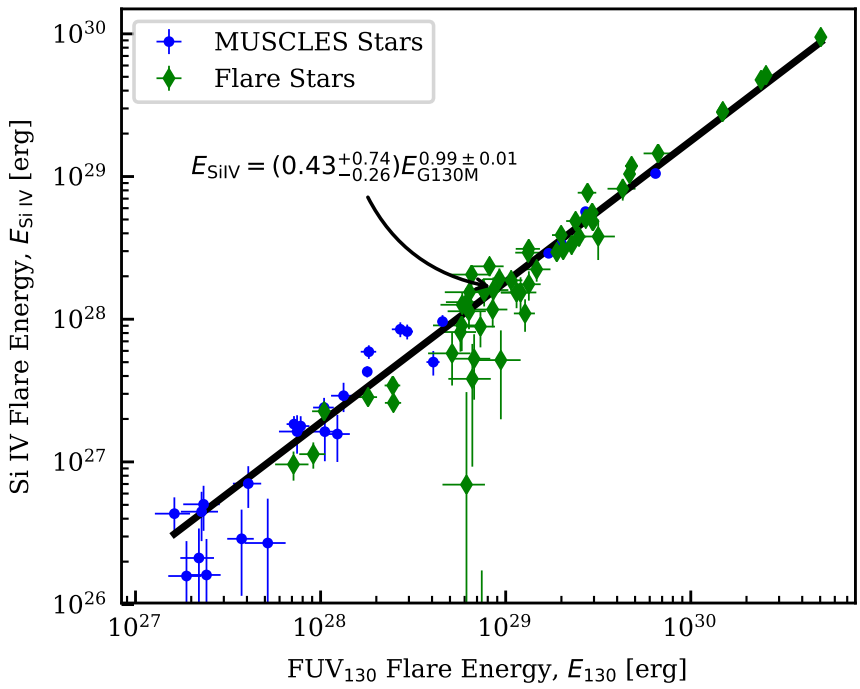

Figure 6.14 Relationship between flare energy emitted in Si IV versus FUV$_{130}$. The relationship is consistent with linear, as are the relationships for energy emitted in all major lines and interline regions. These linear relationships confirm that an average energy budget can be adopted as representative of all FUV flares over the energy range observed. The high uncertainties around 10^{29} erg represent flares near the detection limit in the Prox Cen data. Higher energy flares generally have higher S/N, but differences in instrument sensitivity and target brightness disrupt that trend.

magnitude of flare energies I have observed. I have characterized the typical energy budget in Figure 6.15 by plotting the ratio of the energy, partitioned into the major emission lines and areas between, to Si IV (chosen instead of FUV_{130} to provide a greater likelihood of compatibility with future instruments). The areas between lines are divided into two intervals, 912 Å – 1430 Å and 1430 Å – 1700 Å because the COS G130M spectrograph, from which the MUSCLES observations originate, reaches only to ∼1430 Å. I present the energy budget in Figure 6.15 as a spectral density (computed by dividing by the integration bandpasses) for a more intuitive comparison to flux density spectra. Thus, I use units of $Å^{-1}$. I cull data with S/N<2. and above 1430 Å all data is from the flare stars (taken with the STIS E140M spectrograph). The solid line traces the median values.

6.3.12 Flare Lightcurve Shapes

In general, the largest flares I identified exhibit a rapid rise, followed by phase of sustained elevated emission, and then decay. This structure is well exemplified by the flare in Figure 6.2 and has a heritage of previous observations, with flares frequently divided into an "impulsive" phase (sustained elevated emission) and a decay phase. I explore trends in the shape of the flares in Figure 6.16. The figure demonstrates that, for a given equivalent duration, the FWHM of the flares varies considerably, roughly an order of magnitude. I have not estimated uncertainty in the FWHM measurements, as it is a non-trivial task, but the lower variability in peak fluxes and the consistency of this variability across three orders of magnitude of equivalent duration support the validity of this diversity. The plot also suggests that the flare star flares are very slightly more impulsive (lower FWHM, larger peak/quiescent ratio), on the whole, than the MUSCLES stars.

Figure 6.16 depicts a clear trend in the peak flux ratio with equivalent duration and only a comparatively weak trend in FWHM. Both measurements are biased by the difficulty in resolving the flare peak due to lower count rates in less energetic flares. This would tend to artificially lower peak/quiescent ratio measurements at low δ and correspondingly increase FWHM measurements, artificially moderating the peak flux ratio vs. δ and steepening the FWHM vs δ trends. The < 1

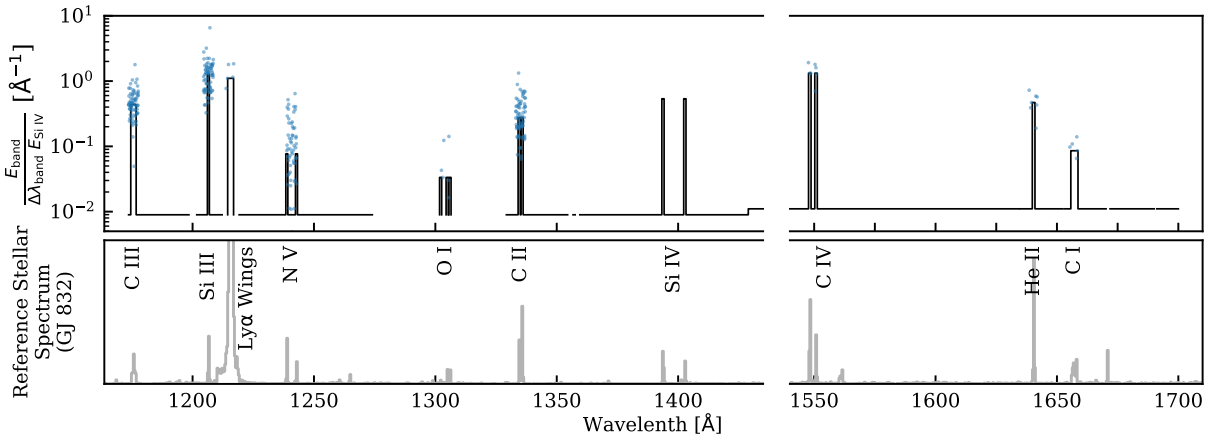

Figure 6.15 Flare spectral energy budget. The lower panel shows the location of major emission lines in an M dwarf spectrum for reference (linear scale). In the upper panel, the translucent blue points (scatter in wavelength added for display) represent single flares and give the ratio of the integrated energy emitted by the flare in the associated line to Si IV emission, divided by the bandpass. The number of points vary because of S/N cuts and differing wavelength coverage of observations. The solid line gives the median value of the points. Its basal level is computed by integrating all flux between the emission line bandpasses (see text).

slope of the peak flux ratio vs. δ trend and the bias implying this slope is likely an upper limit is important when considering possible risks of detector damage in future FUV flare observations.

6.4 Flares and Planets

6.4.1 Recommendation for a Fiducial FUV Flare

Because stellar UV flares could have a significant impact on atmospheric chemistry and loss on orbiting planets, I expect a great deal of modeling of these impacts in ensuing years. As such, I have created a fiducial UV flare for use in modeling to share with the modeling community. Although no such fiducial flare will perfectly represent a true stellar flare, establishing consistency across models in this early stage in the study of the impacts of stellar flares on planetary atmospheres could make future model comparisons more straightforward.

I base the fiducial flare spectrum on the FUV energy budget in Figure 6.15. Because this energy budget does not extend over all photochemically relevant wavelengths, I have extended it by using lines of similar formation temperature as proxies for those that were not observed. These are the Lyα core, Lyβ, Lyγ, and Mg II 2796,2803 Å (proxy O I 1305 Å multiplet), Al II 1671 Å (proxy C II 1334,1335 Å), C III 977 Å (proxy C III 1175 Å multiplet), and O VI 1031,1037 Å (proxy N V 1238,1242 Å). For wavelengths shortward of ∼1170 Å, I use the interline COS G130M flux as a proxy. To compute the energy contribution of the unobserved line (or the interline region), I assumed the unobserved line had the same equivalent duration during flares as the proxy line, then adjusted according to the ratio of fluxes of the unobserved and proxy lines. To compute these ratios, I used archival FUSE and STIS E140M data for AD Leo (C III, Lyγ, Lyβ, O VI, Lyα core, and short wavelength interline regions), quiescent COS G130M and G160M data for GJ 832 (Al II), and the panchromatic SED from the MUSCLES spectral atlas for Prox Cen (Mg II). To this emission, I add a 9000 K blackbody with a bolometric energy relative to Si IV of 160 according the mean of the energy budget values from the multiwavelength AD Leo observations of Hawley et al. (2003). Figures 6.17 and 6.18 show the spectral energy budget of this fiducial flare.

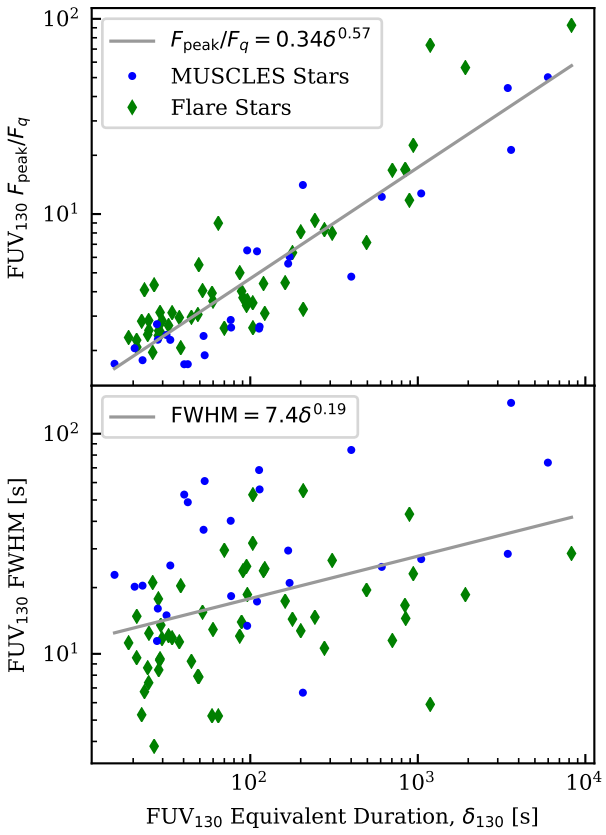

Figure 6.16 Trends in the "shape" of flares, as characterized by their ratio of peak to quiescent flux and FWHM (taken as the cumulative time that flux was above half peak). At lower δ, the flare peak is less well-resolved, introducing a bias implying that the peak ratio trend could be more gradual and the FWHM trend steeper than those shown in the figure.

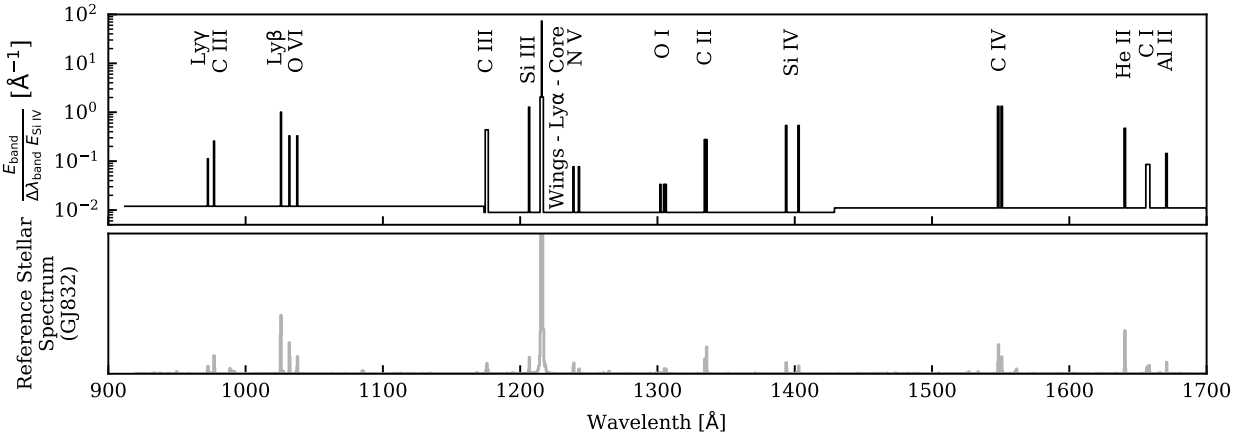

Figure 6.17 Spectral energy budget of the fiducial flare (for photochemical modeling) in the FUV. The lower panel shows the location of major emission lines in an M dwarf spectrum for reference (linear scale).

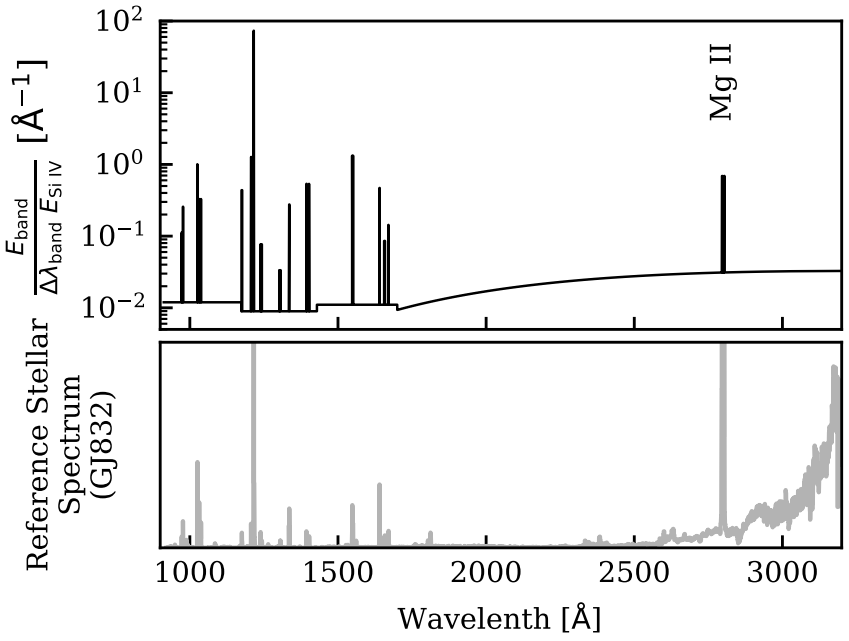

Figure 6.18 Same as Figure 6.17, showing the full wavelength range of the fiducial flare.

The temporal shape of the fiducial flare is a boxcar followed by an exponential decay, chosen as a simple analytic form to approximate the diverse and complex shapes of the observed flares. The decay phase produces half the energy of the boxcar, which has a height equal to the peak flux predicted by the power-law fit of Figure 6.16. The adopted shape is plotted in Figure 6.19. To maintain some semblance of simplicity in an already complex model, I assume that all bands follow the same temporal evolution. Both the spectral and temporal flare profiles are normalized to the Si IV flux. I suggest adopting a quiescent Si IV flux of 0.1 erg s^{-1} cm^{-2} for a generic inactive M dwarf and 1 erg s^{-1} cm^{-2} for a generic active M dwarf at the distance where the bolometric stellar flux is equivalent to Earth's insolation.

To simplify the implementation of the fiducial UV flare, I have developed a short Python module that can be used to generate synthetic FUV flares based on this template. A frozen copy of this code is included the the online version of the paper, and a living copy can be found at `https://github.com/parkus/fiducial_flare`. In addition to providing time-evolving spectra of the fiducial flare, this code can generate simulated series of flares based on the FFD power-law fit to Si IV flares (the parameters of which are shown in Figure 6.9). This should allow modelers to realistically simulate the cumulative effect of FUV flares on atmospheric photochemistry.

6.4.2 An Impulsive Approximation to Flare Photolysis

I created a custom "impulsive photolysis" model to explore the photolysis of N_2, O_2, O_3, H_2O, CO_2, CO, CH_4, and N_2O in an Earth-like atmosphere in response to a single flare event. The model incorporates scattering by Lyα, Lyβ, and Lyγ and the resonant O I 1305 Å multiplet through the plane-parallel, two-stream radiative transfer formulation of Toon et al. (1989) with the quadrature approximation. In normal photochemistry models that step through time, care must be taken in non steady-state scenarios to ensure that time steps are short enough to resolve the flare and associated changes in atmospheric composition. The "impulsive" model differs in that the event is idealized as a single impulse, i.e. photons are treated to have all arrived at essentially the same instant. The model tracks the absorption and scattering of these photons and terminates when all

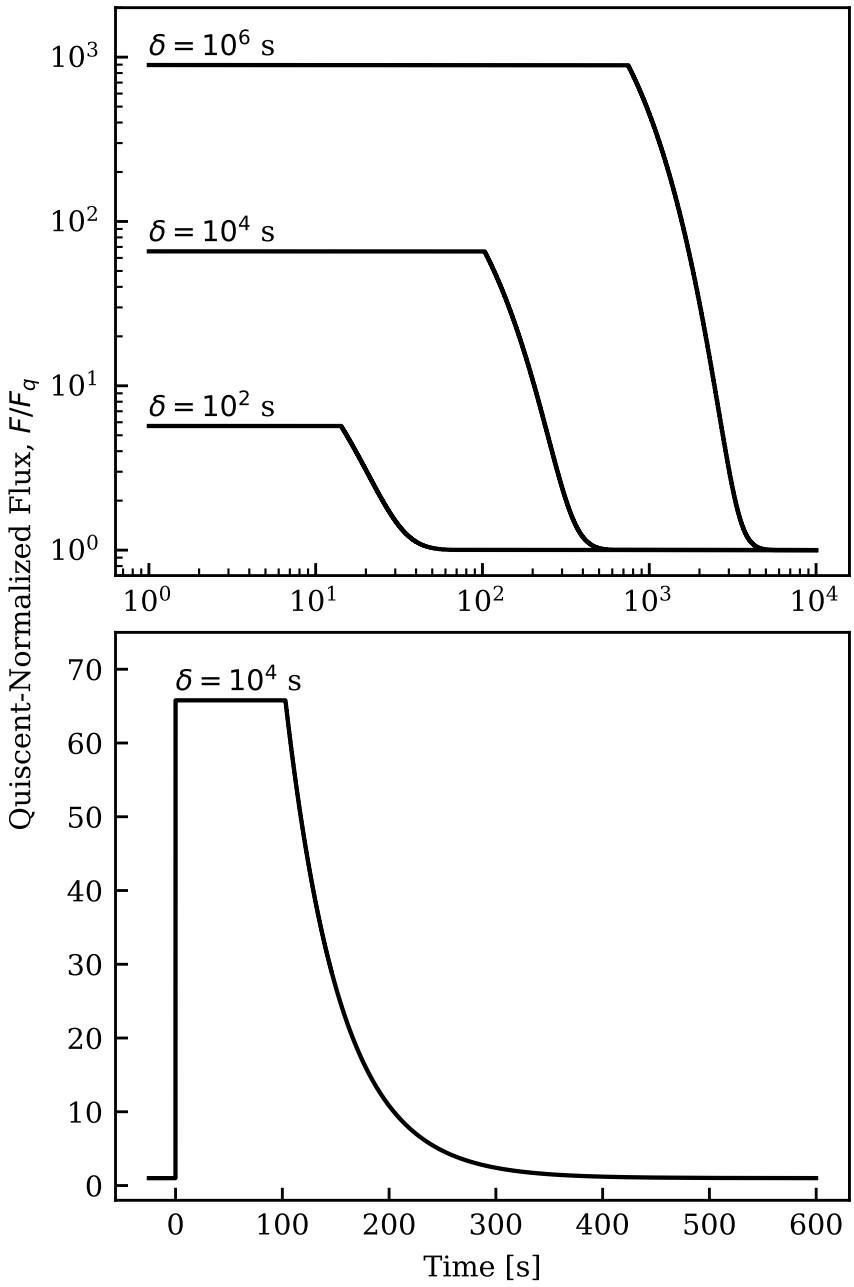

Figure 6.19 Adopted temporal profile of the fiducial flare, shown for several values of equivalent duration, δ, in logarithmic coordinates in the top plot and a single value in linear coordinates in the bottom plot.

photons have been either absorbed within the atmosphere, absorbed by the ground (assumed to be perfectly absorbing), or have exited the top of the atmosphere (scattered out).

I use the inactive star fiducial flare model of Section 6.4.1 to set the spectral content of the flare input. The modeled atmosphere receives a bolometric flux equivalent to Earth's insolation, and I consider only the substellar point in the atmosphere. Its compositional profile is a combination of the NRLMSISE-00 (N_2, O_2, O, H, N, Ar, He), Earth GRAM 2016 (H_2O, O_3, CO_2, CO, CH_4, N_2O), and Hu et al. (2012) (OH, NO, NO_2) empirical models. H_2 and $O(^1D)$ were included purely as dissociation products. For photon scattering, this atmosphere begins with 2.9×10^{13} H and 8.5×10^{17} O atoms cm^{-2} above 100 km (1.1×10^{14} H and 1.1×10^{18} O atoms cm^{-2} at ground level).

Figure 6.20 shows the state of the atmosphere before and after exposure to flares of three representative equivalent durations. The $\delta = 10^4$ s flare is akin to the largest observed in this survey, whereas the the $\delta = 10^8$ s is likely about an order of magnitude less energetic the largest M dwarf flare observed to date (see Section 6.3.5.1). The effects progress from negligible to dramatic over this range. At the highest energy, the atmosphere exhibits clear dissociation fronts among the different species. A standout feature is the increase in CO over pre-flare levels immediately below its dissociation front, a result of the production of CO from the photolysis of CO_2.

To examine the relationship between flare energy and the total affect on various species, I plot the fractional change in column density in Figure 6.21 and the altitude of the dissociation front in Figure 6.22 as a function of flare energy. At present, the dissociation code is computationally costly, so I used only a coarse grid of 25 flare energies. No species is ever completely dissociated save ozone beyond $\delta = 10^8$ s. The change in the slope of the column density relationships is a result of the changing absorption and scattering properties of the atmosphere as flares reach greater and greater depths.

The regular flares observed in this survey would, at least in isolation, have a negligible affect on an Earth-like atmosphere. However, within the range of flare energies observed by surveys in the U and *Kepler* bands, flares begin to have a substantial affect.

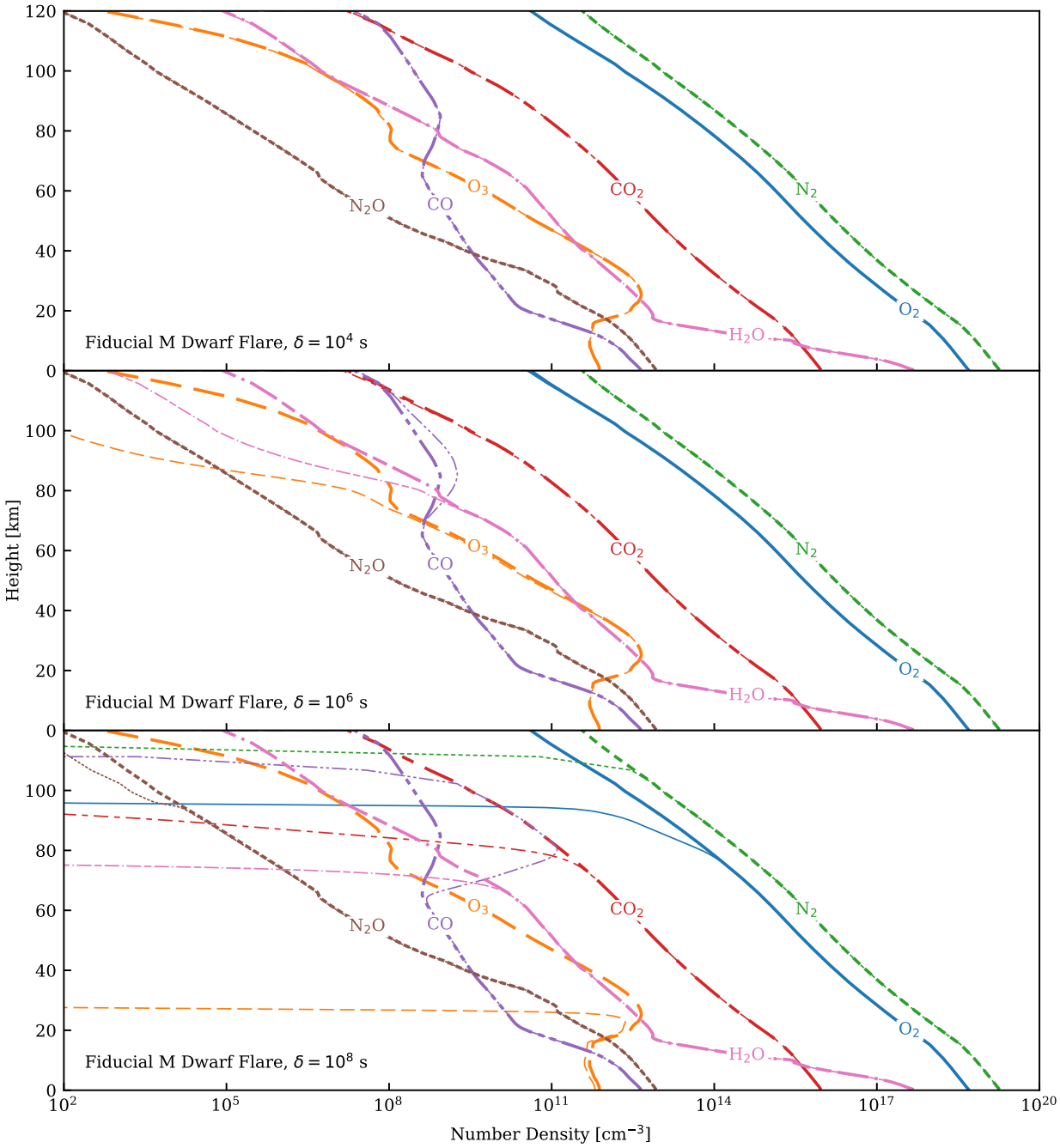

Figure 6.20 Composition of an Earth-like atmosphere at the substellar point following a fiducial flare from a generic, inactive M dwarf for three representative flare equivalent durations. The model incorporates scattering by resonant FUV lines and treats all photons as arriving at the same instant. Thick lines show species concentrations before the flare and thin lines after the flare.

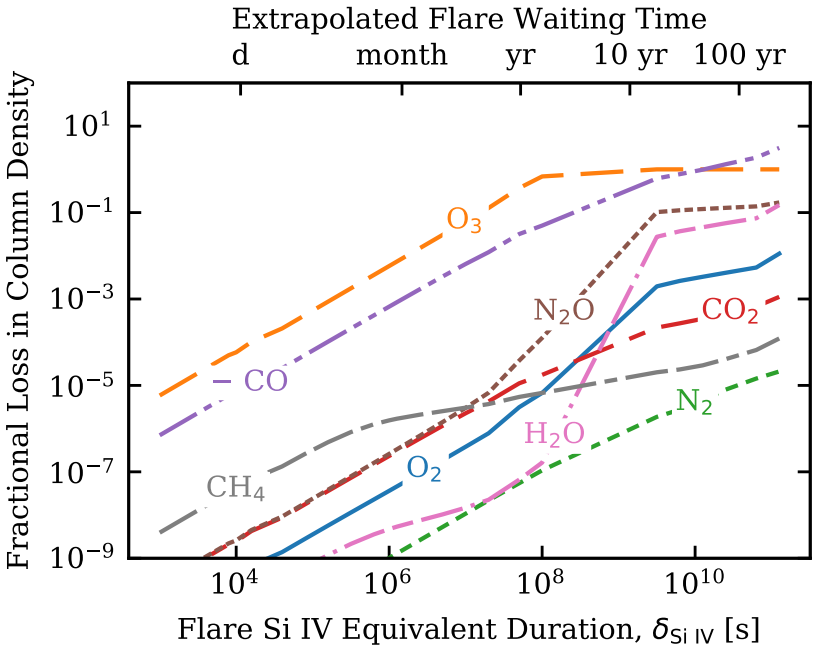

Figure 6.21 Fractional loss in column density as a function of flare energy. Changes in atmospheric opacity and scattering are primarily responsible for the nonlinear behavior of some species. CO is given as the negative of the true value because more CO is created from the dissociation of CO_2 than is lost.

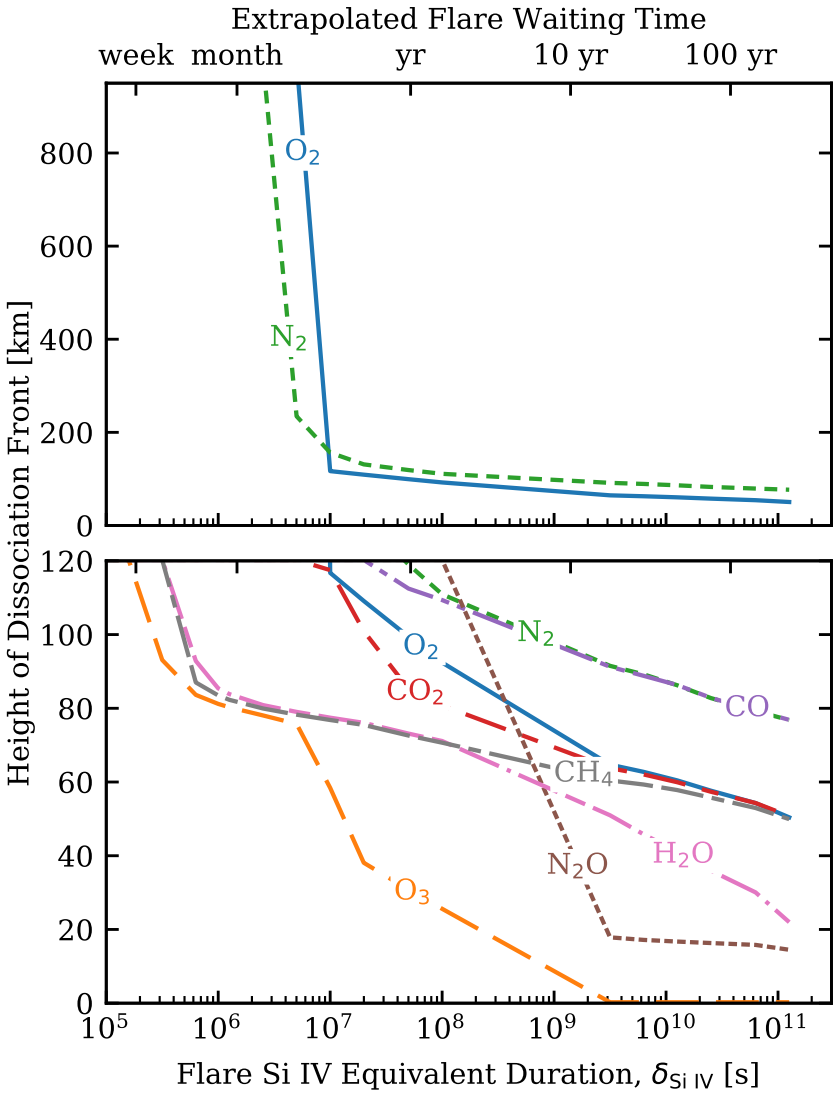

Figure 6.22 Depth of the dissociation as a function of flare energy, defined as the altitude above which at least 90% of the species has been dissociated. The kink in N_2O is a result of the coarse flare energy grid.

6.4.3 Timescale of Recovery from Impulsive Photolysis

To gauge the longevity of the effects predicted in the previous section, I estimated representative recombination timescales for the dissociated species in the model atmospheres. I excluded CH_4 since I did not have data on the preflare concentrations of its dissociation products. To estimate recombination timescales, I traced all possible molecular recombination pathways that net to the desired recombination reaction and involve only the atoms and molecules N_2, O_2, H_2O, CO_2, CH_4, O_3, H_2, H, O, N, C, OH, $O(^1D)$, NO_2, N_2O, NO, and CO. I considered all reactions from the list compiled by Hu et al. (2012) in generating these networks. For example, one such possible network for the recombination of CO_2 is

$$O_2 + O + M \longrightarrow O_3 + M \tag{6.6a}$$

$$O_3 + H \longrightarrow O_2 + OH \tag{6.6b}$$

$$CO + OH \longrightarrow CO_2 + H, \tag{6.6c}$$

though I do not predict this network to be the fastest.

For each pathway, I summed the inverse reaction rates of all reactions in the pathway to approximate the recombination timescale through it. I then selected the shortest timescale of all the attempted pathways as an order-of-magnitude estimate of the timescale for the atmosphere to recover a significant fraction of its original concentration of the molecule in question.

I also considered single recombination reactions that could provide a faster pathway to recombination by including extraneous reactants or products (i.e. that did not net simply to the reverse of the photolysis reaction). If this provided a faster reaction pathway without depleting the reactant stock, I recorded the associated timescale. For example, much of the atmosphere has enough OH to enable reaction 6.6c on its own, without requiring the creation of additional OH for it to continue to completion.

I have plotted the recombination timescales and listed the associated reactions in Figure 6.23. The fastest recombination pathway can vary between altitudes, since composition and temperature change with altitude. Recombination timescales longer than a day only occur for altitudes above

70 km for most species. However, flares occurring with a frequency of days have a typical energy more than four orders of magnitude below those capable of the dissociation considered in the figure. Therefore, for an Earth-like planet, compositional changes related to FUV radiation from M dwarf flares are likely to be restricted to regions well above 70 km. Barring associated affects from particles (see Section 6.4.5), even the largest flares with any observational footing will not produce a significant change in the column density of any species considered lasting more than roughly an hour after the flare ends.

6.4.4 A Discussion of Mass Loss

In addition to inducing photochemsitry in an atmosphere, flares will enhance atmospheric escape. The escape of exoplanet atmospheres, namely of hydrogen, can inhabit many different regimes according to the bottleneck of the process. Earth's hydrogen escape, for example, is diffusion limited: as fast as hydrogen can be transported to the exobase, it escapes. Escape can also be limited by the rate at which atomic hydrogen is photolyzed from a heavy molecule (Hunten, 1982).

For planets orbiting very near their star, photoionization heating of the upper atmosphere by the stellar EUV can be intense enough to power hydrodynamic escape, i.e. an outflow wind (Lammer et al., 2003). Hydrodynamic escape is predicted to be bottlenecked by the rate of energy absorption (energy-limited), the rate of radiative cooling (recombination-limited), or, less-commonly, the rate of ionizations (photon-limited; Murray-Clay et al. 2009; Owen & Adams 2016). The rate of escape is energy-limited (or photon-limited) at low levels of irradiation and scales linearly with the received ionizing radiation flux F. At high levels of irradiation, it transitions to recombination-limited and scales roughly as $F^{1/2}$.

If these relationships roughly hold for the impulsive energy input of flares, then the impact of additional ionizing flux from flares is clear: it will increase the overall escape according to the $F^{1/2}$ – F scaling of the mass loss rate. Assuming the distribution of EUV flare energies follows roughly that of the FUV, then, as discussed in 6.3.5.1, the upper limit on flare energies could drive

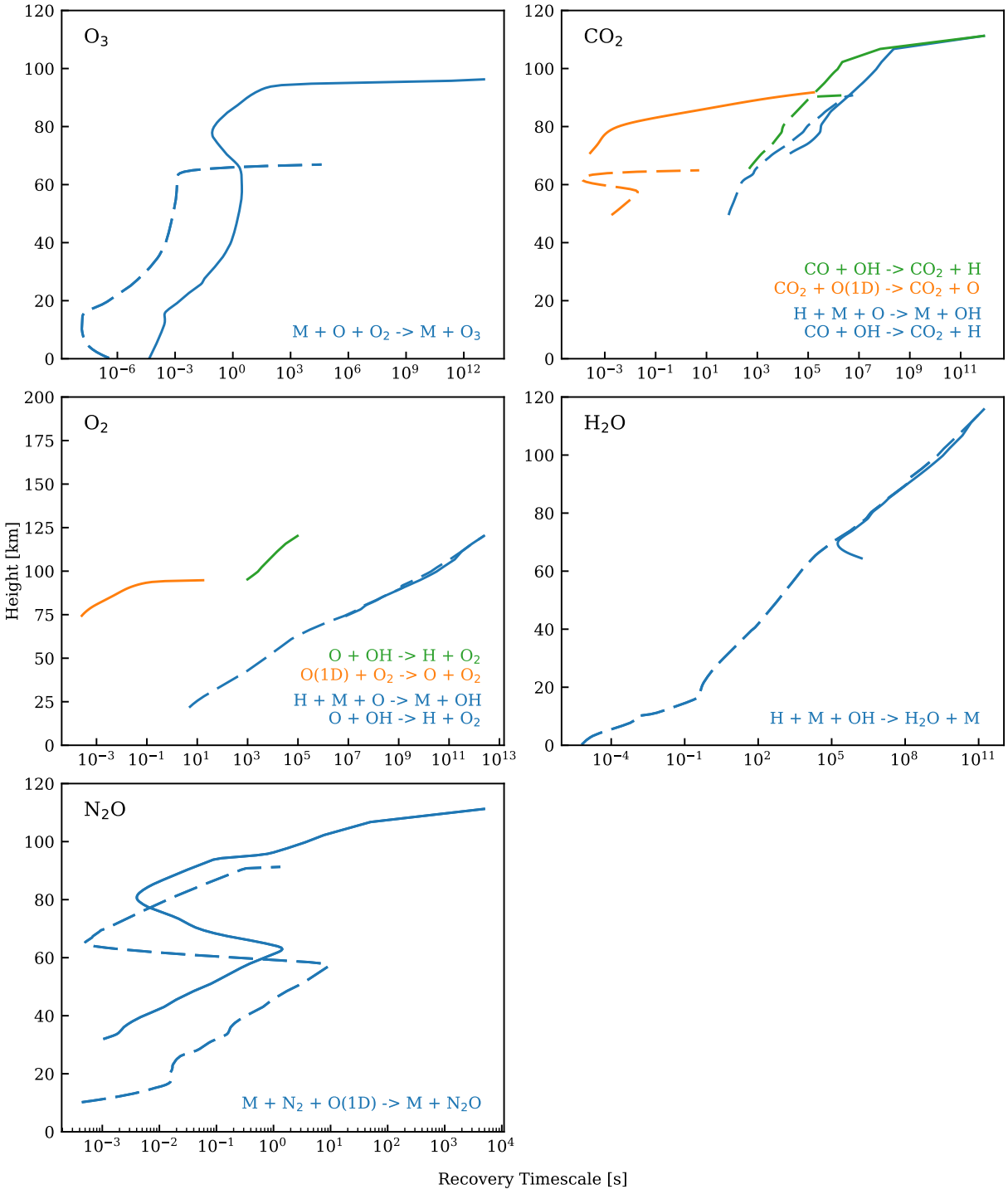

Figure 6.23 Order-of-magnitude estimate of the recombination timescale following dissociation by a $\delta = 10^8$ s flare (solid lines) or a $\delta = 10^{9.5}$ s flare (dashed lines). See text for a description of how this value was computed. Only regions where $> 1\%$ of the molecules were dissociated are plotted (hence the greater depth of the dashed lines). For O_3 and N_2O, at high altitude the dissociation products were themselves dissociated. Recombination timescales were not computed in these areas.

the overall atmospheric escape rate. Indeed, flare driven escape has been conjectured to be the cause of variability observed in the Lyα transit of the hot Jupiter HD 189733b (Lecavelier des Etangs et al., 2012). Future work is needed to determine if the impulsive input of flare energy is as effective as steady-state EUV flux in powering escape.

6.4.5 The Glaring Unknown in Mass Loss: Particle Events

While flare radiation might well dominate over quiescent radiation in powering escape, associated particle events could dominate over both. On the Sun, coronal mass ejections are a daily event (Yashiro et al., 2004), and nearly all solar flares above a particular energy level (roughly GOES X class) are accompanied by CMEs (Aarnio et al., 2011). Both the CMEs themselves and solar energetic particles emanating from the shock ahead of the CME (see, e.g., Ryan et al. 2000) can impact planets and increase escape (e.g. Jakosky et al. 2015). This could potentially remove entire planetary atmospheres (Khodachenko et al., 2007a; Lammer et al., 2007; Airapetian et al., 2017). Further, energetic particles could initiate nonthermal chemistry (beyond that initiated by the FUV photons), synthesizing precursors to organic molecules, generating greenhouse gases, and diminishing ozone (Segura et al., 2010; Airapetian et al., 2016), with effects potentially lasting for thousands of years (Segura et al., 2010).

At present, there is no widely-accepted observational evidence of stellar CMEs or energetic particle events, despite recent searches for radio bursts associated with energetic particles (Crosley et al., 2016; Villadsen et al., 2017). There are physical reasons to believe that M dwarf flares could behave quite differently than solar flares in ejecting mass. Mass and energy budgets inferred from solar scalings produce unphysical results for M dwarfs (Drake et al., 2013), and strong overlying magnetic fields have been proposed as a mechanism by which M dwarfs might contain flare plasma (Osten & Wolk, 2015; Harra et al., 2016; Drake et al., 2016). However, the particle events associated with flares could drive planetary habitability, so an essential step in this field is the development of an observational means of detecting or firmly constraining the particle events associated with stellar flares.

6.5 Conclusions

I have analyzed spectrophotometric FUV data from 7 M dwarfs from the MUSCLES survey and 4 M dwarf flare stars with archival data to identify and characterize flares. All M dwarfs except one (with poor S/N) flared. The fractional contribution of these flares to the stars' FUV emission, did not correlate with Ca II K flux or rotation period, implying that M dwarf flare activity is the rule rather than the exception. The best predictor of flare activity in this sample is a low effective temperature.

Flare frequency distributions (FFDs) created by aggregating all flares from the MUSCLES and flare star M dwarfs as separate groups revealed that the known flare stars flared about and order of magnitude more frequently for a given absolute flare energy. In relative energy (equivalent duration), however, the two distributions are identical. The relative distributions show some 3 orders of magnitude more frequent flaring than the Sun in lines of similar formation temperature. Power-law fits to the cumulative FFDs have an index of ~ -0.7 that implies large, unobserved flares will dominate the FUV emission of the star if the power law holds to energies some 3 orders of magnitude beyond the most energetic flares observed. Results from U band and *Kepler* surveys suggest this is likely. This is an important result due to its implications for photochemsitry in and escape of planetary atmospheres. Consequently, I hypothesize that estimates of mass loss rates from close-in, hydrodynamically-evaporating planets based on brief observations of stellar flux will systematically underpredict escape rates.

The spectral distribution of energy from the flares was generally consistent between events. I quantified the typical flare energy budget over the observed wavelength range, then used various scaling relations to extended it through the full FUV and NUV so that it can be applied to studies of atmospheric photochemistry. A Python module is available to generate consistent model input data from this energy budget. The energy budget consistency does not appear to extend to the X-ray, though the data are too scant for a firm conclusion.

I applied the fiducial flare to a model of impulsive photolysis of species in an Earth-like

atmosphere and found that a significant change in ozone begins for flares about 100× as energetic (in relative units, 10× in absolute units) as the largest detected in this survey. At $10^4\times$ as energetic as the largest flare of this survey, ozone is completely dissociated. However, most other species remain essentially unaffected above about 20 km in the Earth-like atmosphere. An order-of-magnitude estimate of recombination timescales suggests that these perturbations will not generally outlive the flare unless other chemical effects that I did not include play a role. Further nonthermal chemistry from associated particle-events is one such excluded factor. To comprehensively assess the climate implications of M dwarf flares, a means of observationally constraining particle events and CMEs associated with stellar flares is an essential future step.

Chapter 7

Summary

M dwarf stars might represent countless nurseries for life in our galaxy, or they might represent countless false starts. Resolving this unknown will require a detailed knowledge of these stars. In this thesis, I have presented a body of work applying time series far-ultraviolet observations to the study of these stars and the planets that orbit them.

An initial analysis of archival data that also included spectral types as early as F revealed the prevalency of brief flares, over 50% lasting < 4 min in stellar FUV emission. Non-flare fluctuations in emission from FUV lines in these data spanned relative levels of 1 – 41% at minute cadences, implying that variability could mask the transit of Earth-sized disks in FUV emission lines and potentially Jupiter-size disks for the more variable sources.

The body of spectrophotometric ultraviolet data on M dwarfs was greatly expanded in 2015 by the MUSCLES Treasury Survey. I created a panchromatic spectral atlas of the 7 M dwarfs and 4 K dwarfs in this survey. These spectra imply differences in the top-of-the-atmosphere photolysis rates spanning an order of magnitude between sources. For the coolest stars, the spectra dissociate ozone predominantly with visible rather than NUV flux, due simply to the paucity of photospheric NUV flux. The spectrum of one star, ϵ Eri, had sufficient S/N to enable a detailed look at the FUV continuum, revealing that the continuum surrounding 1520 Å might be comprised of a Si II recombination edge.

The MUSCLES data of GJ 436 coincided with the extended transit of that system's hot-Neptune. A search for absorption by C II and Si III in these data showed no transit, despite the

deep $> 50\%$ transit in Lyα. Upper limits on the C II transit proved consistent with photochemical-hydrodynamical modeling that predicted relatively low ionization and a surprising presence of molecules in the GJ 436b outflow.

Of particular importance in the MUSCLES data were stellar flares. These could have critical consequences for the climates of planets orbiting M dwarfs. I analyzed all of the MUSCLES variability data to identify and characterize flares on the MUSCLES targets as well as 4 M dwarf flare stars with archival data. The resulting flare sample confirmed that FUV flares are ubiquitous on M dwarfs. In relative units, flare rates appear unrelated to M dwarf activity levels and rotation rates. Indeed, power law fits to the equivalent duration (a relative measure of energy) of flares aggregated from the sample of flare stars showed no discernible difference to those aggregated from the comparatively inactive MUSCLES stars. However, in absolute energy the flare stars exhibited about an order of magnitude more flares above a given energy threshold. These flares contribute significantly to the FUV radiation budget of the stars, and it appears likely that the rarer, more energetic flares that were not observed dominate this energy budget.

From the flare sample, I created a standardized flare spectral and temporal energy distribution for use in future modeling. I applied this "fiducial flare" input to a custom model of impulsive atmospheric dissociation to gauge the possible magnitude of the effect of the observed flares on an Earth-like atmosphere. The effect of the observed flares was minimal, but flares that a power-law fit to the flare population predicts could occur on a yearly basis could photolyze most of the atmospheric ozone in a single event. Despite the severity of such an event, estimates of recombination timescales suggest that, barring additional nonthermal chemistry, the effect of such an event is short-lived.

Future work will include further observations of the GJ 436b planetary system, development of an observing technique to constrain CMEs associated with stellar flares, and modeling of flare-induced atmospheric escape.

Chapter 8

Future Work

8.1 Investigation of a Potential Star Planet Interaction in the GJ 436 System

The transit observations of GJ 436b led to the discovery of a peak in the star's N V flux during transit that is suggestive of an SPI. Therefore, I have pursued further observations through an HST proposal. The proposed observations were accepted for *HST* observing cycle 25. Below, I have included this proposal, with portions concerning only the practicalities of observing removed. The data will likely arrive in the spring of 2018, revealing whether this tentative SPI is present or not.

8.1.1 Background and Motivation

Exoplanets offer a wealth of laboratories for testing models of stellar and planetary physics in systems far different from our own. One example is systems where planets orbit close enough to their host star to interact. These star planet interactions (SPIs) include tides (Cuntz et al., 2000), mass exchange (Pillitteri et al., 2015), and magnetic disturbances (Cuntz et al., 2000). The study of magnetic interactions could eventually help constrain planetary magnetic fields (Shkolnik et al., 2003, 2005, 2008; Shkolnik, 2013). Recent evidence suggests emission from the transition-region of stellar upper-atmospheres, rarely used in previous SPI experiments, could be a powerful tracer of SPI signals (France et al., 2016a).

Transition-region emission also drives planetary atmospheric photochemistry (e.g. Hu et al. 2012) and permits observations of atmospheric escape (e.g. Linsky et al. 2010), yet observations of

its variability over the course of days (rather than hours or years) are few. I propose augmenting upcoming FUV transit observations (program 14767) of the hot Neptune GJ 436b with out-of-transit observations targeting four phase points in each of two separate planetary orbits. Specifically, I want to solidify a tentative SPI signal and provide the broader variability baseline needed for the interpretation of the planetary transit.

8.1.2 Stellar Hot Spots and the Prospect of Developing Probes for Planetary B Fields

The ability of a planet to influence its host star was postulated shortly after the first exoplanet discoveries with the suggestion that stellar superflares result from magnetic reconnection of stellar and planetary fields (Rubenstein & Schaefer, 2000). Since that suggestion, a variety of mechanisms have been proposed that would create a localized enhancement of stellar emission, i.e. a "hot spot," that traverses the stellar surface as the planet orbits. These can be broadly categorized into magnetic and material interactions.

Magnetic interactions include reconnecting stellar and planetary magnetic fields (Lanza, 2008, 2009; Cohen et al., 2009), and the generation and propagation of Alfvén waves (Preusse et al., 2006; Kopp et al., 2011). If the planet orbits within the stellar Alfvén radius, these perturbations are transmitted to the stellar surface. Magnetic SPIs are of particular importance because they have the potential, with further observational development, of helping to constrain planetary magnetic fields. A magnetic SPI dissipates energy at a rate that is proportional to the relative velocity of the planet, the stellar magnetic field strength, and the planetary magnetic field strength (e.g. Lanza 2009). *All but the planetary field strength can be determined with current observational tools, meaning that a measurement of SPI power would provide an estimate of a planet's magnetic field strength.*

Material interactions include (1) beams of electrons or ions directed through magnetic flux tubes (Gu & Suzuki, 2009) and (2) the accretion of gas escaping a planet's atmosphere (Matsakos et al., 2015). Electron beams (1) have an observational basis in Jupiter, where several moons

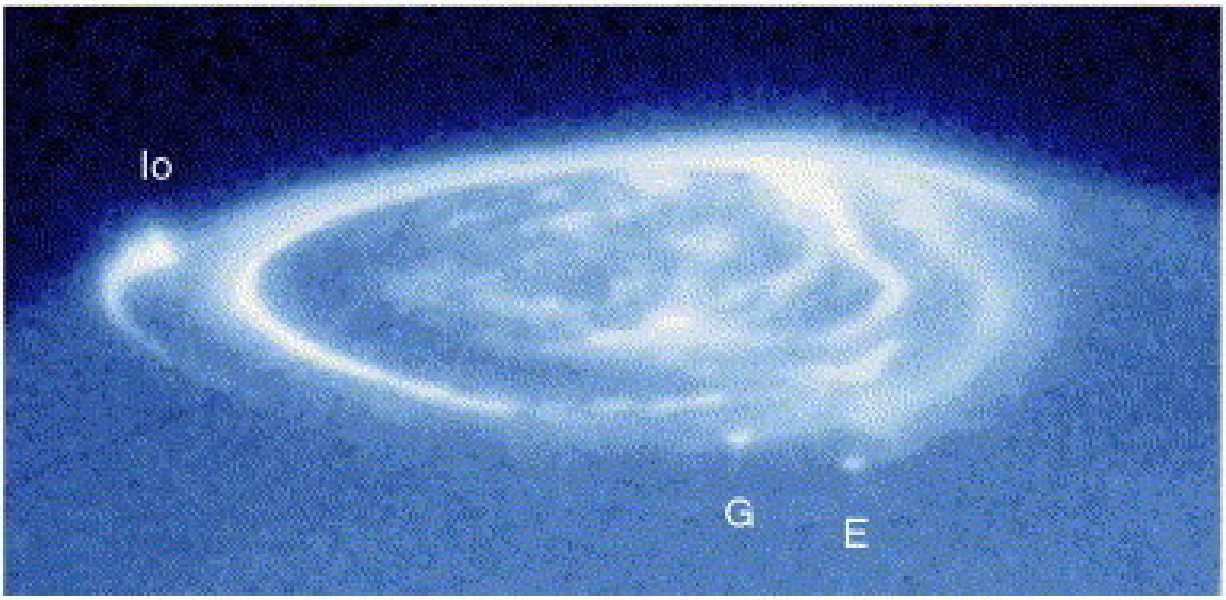

Figure 8.1 *HST* UV image of auroral emission from the north pole of Jupiter, with footprints of charged particles from Io, Ganymede (G), and Europa (E). An analogous scenario could occur for stars with significant dipolar magnetic fields and close-in planets. Image from Clarke et al. (2002).

produce a footprints of UV emission on the planet that are observable with *HST* (Figure 8.1; Clarke et al. 2002). The accretion hypothesis (2) is bolstered by the several exoplanets with atmospheres known to be escaping at hydrodynamic rates (Vidal-Madjar et al., 2003; Lecavelier Des Etangs et al., 2010; Fossati et al., 2010; Kulow et al., 2014). Simulations show that some of the gas escaping such planets could be funneled onto the star (Matsakos et al., 2015; Pillitteri et al., 2015). Both beams and accretion are magnetically controlled, and therefore could also eventually yield observational tools to constrain planetary magnetic fields. By offering a window into intriguing physical interactions and potentially probing magnetic field strengths, SPIs are valuable to stellar and planetary physics.

8.1.3 Previous Work and the Need for Observations Using Transition-Region Emission

SPI observations can be divided into two broad categories: "population statistics" studies that seek to correlate activity among a stellar sample with proxies of SPI strength or "orbit-phased variability" observations that seek to measure modulation in stellar activity from a planet-induced hot spot. The orbit-phased variability approach, applied to Ca II H & K observations of the HD 179949 system, yielded the first-ever evidence of a SPI, with the SPI signal appearing in 20% of the orbits (Shkolnik et al., 2003, 2008; Gurdemir et al., 2012). Tentative SPI evidence through Ca II K emission variability has also been obtained for ν And, HD 189733, τ Boo (Shkolnik et al., 2008; Walker et al., 2008). The HD 189733 system shows consistent X-ray and FUV flares near secondary transit of its hot-Jupiter that have led to the suggestion of an accretion stream (Pillitteri et al., 2011, 2014, 2015).

The population statistics approach has yielded further evidence of SPIs, the first being a correlation between Ca II H & K variability and planet mass over orbital period ($M_{\rm plan}/P_{\rm plan}$), a proxy for the strength of a magnetic SPI (Shkolnik et al., 2005). Overall Ca II H & K emission was found to be elevated for stars with close-in versus far-out planets by Krejčová & Budaj (2012), a result supported by (Gonzalez, 2011) and contradicted by (Canto Martins et al., 2011). In the

X-ray, Kashyap et al. (2008) found evidence of SPI enhancements for stars with close-in planets. Later X-ray studies have yielded results that mostly do not confidently exceed those expected from various selection biases (e.g. Poppenhaeger et al. 2010; Scharf 2010; Poppenhaeger & Schmitt 2011; Miller et al. 2015).

The work mentioned above is only a subset of the SPI observational literature, yet it reveals a theme in the field: studies have relied almost entirely on optical and X-ray wavelengths. As exceptions, Shkolnik (2013) utilized *GALEX* FUV photometry for a population study and Pillitteri et al. 2015 used *HST* FUV spectroscopy to detect flares at the secondary transit of HD 189733b. Yet FUV spectroscopy is a powerful observational tool because emission from lines formed in different regions of the stellar upper atmosphere can be isolated.

Recently, a population study using FUV emission lines was enabled by the MUSCLES Treasury Survey. In these data stellar emission in several FUV lines, such as N V $\lambda\lambda$1238,1242, show a strong correlation with $M_{\rm plan}/a_{\rm plan}$ (Figure 8.2). Importantly, these correlations increase in strength with increasing line formation temperature (Figure 8.3). *This result suggests that transition-region emission, namely N V, could trace SPIs better than the Ca II H & K chromospheric emission so often relied upon for SPI observations. It is essential that this possibility be further explored.*

8.1.4 A Glimpse of a SPI Hot Spot in *HST* COS Observations of the GJ 436 System

The GJ 436 system hosts a hot Neptune, GJ 436b, orbiting closely at 14 $R_\star$ and undergoing vigorous atmospheric escape (Kulow et al., 2014; Ehrenreich et al., 2015). Observations from the recent MUSCLES Treasury Survey happened to catch the GJ 436 system at the transit of the hot-Neptune (Loyd et al., 2017a). During these observations, the N V flux peaked as the planet transited (Figure 8.4). Considering the evidence toward N V as a tracer of SPIs (Figure 8.3), the N V lightcurve of GJ 436 is particularly suggestive. A SPI-induced hot spot traversing the stellar disk in phase with the 2.6 d orbit of the planet produces a model that fits the N V lightcurve well. *Given the high escape rate for this planet, a likely hypothesis is that some fraction of the escaped gas is being*

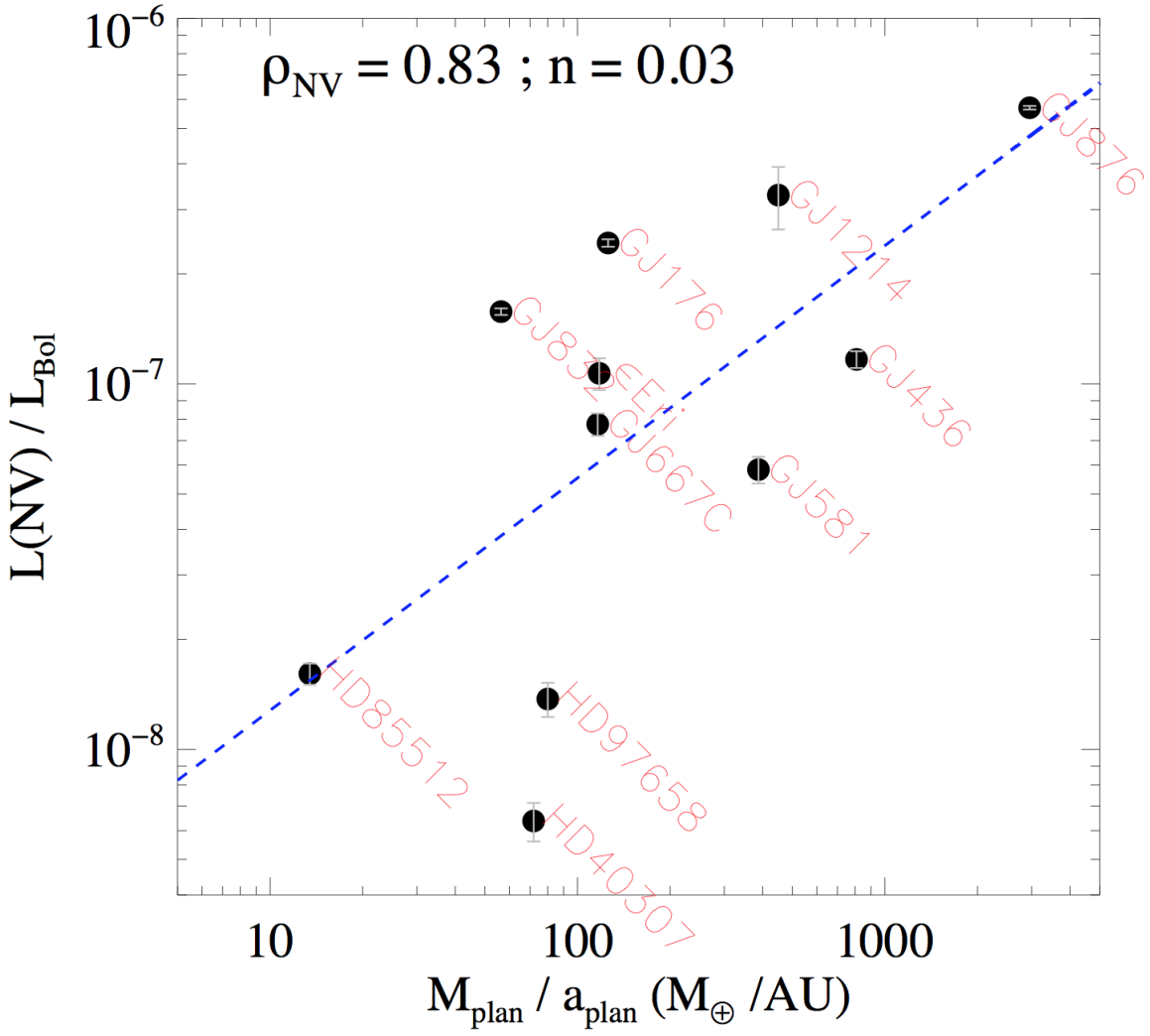

Figure 8.2 N V flux of the MUSCLES K + M dwarfs, normalized by their bolometric flux and plotted against the ratio of mass to semi-major axis, $M_{\rm plan}/a_{\rm plan}$ of the most massive planet in the system. The strong correlation between N V flux and $M_{\rm plan}/a_{\rm plan}$ is evidence that N V flux is influenced by SPIs in these systems. Figure from France et al. (2016a).

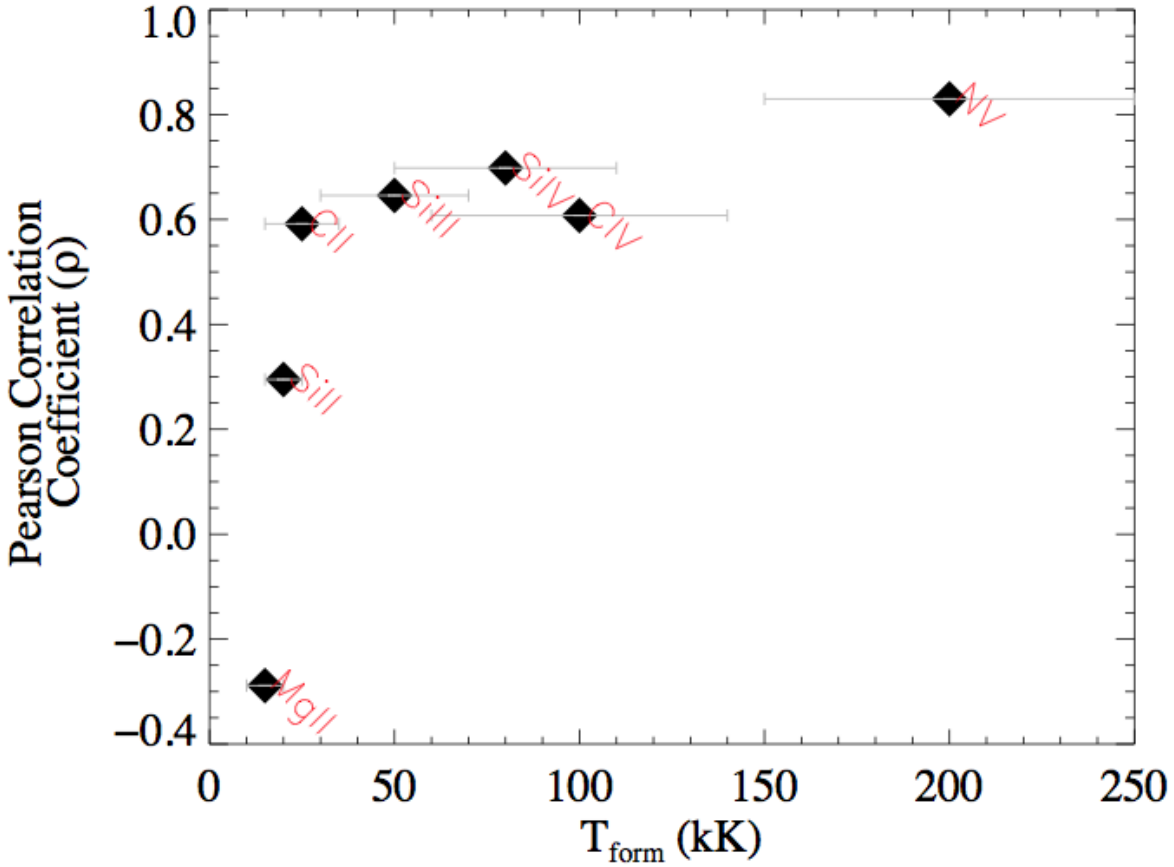

Figure 8.3 Pearson correlation coefficients for normalized line flux versus $M_{\rm plan}/a_{\rm plan}$ (i.e. for scatter plots like Figure 8.2) versus the line formation temperature of major UV emission lines. The increase in correlation strength with temperature suggests that SPIs manifest more strongly higher in the stellar atmosphere. Figure from France et al. (2016a).

accreted by the star. Other mechanisms discussed earlier (Alfvén waves and an electron beam) are possible as well. However, the incomplete phase coverage (-0.06 – 0.05) of the observations restricts the interpretation of this SPI signal to tentative. To confirm this interpretation, I require N V observations with complete phase coverage, sampling N V flux changes over two planetary orbits to eliminate "normal" stellar variability as the source of the observed N V lightcurve shape.

8.1.5 Constraining the Day-Timescale Variability and Facular Emission of GJ 436

The FUV flux of a star drives photochemistry in planetary atmospheres (e.g. Miguel et al. 2015), and the closely-related EUV flux drives atmospheric escape (e.g. Lammer et al. 2003). The variability of FUV emission lines has been constrained over the course of a transit (Loyd & France, 2014), but not over the course of days. *HST* observations spaced by one or a few days are rare; instead, they are usually spread over only a few hours during a single visit, with separate visits spaced by months or years. Because the proposed SPI observations must sample the 2.6 day orbital period of GJ 436b, they will also constrain how the critical FUV input to the hot-Neptune's atmosphere varies over this timescale.

In addition, by spacing the two sets of proposed observations by roughly half the 39.9 d stellar rotation period, the difference in flux between stellar hemispheres can be measured to place a lower limit of the contribution of stellar faculae to FUV emission. This is important given that such faculae can substantially alter the depth of an observed transit, producing large errors in the inferred size of a planet or its extended atmosphere (Llama & Shkolnik, 2015). These constraints will assist in the interpretation of three upcoming FUV transit observations of GJ 436 (program 14767, PI Sing). I therefore waive the proprietary period so that analyses of the transit data from program 14767 can immediately incorporate the observations I propose.

8.1.6 Using *HST* to Probe FUV Variability and a SPI for GJ 436

HST is the only operating observatory that can conduct spectrophotometry of FUV emission lines, addressing a critical gap in SPI experiments. The GJ 436 system makes an excellent

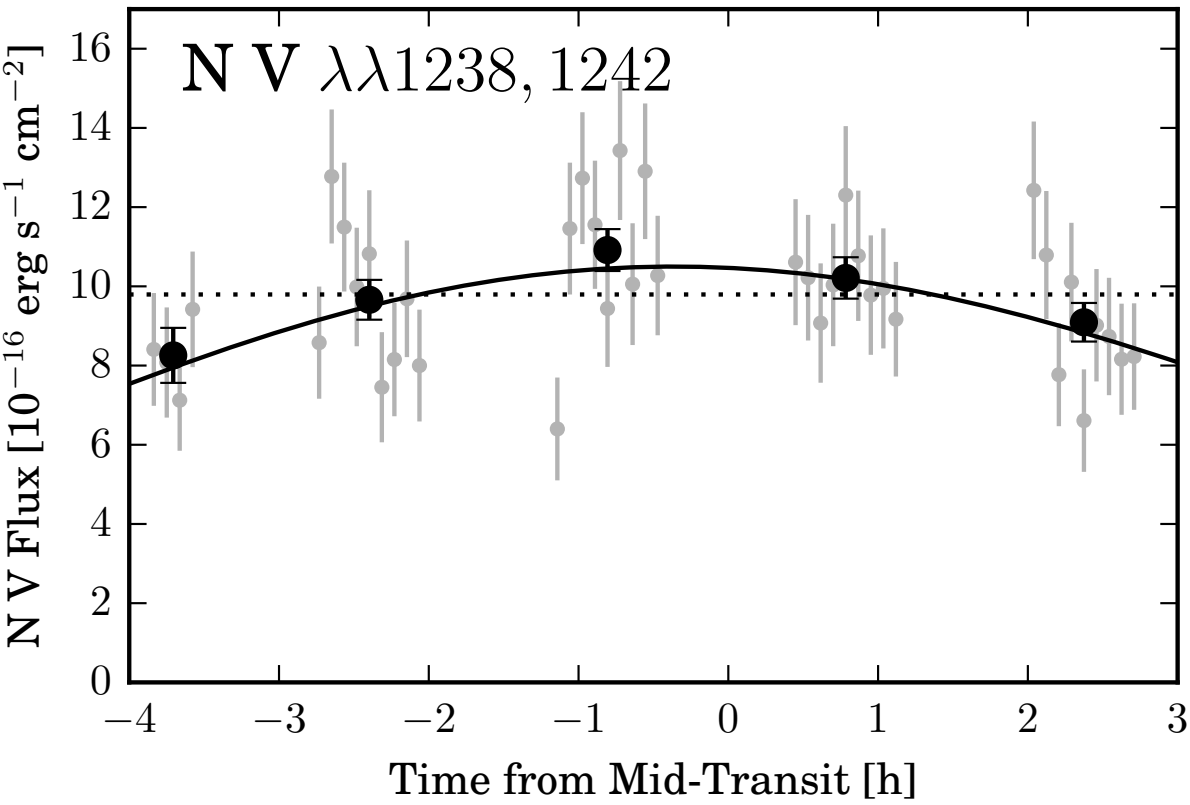

Figure 8.4 Light curve of the N V flux during the MUSCLES observations. The black line is a model of a hot spot traversing the stellar disk as the planet orbits, and yields a reduced χ^2 value of 0.81 (0.8 σ below expectation). The proposed observations will sample the curve well away from its peak to confirm the hot spot model.

subject for such an experiment because of its tentative SPI signal. Further, this system has been demonstrated as safe to observe with COS. If the tentative SPI signal proves robust with further observations, this program will demonstrate a new tool for observing SPIs that could eventually lead to constraints on planetary magnetic fields. A null result will provide valuable evidence against SPI induced hot spots to explain the N V – SPI correlation (Figure 8.3). Independent of the SPI experiment, these data will provide critical constraints on the baseline variability of the GJ 436 system in the FUV needed to interpret transit observations of its extended atmosphere. The FUV capabilities of *HST* are essential to investigating the new window into SPIs that transition-region emission lines provide.

8.2 Pioneering Observations to Constrain Stellar Coronal Mass Ejections through Dimming of FUV Iron Lines

As mentioned in Chapter 6.4, a major unknown for exoplanet climate evolution is stellar particle events. I have estimated that the dimming in coronal lines observed after solar CMEs might also be observable following stellar CMEs using Fe lines in the FUV. Below, I include an *HST* proposal I have written requesting such observations.

8.2.1 Motivation: The Habitability of M Dwarf Exoplanets

Stellar coronal mass ejections (CMEs) are a critical unknown for the climate and evolution of M dwarf exoplanets. Planets in the path of CMEs experience enhanced atmospheric escape and non-thermal atmospheric chemistry (e.g. Jakosky et al. 2015; Airapetian et al. 2016). This is particularly problematic for M dwarf systems, which are currently in the limelight of exoplanet science (see Shields et al. 2016 for an overview). CMEs accompanying the frequent and energetic flares of M dwarfs could potentially remove entire planetary atmospheres (Khodachenko et al., 2007b; Lammer et al., 2007; Airapetian et al., 2017). Further, energetic particles from these CMEs could penetrate the atmosphere to synthesize precursors to organic molecules, generate greenhouse gases, and diminish ozone (Grießmeier et al., 2005; Segura et al., 2010; Airapetian et al., 2016).

The chemical effects of just a single CME could last for thousands of years (Segura et al., 2010). Because of these effects, the true habitability of planets in M dwarf "habitable zones" hinges upon stellar CMEs.

Despite the crucial importance of stellar CMEs to planetary habitability, their frequency, magnitude, and even existence on other stars is observationally unconstrained. On the Sun, CMEs are a daily event (Yashiro et al., 2004), and nearly all solar flares above a particular energy level (roughly GOES X class) are accompanied by CMEs (Aarnio et al., 2011). This suggests that CMEs are more frequent on M dwarfs because of their higher flare rates (Davenport, 2016), but there are reasons to doubt this inference (Drake et al., 2013). The true rate of CMEs on any star will not be known until these events can be directly observed. Direct observations of stellar CMEs would open a new window into the magnetic activity of stars and constrain the potentially significant contribution of CMEs to stellar mass loss and spin down (Aarnio et al., 2012; Drake et al., 2013). I therefore propose a pilot program to resolve the CME unknown. The proposed observations will measure the dimming in coronal emission lines that results when emitting material is ejected, using *HST* to directly detect and constrain stellar CMEs for the first time.

8.2.2 Are M Dwarf Flares Accompanied by Sun-like CMEs?

Thus far, estimates of stellar CME rates and properties have relied on solar empirical relationships (e.g. Segura et al. 2010). However, there is reason to suspect that M dwarf coronae behave differently, rendering solar relationships inapplicable. Taking the flare rates of active M dwarfs and applying CME-flare scalings from the Sun yields a "CME catastrophe": the predicted mass and energy loss are physically unrealistic (Drake et al., 2013, 2016). One way to suppress CME mass loss is through containment of CME plasma by strong overlying magnetic fields (Osten & Wolk, 2015; Harra et al., 2016; Drake et al., 2016). This phenomenon has been observed for high energy solar flares not accompanied by CMEs (Thalmann et al., 2015; Sun et al., 2015). If overlying field is indeed a determining factor in launching a CME, the super-solar (kiloGauss) magnetic fields of M dwarfs could offset their super-solar flare rates. The suppression of CMEs would be a boon to

the potential habitability of M dwarf exoplanets. Whether M dwarfs produce Sun-like CMEs will not be known until observations detect their CMEs or place firm upper limits on their sizes.

8.2.3 Previous Attempts at Detecting Stellar CMEs

While the exoplanet revolution has added a new impetus for understanding stellar CMEs, searches for stellar CMEs predate it. Previous observers have suggested that CMEs caused obscurations of stellar emission (e.g. Ambruster et al. 1986; Favata & Schmitt 1999; Bond et al. 2001); changes in emission line kinematics (Houdebine et al., 1990; Fuhrmeister & Schmitt, 2004; Vida et al., 2016); or anomalously slow decays in flare emission (Cully et al., 1994; Katsova et al., 1999). However, none of these claims has been adopted by the community as definitive evidence of stellar CMEs. Further, additional attempts at detecting CMEs through line kinematics have proved unfruitful (Leitzinger et al., 2011, 2014).

Radio observations present another method to search for stellar CMEs. In the solar corona, CME-driven shocks produce radio emission at the plasma frequency, with a characteristic frequency decay as the CME expands outward into lower density regions (e.g., Kouloumvakos et al. 2014). There are no clear detections of stellar CMEs by this method at present (Leitzinger et al., 2009; Crosley et al., 2016; Villadsen et al., 2017).

8.2.3.1 Coronal Dimming: a Sun-approved Tool for Directly Detecting CMEs

On the Sun, dimming of disk-integrated coronal emission occurs as a direct result of material being ejected during a CME (Woods et al., 2011; Mason et al., 2014). The mechanism is straightforward: the ejected material leaves a dark void in an otherwise bright corona. The effect is only observable in isolated emission lines that trace the temperature of the quiescent coronae. Their emission spikes with the flare, then rapidly decreases below the pre-flare level, recovering gradually over the course of hours. An example is shown in Figure 1. A flare followed by coronal dimming is the most reliable indication that a CME has occurred. When Harra et al. (2016) tested a bevy of disk-integrated observables, they found “only one feature consistently associated with CME-related

flares specifically: coronal dimming in lines characteristic of the quiet-Sun corona."

Mason et al. (2016) demonstrated that solar coronal dimming can be used not only to detect but also to characterize solar CMEs. The amount of emitting material ejected (CME mass) determines the drop in emission (dimming depth) and the speed at which it is ejected (CME velocity) determines the rate of this drop (dimming slope). This same reasoning applies to any star. Further, it implies that M dwarfs will exhibit dimmings deeper than the Sun's: for equivalent CME masses, those on M dwarfs will remove a larger fraction of the emitting coronal material. For example, a $6{\times}10^{15}$ g CME, typical of an X class solar flare (Aarnio et al., 2011), would produce an $\sim$20% dimming for AU Mic (using the coronal emission measure and density estimates of Ness et al. 2004) and an $\sim$6% dimming for the Sun (Mason et al., 2016). (This reasoning is developed more thoroughly in the Description of Observations.) The solar heritage and simplicity of coronal dimming make it the ideal tool for detecting stellar CMEs.

8.2.4 *HST* + *Chandra*: The Key to Constraining Stellar CMEs

Solar coronal dimming observations rely on the many bright coronal emission lines in the EUV. However, for stars the EUV is absorbed by the ISM before reaching Earth. Therefore, other bands must be used to detect stellar coronal dimming. Visible coronal lines exist, but they were largely undetectable in *Very Large Telescope* observations of M dwarfs (Fuhrmeister et al., 2004). Another possibility is the X-ray, but I estimate that the best SNR current X-ray instruments could achieve when integrating only a single coronal line is an order of magnitude too poor to measure dimmings. (However, X-ray observations are needed to provide another critical piece of information, as will be described shortly.)

The most promising band for precise photometry of stellar coronal lines is the FUV. Within the FUV, four major Fe lines are accessible that sample formation temperatures from 2 – 10 MK: Fe XIX 1118 Å, Fe XII 1242,1349 Å, and Fe XXI 1354 Å. This range of formation temperatures is well-suited to observing coronal dimming, which is most pronounced in lines with formation temperatures near that of the quiescent stellar corona. For the $\sim$1 MK corona of the Sun, Fe

XII works well (Figure 1), but for the ∼10 MK corona of active M dwarfs, Fe XXI should work better. All of the FUV coronal lines can be captured using *HST's* COS G130M/1222 configuration. This configuration enables the application of COS's superior sensitivity (>10× that of STIS) to bright targets while avoiding Lyα, Si IV, and C IV emission to ensure detector safety during flares. The resulting photometric precision reaches a few percent for the Fe lines, unlocking the ability to directly observe stellar CMEs.

On its own, *HST* can detect CMEs via dimming. However, including X-ray observations adds the ability to constrain the mass of the CME. This comes from the coronal density diagnostics that can only be accessed in the X-ray, ideally with the high energy transmission grating (LETGS) of *Chandra*. The coronal density (*Chandra*), along with the dimming depth (*HST*) and emission measure (*Chandra* or *HST*), yield an estimate of the mass of the CME (see Description of Observations). As a bonus, *Chandra* observations enable the classification of the observed stellar flares in the ubiquitous solar GOES 1 – 8 Å scheme, directly connecting them to solar flare observations.

The feasibility of observing a dimming signal with *HST* has been demonstrated by COS FUV observations of the K2 star ϵ Eri acquired for the MUSCLES survey (France et al., 2016a). These observations achieved photometric precisions of a few percent for Fe lines. Further, these data revealed a tantalizing hint of an ∼50% dimming in the coronal Fe XXI line following a flare that occurred only ∼200 s after the start of the observations (Figure 2). This is highly suggestive of a CME. Further, the high time-averaged mass loss rate of ϵ Eri measured by Wood et al. (2005) supports the idea that large CMEs could be common for this star. The uncertain pre-flare flux in these data make this possible dimming tentative, yet these observations provide a hint as to what is possible.

To clearly detect stellar CMEs via coronal dimming, I propose a pilot program of dedicated *HST* COS G130M/1222 observations with contemporaneous *Chandra* LETGS coverage of three well-characterized flare stars with the aim of capturing several flares that, on the Sun, would have a high probability of producing a measurable CME-induced dimming. The hard empirical estimates (or upper limits) on the rate and masses of CMEs these observations provide will be the

first for stars other than the Sun and validate a technique that can be expanded in later cycles to constrain CMEs on bright exoplanet hosts. ***HST* is the only operating observatory capable of detecting CMEs through coronal dimming. In so doing, it will address a critical unknown regarding the erosion of planetary atmospheres and the habitability of M dwarf planets.**

I propose a joint *HST* and *Chandra* observing campaign. The *HST* observations, consisting of three 6 orbit visits to three active, low-mass flare stars, will provide the high precision coronal line photometry needed to detect CME-induced coronal dimming. Contemporaneous *Chandra* observations will provide the coronal emission measure and density measurements necessary to constrain the mass of the CME associated with any observed dimming (or lack thereof).

8.2.5 Theoretical Framework for Constraining CMEs with Dimmings

As discussed in the Scientific Justification, coronal dimming directly results from the void created in the emitting corona by the CME. Thus, the depth of the dimming signal is the ratio of the emission measure of the ejected material to the emission measure of the entire visible corona. The emission measure of the ejected material, $EM_{\rm CME}$, is related to its mass via

$$EM_{\rm CME} = n_e^2 V_{\rm CME} = \frac{n_e m_{\rm CME}}{\mu}, \tag{8.1}$$

where n_e is the coronal electron density, $V_{\rm CME}$ is the volume of the CME void, $m_{\rm CME}$ is the mass of the CME, and μ is the mean atomic mass of the emitting material. Thus, the dimming depth, δ, is

$$\delta = \frac{EM_{\rm CME}}{EM} = \frac{n_e m_{\rm CME}}{\mu EM}, \tag{8.2}$$

where EM is the emission measure of the entire visible corona. The mass of the CME can thus be estimated from the dimming depth as

$$m_{\rm CME} = \frac{\delta \mu EM}{n_e} \tag{8.3}$$

The proposed program will measure δ using *HST* and n_e using *Chandra*. Both observations can yield estimates of EM, and μ can be safely assumed to be near that of hydrogen. Combined,

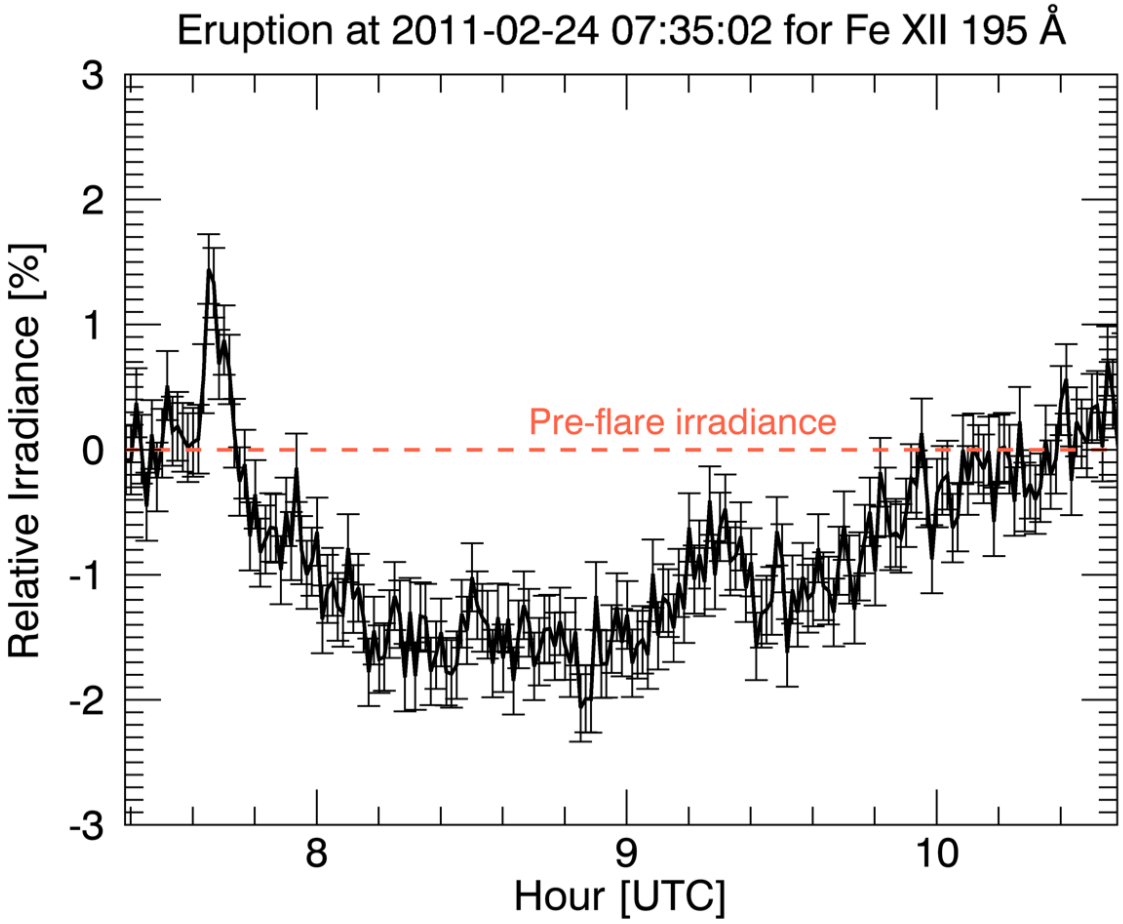

Figure 8.5 Example of the signal I will observe, but from the Sun. This is a coronal dimming lightcurve from a solar CME, showing integrated Fe XII 195 Å emission. The dimming signal is the ∼2% drop below the pre-flare value following the flare. I estimate dimming signals from Sun-like CMEs would reach tens of percent for the stellar flares I expect to observe.

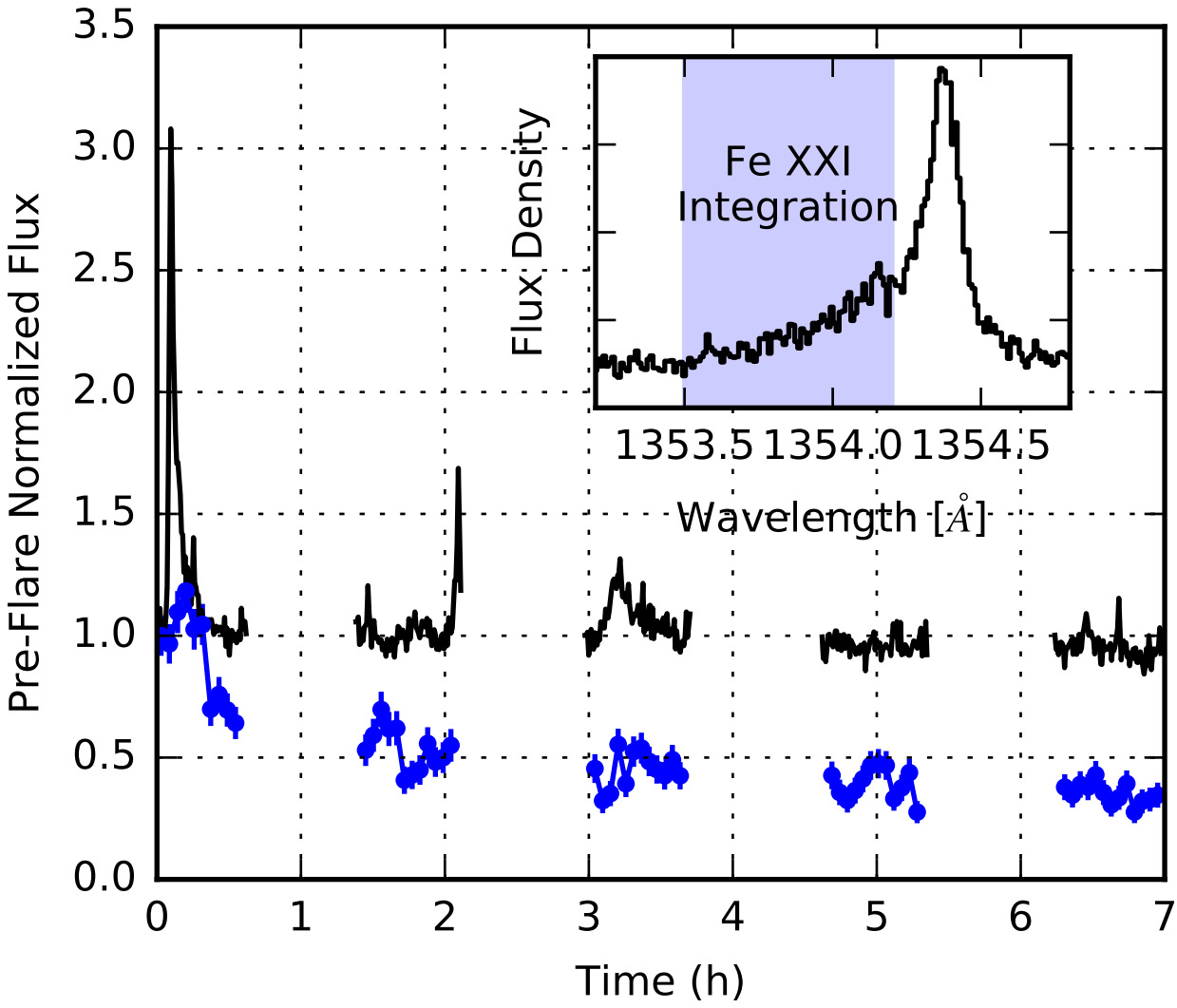

Figure 8.6 A tentative detection of coronal dimming for the star ϵ Eri in Fe XXI 1354 Å. The detection is tentative because the flare occured too close to the start of observations ($\sim$200 s) for a robust measurement of the pre-flare flux. Fe XXI is blended with C I, so I integrate only the unblended portion of the line (see inset). For comparison, a lightcurve of integrated Si IV 1393,1402 Å emission (black) is also shown. More observations are needed to capture a flare prior to its start.

these observations permit CME mass estimates that are the critical missing piece to determining the effect of stellar activity on exoplanet atmospheres.

8.2.6 Targets, their Flares, and CME Sensitivity

Given that the true CME behavior of stars is unknown, I propose multiple targets to maximize the likelihood of observing a stellar CME. The three I have selected are well-studied active stars that span a range of low-mass stellar types: M3 (AD Leo), M1 (AU Mic), and K2 (ϵ Eri). All targets have measured Fe XII 1242,1349 Å and Fe XXI 1354 Å fluxes sufficient to enable photometry at the few-percent level.

Previous X-ray observations of these stars permit an estimate of their flare rates using the GOES classification system for solar flares. This classification is based on the peak flux in the 1 – 8 Å band at 1 AU: M = 10^{-5} W m^{-2}, X = 10^{-5} W m^{-4}, X10 = 10^{-3} W m^{-2}, etc. Past data imply that the proposed observations should capture roughly one flare of >X class for AD Leo (Sciortino et al., 1999), >X10 class for AU Mic (Mitra-Kraev et al., 2005), and >M class for ϵ Eri (Pye et al., 2015; France et al., 2016a) in the 6 orbits ($\sim$9 h) devoted to each. The comparatively less energetic flares of ϵ Eri are offset by its measured cumulative mass-loss rate (per unit surface area) of $\sim$50$\times$ solar (Wood et al., 2005), increasing the likelihood that the star is exhibiting regular CMEs. This and the tentative dimming signal detected through the MUSCLES program make it worthwhile to include ϵ Eri with the two M dwarfs.

The proposed observations should be able to detect CMEs producing a $> 3\%$ dimming (taken as a representative value given the SNR estimates in the Description of Observations). Employing the framework from the previous section, this sensitivity can be translated into an estimate of the minimum detectable CME mass. For this, I use the emission measure and density estimates of Ness et al. (2004) made with multiplet lines of Ne IX (4-9 MK; AD Leo and AU Mic) and O VII (1-4 MK; ϵ Eri). This yields minimum detectable CME masses of 2×10^{14} g (AD Leo), 8×10^{14} g (AU Mic), and 7×10^{14} g (ϵ Eri). For comparison, typical solar CME masses for the >M class flares I expect to observe are a few 10^{14} to a few 10^{15} g.

8.3 Hydrodynamic Modeling of the Impact of Flares on Atmospheric Escape

The results of the MUSCLES flare observations beg for a detailed investigation of what affects flares have on exoplanet atmospheric escape. As such, I have previously applied and intend to reapply for fellowships to support modeling work that would address this question. Below is my research proposal on this topic for the 2016 Hubble fellowship.

8.3.1 Motivation

Many of the myriad exoplanets presently known are exposed to intense stellar flares. Prime examples are the habitable-zone, Earth-size planets Proxima b and Kepler-438 b, both of which are exposed to regular "superflares," flares orders of magnitude more energetic than those on the Sun (Davenport, 2016; Armstrong et al., 2016). Flares "bombard" atmospheres with increased electromagnetic (EM) flux and, for the largest flares, bursts of energetic particles that, among other effects, erode planetary atmospheres. Understanding atmospheric erosion by flares is essential to understanding the evolution of solar and extrasolar planets.

Flare bombardment of exoplanets is made particularly relevant by the preponderance of M star planet hosts. More planets orbit M stars than any other stellar type (Loyd et al. 2016 and references therein), and these stars have a long heritage of observed flaring (e.g. Hawley et al. 2014 and references therein). In a recent far ultraviolet (FUV) survey of 7 M star exoplanet hosts, 6 flared in just a few hours of observing (the MUSCLES survey; France et al. 2016b; Loyd et al. 2017a in prep). The MUSCLES flares follow a power law in frequency versus energy (Figure 6.6) that, if extended by 1 – 2 orders of magnitude, implies flares dominate the emitted energy in several strong FUV lines. Thus, flares likely contribute the bulk of the short-wavelength energy incident upon planets orbiting M-stars.

Several studies have examined the erosion of atmospheres by flare particle events (e.g. Lammer et al. 2007). However, differences in stellar magnetic field strengths and topologies can alter this process (Kay et al., 2016), and, at present, no observations of stellar particle events exist.

Meanwhile, erosion by XUV flare radiation, rather than particles, remains largely unexplored. XUV photons heat planetary upper atmospheres through photoionization and photodissociation, driving thermal atmospheric escape. Scaling solar flares to superflare levels implies that a planet at 1 AU could receive enough XUV energy over 1 Gyr to remove up to tens of bars of atmosphere. For stars, much of the XUV cannot be directly observed due to interstellar absorption, but there exist many observations of stellar flares in FUV lines that trace the same emitting regions of the stellar atmosphere as the XUV. Thus, unlike particle events, XUV flares can be empirically constrained with existing observations.

Much work has been done to address the effects of quiescent (i.e. non-flaring) XUV irradiation on atmospheric escape. This work is often motivated by known, highly-irradiated exoplanets, some of which exhibit observable atmospheric escape (e.g. Vidal-Madjar et al. 2003, Koskinen et al. 2013b). One such observation of HD 189733b led to the suggestion that this planet's atmospheric escape is mediated by flares (Lecavelier des Etangs et al., 2012). A general conclusion from the body of work on atmospheric escape is that the lifetime mass loss of highly-irradiated, Jovian-mass planets is likely negligible, whereas this might not be true for Earth-mass planets. The additional XUV energy from flares could be a critical factor in planetary atmospheric loss, motivating the research here proposed: a detailed study of atmospheric erosion by XUV flares.

8.3.2 Proposed Research

The proposed research will examine the effect of flaring XUV radiation on atmospheric escape through a 1D atmospheric model that incorporates photoionization, photochemistry, radiative transfer, and hydrodynamics. The effect of particle events, which are not observationally constrained for stars, is beyond the scope of this work.

8.3.2.1 Determining the XUV Fluence of Observed Flares

Interstellar Lyman continuum absorption prevents the direct observation of stellar XUV flare energies. However, the XUV can be estimated by scaling from other emission expected to trace it,

namely the Si IV 1393,1402 Å and He II 1640 Å emission lines for which there are extensive stellar flare observations (Loyd & France 2014; Loyd et al. 2017a in prep). I will compare two methods to estimate stellar XUV emission during flares (1) scaling via ratios of flux in these lines to the XUV as estimated by (Youngblood et al., 2016b) for several stars and (2) scaling from the ratio of solar flare energy in the broadband XUV to the He II 304 Å line. (Observations of solar flares in Si IV 1393,1402 Å and He II 1640 Å are rare, but He II 304 Å has a nearly identical formation temperature.)

8.3.2.2 Model Creation and Exploring the Parameter Space

I will work with Tommi Koskinen to adapt the 1D photochemical-dynamical model described in Koskinen et al. (2013a) for use with time-varying radiation fields. Koskinen and I have previously collaborated to apply this model to GJ 436b in the context of recent *HST* C II and Si III observations of GJ 436b (Figure 5.4; Loyd et al. 2017a). I will then run the model over broad ranges of XUV fluence, planetary properties, and quiescent XUV levels. This will determine the relationship of the XUV flare fluence to the atmospheric mass it removes throughout the parameter space.

8.3.2.3 Dissecting the Results

To understand the numerical results, I will examine how input flare energy is budgeted by an atmosphere to determine the ultimate fate of the received XUV energy, the ionization state of the atmosphere, altitude of energy deposition, and changes in the hydrodynamics. Of particular interest will be the relationship of various relevant timescales in the hypothetical systems: the flare duration, sound crossing time, flow time, and recombination time at the location of greatest heating.

8.3.2.4 Determining the Effect of Regular Flares

Using known energy-frequency distributions of flares, I will generate synthetic XUV time series to use as input to the flare model. These will be used to compute the mass loss due to the

continual action of flaring on M stars for timescales of days. When combined with estimates of mass loss from rare, highly-energetic flares, this will determine whether the elevated XUV irradiation from regular flaring is a significant contributor to mass loss for M star planets when extrapolated to Gyr baselines.

8.3.2.5 Extension to Escape of C and O Species

Once I have addressed the flare erosion of pure H and He atmospheres, Koskinen and I will incorporate C and O species, including water, into the model. The model is already built to include multi-species chemistry and dynamics, a unique capability. The addition of C and O species will permit modeling of escape from terrestrial atmospheres that have lost their natal H/He envelopes, addressing their habitability.

8.3.2.6 Application to Known Planets

I will apply the model to specific planets of interest, using, if available, data on actual flares from the host star to guide the input XUV time series. In particular, I will determine the plausibility that XUV flares could be responsible for the large changes in the H I cloud and thus transit depth of HD 189733b (Lecavelier des Etangs et al., 2012) and that flare erosion could strip the atmosphere from, and thus sterilize, Proxima b.

Bibliography

Aarnio, A. N., Matt, S. P., & Stassun, K. G. 2012, ApJ, 760, 9

Aarnio, A. N., Stassun, K. G., Hughes, W. J., & McGregor, S. L. 2011, Sol. Phys., 268, 195

Abe, Y., Abe-Ouchi, A., Sleep, N. H., & Zahnle, K. J. 2011, Astrobiology, 11, 443

Abrahamyan, H. V., Mickaelian, A. M., & Knyazyan, A. V. 2015, Astronomy and Computing, 10, 99

Acharova, I. A., Mishurov, Y. N., & Kovtyukh, V. V. 2012, MNRAS, 420, 1590

Aigrain, S., Collier Cameron, A., Ollivier, M., et al. 2008, A&A, 488, L43

Airapetian, V. S., Glocer, A., Gronoff, G., Hébrard, E., & Danchi, W. 2016, Nature Geoscience, 9, 452

Airapetian, V. S., Glocer, A., Khazanov, G. V., et al. 2017, ApJ, 836, L3

Alcala, J. M., Krautter, J., Schmitt, J. H. M. M., et al. 1995, A&AS, 114, 109

Allende Prieto, C., & Lambert, D. L. 1999, VizieR Online Data Catalog, 335, 20555

Ambruster, C. W., Pettersen, B. R., Hawley, S., Coleman, L. A., & Sandmann, W. H. 1986, in ESA Special Publication, Vol. 263, New Insights in Astrophysics. Eight Years of UV Astronomy with IUE, ed. E. J. Rolfe

Ammons, S. M., Robinson, S. E., Strader, J., et al. 2006, ApJ, 638, 1004

Anderson, E., & Francis, C. 2012, Astronomy Letters, 38, 331

Anglada-Escudé, G., & Butler, R. P. 2012, ApJS, 200, 15

Aparicio Villegas, T., Alfaro, E. J., Cabrera-Caño, J., et al. 2010, AJ, 139, 1242

Ardila, D. R., Herczeg, G., Gregory, S. G., et al. 2013, in American Astronomical Society Meeting Abstracts, Vol. 221, American Astronomical Society Meeting Abstracts, 117.04

Armitage, P. J. 2007, ArXiv Astrophysics e-prints, astro-ph/0701485

—. 2013, Astrophysics of Planet Formation

Armstrong, D. J., Pugh, C. E., Broomhall, A.-M., et al. 2016, MNRAS, 455, 3110

Arnaud, K. A. 1996, in Astronomical Society of the Pacific Conference Series, Vol. 101, Astronomical Data Analysis Software and Systems V, ed. G. H. Jacoby & J. Barnes, 17

Athay, R. G., ed. 1976, Astrophysics and Space Science Library, Vol. 53, The solar chromosphere and corona: Quiet sun

Audard, M., Güdel, M., Drake, J. J., & Kashyap, V. L. 2000, ApJ, 541, 396

Avrett, E. H., & Loeser, R. 2008, ApJS, 175, 229

Ayres, T., & France, K. 2010, ApJ, 723, L38

Bailer-Jones, C. A. L. 2011, MNRAS, 411, 435

Bailey, J., Butler, R. P., Tinney, C. G., et al. 2009, ApJ, 690, 743

Baliunas, S., Sokoloff, D., & Soon, W. 1996, ApJ, 457, L99

Ballester, G. E., & Ben-Jaffel, L. 2015, ApJ, 804, 116

Barks, H. L., Buckley, R., Grieves, G. A., et al. 2010, ChemBioChem, 11, 1240

Basri, G., Walkowicz, L. M., Batalha, N., et al. 2010, ApJ, 713, L155

Bastian, N., Covey, K. R., & Meyer, M. R. 2010, ARA&A, 48, 339

Bastien, F. A., Stassun, K. G., Basri, G., & Pepper, J. 2013, Nature, 500, 427

Ben-Jaffel, L., & Ballester, G. E. 2013, A&A, 553, A52

Berta, Z. K., Charbonneau, D., Bean, J., et al. 2011, ApJ, 736, 12

Bertout, C., Siess, L., & Cabrit, S. 2007, A&A, 473, L21

Bianchi, L., Herald, J., Efremova, B., et al. 2011, Ap&SS, 335, 161

Biretta, J., et al. 2015, STIS Instrument Handbook, Version 14.0 (STScI)

Bochanski, J. J., Hawley, S. L., Covey, K. R., et al. 2010, AJ, 139, 2679

Bohlin, R., & Hartig, G. 1998, Clear Aperture Fractional Transmission for Point Sources, Tech. rep.

Bond, H. E., Mullan, D. J., O'Brien, M. S., & Sion, E. M. 2001, ApJ, 560, 919

Bonfanti, A., Ortolani, S., & Nascimbeni, V. 2016, A&A, 585, A5

Bonfils, X., Delfosse, X., Udry, S., et al. 2013, A&A, 549, A109

Borucki, W. J., Koch, D., Jenkins, J., et al. 2009, Science, 325, 709

Bostroem, K., & Proffitt,, C. 2011, STIS Data Handbook, Version 6.0 (STScI)

Bouchy, F., Udry, S., Mayor, M., et al. 2005, A&A, 444, L15

Bourrier, V., Ehrenreich, D., & Lecavelier des Etangs, A. 2015a, A&A, 582, A65

Bourrier, V., Lecavelier des Etangs, A., Ehrenreich, D., Tanaka, Y. A., & Vidotto, A. A. 2016, A&A, 591, A121

Bourrier, V., Lecavelier des Etangs, A., & Vidal-Madjar, A. 2014, A&A, 565, A105

—. 2015b, A&A, 573, A11

Bourrier, V., Lecavelier des Etangs, A., Dupuy, H., et al. 2013, A&A, 551, A63

Boyajian, T. S., von Braun, K., van Belle, G., et al. 2012, ApJ, 757, 112

Brekke, P., Rottman, G. J., Fontenla, J., & Judge, P. G. 1996, ApJ, 468, 418

Brown, S. A., Fletcher, L., & Labrosse, N. 2016, A&A, 596, A51

Bryden, G., Beichman, C. A., Carpenter, J. M., et al. 2009, ApJ, 705, 1226

Canto Martins, B. L., Das Chagas, M. L., Alves, S., et al. 2011, A&A, 530, A73

Caputo, F., Bono, G., Fiorentino, G., Marconi, M., & Musella, I. 2005, ApJ, 629, 1021

Carter, J. A., Winn, J. N., Holman, M. J., et al. 2011, ApJ, 730, 82

Casagrande, L., Schönrich, R., Asplund, M., et al. 2011, A&A, 530, A138

Cassak, P. A., Mullan, D. J., & Shay, M. A. 2008, ApJ, 676, L69

Cauley, P. W., Redfield, S., Jensen, A. G., & Barman, T. 2016, AJ, 152, 20

Cauley, P. W., Redfield, S., Jensen, A. G., et al. 2015, ApJ, 810, 13

Cenarro, A. J., Peletier, R. F., Sánchez-Blázquez, P., et al. 2007, MNRAS, 374, 664

Che, X., Monnier, J. D., Zhao, M., et al. 2011, ApJ, 732, 68

Christian, D. J., Mathioudakis, M., Bloomfield, D. S., Dupuis, J., & Keenan, F. P. 2004, ApJ, 612, 1140

Ciardi, D. R., von Braun, K., Bryden, G., et al. 2011, AJ, 141, 108

Cieza, L. A., Mathews, G. S., Williams, J. P., et al. 2012, ApJ, 752, 75

Clarke, J. T., Ajello, J., Ballester, G., et al. 2002, Nature, 415, 997

Cohen, O., Drake, J. J., Glocer, A., et al. 2014, ApJ, 790, 57

Cohen, O., Drake, J. J., Kashyap, V. L., et al. 2009, ApJ, 704, L85

Consortium, T. D. 2005, VizieR Online Data Catalog

Correia, A. C. M., Couetdic, J., Laskar, J., et al. 2010, A&A, 511, A21

Cowan, N. B., Greene, T., Angerhausen, D., et al. 2015, PASP, 127, 311

Crawford, D. F., Jauncey, D. L., & Murdoch, H. S. 1970, ApJ, 162, 405

Crosley, M. K., Osten, R. A., Broderick, J. W., et al. 2016, ApJ, 830, 24

Cully, S. L., Fisher, G. H., Abbott, M. J., & Siegmund, O. H. W. 1994, ApJ, 435, 435

Cuntz, M., Saar, S. H., & Musielak, Z. E. 2000, ApJ, 533, L151

Cutri, R. M., & et al. 2012, VizieR Online Data Catalog, 2311

—. 2014, VizieR Online Data Catalog, 2328

Cutri, R. M., Skrutskie, M. F., van Dyk, S., et al. 2003, VizieR Online Data Catalog, 2246

Davenport, J. R. A. 2016, ApJ, 829, 23

Davenport, J. R. A., Becker, A. C., Kowalski, A. F., et al. 2012, ApJ, 748, 58

de Bruijne, J. H. J., & Eilers, A.-C. 2012, A&A, 546, A61

Debes, J., et al. 2016, Cosmic Origins Spectrograph Instrument Handbook, Version 8.0

Debes, J. H., Jang-Condell, H., Weinberger, A. J., Roberge, A., & Schneider, G. 2013, ApJ, 771, 45

Delfosse, X., Bonfils, X., Forveille, T., et al. 2013, A&A, 553, A8

Deming, D., Seager, S., Winn, J., et al. 2009, PASP, 121, 952

Demory, B.-O., Gillon, M., Barman, T., et al. 2007, A&A, 475, 1125

Demory, B.-O., Ségransan, D., Forveille, T., et al. 2009, A&A, 505, 205

Dere, K. P., Landi, E., Young, P. R., et al. 2009, A&A, 498, 915

Domagal-Goldman, S. D., Segura, A., Claire, M. W., Robinson, T. D., & Meadows, V. S. 2014, ApJ, 792, 90

Donahue, R. A., Saar, S. H., & Baliunas, S. L. 1996, ApJ, 466, 384

Dragomir, D., Matthews, J. M., Kuschnig, R., et al. 2012, ApJ, 759, 2

Draine, B. T. 2011, Physics of the Interstellar and Intergalactic Medium

Drake, J. J., Cohen, O., Garraffo, C., & Kashyap, V. 2016, in IAU Symposium, Vol. 320, Solar and Stellar Flares and their Effects on Planets, ed. A. G. Kosovichev, S. L. Hawley, & P. Heinzel, 196–201

Drake, J. J., Cohen, O., Yashiro, S., & Gopalswamy, N. 2013, ApJ, 764, 170

Dressing, C. D., & Charbonneau, D. 2013, ApJ, 767, 95

—. 2015, ApJ, 807, 45

Ducati, J. R. 2002, VizieR Online Data Catalog, 2237

Eggen, O. J., & Iben, Jr., I. 1989, AJ, 97, 431

Ehrenreich, D., Bourrier, V., Bonfils, X., et al. 2012, A&A, 547, A18

Ehrenreich, D., Bourrier, V., Wheatley, P. J., et al. 2015, Nature, 522, 459

Eiroa, C., Marshall, J. P., Mora, A., et al. 2013, A&A, 555, A11

Evans, N. R., Schaefer, G. H., Bond, H. E., et al. 2008, AJ, 136, 1137

Eyer, L., & Grenon, M. 1997, in ESA Special Publication, Vol. 402, Hipparcos - Venice '97, ed. R. M. Bonnet, E. Høg, P. L. Bernacca, L. Emiliani, A. Blaauw, C. Turon, J. Kovalevsky, L. Lindegren, H. Hassan, M. Bouffard, B. Strim, D. Heger, M. A. C. Perryman, & L. Woltjer, 467–472

Fabricius, C., Høg, E., Makarov, V. V., et al. 2002, A&A, 384, 180

Fares, R., Donati, J.-F., Moutou, C., et al. 2010, MNRAS, 406, 409

Farihi, J., Gänsicke, B. T., & Koester, D. 2013, Science, 342, 218

Favata, F., & Schmitt, J. H. M. M. 1999, A&A, 350, 900

Finch, C. T., Zacharias, N., Subasavage, J. P., Henry, T. J., & Riedel, A. R. 2014, AJ, 148, 119

Fontenla, J. M., Curdt, W., Haberreiter, M., Harder, J., & Tian, H. 2009, ApJ, 707, 482

Fontenla, J. M., Linsky, J. L., Witbrod, J., et al. 2016, ApJ, 830, 154

Foreman-Mackey, D., Hogg, D. W., Lang, D., & Goodman, J. 2013, PASP, 125, 306

Fortney, J. J. 2005, MNRAS, 364, 649

Fossati, L., Ayres, T. R., Haswell, C. A., et al. 2013, ApJ, 766, L20

Fossati, L., Haswell, C. A., Froning, C. S., et al. 2010, ApJ, 714, L222

Fox, A. J., et al. 2017, Cosmic Origins Spectrograph Instrument Handbook, Version 9.0

France, K., Linsky, J. L., Tian, F., Froning, C. S., & Roberge, A. 2012a, ApJ, 750, L32

France, K., Schindhelm, E., Bergin, E. A., Roueff, E., & Abgrall, H. 2014, ApJ, 784, 127

France, K., Schindhelm, E., Burgh, E. B., et al. 2011, ApJ, 734, 31

France, K., Schindhelm, E., Herczeg, G. J., et al. 2012b, ApJ, 756, 171

France, K., Froning, C. S., Linsky, J. L., et al. 2013, ApJ, 763, 149

France, K., Parke Loyd, R. O., Youngblood, A., et al. 2016a, ApJ, 820, 89

France, K., Loyd, R. O. P., Youngblood, A., et al. 2016b, ApJ, 820, 89

Franchini, M., Morossi, C., & Malagnini, M. L. 1998, ApJ, 508, 370

Fressin, F., Torres, G., Charbonneau, D., et al. 2013, ApJ, 766, 81

Fuhrmeister, B., & Schmitt, J. H. M. M. 2004, A&A, 420, 1079

Fuhrmeister, B., Schmitt, J. H. M. M., & Hauschildt, P. H. 2005, A&A, 439, 1137

—. 2010, A&A, 511, A83

Fuhrmeister, B., Schmitt, J. H. M. M., & Wichmann, R. 2004, A&A, 417, 701

Gaidos, E., & Mann, A. W. 2013, ApJ, 762, 41

Gaidos, E., Mann, A. W., Lépine, S., et al. 2014, MNRAS, 443, 2561

Gaidos, E. J., Henry, G. W., & Henry, S. M. 2000, AJ, 120, 1006

Gautschy, A., & Saio, H. 1995, ARA&A, 33, 75

—. 1996, ARA&A, 34, 551

Gershberg, R. E. 1972, Ap&SS, 19, 75

—. 2005, Solar-Type Activity in Main-Sequence Stars, doi:10.1007/3-540-28243-2

Gilliland, R. L., Brown, T. M., Christensen-Dalsgaard, J., et al. 2010, PASP, 122, 131

Gilliland, R. L., Chaplin, W. J., Dunham, E. W., et al. 2011, ApJS, 197, 6

Girard, T. M., van Altena, W. F., Zacharias, N., et al. 2011, AJ, 142, 15

Glebocki, R., & Gnacinski, P. 2005, VizieR Online Data Catalog, 3244, 0

Gold, T. 1964, NASA SP-50, 824, 389

Gonzalez, G. 2011, MNRAS, 416, L80

Gould, B. G. 1879, VizieR Online Data Catalog

Gray, R. O., Corbally, C. J., Garrison, R. F., et al. 2006, AJ, 132, 161

Green, J. C., Froning, C. S., Osterman, S., et al. 2012, ApJ, 744, 60

Grenfell, J. L., Gebauer, S., v. Paris, P., Godolt, M., & Rauer, H. 2014, Planet. Space Sci., 98, 66

Grießmeier, J.-M., Stadelmann, A., Motschmann, U., et al. 2005, Astrobiology, 5, 587

Gu, P.-G., & Suzuki, T. K. 2009, ApJ, 705, 1189

Gurdemir, L., Redfield, S., & Cuntz, M. 2012, PASA, 29, 141

Haakonsen, C. B., & Rutledge, R. E. 2009, ApJS, 184, 138

Haisch, B., Strong, K. T., & Rodono, M. 1991, ARA&A, 29, 275

Hall, J. C., Henry, G. W., Lockwood, G. W., Skiff, B. A., & Saar, S. H. 2009, AJ, 138, 312

Hansteen, V. H., Hara, H., De Pontieu, B., & Carlsson, M. 2010, ApJ, 718, 1070

Harman, C. E., Schwieterman, E. W., Schottelkotte, J. C., & Kasting, J. F. 2015, ApJ, 812, 137

Harra, L. K., Schrijver, C. J., Janvier, M., et al. 2016, Sol. Phys., 291, 1761

Hartman, J. D., Bakos, G. Á., Kovács, G., & Noyes, R. W. 2010, MNRAS, 408, 475

Hashimoto, J., Dong, R., Kudo, T., et al. 2012, ApJ, 758, L19

Hatzes, A. P., & Cochran, W. D. 1995, ApJ, 452, 401

Hauschildt, P. H., & Baron, E. 1999, Journal of Computational and Applied Mathematics, 109, 41

Hawley, S. L., Davenport, J. R. A., Kowalski, A. F., et al. 2014, ApJ, 797, 121

Hawley, S. L., & Pettersen, B. R. 1991, ApJ, 378, 725

Hawley, S. L., Allred, J. C., Johns-Krull, C. M., et al. 2003, ApJ, 597, 535

Heintz, W. D. 1984, PASP, 96, 557

Hempelmann, A., Schmitt, J. H. M. M., Schultz, M., Ruediger, G., & Stepien, K. 1995, A&A, 294, 515

Henry, G. W., Howard, A. W., Marcy, G. W., Fischer, D. A., & Johnson, J. A. 2011, ArXiv e-prints, arXiv:1109.2549

Henry, G. W., & Winn, J. N. 2008, AJ, 135, 68

Henry, T. J., Jao, W.-C., Subasavage, J. P., et al. 2006, AJ, 132, 2360

Herbig, G. H., & Bell, K. R. 1988, Third Catalog of Emission-Line Stars of the Orion Population : 3 : 1988

Herczeg, G. J., Linsky, J. L., Valenti, J. A., Johns-Krull, C. M., & Wood, B. E. 2002, ApJ, 572, 310

Hilton, E. J. 2011, PhD thesis, University of Washington

Hilton, E. J., West, A. A., Hawley, S. L., & Kowalski, A. F. 2010, AJ, 140, 1402

Høg, E., Fabricius, C., Makarov, V. V., et al. 2000, A&A, 355, L27

Holmberg, J., Nordström, B., & Andersen, J. 2009a, A&A, 501, 941

—. 2009b, A&A, 501, 941

Houdebine, E. R. 2003, A&A, 397, 1019

—. 2010, MNRAS, 407, 1657

Houdebine, E. R., & Doyle, J. G. 1994, A&A, 289, 169

Houdebine, E. R., Foing, B. H., & Rodono, M. 1990, A&A, 238, 249

Houdebine, E. R., Mullan, D. J., Paletou, F., & Gebran, M. 2016, ApJ, 822, 97

Howard, A. W., Marcy, G. W., Bryson, S. T., et al. 2012, ApJS, 201, 15

Hu, R., & Seager, S. 2014, ApJ, 784, 63

Hu, R., Seager, S., & Bains, W. 2012, ApJ, 761, 166

Hudson, H. S. 1991, Sol. Phys., 133, 357

—. 2011, Space Sci. Rev., 158, 5

Hunt-Walker, N. M., Hilton, E. J., Kowalski, A. F., Hawley, S. L., & Matthews, J. M. 2012, PASP, 124, 545

Hunten, D. M. 1982, Planet. Space Sci., 30, 773

Hunten, D. M., Pepin, R. O., & Walker, J. C. G. 1987, Icarus, 69, 532

Husser, T.-O., Wende-von Berg, S., Dreizler, S., et al. 2013, A&A, 553, A6

Isaacson, H., & Fischer, D. 2010, ApJ, 725, 875

Jakosky, B. M., Grebowsky, J. M., Luhmann, J. G., et al. 2015, Science, 350, 0210

Jenkins, J. S., Ramsey, L. W., Jones, H. R. A., et al. 2009a, ApJ, 704, 975

—. 2009b, ApJ, 704, 975

Jess, D. B., Morton, R. J., Verth, G., et al. 2015, Space Sci. Rev., 190, 103

Jetsu, L., Pelt, J., & Tuominen, I. 1993, A&A, 278, 449

Jones, D. O., & West, A. A. 2016, ApJ, 817, 1

Jones, M. I., Jenkins, J. S., Rojo, P., Melo, C. H. F., & Bluhm, P. 2013, A&A, 556, A78

Kalas, P., Liu, M. C., & Matthews, B. C. 2004, Science, 303, 1990

Kaltenegger, L., Sasselov, D., & Rugheimer, S. 2013, ApJ, 775, L47

Kamper, K. W. 1996, JRASC, 90, 140

Kane, S. R., Dragomir, D., Ciardi, D. R., et al. 2011, ApJ, 737, 58

Kashyap, V. L., Drake, J. J., & Saar, S. H. 2008, ApJ, 687, 1339

Kasting, J. F., Whitmire, D. P., & Reynolds, R. T. 1993, Icarus, 101, 108

Katsova, M. M., Drake, J. J., & Livshits, M. A. 1999, ApJ, 510, 986

Kay, C., Opher, M., & Kornbleuth, M. 2016, ApJ, 826, 195

Kerwin, B. A., & Remmele, R. L. 2007, Journal of Pharmaceutical Sciences, 96, 1468

Kharchenko, N. V. 2001, Kinematika i Fizika Nebesnykh Tel, 17, 409

Khodachenko, M. L., Ribas, I., Lammer, H., et al. 2007a, Astrobiology, 7, 167

Khodachenko, M. L., Lammer, H., Lichtenegger, H. I. M., et al. 2007b, Planet. Space Sci., 55, 631

Kiraga, M., & Stepien, K. 2007, Acta Astron., 57, 149

Knutson, H. A., Madhusudhan, N., Cowan, N. B., et al. 2011, ApJ, 735, 27

Knutson, H. A., Dragomir, D., Kreidberg, L., et al. 2014, ApJ, 794, 155

Koch, D. G., Borucki, W. J., Basri, G., et al. 2010, ApJ, 713, L79

Koen, C., Kilkenny, D., van Wyk, F., & Marang, F. 2010, MNRAS, 403, 1949

König, B., Guenther, E. W., Woitas, J., & Hatzes, A. P. 2005, A&A, 435, 215

Kopp, A., Schilp, S., & Preusse, S. 2011, ApJ, 729, 116

Kopp, G., & Lean, J. L. 2011, Geophys. Res. Lett., 38, L01706

Kopparapu, R. K. 2013, ApJ, 767, L8

Koskinen, T. T., Harris, M. J., Yelle, R. V., & Lavvas, P. 2013a, Icarus, 226, 1678

Koskinen, T. T., Yelle, R. V., Harris, M. J., & Lavvas, P. 2013b, Icarus, 226, 1695

Koskinen, T. T., Yelle, R. V., Lavvas, P., & Lewis, N. K. 2010, ApJ, 723, 116

Kouloumvakos, A., Patsourakos, S., Hillaris, A., et al. 2014, Sol. Phys., 289, 2123

Kowalski, A. F., Hawley, S. L., Hilton, E. J., et al. 2009, AJ, 138, 633

Kowalski, A. F., Hawley, S. L., Wisniewski, J. P., et al. 2013, ApJS, 207, 15

Kramida, A., Ralchenko, Y., Reader, J., & NIST ASD Team. 2012

Kraus, A. L., & Hillenbrand, L. A. 2009, ApJ, 704, 531

Kraus, A. L., & Ireland, M. J. 2012, ApJ, 745, 5

Kraus, A. L., Ireland, M. J., Martinache, F., & Hillenbrand, L. A. 2011, ApJ, 731, 8

Kreidberg, L., Bean, J. L., Désert, J.-M., et al. 2014, Nature, 505, 69

Krejčová, T., & Budaj, J. 2012, A&A, 540, A82

Kulow, J. R., France, K., Linsky, J., & Loyd, R. O. P. 2014, ApJ, 786, 132

Lacy, C. H., Moffett, T. J., & Evans, D. S. 1976, ApJS, 30, 85

Ladislas Wiza, J. 1979, Nuclear Instruments and Methods, 162, 587

Lalitha, S., Poppenhaeger, K., Singh, K. P., Czesla, S., & Schmitt, J. H. M. M. 2014, ApJ, 790, L11

Lammer, H., Selsis, F., Ribas, I., et al. 2003, ApJ, 598, L121

Lammer, H., Lichtenegger, H. I. M., Kulikov, Y. N., et al. 2007, Astrobiology, 7, 185

Landolt, A. U. 2009, AJ, 137, 4186

Lanotte, A. A., Gillon, M., Demory, B.-O., et al. 2014, A&A, 572, A73

Lanza, A. F. 2008, A&A, 487, 1163

—. 2009, A&A, 505, 339

—. 2011, Ap&SS, 336, 303

Lavvas, P., Koskinen, T., & Yelle, R. V. 2014, ApJ, 796, 15

Lawler, S. M., Beichman, C. A., Bryden, G., et al. 2009, ApJ, 705, 89

Lecavelier Des Etangs, A., Ehrenreich, D., Vidal-Madjar, A., et al. 2010, A&A, 514, A72

Lecavelier des Etangs, A., Bourrier, V., Wheatley, P. J., et al. 2012, A&A, 543, L4

Leitzinger, M., Odert, P., Greimel, R., et al. 2014, MNRAS, 443, 898

Leitzinger, M., Odert, P., Hanslmeier, A., et al. 2009, in American Institute of Physics Conference Series, Vol. 1094, 15th Cambridge Workshop on Cool Stars, Stellar Systems, and the Sun, ed. E. Stempels, 680–683

Leitzinger, M., Odert, P., Ribas, I., et al. 2011, A&A, 536, A62

Lépine, S., & Gaidos, E. 2011, AJ, 142, 138

Lequeux, J. 2013, Birth, Evolution and Death of Stars (World Scientific Publishing Co), doi:10.1142/8820

Lin, R. P., Schwartz, R. A., Kane, S. R., Pelling, R. M., & Hurley, K. C. 1984, ApJ, 283, 421

Line, M. R., Knutson, H., Wolf, A. S., & Yung, Y. L. 2014, ApJ, 783, 70

Linsky, J. L. 2017, ARA&A, 55, 159

Linsky, J. L., Bushinsky, R., Ayres, T., Fontenla, J., & France, K. 2012a, ApJ, 745, 25

Linsky, J. L., Bushinsky, R., Ayres, T., & France, K. 2012b, ApJ, 754, 69

Linsky, J. L., Fontenla, J., & France, K. 2014, ApJ, 780, 61

Linsky, J. L., Yang, H., France, K., et al. 2010, ApJ, 717, 1291

Llama, J., & Shkolnik, E. L. 2015, ApJ, 802, 41

Lodders, K. 2003, ApJ, 591, 1220

Lovelock, J. E. 1965, Nature, 207, 568

Loyd, R. O. P., & France, K. 2014, ApJS, 211, 9

Loyd, R. O. P., Koskinen, T. T., France, K., Schneider, C., & Redfield, S. 2017a, ApJ, 834, L17

Loyd, R. O. P., France, K., Youngblood, A., et al. 2016, ApJ, 824, 102

Loyd, R. O. P., et al. 2017b, ApJ in prep.

Luger, R., & Barnes, R. 2015, Astrobiology, 15, 119

Lyubimkov, L. S., Lambert, D. L., Rostopchin, S. I., Rachkovskaya, T. M., & Poklad, D. B. 2010, MNRAS, 402, 1369

Madhusudhan, N., & Seager, S. 2011, ApJ, 729, 41

Mamajek, E. E., & Hillenbrand, L. A. 2008, ApJ, 687, 1264

Manara, C. F., Testi, L., Rigliaco, E., et al. 2013, A&A, 551, A107

Marsden, S. C., Petit, P., Jeffers, S. V., et al. 2014, MNRAS, 444, 3517

Martin, E. L., Rebolo, R., & Magazzu, A. 1994, ApJ, 436, 262

Mason, J. P., Woods, T. N., Caspi, A., Thompson, B. J., & Hock, R. A. 2014, ApJ, 789, 61

Mason, J. P., Woods, T. N., Webb, D. F., et al. 2016, ApJ, 830, 20

Matsakos, T., Uribe, A., & Königl, A. 2015, A&A, 578, A6

Matsui, T., & Abe, Y. 1986, Nature, 319, 303

Matsunaga, T., Hieda, K., & Nikaido, O. 1991, Photochemistry and Photobiology, 54, 403

Mayor, M., & Queloz, D. 1995, Nature, 378, 355

McCarthy, K., & White, R. J. 2012, AJ, 143, 134

McKee, C. F., & Ostriker, E. C. 2007, ARA&A, 45, 565

McQuillan, A., Aigrain, S., & Roberts, S. 2012, A&A, 539, A137

Mermilliod, J.-C. 1986, Catalogue of Eggen's UBV data., 0 (1986)

Messina, S., Desidera, S., Lanzafame, A. C., Turatto, M., & Guinan, E. F. 2011, A&A, 532, A10

Messina, S., Desidera, S., Turatto, M., Lanzafame, A. C., & Guinan, E. F. 2010, A&A, 520, A15

Metchev, S. A., & Hillenbrand, L. A. 2009, ApJS, 181, 62

Miguel, Y., & Kaltenegger, L. 2014, ApJ, 780, 166

Miguel, Y., Kaltenegger, L., Linsky, J. L., & Rugheimer, S. 2015, MNRAS, 446, 345

Miller, B. P., Gallo, E., Wright, J. T., & Pearson, E. G. 2015, ApJ, 799, 163

Mitra-Kraev, U., Harra, L. K., Güdel, M., et al. 2005, A&A, 431, 679

Moffett, T. J. 1972, Nature Physical Science, 240, 41

Montes, D., López-Santiago, J., Fernández-Figueroa, M. J., & Gálvez, M. C. 2001a, A&A, 379, 976

Montes, D., López-Santiago, J., Gálvez, M. C., et al. 2001b, MNRAS, 328, 45

Moses, J. I. 2014, Philosophical Transactions of the Royal Society of London Series A, 372, 20130073

Moses, J. I., Visscher, C., Fortney, J. J., et al. 2011, ApJ, 737, 15

Moses, J. I., Line, M. R., Visscher, C., et al. 2013, ApJ, 777, 34

Mullan, D. J., Mathioudakis, M., Bloomfield, D. S., & Christian, D. J. 2006, ApJS, 164, 173

Murray-Clay, R. A., Chiang, E. I., & Murray, N. 2009, ApJ, 693, 23

Myers, J. R., Sande, C. B., Miller, A. C., Warren, Jr., W. H., & Tracewell, D. A. 2015, VizieR Online Data Catalog, 5145

Ness, J.-U., Güdel, M., Schmitt, J. H. M. M., Audard, M., & Telleschi, A. 2004, A&A, 427, 667

Ness, N. F. 1965, J. Geophys. Res., 70, 2989

Neuhäuser, R., Brandner, W., Eckart, A., et al. 2000, A&A, 354, L9

Neves, V., Bonfils, X., Santos, N. C., et al. 2013, A&A, 551, A36

—. 2014, A&A, 568, A121

Newton, E. R., Irwin, J., Charbonneau, D., et al. 2016, ApJ, 821, 93

Nita, G. M., Gary, D. E., Lanzerotti, L. J., & Thomson, D. J. 2002, ApJ, 570, 423

Noyes, R. W., Hartmann, L. W., Baliunas, S. L., Duncan, D. K., & Vaughan, A. H. 1984, ApJ, 279, 763

Ochsenbein, F., Bauer, P., & Marcout, J. 2000, A&AS, 143, 23

Önehag, A., Heiter, U., Gustafsson, B., et al. 2012, A&A, 542, A33

Osten, R. A., Hawley, S. L., Allred, J. C., Johns-Krull, C. M., & Roark, C. 2005, ApJ, 621, 398

Osten, R. A., & Wolk, S. J. 2015, ApJ, 809, 79

Osten, R. A., Godet, O., Drake, S., et al. 2010, ApJ, 721, 785

Osten, R. A., Kowalski, A., Drake, S. A., et al. 2016, ApJ, 832, 174

Owen, J. E., & Adams, F. C. 2016, MNRAS, 456, 3053

Owen, J. E., & Alvarez, M. A. 2016, ApJ, 816, 34

Palla, F., & Stahler, S. W. 2002, ApJ, 581, 1194

Parker, E. N. 1972, ApJ, 174, 499

Patel, B. H., Percivalle, C., Ritson, D. J., Duffy, C. D., & Sutherland, J. D. 2015, Nature Chemistry, 7, 301

Peacock, S., Barman, T. S., & Shkolnik, E. 2015, in American Astronomical Society Meeting Abstracts, Vol. 225, American Astronomical Society Meeting Abstracts, 138.26

Perryman, M. 2014, American Journal of Physics, 82, 552

Peter, H. 2006, A&A, 449, 759

Petit, P., Dintrans, B., Solanki, S. K., et al. 2008, MNRAS, 388, 80

Pettersen, B. R. 1989, Sol. Phys., 121, 299

Pettersen, B. R., Coleman, L. A., & Evans, D. S. 1984, ApJS, 54, 375

Pickles, A., & Depagne, É. 2010, PASP, 122, 1437

Pierrehumbert, R., & Gaidos, E. 2011, ApJ, 734, L13

Pillitteri, I., Günther, H. M., Wolk, S. J., Kashyap, V. L., & Cohen, O. 2011, ApJ, 741, L18

Pillitteri, I., Maggio, A., Micela, G., et al. 2015, ApJ, 805, 52

Pillitteri, I., Wolk, S. J., Lopez-Santiago, J., et al. 2014, ApJ, 785, 145

Plavchan, P., Werner, M. W., Chen, C. H., et al. 2009, ApJ, 698, 1068

Pojmanski, G., Pilecki, B., & Szczygiel, D. 2005, Acta Astron., 55, 275

Poppenhaeger, K., Robrade, J., & Schmitt, J. H. M. M. 2010, A&A, 515, A98

Poppenhaeger, K., & Schmitt, J. H. M. M. 2011, ApJ, 735, 59

Poppenhaeger, K., & Wolk, S. J. 2014, A&A, 565, L1

Press, W. H., Teukolsky, S. A., Vetterling, W. T., & Flannery, B. P. 2002, Numerical recipes in C++ : the art of scientific computing

Preusse, S., Kopp, A., Büchner, J., & Motschmann, U. 2006, A&A, 460, 317

Pye, J. P., Rosen, S., Fyfe, D., & Schröder, A. C. 2015, A&A, 581, A28

Reid, I. N., Cruz, K. L., Allen, P., et al. 2004, AJ, 128, 463

Reiners, A., & Basri, G. 2009, ApJ, 705, 1416

Riboni, E., Poretti, E., & Galli, G. 1994, A&AS, 108, 55

Ricker, G. R., Winn, J. N., Vanderspek, R., et al. 2014, in Proc. SPIE, Vol. 9143, Space Telescopes and Instrumentation 2014: Optical, Infrared, and Millimeter Wave, 914320

Riley, A., et al. 2017, STIS Instrument Handbook, Version 16.0

Ritson, D., & Sutherland, J. D. 2012, Nature Chemistry, 4, 895

Rivera, E. J., Lissauer, J. J., Butler, R. P., et al. 2005, ApJ, 634, 625

Riviere-Marichalar, P., Ménard, F., Thi, W. F., et al. 2012, A&A, 538, L3

Robinson, R. D., Carpenter, K. G., & Percival, J. W. 1999, ApJ, 516, 916

Robrade, J., Schmitt, J. H. M. M., & Favata, F. 2012, A&A, 543, A84

Rodríguez, E., López-González, M. J., & López de Coca, P. 2000, A&AS, 144, 469

Roeser, S., Demleitner, M., & Schilbach, E. 2010, AJ, 139, 2440

Rojas-Ayala, B., Covey, K. R., Muirhead, P. S., & Lloyd, J. P. 2012, ApJ, 748, 93

Röser, S., Schilbach, E., Schwan, H., et al. 2008, A&A, 488, 401

Rubenstein, E. P., & Schaefer, B. E. 2000, ApJ, 529, 1031

Rugheimer, S., Kaltenegger, L., Segura, A., Linsky, J., & Mohanty, S. 2015, ApJ, 809, 57

Ryan, J. M., Lockwood, J. A., & Debrunner, H. 2000, Space Sci. Rev., 93, 35

Rybicki, G. B., & Lightman, A. P. 2004, Radiative Processes in Astrophysics, 400

Rybicki, G. B., & Press, W. H. 1995, Physical Review Letters, 74, 1060

Salim, S., & Gould, A. 2003, ApJ, 582, 1011

Santos, N. C., Israelian, G., Mayor, M., et al. 2005, A&A, 437, 1127

Santos, N. C., Sousa, S. G., Mortier, A., et al. 2013a, A&A, 556, A150

—. 2013b, A&A, 556, A150

Scharf, C. A. 2010, ApJ, 722, 1547

Schlawin, E., Agol, E., Walkowicz, L. M., Covey, K., & Lloyd, J. P. 2010, ApJ, 722, L75

Schmieder, B., Aulanier, G., & Vršnak, B. 2015, Sol. Phys., 290, 3457

Sciortino, S., Maggio, A., Favata, F., & Orlando, S. 1999, A&A, 342, 502

Seager, S., Bains, W., & Hu, R. 2013, ApJ, 777, 95

Seager, S., & Deming, D. 2010, ARA&A, 48, 631

Segura, A., Kasting, J. F., Meadows, V., et al. 2005, Astrobiology, 5, 706

Segura, A., Meadows, V. S., Kasting, J. F., Crisp, D., & Cohen, M. 2007, A&A, 472, 665

Segura, A., Walkowicz, L. M., Meadows, V., Kasting, J., & Hawley, S. 2010, Astrobiology, 10, 751

Selsis, F., Despois, D., & Parisot, J.-P. 2002, A&A, 388, 985

Selsis, F., Kasting, J. F., Levrard, B., et al. 2007, A&A, 476, 1373

Senanayake, S. D., & Idriss, H. 2006, Proceedings of the National Academy of Science, 103, 1194

Shakhovskaia, N. I. 1989, Sol. Phys., 121, 375

Shenavrin, V. I., Taranova, O. G., & Nadzhip, A. E. 2011, Astronomy Reports, 55, 31

Shields, A. L., Ballard, S., & Johnson, J. A. 2016, ArXiv e-prints, arXiv:1610.05765

Shkolnik, E. 2004, PhD thesis, University of British Columbia

Shkolnik, E., Bohlender, D. A., Walker, G. A. H., & Collier Cameron, A. 2008, ApJ, 676, 628

Shkolnik, E., Liu, M. C., & Reid, I. N. 2009, ApJ, 699, 649

Shkolnik, E., Walker, G. A. H., & Bohlender, D. A. 2003, ApJ, 597, 1092

Shkolnik, E., Walker, G. A. H., Bohlender, D. A., Gu, P.-G., & Kürster, M. 2005, ApJ, 622, 1075

Shkolnik, E. L. 2013, ApJ, 766, 9

Shkolnik, E. L., & Barman, T. S. 2014, AJ, 148, 64

Shkolnik, E. L., Liu, M. C., Reid, I. N., Dupuy, T., & Weinberger, A. J. 2011, ApJ, 727, 6

Silva-Valio, A. 2008, ApJ, 683, L179

Skumanich, A. 1972, ApJ, 171, 565

Smith, M. D. 2004, The Origin of Stars (World Scientific Publishing Co), doi:10.1142/p353

Smith, R. K., Brickhouse, N. S., Liedahl, D. A., & Raymond, J. C. 2001, ApJ, 556, L91

Soubiran, C., Le Campion, J.-F., Cayrel de Strobel, G., & Caillo, A. 2010a, A&A, 515, A111

—. 2010b, A&A, 515, A111

Sousa, S. G., Santos, N. C., Israelian, G., et al. 2011, A&A, 526, A99

Sterzik, M. F., Alcalá, J. M., Covino, E., & Petr, M. G. 1999, A&A, 346, L41

Stevenson, K. B., Harrington, J., Nymeyer, S., et al. 2010, Nature, 464, 1161

Strassmeier, K. G. 2009, A&A Rev., 17, 251

Strassmeier, K. G., & Rice, J. B. 1998, A&A, 330, 685

Suárez Mascareño, A., Rebolo, R., González Hernández, J. I., & Esposito, M. 2015, MNRAS, 452, 2745

Sun, X., Bobra, M. G., Hoeksema, J. T., et al. 2015, ApJ, 804, L28

Takeda, G., Ford, E. B., Sills, A., et al. 2007, ApJS, 168, 297

Telleschi, A., Güdel, M., Briggs, K., et al. 2005, ApJ, 622, 653

Tetzlaff, N., Neuhäuser, R., & Hohle, M. M. 2011, MNRAS, 410, 190

Tevini, M. 1993, UV-B radiation and ozone depletion: effects on humans, animals, plants, microorganisms, and materials / edited by Manfred Tevini (Boca Raton, Florida: Lewis Publishers,)

Thalmann, J. K., Su, Y., Temmer, M., & Veronig, A. M. 2015, ApJ, 801, L23

Tian, F., France, K., Linsky, J. L., Mauas, P. J. D., & Vieytes, M. C. 2014, Earth and Planetary Science Letters, 385, 22

Tian, F., Toon, O. B., Pavlov, A. A., & De Sterck, H. 2005, ApJ, 621, 1049

Tofflemire, B. M., Wisniewski, J. P., Kowalski, A. F., et al. 2012, AJ, 143, 12

Toon, O. B., McKay, C. P., Ackerman, T. P., & Santhanam, K. 1989, J. Geophys. Res., 94, 16287

Torres, C. A. O., Quast, G. R., da Silva, L., et al. 2006, A&A, 460, 695

Torres, G. 2007, ApJ, 671, L65

Torres, G., Winn, J. N., & Holman, M. J. 2008, ApJ, 677, 1324

Tovmassian, H. M., Zalinian, V. P., Silant'ev, N. A., Cardona, O., & Chavez, M. 2003, A&A, 399, 647

Traub, W. A. 2012, ApJ, 745, 20

Triaud, A. H. M. J., Lanotte, A. A., Smalley, B., & Gillon, M. 2014, MNRAS, 444, 711

Tsantaki, M., Sousa, S. G., Adibekyan, V. Z., et al. 2013, A&A, 555, A150

Valenti, J. A., & Fischer, D. A. 2005, ApJS, 159, 141

van Belle, G. T., & von Braun, K. 2009, ApJ, 694, 1085

van Eyken, J. C., Ciardi, D. R., von Braun, K., et al. 2012, ApJ, 755, 42

Van Grootel, V., Gillon, M., Valencia, D., et al. 2014, ApJ, 786, 2

van Leeuwen, F. 2007a, A&A, 474, 653

—. 2007b, A&A, 474, 653

Vaughan, A. H., Preston, G. W., Baliunas, S. L., et al. 1981, ApJ, 250, 276

Vida, K., Kriskovics, L., Oláh, K., et al. 2016, A&A, 590, A11

Vidal-Madjar, A., Lecavelier des Etangs, A., Désert, J.-M., et al. 2003, Nature, 422, 143

Vidal-Madjar, A., Désert, J.-M., Lecavelier des Etangs, A., et al. 2004, ApJ, 604, L69

Vidal-Madjar, A., Huitson, C. M., Bourrier, V., et al. 2013, A&A, 560, A54

Vilhu, O. 1984, A&A, 133, 117

Villadsen, J., Hallinan, G., Monroe, R., Bourke, S., & Starburst Program Team. 2017, in American Astronomical Society Meeting Abstracts, Vol. 229, American Astronomical Society Meeting Abstracts, 116.05

Voet, D., Gratzer, W. B., Cox, R. A., & Doty, P. 1963, Biopolymers, 1, 193

Vogt, S. S., Butler, R. P., Rivera, E. J., et al. 2010, ApJ, 723, 954

von Braun, K., Boyajian, T. S., Kane, S. R., et al. 2012, ApJ, 753, 171

von Braun, K., Boyajian, T. S., van Belle, G. T., et al. 2014, MNRAS, 438, 2413

Wahlstrom, C., & Carlsson, M. 1994, ApJ, 433, 417

Walker, G. A. H., Croll, B., Matthews, J. M., et al. 2008, A&A, 482, 691

Watson, C. L. 2006, Society for Astronomical Sciences Annual Symposium, 25, 47

Wedemeyer-Böhm, S., Lagg, A., & Nordlund, Å. 2009, Space Sci. Rev., 144, 317

Weis, E. W. 1996, AJ, 112, 2300

Weise, P., Launhardt, R., Setiawan, J., & Henning, T. 2010, A&A, 517, A88

Welsh, B. Y., Wheatley, J. M., Seibert, M., et al. 2007, ApJS, 173, 673

Wenger, M., Ochsenbein, F., Egret, D., et al. 2000, A&AS, 143, 9

West, R. G., Almenara, J.-M., Anderson, D. R., et al. 2013, ArXiv e-prints, arXiv:1310.5607

White, R. J., Gabor, J. M., & Hillenbrand, L. A. 2007, AJ, 133, 2524

Wilson, O. C. 1963, ApJ, 138, 832

Wilson, R. E., & Devinney, E. J. 1971, ApJ, 166, 605

Winters, J. G., Henry, T. J., Lurie, J. C., et al. 2015, AJ, 149, 5

Wood, B. E., Linsky, J. L., & Ayres, T. R. 1997, ApJ, 478, 745

Wood, B. E., Müller, H.-R., Zank, G. P., Linsky, J. L., & Redfield, S. 2005, ApJ, 628, L143

Woodgate, B. E., Kimble, R. A., Bowers, C. W., et al. 1998, PASP, 110, 1183

Woods, T. N., Chamberlin, P. C., Harder, J. W., et al. 2009, Geophys. Res. Lett., 36, L01101

Woods, T. N., Hock, R., Eparvier, F., et al. 2011, ApJ, 739, 59

Wordsworth, R., & Pierrehumbert, R. 2014, ApJ, 785, L20

Wright, J. T., Fakhouri, O., Marcy, G. W., et al. 2011a, PASP, 123, 412

—. 2011b, PASP, 123, 412

Xiao, H. Y., Covey, K. R., Rebull, L., et al. 2012, ApJS, 202, 7

Yashiro, S., Akiyama, S., Gopalswamy, N., & Howard, R. A. 2006, ApJ, 650, L143

Yashiro, S., Gopalswamy, N., Michalek, G., et al. 2004, Journal of Geophysical Research (Space Physics), 109, A07105

Yelle, R. V. 2004, Icarus, 170, 167

Yıldız, M. 2007, MNRAS, 374, 1264

Yoshino, K., Esmond, J. R., Cheung, A. S.-C., Freeman, D. E., & Parkinson, W. H. 1992, Planet. Space Sci., 40, 185

Youdin, A. N., & Kenyon, S. J. 2013, From Disks to Planets, ed. T. D. Oswalt, L. M. French, & P. Kalas, 1

Youngblood, A., France, K., Parke Loyd, R. O., et al. 2016a, ApJ, 824, 101

Youngblood, A., France, K., Loyd, R. O. P., et al. 2016b, ApJ, 824, 101

—. 2017, ApJ, 843, 31

Zacharias, N., Finch, C. T., Girard, T. M., et al. 2012, VizieR Online Data Catalog, 1322

Zacharias, N., Monet, D. G., Levine, S. E., et al. 2004a, in Bulletin of the American Astronomical Society, Vol. 36, American Astronomical Society Meeting Abstracts, 1418

Zacharias, N., Urban, S. E., Zacharias, M. I., et al. 2004b, AJ, 127, 3043

Appendix A

Appendices to Chapter 3

A.1 Target Confusion

For some of the targets, other FUV sources were present within the instrument aperture. Targets with known or suspected companions within the field of view of the instrument, but that should not contribute more than 10% of the measured FUV flux, are as follows.

- EK Dra has low-mass (0.5±0.1 $M_{\odot}$) binary companion GJ559.1B at 0.7" angular separation as of 2002 Oct and an orbital period of 45±5 years with a V band magnitude difference of 6 (König et al., 2005).
- Polaris Aa has binary companion Polaris Ab of spectral type F6V at 0.170±0.003" separation as of 2006 Aug and an orbital period of 29.59±0.02 years with a V band magnitude difference of 7.2 (Kamper, 1996; Evans et al., 2008).
- HD103095 might have companion CF UMa, but its existence is uncertain (Heintz, 1984).

A.2 Sensitivity to Excess Noise

A brief look at the sample variance statistic, $\hat{\sigma}^2$, provides insight into the driving factors concerning the sensitivity of excess noise measurements. Since $\hat{\sigma}$ monotonically increases with $\hat{\sigma}^2$, greater sensitivity to one translates to the other. When $\hat{\sigma}^2$ is computed from a set of N points drawn from a Gaussian distribution with true variance σ^2, the statistic $(N-1)\hat{\sigma}^2/\sigma^2$ follows a χ^2

distribution of $N-1$ degrees of freedom. Thus, the variance of this statistic is

$$\mathrm{V}\left[\frac{(N-1)\hat{\sigma}^2}{\sigma^2}\right] = 2(N-1). \tag{A.1}$$

However, when examining the stochastic fluctuations of a star, we are concerned with the magnitude of the sample variance relative to the mean, $\hat{\sigma}^2/\mu^2$. Assuming the null hypothesis that the data are described by a Poisson distribution such that $\sigma^2 = \mu$,

$$\mathrm{V}\left[\frac{\hat{\sigma}^2}{\mu^2}\right] = \frac{2}{(N-1)\mu^2}. \tag{A.2}$$

Thus, for a given measurement of $\hat{\sigma}^2$, the null hypothesis can be rejected with greater confidence as μ and N increase. In other words, sensitivity to excess variance ($\hat{\sigma}^2$ above μ) is better for targets with stronger signal and longer durations of observations, as one might intuitively expect. Although we employ a maximum-likelihood method when estimating excess noise in the lightcurves rather than computing $\hat{\sigma}^2$, these drivers of sensitivity are apparent in the results.

Of further interest would be a cadence that minimizes the variance on the cadence-independent quantity

$$\frac{\hat{\sigma}^2}{\mu^2}\Delta t.$$

The mean is directly proportional to the cadence length, $\mu \propto \Delta t$, and, for a fixed quantity of data, $N \propto \Delta t^{-1}$. Additionally, if each lightcurve point is uncorrelated to surrounding points no matter how short of a cadence is employed, then σ^2 scales as Δt. For large N such that the 1 in the $(N-1)$ terms of Equation (A.1) can be neglected,

$$\mathrm{V}\left[\frac{\hat{\sigma}^2}{\mu^2}\Delta t\right] \propto \Delta t. \tag{A.3}$$

Hence, by this analysis it is always beneficial to choose the shortest possible cadence. However, σ^2 does not scale as Δt for all Δt as we have assumed in this analysis. This factor is part of what drives the choice of Δt, as discussed in Section 3.2.2.

A.3 Maximum-Likelihood Estimation of Excess Noise

To explain in detail how we estimated σ_x, we must first discuss again the high-pass filtering to which we subjected the data. This filtering alters a series of points even if they exhibit pure white noise (i.e. no periodic signals). Yet the white noise in the data is exactly what we wished to preserve and measure. Thus, we attempted a simple correction. To formulate our correction, we assumed the high-pass filtering scales the white-noise scatter in a lightcurve by a constant factor, α. However, this factor was unknown for the actual data because the portion of the data represented by white noise was also unknown. For a set of simulated data (i.e. data known to be purely white noise), the factor could be determined by computing the standard deviation before filtering, σ, and after filtering, σ'. Then $\alpha = \sigma/\sigma'$. Thus, each simulated dataset would produce a different value for α. After simulating many datasets and recording α for each, the results could be histogrammed to estimate the probability density function (PDF) of α. The shape of the PDF depends on the spacing of the points and the cutoff frequency of the high-pass filter, but the PDF is independent of the amplitude of σ. For our purposes, we estimated the PDF of α using 10^4 white-noise simulations of each lightcurve separately. The PDFs were often noticeably asymmetric, with means generally within a few percent of unity.

With PDFs for α in hand, we computed maximum-likelihood values of σ_x as follows. First, we modeled each high-pass filtered lightcurve as points randomly drawn from independent Gaussians (one for each point). The variance of the Gaussian for point i we assumed to be

$$\sigma_i^2 = \sigma_{p,i}^2 + \sigma_x^2 = F_{signal,i} + F_{bkgnd,i} + \sigma_x^2, \tag{A.4}$$

where $F_{signal,i}$ and $F_{bkgnd,i}$ are the signal counts and expected background counts in the extraction region for lightcurve point i. Then we assumed this white-noise lightcurve (more specifically the mean-normalized, mean-subtracted lightcurve) was scaled by α, the unknown factor discussed above, due to the high pass filtering. Thus, the set of $\sigma_{p,i}$, σ_x, and α fully specified a given lightcurve in our model. The $\sigma_{p,i}$ we estimated as the quadratic sum the signal and background Poisson noise for each point. The values of σ_x and α we sampled over a grid and computed the likelihood of the

data, $\mathcal{L}(\mathbf{F}\ |\sigma_x, \alpha)$, at every grid point. Here $\mathbf{F}$ represents the vector of N lightcurve points.

We found $\mathcal{L}(\mathbf{F}\ |\sigma_x, \alpha)$ as follows. First, we scaled the data back by α^{-1}. In other words, we computed $\alpha^{-1}(\mathbf{F} - \langle\mathbf{F}\rangle)$, where $\langle\mathbf{F}\rangle$ is the mean value of the lightcurve. If the sampled α were the true α, this would have rescaled the white noise in the data to its original state (without the filtered low-frequency signals). Next, we computed the likelihood that the lightcurve points were randomly drawn from the Gaussians with variances augmented by σ_x. Finally, we multiplied this by the probability, $p(\alpha)$, of the α we assumed. This determined the likelihood that the original data were randomly drawn from the specified Gaussians **and** were then scaled by α. Altogether, this gives

$$\mathcal{L}(\mathbf{F}\ |\sigma_x, \alpha) = p(\alpha) \prod_{i=1}^{N} \frac{1}{\sigma_i\sqrt{2\pi}} e^{-\alpha^{-2}(F_i - \langle\mathbf{F}\rangle)^2/2\sigma_i^2}. \tag{A.5}$$

We computed likelihood values in log space, such that

$$\ln\left[\mathcal{L}(\mathbf{F}\ |\sigma_x, \alpha)\right] = \ln\left[p(\alpha)\right] - \sum_{i=1}^{N}\left[\ln\left(\sigma_i\sqrt{2\pi}\right) + \frac{\alpha^{-2}(F_i - \langle\mathbf{F}\rangle)^2}{2\sigma_i^2}\right] + A, \tag{A.6}$$

where A is a normalization factor, constant for all sampled values of σ_x for which we computed $\mathcal{L}$. We chose it to avoid arithmetic underflow when we returned to $\mathcal{L}$ from $\ln\mathcal{L}$. After returning from log-space, for each sampled value of σ_x we marginalized over all sampled values of α to estimate

$$\mathcal{L}(\mathbf{F}\ |\sigma_x) = \int_{-\infty}^{\infty} \mathcal{L}(\mathbf{F}\ |\sigma_x, \alpha) d\alpha. \tag{A.7}$$

The quantity of interest was the likelihood of σ_x given the data $\mathbf{F}$ rather than the likelihood of the data given a value of σ_x. Thus, we turned to Bayes Theorem and enforced the prior probability distribution that all $\sigma_x \geq 0$ were uniformly probable while all $\sigma_x < 0$ were impossible. Values of $\sigma_x < 0$ are nonsensical. Bayes Theorem simply yields

$$\mathcal{L}(\sigma_x|\mathbf{F}\ ) = \begin{cases} \mathcal{L}(\mathbf{F}\ |\sigma_x) & : \sigma_x \geq 0 \\ 0 & : \sigma_x < 0 \end{cases} \tag{A.8}$$

We then used the likelihood distribution to compute the maximum-likelihood value and 68.3% error bars or the 95% upper limit.

Appendix B

Appendices to Chapter 6

B.1 Details on the Flare Identification Algorithm

For the identification of flares, FUV lightcurves were created with a time binning that provided a median S/N of 2. This optimization of the time binning is possible because of the data consist of discrete detector events rather than integrated counts. Thus, lightcurves can be created with arbitrary cadences, limited in practice only by S/N considerations and the exposure lengths. We imposed a floor of 5 s on the time bins. Data were rejected if count rates were too low to achieve the desired S/N with time bins shorter than 5 min or if there were fewer than 20 lightcurve points.

We smoothed the lightcurves using the exponential rectification scheme of (Rybicki & Press, 1995) and a decorrelation length of 5×10^4 s. This algorithm allowed us to project the smoothed lightcurve (i.e. rectify the data) into regions of data culled because they were within a flare. Because large flares often strongly influence the shape of the smoothed lightcurve, particularly as the decorrelation length is reduced, we began each flare identification run using a decorellation length 100 times that of the final value (creating a "smoother" curve), then progressively reduced this parameter to its final value.

As described above, runs were identified relative to the smoothed lightcurves. We did not allow runs to extend over exposure gaps. Therefore, flares spanning multiple exposures are identified as separate flares, but no such flares were identified in the FUV_{130} band. After large positive runs were identified as flares, we combined any flares that were separated by a gap shorter than half the

duration of the shorter of the abutting flares.

The factor by which the area of a positive run had to exceed the median run area in order to be identified as a flare, the "flag factor," was determined using a Monte Carlo method to determine the factor that would ensure a false alarm rate of $< 1\%$ per 2700 s of data (typical length of a single *HST* exposure). This factor depends on the (1) count rate and (2) time binning of the data, (1) because of skewness in the Poisson noise that depends on the count rate and (2) because this determines the number of points in a given span of data and thus the number of "chances" random fluctuations have to mimic a flare. Thus, we computed appropriate factors with Monte Carlo simulations over a grid of count rates and time bin sizes. Factors spanned values of roughly $7 - 11$ and depend primarily on the time binning rather than count rate. The appropriate factor for count rates in the range of $6 - 100$ is well approximated by the empirical fit $f = 2.73 \log_{10} N + 4.13$, where N is the number of points and f is the desired factor. The product of this factor and the median run area in a dataset provides a well-defined detection limit for the minimum detectable flare energy in a dataset.

In some cases, most notably for Prox Cen, the count rate varied considerably between exposures despite a roughly constant quiescent flux. This changed the median run area substantially, so we grouped these exposures into separate sets based on 0.4 dex S/N intervals, determined by experimenting with the tradeoff between smaller intervals and the resulting shorter data baselines.

Our algorithm occasionally reached a steady-state oscillation, associating points with a flare in one iteration, then de-associating them in the next iteration using the new version of the smoothed lightcurve, then associating them again, ad infinitum. We programmed the pipeline to resolve the problem by resampling the lightcurve with 10% longer time bins if a maximum iteration threshold was hit.